REACHING NEW HEIGHTS: RECENT PROGRESS IN PALEOTOPOGRAPHY

EDITED BY: Paolo Ballato, Carina Hoorn, Alexis Licht, Katharina Aenne Methner and Heiko Pingel

PUBLISHED IN: Frontiers in Earth Science

frontiers Research Topics

ISSN 1664-8714
ISBN 978-2-88971-612-8
DOI 10.3389/978-2-88971-612-8

About Frontiers

Frontiers is more than just an open-access publisher of scholarly articles: it is a pioneering approach to the world of academia, radically improving the way scholarly research is managed. The grand vision of Frontiers is a world where all people have an equal opportunity to seek, share and generate knowledge. Frontiers provides immediate and permanent online open access to all its publications, but this alone is not enough to realize our grand goals.

Frontiers Journal Series

The Frontiers Journal Series is a multi-tier and interdisciplinary set of open-access, online journals, promising a paradigm shift from the current review, selection and dissemination processes in academic publishing. All Frontiers journals are driven by researchers for researchers; therefore, they constitute a service to the scholarly community. At the same time, the Frontiers Journal Series operates on a revolutionary invention, the tiered publishing system, initially addressing specific communities of scholars, and gradually climbing up to broader public understanding, thus serving the interests of the lay society, too.

Dedication to Quality

Each Frontiers article is a landmark of the highest quality, thanks to genuinely collaborative interactions between authors and review editors, who include some of the world's best academicians. Research must be certified by peers before entering a stream of knowledge that may eventually reach the public - and shape society; therefore, Frontiers only applies the most rigorous and unbiased reviews.
Frontiers revolutionizes research publishing by freely delivering the most outstanding research, evaluated with no bias from both the academic and social point of view. By applying the most advanced information technologies, Frontiers is catapulting scholarly publishing into a new generation.

What are Frontiers Research Topics?

Frontiers Research Topics are very popular trademarks of the Frontiers Journals Series: they are collections of at least ten articles, all centered on a particular subject. With their unique mix of varied contributions from Original Research to Review Articles, Frontiers Research Topics unify the most influential researchers, the latest key findings and historical advances in a hot research area! Find out more on how to host your own Frontiers Research Topic or contribute to one as an author by contacting the Frontiers Editorial Office: frontiersin.org/about/contact

REACHING NEW HEIGHTS: RECENT PROGRESS IN PALEOTOPOGRAPHY

Topic Editors:
Paolo Ballato, Roma Tre University, Italy
Carina Hoorn, University of Amsterdam, Netherlands
Alexis Licht, University of Washington, United States
Katharina Aenne Methner, Stanford University, United States
Heiko Pingel, University of Potsdam, Germany

Citation: Ballato, P., Hoorn, C., Licht, A., Methner, K. A., Pingel, H., eds. (2021). Reaching New Heights: Recent Progress in Paleotopography. Lausanne: Frontiers Media SA. doi: 10.3389/978-2-88971-612-8

Table of Contents

frontiers in Earth Science

EDITORIAL
published: 23 September 2021
doi: 10.3389/feart.2021.772818

Editorial: Reaching New Heights: Recent Progress in Paleotopography

Paolo Ballato[1]*, *Carina Hoorn*[2], *Alexis Licht*[3], *Katharina Aenne Methner*[4] and *Heiko Pingel*[5]

[1]Department of Science, University of Roma Tre, Rome, Italy, [2]Paleoecology and Landscape Ecology, Institute for Biodiversity and Ecosystem Dynamics (IBED), University of Amsterdam, Amsterdam, Netherlands, [3]Aix-Marseille Université, CNRS, IRD, INRAE, CEREGE, Aix-en-Provence, France, [4]Department of Geological Sciences, Stanford University, Stanford, CA, United States, [5]Institute of Geosciences, University of Potsdam, Potsdam, Germany

Keywords: mountain building, orogenic plateaus, paleoaltimetry, stable isotopes, computational modeling, landscape evolution

Editorial on the Research Topic

Reaching New Heights: Recent Progress in Paleotopography

Although mountain belts and orogenic plateaus occupy only a limited portion of the Earth's surface (about 4% above 2 km in elevation), they are among the most prominent landscape features with global implications for tectonic deformation, climate, hydrology, and biodiversity. Topographic growth locally modifies the crustal stress field and the locus of active deformation; it re-arranges fluvial networks and atmospheric circulation patterns; it generates highly asymmetric precipitation and marked temperature gradients, and favors the development of diverse ecosystems over geographically limited areas; it thus dramatically impacts biodiversity and the evolution of flora and fauna over geological scales.

In recent years, a growing number of studies have tried to investigate the chronology and amplitude of topographic growth in deep time (millions of years), using various field-, laboratory-, and computer-based approaches from a wide range of scientific disciplines. The accuracy and uncertainty associated with these approaches are still being discussed, and studies providing quantitative paleoaltimetry estimates remain rare despite their relevance. Moreover, most quantitative studies so far have concentrated on the youngest and most extensive mountain ranges such as the Himalayas or the American Cordilleras, while the topographic evolution of smaller or much older orogens remain virtually undocumented.

This Research Topic contains 11 articles covering a wide range of paleotopography research, from short reviews and perspectives of either established or innovative paleo-topographic approaches, new datasets and syntheses of topographic uplift in well-known and understudied areas, and outlooks on the future development and improvement of paleoaltimetry.

Botsyun and Ehlers present recent advances and caveats in high-resolution isotope-based general circulation models (iGCMs) to calibrate stable isotope paleoaltimetry approaches, a growing and dynamic direction for paleotopographic reconstructions. Hren and Ouimet propose a new method to quantify paleotopography based on the isotopic signature of organic molecular biomarkers integrated over river catchments. Following the recent development of triple oxygen analysis, Chamberlain et al. review the application of this method to crystalline rocks and their high potential for paleoaltimetry on the crystalline cores of mountain belts. Ibarra et al. propose to use triple oxygen on lacustrine sediment as a paleoaltimetry tool, which they combine with carbonate clumped isotope data to reconstruct the paleoelevation of Eocene Nevadaplano rocks (North American Cordillera).

Gébelin et al. report present-day stream water isotopic lapse rates from the west facing slopes of the equatorial Andes in Ecuador, underscoring that tropical regions can be targeted for future paleoaltimetry studies. Ingalls and Snell provide an exhaustive review of state-of-the-art and emerging tools to investigate the diagenetic alteration of carbonates, a crucial step in stable isotope paleoaltimetry, with an illustration of their impact on Tibetan paleoelevation estimates.

Edited and reviewed by:
Steven L. Forman,
Baylor University, United States

***Correspondence:**
Paolo Ballato
paolo.ballato@uniroma3.it

Specialty section:
This article was submitted to Quaternary Science, Geomorphology and Paleoenvironment, a section of the journal Frontiers in Earth Science

Received: *08 September 2021*
Accepted: *13 September 2021*
Published: *23 September 2021*

Citation:
Ballato P, Hoorn C, Licht A, Methner KA and Pingel H (2021) Editorial: Reaching New Heights: Recent Progress in Paleotopography. Front. Earth Sci. 9:772818. doi: 10.3389/feart.2021.772818

McLean and Bershaw investigate the isotopic composition of carbonates while Kukla et al. focus on authigenic clays in paleosols from the John Day Formation (Eocene to Miocene), United States, in the rainshadow of the modern Oregon Cascades, with contrasting interpretations regarding the evolution of regional topography.

Beyond stable isotope paleoaltimetry, Montes et al. combine field mapping and detrital zircon geochronology to show that the northern and central Andes were separated between ca. 13–4 Ma by lowlands that connected this region with western Amazonia at ca. 3°N, providing a pathway for biotic exchange. Fox et al. examine the role of fluvial reorganization in the formation of elevated landscapes that resemble uplifted formerly contiguous low-relief landscapes. Taking the southeastern Tibetan highlands as an example, they propose that an interpolated paleosurface across low-relief remnants cannot be used to robustly measure geodynamic processes in space and time. Finally, Heitmann et al. review the recent paleoaltimetry work from the Colorado Plateau and propose several test studies to fill the gap in its uplift history.

In summary, this research topic presents new ideas, tools, and results on a wide range of aspects of the paleotopography of mountain and plateau regions around the world. It emphasizes that the future of paleoaltimetry has to be interdisciplinary and combine multiple proxies, considering the numerous uncertainties of individual tools. To increase their robustness and accuracy, the next generation of paleotopography studies will have to incorporate results from a variety of approaches, which is well-illustrated by the array of methods and applications in the eleven articles of this research topic.

AUTHOR CONTRIBUTIONS

All authors listed have made a substantial, direct and intellectual contribution to the work, and approved it for publication.

Conflict of Interest: The authors declare that the research was conducted in the absence of any commercial or financial relationships that could be construed as a potential conflict of interest.

Publisher's Note: All claims expressed in this article are solely those of the authors and do not necessarily represent those of their affiliated organizations, or those of the publisher, the editors and the reviewers. Any product that may be evaluated in this article, or claim that may be made by its manufacturer, is not guaranteed or endorsed by the publisher.

frontiers in Earth Science

ORIGINAL RESEARCH
published: 12 November 2020
doi: 10.3389/feart.2020.587597

How Continuous Are the "Relict" Landscapes of Southeastern Tibet?

Matthew Fox[1]*, *Andrew Carter*[2] and *Jin-Gen Dai*[3]

[1]Department of Earth Sciences, University College London, London, United Kingdom, [2]Department Earth and Planetary Sciences, Birkbeck College, London, United Kingdom, [3]School of Earth Science and Resources, and Research Center for Tibetan Plateau Geology, China University of Geosciences, Beijing, China

Pervasive low-relief, high-elevation surfaces separated by incised canyons are common across the Southeastern margin of the Tibetan Plateau and have been used to define the nature of crustal deformation that drove plateau growth. A common assumption is that these surfaces were once part of a continuous low-relief paleotopography that has undergone surface uplift and dissection. Recent research, however, has questioned this assumption and the derived geodynamic models, which suggests that these surfaces formed *in situ* through drainage network reorganization and the piracy of upstream drainage area. Here, we test the continuity of the low-relief surfaces across SE Tibet using a new inversion scheme that also illuminates the nature of conflicting hypotheses. Our analysis is based on combining the local information contained in maps of normalized channel steepness with the more distributed and integrated information contained in maps of normalized landscape response time. This allows us to model the formation of a hypothetical landscape prior to rock uplift and dissection. We find that large variations in channel steepness are required along the trunk channels within the inferred paleotopography. This is inconsistent with a low-relief surface prior to surface uplift and indicates that a surface interpolated between remnants cannot be used to robustly measure geodynamic processes in space and time. Furthermore, our inverse framework highlights many different solutions to this ill-posed problem and thus provides an explanation as to why the topography alone cannot be used to provide a unique solution to the debate.

Keywords: paleotopographic reconstruction, South East Tibet, geodynamics, landscape evolution, river incision

OPEN ACCESS

Edited by:
Paolo Ballato,
Roma Tre University, Italy

Reviewed by:
Adam Forte,
Louisiana State University, United States
Wolfgang Schwanghart,
University of Potsdam, Germany

***Correspondence:**
Matthew Fox
m.fox@ucl.ac.uk

Specialty section:
This article was submitted to Quaternary Science, Geomorphology and Paleoenvironment, a section of the journal Frontiers in Earth Science

Received: *26 July 2020*
Accepted: *14 October 2020*
Published: *12 November 2020*

Citation:
Fox M, Carter A and Dai J-G (2020) How Continuous Are the "Relict" Landscapes of Southeastern Tibet?. Front. Earth Sci. 8:587597. doi: 10.3389/feart.2020.587597

INTRODUCTION

The South Eastern margin of the Tibetan Plateau has grown during the last 50 million years (Myr) through a combination of geodynamic processes: eastwards extrusion driven by motion on strike slip faults (Tapponnier et al., 1982); crustal thickening induced by lower crustal flow (Clark and Royden, 2000; Copley, 2008); slab rollback below its eastern margin (Sternai et al., 2012); and general shortening and crustal thickening due to collision of the Indian plate and Eurasia (Yang et al., 2015; Tan et al., 2019). In order to assess how these mechanisms have contributed to the current topography, it is crucial to determine rock uplift in space and time, commonly, through geochronology and geomorphology. One of the key geomorphic features that has been used to aid in this mapping are pervasive low-relief, high-elevation topography that is separated by incised canyons with high relief. These low-relief surfaces, that have areas typically 10 s of km^2, have been identified across SE Tibet and decrease gradually in elevation from ~5 km to less than 1 km over a

lengthscale of approximately 1,000 km (Clark et al., 2006). The relief averaged over 5 km within these low-relief landscapes is typically less than 1 km. This landscape has been argued to result from an increase in rock uplift rate (Clark and Royden, 2000). Rivers respond to rock uplift by steepening and these steepened sections incise backwards into slowly eroding areas that have not yet equilibrated to the new rock uplift rate. These patches of low-relief areas are therefore assumed to be parts of the landscape that have not yet adjusted to the new rock uplift rate. The deeply incised canyons, however, have responded to this change in rock uplift rate.

By mapping the extent of these uplifted surfaces, the region that experienced a change in rock uplift can be estimated. In addition, if the difference between erosion rates on the surfaces and in the canyons can be estimated, the time required for these surfaces to reach their current elevation above the surrounding canyons can be inferred.

For example, Clark and Royden (2000) proposed that a low-viscosity channel in the lower crust accommodates the movement of crustal material from high pressures below the plateau to lower pressures away from the plateau. This mechanism simplifies to a diffusion equation in which elevation diffuses from the plateau leading to spatial and temporal variations in surface uplift (England and Molnar, 1990). Because crustal thickening occurs due to flow in the lower crust, the surface is uplifted but deformation is small and there is limited lateral transport of the surfaces. If the erosion rates on the low-relief surfaces are assumed to be close to zero, mapping these surfaces and dating incision can constrain the uplift rate history and the effective viscosity of the low-viscosity channel (Clark and Royden, 2000; Schoenbohm et al., 2004; Clark et al., 2006; Ouimet et al., 2010; Liu-Zeng et al., 2018). Furthermore, this scenario leads to an overall increase in topographic elevation through time. Throughout this study, we will refer to the idea that the low-relief surfaces are remnants of a relict low-relief landscape that has been dissected with minimal drainage network reorganization as Hypothesis 1 and stress that this is a simplification of the proposed model (**Figure 1**).

Importantly, the assumption that enables low-relief high-elevations surfaces to map rock uplift rates is that erosion rates on the surfaces were low prior to the change in rock uplift and have not changed since this adjustment, or at least that changes in erosion rate can be quantified. Several factors, however, may lead to temporal changes in erosion rate across low-relief surfaces as they are uplifted and some of these factors may even form these surfaces: the surfaces may experience changing elevation-dependent climatic conditions as they increase in elevation leading to changes in vegetation and changes in weathering processes that will influence erosion rates (Hales and Roering, 2007; Roering et al., 2010; Schaller et al., 2018); climate may change regionally due to the changes in topography resulting from surface uplift leading to changes in the patterns, in space and time, of rainfall (Molnar et al., 2010; Ferrier, et al., 2013; Scherler et al., 2017); Quaternary global climate change may have resulted in enhanced or reduced erosion across some of these surfaces (Egholm et al., 2009; Fox et al., 2015a; Egholm et al., 2017).

Recently, however, a model has been proposed in which the surfaces are formed by changes in erosion rate but no significant change in rock uplift rate driven by dynamic adjustment of the drainage networks due to tectonic strain (Hallet and Molnar, 2001; Yang et al., 2015). In this scenario, low slope rivers with large upstream drainage area and equilibrated channel steepness, lose upstream drainage area, reducing channel steepness and thus erosion rate. Once this erosion rate is reduced, the landscape is out of equilibrium with the regional rock uplift rate and would be advected upwards, while surrounding channels continue to erode at the rock uplift rate. As this low-relief surface is being uplifted, rivers incise into the boundaries of these isolated surfaces. In this scenario, the general features of the topography may stay relatively constant, with new low-relief surfaces forming and being lost to erosion through time. Throughout this study we will refer to this model as Hypothesis 2 (**Figure 2**). This hypothesis remains controversial and it is currently unclear whether the low-relief surfaces are relicts of a remnant topography and can be used to map rock uplift rates in space and time. In particular, Whipple et al. (2017) argued that the low-relief upland landscape patches are approximately co-planar and decrease in elevation from the northwest to the southeast and that variability in the elevations of bounding knickpoints is expected in natural landscapes. It remains unclear how much variability is expected and how much is due to regional geodynamics or the expected change in elevation along the trunk river profiles. Willett (2017) argued that Whipple et al. (2017a) only analyzed topography at the 100 –1,000 km scale but did not look at individual drainage basins. Furthermore, Willett (2017) suggested that the topography might be consistent with incision into a pre-existing landscape if spatially variable rock uplift is accounted for "pending a detailed study". In response, Whipple et al. (2017b) agreed that diagnostic criteria in landscape evolution are not easily determined and that it is important to examine multiple criteria in a regional context. Whipple et al. (2017b) also maintained that the low-relief topography was co-planar and defines an upper envelope to the topography and thus the topography of SE Tibet does result from incision into a pre-existing low-relief landscape. Importantly, these studies use a stream-power framework and we will adopt these same assumptions here. For simplicity, we have distilled the two concepts into endmember hypotheses. In reality, it is important to note that neither hypothesis is mutually exclusive nor collectively exhaustive (Whipple et al., 2017a; Whipple et al., 2017b; Willett, 2017).

To test these hypotheses and to help diagnose how low-relief, high-elevation topography may form, we utilize linear inverse methods to interpolate a hypothetical topographical surface between the low-relief high-elevation surfaces (Fox, 2019). Importantly, we are not simply testing how co-planar the low-relief high-elevation surfaces are, but ensuring that the topographical surface must follow slope-area relationships with variable channel steepness. Furthermore, we account for the fact that the topographic surface might have been warped

by geodynamic processes or offset by brittle faulting. If a topographical surface can be found with "relatively uniform" normalized rock uplift rate, u^*, this supports the hypothesis that SE Tibet was a low-relief low-elevation surface that has been uplifted and dissected. Here "relatively uniform" would mean that the inferred normalized rock uplift rate between the low-relief surfaces is similar to the normalized rock uplift rate values observed on the low-relief surfaces. Alternatively, if a surface with large variations in normalized rock uplift rate is found, even without the inclusion of the incised portions of the landscape, this is inconsistent with Hypothesis 1 and instead supports Hypothesis 2. In this way, our approach does not explicitly test Hypothesis 2, but if a low-relief paleotopography can be constructed, the importance of Hypothesis 2 is reduced.

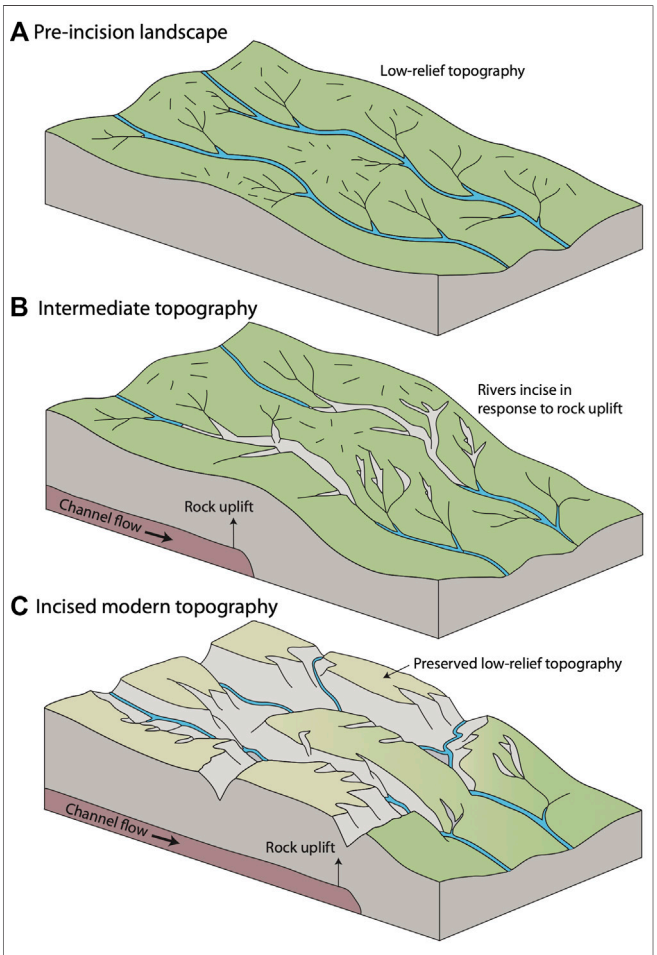

FIGURE 1 | Hypothesis 1. **(A)** Before the onset of rock uplift across SE Tibet, Hypothesis 1 proposes that there was a low-relief landscape with low erosion rates. **(B)** Due to lower-crustal channel flow, rock uplift rates increased and rivers incised into the low-relief landscape. **(C)** Remnants of the low-relief landscape are preserved today and have not been removed by erosion. Therefore, the low-relief remnants can potentially be used to map geodynamic processes.

USING FLUVIAL METRICS TO TEST THE HYPOTHESES

Fluvial geomorphology, and the associated metrics based on the stream power model, provide insight into how landscapes respond to changes in tectonic forcing (Howard, 1994). The rate of change of river long-profiles, dz/dt, increases with rock uplift rate, u, and decreases with erosion rate, e. In the stream power model, erosion rate is proportional to the upstream drainage area, A and the local channel slope, S, raised to the powers of m and n respectively. The constant of proportionality is

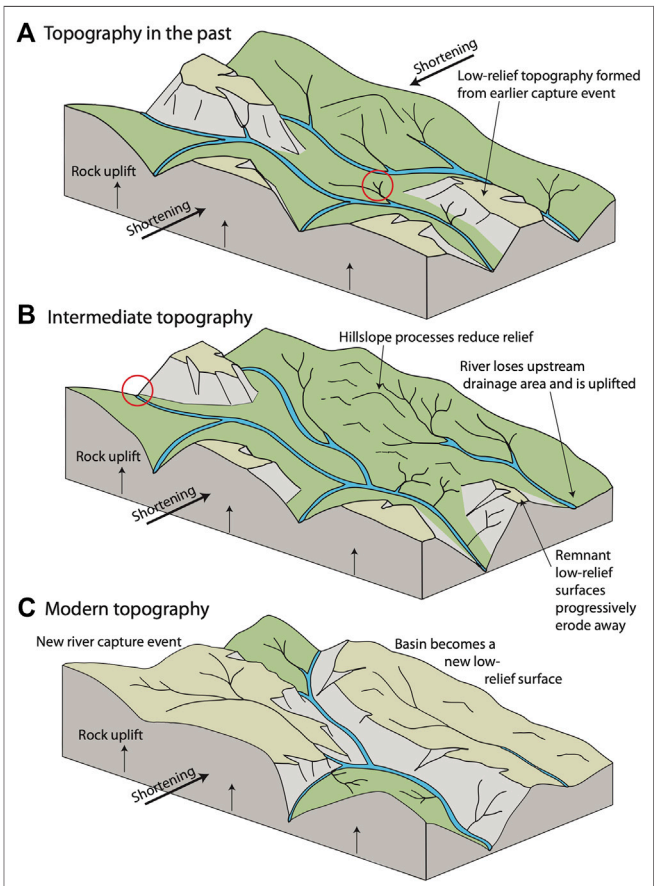

FIGURE 2 | Hypothesis 2. **(A)** After a topography had developed across SE Tibet, Hypothesis 2 proposes there would have been some low-relief landscapes due to drainage reorganization. **(B)** During ongoing drainage reorganization driven by shortening perpendicular to major rivers, the tributary circled in **(A)** captures the upper river. The associated loss in upstream drainage area reduces the erosion rate of the river leading to surface uplift. Hillslope processes continue to erode hillslopes however the river has lost the ability to incise, leading to a reduction in topographic relief. Low-relief surfaces from previous capture events are eaten away by erosion. **(C)** The basin that lost upstream drainage area continues to have less and less relief and is eaten away by erosion. A capture event upstream of the red circle in **(B)** leads to the beginning of new low-relief topography. This process is continuous and leads to the lowest-relief landscape being preserved for short amounts of time at the highest elevations. Therefore, the modern topography reveals a snapshot of this process and patches of low-relief landscape at high elevations are not remnant of a pervasive low-relief landscape.

the erodibility, K, which encompasses bedrock strength, bedload, hydraulic parameters and climate. Therefore,

$$\frac{dz}{dt} = u - KA^m S^n \quad (1)$$

and, if $dz/dt = 0$, $u = KA^m S^n$. Because K cannot be inferred directly from a landscape, it is common to measure the normalized channel steepness $k_{sn=}A^{m/n}S$, where m/n = 0.3–0.8 (Mudd et al., 2018) directly from a digital elevation model (DEM) which provides an estimate of the uplift rate at steady state (Kirby and Whipple, 2012). We build on previous work that has used the stream power model to debate the origin of the topography of SE Tibet and assume $n = 1$ and discuss the implications of this assumption in *Dicussion* (Yang et al., 2015; Whipple et al. 2017a; Whipple et al., 2017b; Willett, 2017). A value of m = 0.45 has been determined for parts of SE Tibet and we will use this same value (Kirby et al., 2003; Ouimet et al., 2009; Yang et al., 2015). The normalized channel steepness index approach to asses the topography of SE Tibet assumes steady state rock uplift, a fixed drainage network and a uniform K value in space and time. An advantage of this approach is that normalized channel steepness values can be calculated for every river node in a large digital elevation model, and it is therefore easy to interpret spatial patterns in the data (Kirby et al., 2003). In this respect, this approach is ideal to exploit the large topographic datasets available. A potential limitation is that by calculating slope from a DEM, noise in the dataset is amplified resulting in maps that can be hard to interpret. Therefore, averaging and smoothing is required to interpret normalized channel steepness maps. If low-relief surfaces were part of a continuous and former steady-state surface developed under relatively spatially constant rock uplift rate, similar channel steepness values would be expected across all low-relief surfaces and this has been argued by Whipple et al. (2017a). This would support Hypothesis 1. It is worth noting that Whipple et al. (2017b) do expect some variability in the form of the low-relief surface due to drainage re-arrangement and expected spatial variations in initial conditions, forcing mechanisms, and landscape response.

If the rock uplift rate increases, a fluvial knickpoint will form at the baselevel and propagate upstream at a speed given by KA^m, if $n = 1$. Therefore, the response time at a specific location, x, in the landscape from the baselevel, x_b, is given by

$$\tau = \int_{x_b}^{x} \frac{dx'}{KA(x')^m} dx' \quad (2)$$

As with the normalized channel steepness, K is often unknown and thus it is useful to use a modified response time, or χ (Perron and Royden, 2012), that can be written as $\chi = A_0^m K\tau$. The integral quantity χ can be used to identify whether drainage divides are stable with the assumption being that if baselevel falls at a confluence, a steepened section of a river profile, or knickpoint, will propagate upstream, potentially to a shared drainage divide. If knickpoints arrive at the drainage divide at different times, erosion rates will be different and the divide will migrate (Willett et al., 2014). Divide migration rate is expected to be relatively slow (Whipple et al., 2017c) but, in some cases, can be faster than the rate of knickpoint retreat (Schwanghart and Scherler, 2020) Therefore, χ values either side of drainage divides should be similar if divides are stationary but may be different if divides are moving. It is important to bear in mind that the interpretation of χ maps assumes spatially uniform K values and rock uplift rate, and that spatial variability in K or rock uplift rates may lead to stationary divides that have different large χ differences. As with maps of channel steepness, entire drainage networks can be analyzed simultaneously without the requirement that the erodibility is known. Maps of χ, however, have no information about the normalized channel steepness of river profiles. Large differences in χ across drainage divides would support Hypothesis 2, but is also expected in Hypothesis 1 due to drainage capture (Clark et al., 2004).

To provide information on relative channel steepness values, χ can be plotted as a function of elevation for rivers and the slope of this curve is proportional to normalized channel steepness (Perron and Royden, 2012; Goren et al., 2014; Mudd et al., 2014). This is because, at steady state with $n = 1$, **Eq. 1** reduces to:

$$z(x) = z(x_b) + \left(\frac{u}{KA_0^m}\right)\chi \quad (3)$$

and the normalized rock uplift rate is $u^* = u/A_0^m K$, which is also proportional to the normalized channel steepness, i.e., $u^* = k_{sn}/A_0^m$. We discuss the implications of the $n = 1$ and highlight how we can account for nonlinearity in the discussion. Furthermore, rivers that have experienced similar rock uplift rate histories should have similar forms as knickpoints will have traveled to similar χ values (Ma et al., 2020). Importantly, this provides an additional means to test Hypothesis 1 as the χ-elevation relationship of the low-relief surfaces should be the same. The additional information that is obtained by using χ-elevation plots is that the χ values of the knickpoints separating the low-relief surfaces from the incising canyons should be similar across much of the landscape if Hypothesis 1 is correct. However, spatial variability in the geodynamics driving incision into the low-relief surface may distort χ-elevation relationships making this analysis complicated. A disadvantage of extracting channel profiles and plotting the topographic data in this form is that it is much harder to interpret spatial patterns in the data. Furthermore, channels must be extracted for analysis and this prevents entire datasets being analyzed simultaneously. χ-elevation plots have been used to argue in favor of both Hypothesis 1 and Hypothesis 2 (Yang et al., 2015; Whipple et al., 2017a; Whipple et al., 2017b; Willett, 2017).

METHODS

Our approach is based on the normalized analytical, steady state stream power model but allows for spatial variations in u^* and surface uplift (*S.U.*) after the formation of the low-relief landscape. In this way, we adopt the same sets of assumptions that are the basis for the ongoing debate about the origin of the

topography of SE Tibet and attempt to highlight why there is ongoing debate. If u^* and *S.U.* vary in space, we can write a discrete version of **Eq. 1** for a node in a DEM along a channel,

$$z_i = z_j + \left(\chi_i - \chi_j\right)u_j^* + S.U._i \quad (4)$$

where the *i*th pixel is upstream of the *j*th pixel and the lowest most pixel has an elevation of *B.L.* (baselevel). $S.U._i$ is the surface uplift that the low-relief landscape has experienced following dissection. If *S.U.* is constant across all of the low-relief landscape, this represents a block uplift scenario but it can also be spatially variable reflecting processes that might lead to surface uplift of the low-relief surface. Long wavelength features might be associated with lower crustal channel flow while shorter features might be driven by local faulting. Importantly, *S.U.* represents the total amount of surface uplift averaged since the low-relief landscape formed and this surface uplift might have occurred at any point in time. In turn, the elevation of any fluvial node can be predicted using a summation of expressions for downstream pixels, and any u^* pattern and *S.U.* pattern. For a single channel, the *i*th fluvial node is the sum of differences in χ between a node and the downstream node ($\Delta\chi$) multiplied by the u^* value at the relevant location from the first node to the *i*th node, plus an additional surface uplift term:

$$z_i - B.L. = \sum_{j=1}^{i}\left(\Delta\chi_j\right)u_j^* + S.U._i \quad (5)$$

Changes in the u^* values along the trunk streams will change the elevations upstream of that specific pixel. If tributaries are utilized in the analysis, these changes will propagate across all the upstream river network. Therefore, the response of the landscape to local changes in *S.U.* and u^* is distinct: increasing u^* leads to small increases in elevation of rivers with large upstream drainage areas due to the small changes in χ but large changes in elevations of rivers with small upstream drainage area; increasing *S.U.* leads to uniform increases in elevation.

Maps of u^* and surface uplift can be determined using inverse methods. For a single channel, **Eq. 5** shows that *i+1* model parameters are used to describe the single elevation node resulting in an ill-posed inverse problem. However, the node downstream constrains *i-1* of the same u^* model parameters and thus only an additional two parameters are required to describe the elevation of the *i*th node: one u^* parameter and one *S.U.* parameter. This is still an ill-posed inverse problem which is exacerbated by the fact that we only use nodes from the low-relief surfaces to constrain the model parameters. It is the branching network of river channels that provides redundant information and smoothness constraints that enables maps of u^* to be inferred from limited elevation pixels (Sternai et al., 2012). This is achieved by simplifying the drainage network to reduce the number of nodes, by discretizing space into blocks of constant u^* and *S.U.* values that are 25 km by 25 km large and by introducing smoothness constraints on u* and *S.U.* (Fox, 2019). This smoothness is important where the data do not resolve the parameters, but rough maps can be produced if required by the data.

The aim of the inversion is to find a topography that represents the pre-incision landscape plus surface uplift and this requires finding the model parameters (u^* and *S.U.* values) that minimize the misfit between predicted and observed elevations of low-relief surfaces, and the roughness of the u^* and *S.U.* maps. Some form of regularization is required for most interpolation algorithms. For example, Clark et al. (2006) used a spline to interpolate between low-relief landscapes with a tension parameter determining how smooth the surface is. Here we use negative Laplacian operators to quantify smoothness. Weighting terms, α and λ, are used to determine how to minimize smoothness constraints compared to the fit to the low-relief surfaces. This results in a linear system of equations:

$$\begin{pmatrix} G & \\ \alpha W_u & \\ . & \lambda W_{SU} \end{pmatrix}\begin{pmatrix} u^* \\ SU \end{pmatrix} = \begin{pmatrix} z \\ 0 \\ 0 \end{pmatrix} \quad (6)$$

where G is the $2n_{pixel} \times n_{nodes}$ forward model as defined in **Eq. 5**. Each row of G contains differences in χ so that the sum of these χ values is equal to the χ value of the corresponding low-relief node. The differences in χ values are at columns that correspond to the spatial positions of specific nodes in the discretized blocks of u^*. An additional entry of unity is in each row and this corresponds to the spatial position of the low-relief node for the map of *S.U.* Therefore, multiplying this row by the model parameter vector provides an elevation that combines the drop on the fluvial network of the low-relief landscape and the surface uplift that this position has experienced. Solving this upper system of equations (G matrix multiplied by model parameters equals elevation) finds model parameters that reproduce the observed low-relief elevations. αW_u ($n_{pixel} \times n_{pixel}$) is the weighting matrix for the normalized uplift rate parameters and λW_{SU} ($n_{pixel} \times n_{pixel}$) is the weighting matrix for the cumulative surface uplift rate. The dots in the matrix are $n_{pixel} \times n_{pixel}$ matrices of zeros entries to ensure that the combined left-hand side linear operator is rectangular. In actuality, we use sparse matrices to save memory. W_u and W_{SU} are negative Laplacian operators that calculate the second order spatial derivative of the u^* and *S.U.* maps, respectively. Solving the middle system of equations, αW_u (padded with zeros) multiplied by the model parameters equals zero, finds maps of u^* that have second derivatives of zero and vary smoothly in space. Similarly, solving lower system of equations containing λW_{SU} finds a map of S.U. values that vary smoothly in space. The combination of α and λ therefore control the degree to which these different and potentially conflicting constraints control the model parameters. Importantly, λ can control both the roughness of u^* and *S.U.* and λ can similarly control the roughness of u^* and *S.U.* This equation can be solved for the unknown relief parameters using a non-negative least squares solution (see Fox, 2019 for further details).

The dataset used for the inversion is therefore just the elevations and χ values of the low-relief surfaces calculated with respect to a common baselevel and is shown in **Figures 3**, **4**. The topographic data used here is the HydroSheds hydrologically conditioned topographic dataset with a

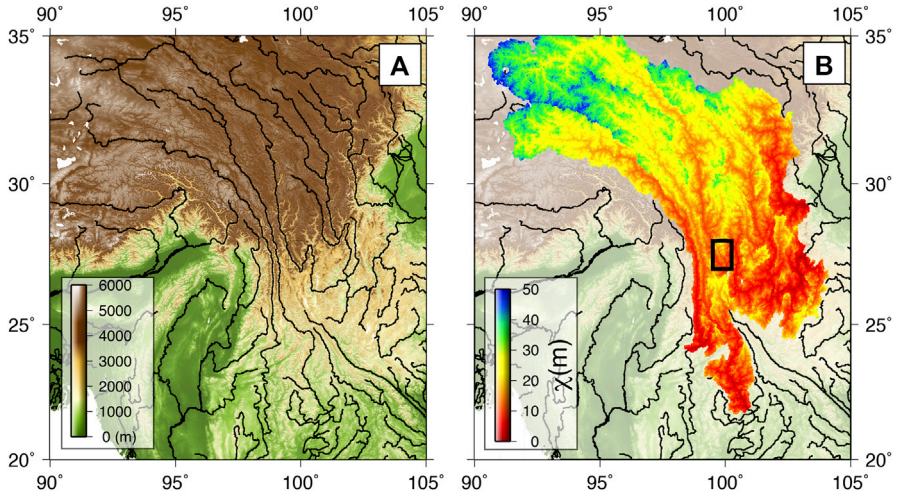

FIGURE 3 | The dataset used for the analysis. **(A)** The HydroSheds hydrologically conditioned topographic dataset with a resolution of ~90 m (Lehner et al., 2008). **(B)** Drainage network topology, upstream drainage area and values of were calculated from this dataset with a baselevel set at 500 m for pixels with an upstream drainage area >5 km^2, with an m value of 0.45, and n value of 1 and a scaling area A_0 of 1 m^2 after (Yang et al., 2015). The box outlines the extent of **Figure 4**.

resolution of ~90 m (Lehner et al., 2008). The elevations of the low-relief surfaces range from approximately 1,000 and increase to over 5,000 m χ increases from the baselevel to values of approximately 50 m with clear discontinuities across drainage divides (**Figure 3B**). The outlines of the low-relief surfaces are taken from Clark and Royden (2000) and 75% of fluvial nodes are removed from within these areas to reduce the dataset (**Figure 4A**) for the inversion. u^* values ($\Delta z/\Delta_\chi$) of the nodes within the low-relief surfaces show considerable variability (**Figures 4B,C**). The average u^* value for all the fluvial nodes within the low-relief surfaces is 89.8 with 90% of the nodes having values below 200. This suggests that the hypothetical pre-incision topography would have been made up of a landscape with relatively uniform u^* values of less than about 200. Furthermore, a topography interpolated between these low-relief surfaces should therefore have relatively uniform u^*

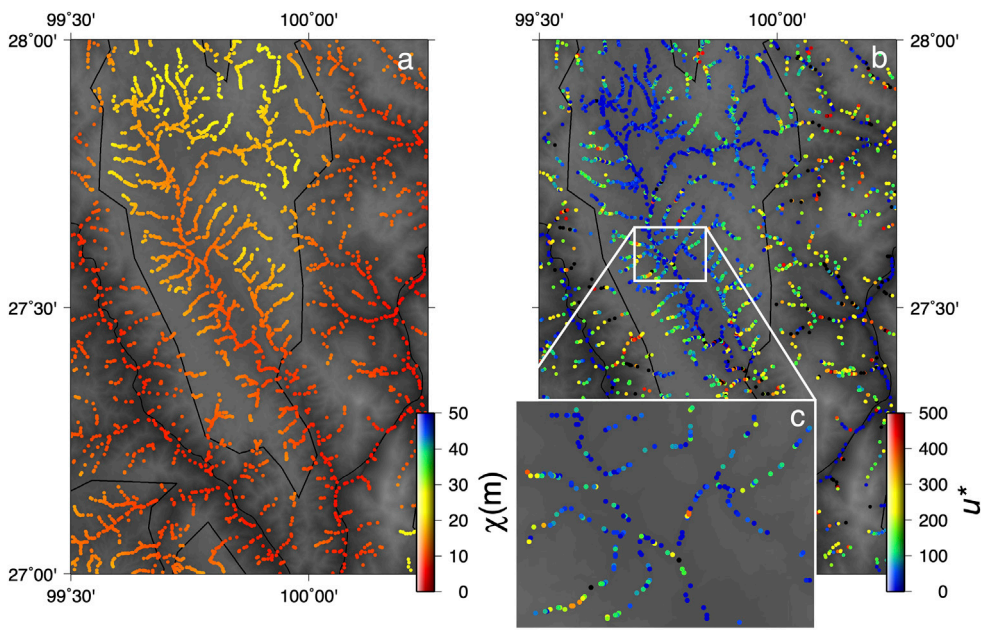

FIGURE 4 | 4Subsampling the data. **(A)** The complete dataset was trimmed by randomly removing 90% of the pixels outside of the low-relief surfaces and 75% within the low-relief surfaces. **(B)** Local normalized channel steepness maps values highlight regional patterns but are very noisy and thus must be filtered or averaged to make interpretations. **(C)** Zoomed in portion showing data distribution and variability in the normalized steepness data.

values that are lower than 200, if Hypothesis 1 is correct. In contrast, higher values and more variability is expected if Hypothesis 2 is correct.

RESULTS

The results are presented as two maps, u^* and *S.U.* and the corresponding misfit value (**Figure 5**). Here we focus on one result out of several models produced with different values of α and λ. We show the other results in **Supplementary Movie S1** and this also provides a means to visualize the sensitivity of the results to the smoothing parameters. In general, small values of the weighting parameters lead to rough models that fit the data well, whereas large weighting parameters produce smoother results that may fit the data poorly (**Figure 5A**; **Supplementary Movie S1**). With large values for the weighting parameters, the inversion attempts to minimize the misfit associated with the smoothness constraints (that the Laplacian of the u^* values and the *S.U.* values should be close to zero) resulting in smooth maps. With small values for the weighting parameters, the inversion finds results that fit the data well but are more sensitive to anomalous topography and geomorphic noise, and therefore, results may be meaningless. Within this context, geomorphic noise encapsulates artifacts in the DEM, landslides blocking rivers and over-steepening rivers and small-scale variations in erodibility. It is expected that this noise far exceeds the uncertainty of the DEM (Fox et al., 2015b).

In order to choose a preferred model, we employ the same principles behind the L-curve (Hansen, 1992) and search for the damping variables that result in a model with low model roughness and low misfit (i.e., close to the corner of a 2-D L-surface, Richards et al., 2016). A misfit value of approximately 100 m is reasonable: misfit values lower than this suggest that we are fitting noise and misfit values higher than this indicate that the model is not fitting the data. We focus our discussion of the results on features that are robust across a range of values for the damping parameters.

Results show that there are clear short wavelength variations in normalized rock uplift rate and that high values are observed at large confluences and large bends in trunk rivers. By contrast, if the network geometry and values were consistent with a landscape that is being dissected by a wave of incision due to increased rock uplift, a map of relatively uniform u^* values less than approximately 200 would be expected. This is because values less than 200 are observed across the low-relief surfaces. We refer to areas with higher than expected u^* values as anomalies and these indicate that a topographic surface with low u^*, or a low-relief paleotopography, cannot be interpolated between low-relief surfaces and that considerable drainage network reorganization has occurred. In particular, we see high anomalies at the prominent bends in two major tributaries to the Yangtze, the Jinsha and Yalong Rivers, at a confluence with the Niuling River and in the upper reaches within the Dadu (Yang et al., 2020; Suhail et al., 2020) catchment (**Figure 5B**). The timings of the capture events that formed these anomalies are debated, with the First Bend of the Yangtze either forming in the Eocene (Zheng et al., 2020) or the Pleistocene (Deng et al., 2020). High anomalies also follow these rivers, along with the Lancang, up into Tibet. These anomalies are most pronounced when maps of *S.U.* are

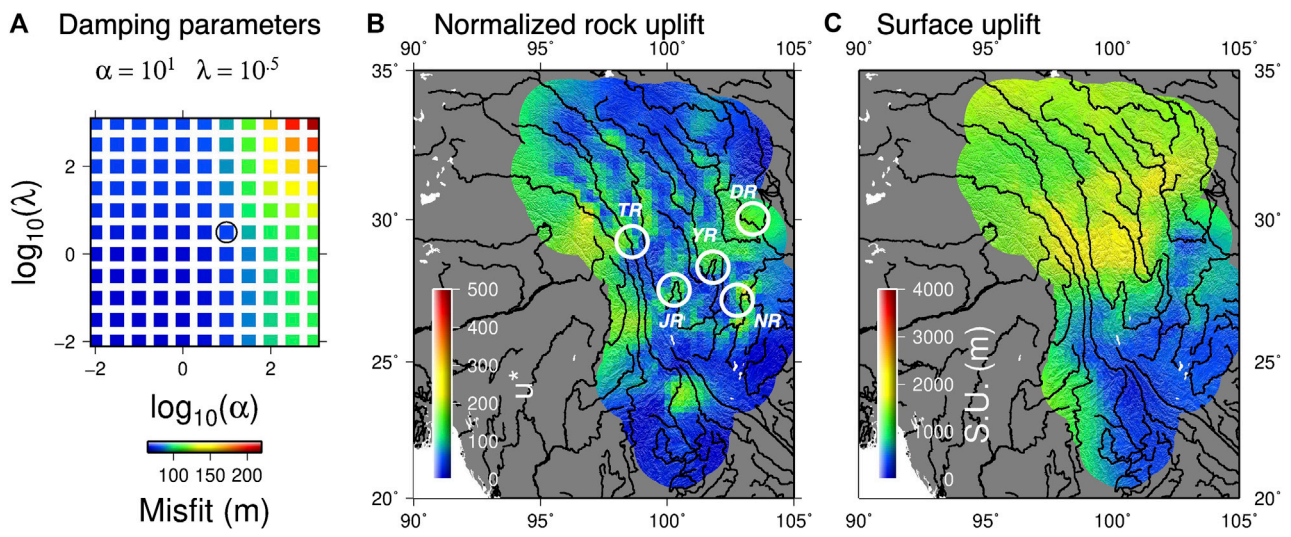

FIGURE 5 | Predicted normalized rock uplift rates and spatially variable surface uplift. **(A)** A two-dimensional L-surface showing the trade-off between model misfit and the two damping parameters which control the roughness of the normalized rock uplift (α) and the surface uplift map (λ). However, each damping parameters influences both maps as the u* and S.U. both predict the topography and control the misfit between the observed and predicted topography, which is minimized by the inversion. A model is preferred that has a small misfit value, but also results in smooth maps. This model is shown by the circle in **(A)** and the maps are presented in **(B)** and **(C)**. The sensitivity of the inversion to the damping parameters is presented in **Supplementary Movie S1**. Low u^* values are observed where low-relief surfaces are found but higher values are observed along the trunk streams and the confluence of the Jinsha river with the Niulan River (NR) and aspects of the drainage network, such as large parallel rivers in the Three Rivers area (TR) and the large bends in the Jinsha River (JR), and the Yalong River (YR). High values are also observed close to the Dadu River (DR) which is related to the steep Longmen Shan. These anomalies are more apparent in the rougher models.

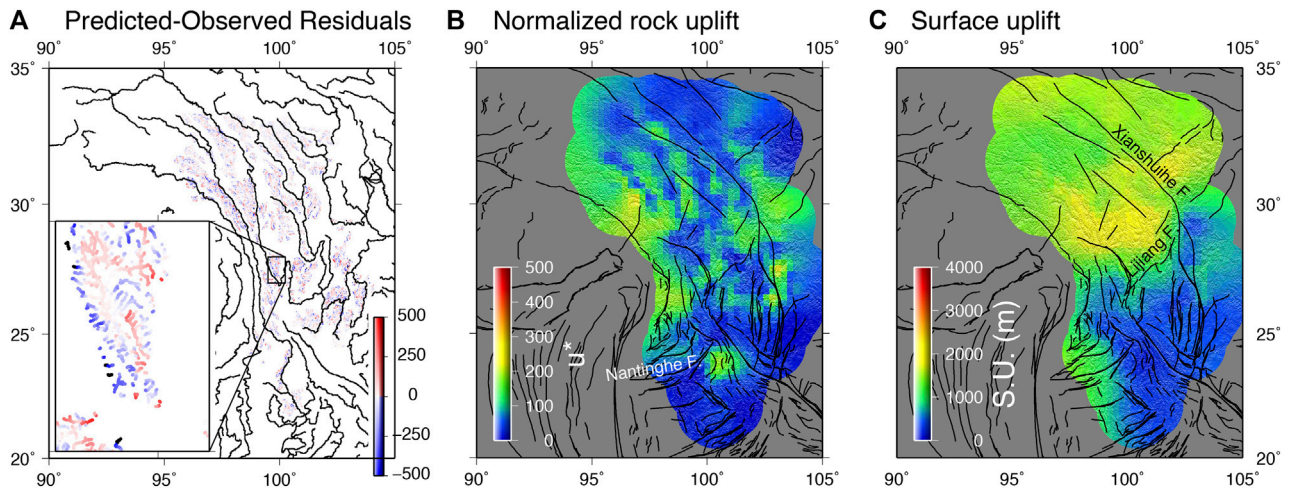

FIGURE 6 | Investigating the results of the inversion. **(A)** The predicted - observed residuals for the low-relief surfaces show that in areas where the misfit is large and positive there are often negative residuals close by. This suggests that drainage divides and river capture are causing pairs of over- and under- steepened χ-elevation relationships. **(B)** Active faults from GEM database (Styron et al., 2017) compared to the normalized rock uplift map and the surface uplift map **(C)**. Aspects of the results are controlled by active structures, see text for details.

least variable (**Supplementary Movie S1**) and this is because changes in elevation can be produced with changes in *S.U.* or changes in u^*. Therefore, decreasing changes in *S.U.* leads to increased variability in u^*. A high anomaly is also observed in the Three Gorges area. Crucially, the elevations of the large rivers, where unusual drainage has been previously mapped (Clark et al., 2004), are not used in the inversion. The high normalized channel steepness values that we predict are the result of rivers from low-relief surfaces flowing into the trunk stream at elevations that require anomalously steep trunk river segments. High values are also observed at the eastern end of the Nantinghe Fault (**Figure 5B**).

Across many of the low-relief surfaces, the residuals are coupled (**Figure 6A**): large positive values are associated with large negative values, which is caused by drainage divide migration (Fox et al., 2014). Importantly, these residuals highlight that the model is not fitting all channels that are over-steepened and under-steepened by drainage divide migration and capture. To explain all these residuals with the model, the normalized channel steepness map would be even rougher, providing further support for drainage network reorganization.

We see evidence that active structures across SE Tibet are influencing our inferred values of *S.U.* (**Figures 6B**,C), and this correspondence highlights that short wavelength structures are also contributing to deformation of the low-relief surface. Furthermore, this suggests that damping parameters used in the inversion are not obscuring expected features. In particular, there is a clear change in *S.U.* across the Lijiang Fault, which is also an area of high strain rates (Copley, 2008; Pan and Shen, 2017; Li et al., 2019). Low values are observed to the east of the Lijiang fault where the Xianschuihe fault splits and to the west of the Lijiang fault, and these areas correspond to areas of GPS-resolved subsidence (Pan and Shen, 2017).

Our predicted elevations can also be displayed along the paths of rivers (**Figures 7B,C**). This provides an indication of how much incision has occurred at a specific location, if Hypothesis 1 is correct. It is important to point out that here we use incision to indicate the amount of deepening of valleys with respect to the surrounding peaks. In this respect incision is not equal to total erosion. If the erosion rates on the low-relief landscape are assumed to be close to zero, however, this incision is equal to the amount of erosion and could be measured with thermochronometry. The predicted elevations are a function of the pre-incision topography, itself, a result of the χ distribution and u^* values, and the subsequent surface uplift. The predicted elevations follow the low-relief parts of the landscape (cross symbols which appear as solid lines on **Figures 7B,C**) but plot high above the modern channels in other places. This is because there has been significant rock uplift at these locations and the rivers have incised downwards. Furthermore, there is no requirement that predicted elevations need to decrease with distance downstream as *S.U.* may be focused at a specific location, warping surfaces upwards. We see that in tributaries of the Yangtze (**Figure 7B**) the predicted elevations match the low-relief topography relatively well. This also provides insight into how the method works: the low-relief landscapes in river 1 set a regional normalized channel steepness value that is used to project the reconstructed river downstream. Rivers 2 and 3 join river 1 and the information contained in these low-relief surfaces is used to average the normalized channel steepness values. River 4 provides local information on the height of the reconstructed surface and forces the reconstructed surface to remain at high elevations. In reality, there are hundreds of confluences that are simultaneously providing constraints on elevations. In order to match those constraints, variability in u^* and/or *S.U.* is required. These confluences lead to the surface being approximately 1,000 m above the modern river in some locations, predicting

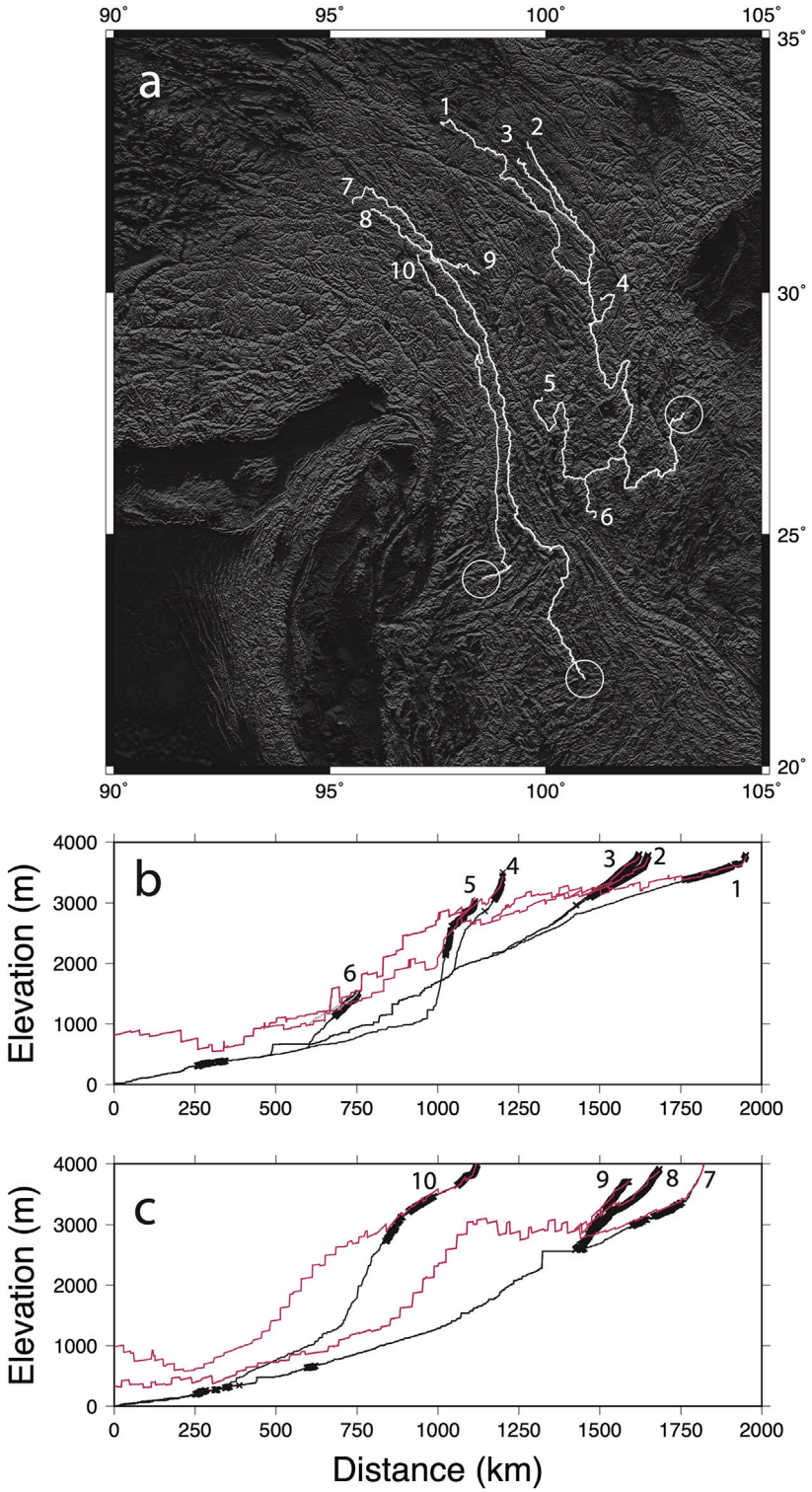

FIGURE 7 | Comparison with river profiles. **(A)** Location map showing the rivers plotted in **(B)** and **(C)**; **(B)** River long-profiles extracted from the down sampled DEM, black lines. The crosses are the low-relief nodes used in the inversion, these appear as thick black lines where they are closely spaced. The pink lines are the predicted elevations and account for spatial variability in u^* and *S.U.* and are therefore not monotonic. The stepped nature is due to the fine resolution of the pixels used for the inversion and the fact that the values of u^* and *S.U.* vary over short wavelengths; **(C)** River long-profiles extracted from Mekong and a tributary of the Salween. Larger amounts of incision are predicted for these rivers.

1,000 m of incision. In contrast, for rivers 7, 8, 9, and 10 the maximum predicted incision is approximately 2000 m. The stepped nature of the predicted elevations reflects short wavelength variations in surface uplift and the fact that the rivers may cross the discretized grid in complex ways so that some pixels in the grid may be sampled more than other pixels. A map of predicted incision shows that incision is focused in the Three Gorges region (**Figure 8**), but does not predict more than approximately 2000 m at any location.

DISCUSSION

Temporal Discretization

We have chosen to discretize the tectonic history into two stages. The first stage represents a steady state landscape before the onset of enhanced rock uplift. The second stage represents the cumulative uplift and incision of this landscape and does not make any assumptions about how this varies in time. However, in Hypothesis 1 channel flow would lead to spatial and temporal variations in surface uplift (Clark and Royden, 2000; Schoenbohm et al., 2004). A full inversion of the landscape using river profile modeling with rock uplift rate variable in space and time (Roberts et al., 2012; Fox et al., 2014; Rudge et al., 2015) would require inferring maps of u^* at many times in the past. Given that one of our goals is to investigate whether the planform geometry of the drainage network has evolved through time by using a simplified interpolation method, a full inversion that requires assuming this is not justified. Nevertheless, it is important to consider how our simplifications may impact our results. If the areas closest to the plateau were uplifted first, fluvial incision would begin earlier here and there would be less of the paleotopography preserved. Because areas outside of the low-relief surfaces are not used in the analysis, this simply means that we have less data to constrain the surface at these locations.

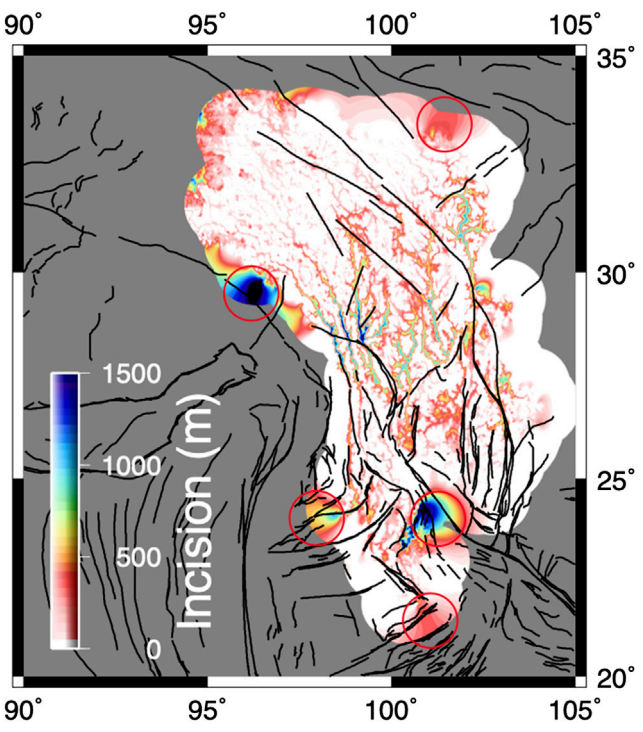

FIGURE 8 | Predicted incision. The amount of predicted incision across SE Tibet assuming that the low-relief topographical surface represents a pre-incision landscape. Incision is focused along the rivers in the Three Rivers region, as would be expected from a simple topographic interpolation. Several plotting artifacts are highlighted with red circles and these reflect areas that are unconstrained by the dataset.

Effects of Non-Linear Relationships Between Channel Steepness and Erosion Rate

Previous models used to support the conflicting hypotheses, are based on the linear stream power model (i.e., $n = 1$) and if this underlying model is incorrect then the hypotheses might be slightly different (Goren et al., 2014). We do not attempt to quantify the implications of these underlying assumptions and have adopted the simplified linear stream power model. If $n > 1$, river segments that are steeper will propagate upstream faster than less steep river segments and vice versa. This would lead to the margins of the low-relief landscape having different χ values. However, because we only use the elevation data from within the low-relief surfaces to map u^* and *S.U.*, the exact χ value at the edge of the plateau is not significant. Furthermore, the steady state assumption utilized here reduces the dependency on n as variability in n can be mapped into variability in K (Croissant and Braun, 2014).

Cosmogenic-derived catchment averaged erosion rates from across SE Tibet show a non-linear relationship with catchment averaged normalized channel steepness and this suggests that $n = 2$ (Ouimet et al., 2009). This is based on the assumption that bedrock erodibility is spatially uniform across the study area, that the catchments analyzed are in steady state, and that erosion rates are set by fluvial erosion. Therefore, we explore how increasing the value of n from 1 to 2 would impact our analysis. Royden and Perron (2013), show that the steady state stream power model can be written as

$$v^{1/n} = \frac{dh}{d\chi} \tag{7}$$

where u^* is a simplification of v and $h = z/h_0$ where h_0 is a reference elevation (see Equation 9 of Royden and Perron, 2013). If h_0 is set to 1 m, we can generalize our inversion by treating u^* as a dummy variable for $(u^*)^{1/n}$. Thus we can simply raise our maps of u^* by the power of n to get maps of $u/(A_0K)$ for a nonlinear case. If $n > 1$ spatial variability in the normalized channel steepness values will be amplified, increasing the degree of roughness of the inferred u^* map. In contrast if $n < 1$, variations will be reduced (**Figure 9**). Future work could leverage this dependency to help constrain the value for n.

In an attempt to determine a value for n for a separate study, Ma et al. (2020) selected the catchment wide erosion rates from Ouimet et al. (2009) for only the Dadu catchment. They found a

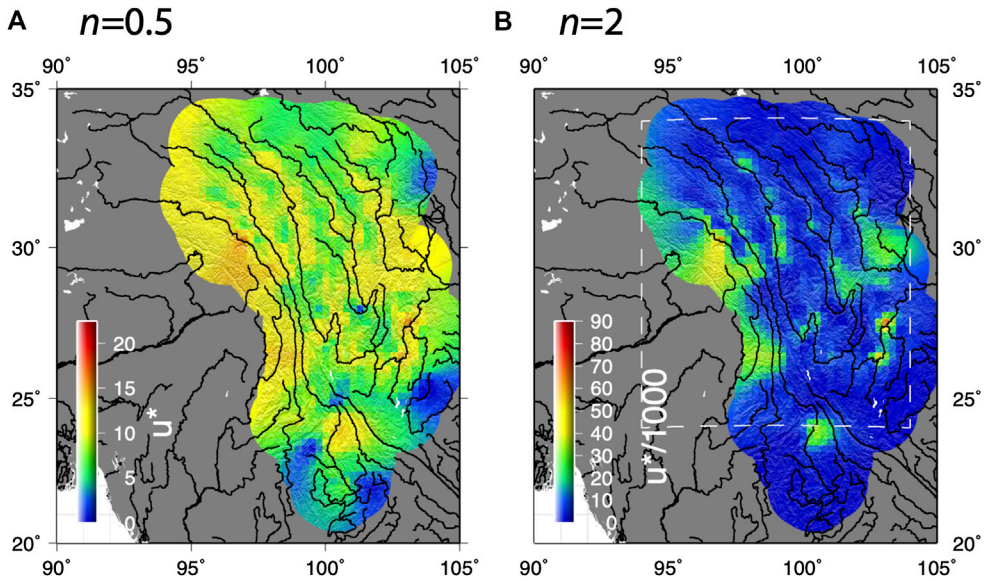

FIGURE 9 | Nonlinearities in the stream power model. **(A)** Normalized channel steepness values for $n = 0.5$. Overall magnitudes are reduced and there is less spatial variability in the u^* map; **(B)** If $n = 2$, more spatial variability is predicted, and magnitudes increase. The box shows the regional extent of the map in **Figure 10**.

linear relationship between channel steepness and catchment averaged erosion rates could explain the data. It is unclear whether this is simply because the area analyzed was much smaller or whether slightly different methods were used to calculate normalized channel steepness. Therefore, the value of n for SE Tibet remains debated.

Effects of Spatial Variations in Erodibility

Importantly, we assume that over the scale of SE Tibet there is an effective average erodibility, enabling us to calculate χ and relate χ to elevation, and that any erodibility patterns do not correlate with the long wavelength variations in u^* or surface uplift. Local studies using a range of methods have determined that the main shape of fluvial long-profiles is not controlled by bedrock lithologies. For example, Kirby et al. (2003) identify spatial variability in erodibility that is limited to local reaches and argue that there is little influence of variable lithology on channel profiles across the Eastern Margin of the Tibetan Plateau. The main knickzone of the middle Mekong River valley is not associated with any variability in lithology (Replumaz et al., 2020). Steep sections of the Dadu River include both sedimentary strata and granites indicating no systematic impact of lithology on river channel steepness (Yang et al., 2020). In the Three Rivers region, Henck et al. (2011) argued that spatial patterns in catchment wide erosion rates are not controlled by spatial variability in lithology. In addition, the elevation and/or preservation of the low-relief surfaces does not correlate with lithology (Clark et al., 2006). From our study, we identify no clear evidence for a correlation between lithology and normalized rock uplift rate and anomalies appear to be associated with river capture events. If the rock uplift rate were uniform across the paleotopography, a steady state had been reached and lithology was responsible for spatial variability in u^*, we would expect to see high u^* values associated with low K values, and vice versa. Although we see high u^* values within an area associated with dense intrusive outcrops (**Figure 10A**), we also see low values of u^* within the lithological boundaries of intrusive igneous rocks, which, to first order, are expected to be the least erodible (Bernard et al., 2019). We also see a wide range in u^* values in areas where intrusive rocks are not exposed (**Figure 10B**). Of course, other lithologies can also be very resistant to erosion, suffice it to say that we do not see a clear correlation between lithology and u^* value. Many features of the u^* results are relatively long-wavelength features compared to lithological variations. We selected this result to discuss as it represented a good compromise between data fit and smoothness (**Supplementary Movie S1**). If lithological variations were responsible for the anomalies we detect, this compromise would have led us to select a rougher model. However, even with rougher u^* maps (**Supplementary Movie S1**), there is no clear correlation between lithological variations and u^* values. Future work could attempt to assign erodibility values for specific lithologies and recalculate χ, run the inversion, determine how χ could be modified to smooth the u* maps, update the erodibility values to achieve this χ distribution and then iterate in this way. However, different lithologies are exposed today compared to when the low-relief landscape was originally formed and this makes this analysis challenging.

It is also important to recognize that other factors may lead to differences between the erodibility of the trunk rivers and the low-relief surfaces, potentially enhancing the development of these low-relief surfaces by increasing K (decreasing our inferred u^*), facilitating trunk river incision. For example, the bedload of the large rivers may contain a significant amount of

material from hard lithologies from higher up the catchment that would not make up the bedload of the locally drained low-relief surfaces. This would lead to a difference in the contrast between bedrock and bedload in the trunk rivers compared to the low-relief surfaces, and it is this contrast that may lead to local differences in erodibility (Sklar and Dietrich, 2001). In addition, it is clear that the trunk streams flow parallel to major structures, such as suture zones and strike slip faults. It may be expected that these structures would locally increase the erodibility (Roy et al., 2016) and this may facilitate erosion of the trunk rivers and the preservation of the potentially harder low-relief surfaces. Both of these factors may also change through time as different rocks are exhumed leading to changes in bedload or different structures are revealed for rivers to incise into.

We have also assumed that precipitation is uniform in order to relate calculate χ and relate χ to elevation. Previous work has accounted for the spatial variability in precipitation to calculate χ (Yang et al., 2015) however there is also clear evidence that the pattern of precipitation has changed significantly from when the low-relief surface is hypothesized to have been formed to today (Botsyun et al., 2019). Therefore, we have kept precipitation uniform and, in this respect, our study serves as a baseline and factors such as spatially and temporally variable erodibility can be incorporated in future analyses.

SUMMARY

Our approach provides a means to quantitatively assess the continuity of a hypothetical paleo-topography with relatively uniform normalized rock uplift rate. We find that large variability in u* is required if surface uplift is uniform, but that a relatively smooth surface can be found if spatial variability is permitted. However, even with this increased flexibility, anomalously high u* values are found along the main trunk streams. In addition, differences between model-predicted elevations and observed elevations are often positive one side of a drainage divide, but negative on the other side suggesting that these tributaries are out of equilibrium with the regional topography. It should be noted that these residuals only correspond to the low-relief high-elevation parts of the landscape. In order for the u^* to be smoother and more uniform, without significantly increasing model misfit, a rougher *S.U.* map is required, however, this would require short wavelength surface uplift structures, as opposed to a long wavelength mechanism such as lower crustal flow (Clark and Royden, 2000). Ultimately, this choice represents a compromise between roughness and data fit, however, our framework provides a method to ask: what is the relative importance of the two hypotheses? The preferred inversion result (**Figure 4**) fits almost 75% of the analyzed low-relief nodes to within 100 m, however a model that has smooth u^* and *S.U.* maps, consistent with Hypothesis 1 ($\alpha = 10^2, \lambda = 10^{1.5}$) only fits approximately 55% of the data. Therefore, low-relief paleotopography might have existed but the processes required by this model (reduced to its simplest form) only explains about half the data.

While our results lend support to the existence of a low-relief surface that has been uplifted and dissected, this model cannot explain all of the data, and additional factors may have modified erosion rates across the low-relief surfaces, either driven by

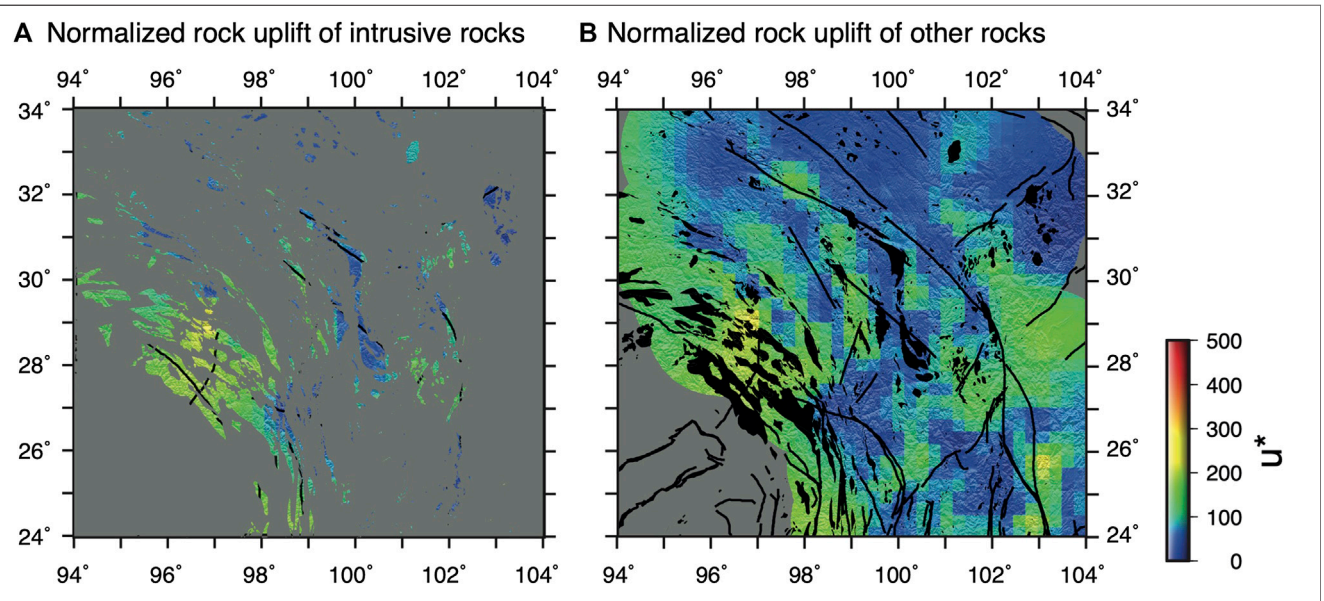

FIGURE 10 | The influence of lithology on predicted normalized rock uplift rate. **(A)** Intrusive rocks colored by the predicted normalized rock uplift rates with the faults included as in **Figure 5B**. A band of high u^* can be seen at approximately 28°N 97°W which corresponds to a dense band of intrusive units. However, high and low values of u^* are observed across the area; **(B)** The opposite of **Figure 10A** showing the predicted normalized rock uplift rates for the other lithologies, with the outcrops of intrusive rocks shown in black. High and low values of u^* are observed across both lithological categories and the correlation is not clear. Geological units are simplified after Pan et al. (2004).

climatic changes (Zhang et al., 2016; Nie et al., 2018), drainage reorganization (Clark et al., 2004; McPhillips et al., 2016) by drainage divide migration (Yang et al., 2015; Willett, 2017). In addition, the surface is likely to have been deformed by local faulting and lateral movement of low-relief topography as SE Tibet extrudes. However, then the role of a lower crustal low-viscosity channel becomes less clear. What is clear from this analysis is that a topographic surface interpolated between low-relief surfaces found across SE Tibet cannot be used to measure geodynamic processes in time and space. There is limited evidence for low-relief paleotopography in the current topographic data alone and other processes may have entirely shaped modern SE Tibet. Our approach also highlights the limit of utilizing topography alone to interpret landscapes in terms of hypotheses as it is can be an ill-posed inverse problem with multiple scenarios that will lead to indistinguishable features. It is this non-uniqueness that leads to debates about the development of SE Tibet (Yang et al., 2015; Whipple et al., 2017a; Whipple et al., 2017b; Willett, 2017). Future work could use our approach and incorporate diverse datasets and more complexity directly into the analysis. This could include spatially and temporally variable precipitation and erodibility, lateral translation of topography and river networks or hypothesized drainage capture events.

Although our approach provides a means to quantitatively diagnose the continuity of a hypothetical low-relief topographic surface that follows expected slope-area scaling, it does not provide a quantitative test of Hypothesis 1 or 2. In part, this is because the exact smoothness of the two surfaces and degree of data misfit required for Hypothesis 1 have not been specified in the literature. Our approach incorporates the strengths of the different approaches used to extract information from river networks, outlined in *Using Fluvial Metrics to Test the Hypotheses*, but adds additional flexibility. Furthermore, because we are not extracting individual channels from the DEM our approach potentially uses more of the data and we are not selecting which channels to highlight. In order to really understand the topographic development of SE Tibet, data that resolve temporal changes in erosion through time at the scale of individual patches of low-relief topography are required. Thermochronology would be the ideal tool to measure the exhumation rate history across the low-relief landscapes and the surrounding canyons (Gourbet et al., 2020) however, the amount of relief change is right at the limits of the method (Braun, 2002). What is clear from thermochronology is that exhumation rates have been highly variable in space and time, with the amount of exhumation at some locations being far greater than the amount predicted from valley incision alone (Zhang et al., 2016; Cook et al., 2018; Liu-Zeng et al., 2018; Ge et al., 2020; Replumaz et al., 2020). If this exhumation is associated with local high rates of rock uplift, and if the erosion rates on the surrounding low-relief surfaces remain low, large amounts of S.U. would be observed leading to obvious discontinuities in the low-relief surface. These have not been observed and thus this highlights the importance of processes that create low-relief surfaces *in situ*, supporting Hypothesis 2.

In order to falsify Hypothesis 2, future work could search for an absence of low-relief landscapes at intermediate elevations. This is challenging however as Hypothesis 2 predicts that landscapes that have lost upstream drainage area progressively lose relief and are thus most prominent at the highest elevations. Furthermore, the landscape is developing in an area of active deformation. This means that tectonics may respond to changes in surface topography in such a way that sets a limit on how high the low-relief landscapes can be uplifted. This would mean that all the low-relief landscapes might attain coherent, gradually varying, elevations set by the strength of the crust and faults. If only the elevations of the low-relief surfaces were used, this would support Hypothesis 1. We have not mapped low-relief surfaces across SE Tibet and have used published surfaces for our analysis (Clark et al., 2004), however, there does appear to be low-relief landscapes at intermediate elevations across the Upper Yangtze River (Liu et al., 2019). Alternatively, *in situ* erosion rate histories within the low-relief landscapes could be measured using low-temperature thermochronometry. The fingerprint of Hypothesis 2 would be decreases in exhumation rate associated with area loss coupled with increases in exhumation in surrounding canyons.

DATA AVAILABILITY STATEMENT

Publicly available datasets were analyzed in this study. This data can be found here: https://www.hydrosheds.org.

AUTHOR CONTRIBUTIONS

All authors contributed to the design, analysis, and writing of the manuscript.

ACKNOWLEDGMENTS

We thank G. Hilley, J. P. Avouac and two reviewers for providing helpful feedback and S. D. Willett for stimulating discussions. This study was supported by NERC (NE/N015479/1).

SUPPLEMENTARY MATERIAL

The Supplementary Material for this article can be found online at: https://www.frontiersin.org/articles/10.3389/feart.2020.587597/full#supplementary-material

REFERENCES

Bernard, T., Sinclair, H. D., Gailleton, B., Mudd, S. M., and Ford, M. (2019). Lithological control on the post-orogenic topography and erosion history of the Pyrenees. *Earth Planet Sci. Lett.* 518, 53–66. doi:10.1016/j.epsl.2019.04.034

Botsyun, S., Sepulchre, P., Donnadieu, Y., Risi, C., Licht, A., and Rugenstein, J. K. C. (2019). Revised paleoaltimetry data show low Tibetan Plateau elevation during the Eocene. *Science* 363 (6430), eaaq1436. doi:10.1126/science.aaq1436

Braun, J. (2002). Quantifying the effect of recent relief changes on age–elevation relationships. *Earth Planet Sci. Lett.* 200 (3–4), 331–343. doi:10.1016/s0012-821x(02)00638-6

Clark, M. K., and Royden, L. H. (2000). Topographic ooze: building the eastern margin of Tibet by lower crustal flow. *Geology* 28, 703–706. doi:10.1130/0091-7613(2000)28<703:tobtem>2.0.co;2

Clark, M. K., Royden, L. H., Whipple, K. X., Burch el, B. C., Zhang, X., and Tang, W. (2006). Use of a regional, relict landscape to measure vertical deformation of the eastern Tibetan Plateau. *J. Geophys. Res. Earth Surface* 111, 187-10. doi:10.1029/2005jf000294

Clark, M. K., Schoenbohm, L. M., Royden, L. H., Whipple, K. X., Burchfiel, B. C., Zhang, X., et al. (2004). Surface uplift, tectonics, and erosion of eastern Tibet from large-scale drainage patterns. *Tectonics* 23 (1). doi:10.1029/2002tc001402

Cook, K. L., Hovius, N., Wittmann, H., Heimsath, A. M., and Lee, Y.-H. (2018). Causes of rapid uplift and exceptional topography of Gongga Shan on the eastern margin of the Tibetan Plateau. *Earth Planet Sci. Lett.* 481, 328–337. doi:10.1016/j.epsl.2017.10.043

Copley, A. (2008). Kinematics and dynamics of the southeastern margin of the Tibetan Plateau. *Geophys. J. Int.* 174, 1081–1100. doi:10.1111/j.1365-246x.2008.03853.x

Croissant, T., and Braun, J., (2014). Constraining the stream power law: a novel approach combining a landscape evolution model and an inversion method. *Earth Surf. Dynam. Discuss.* 2 (1), 155–166. doi:10.5194/esurf-2-155-2014

Deng, B., Chew, D., Mark, C., Liu, S., Cogné, N., Jiang, L., et al. (2020). Late Cenozoic drainage reorganization of the paleo-Yangtze river constrained by multi-proxy provenance analysis of the Paleo-lake Xigeda. *Geol. Soc. Am. Bull.* doi:10.1130/b35579.1

Egholm, D. L., Jansen, J. D., Brædstrup, C. F., Pedersen, V. K., Andersen, J. L., Ugelvig, S. V., et al. (2017). Formation of plateau landscapes on glaciated continental margins. *Nat. Geosci.* 10 (8), 592. doi:10.1038/ngeo2980

Egholm, D. L., Nielsen, S. B., Pedersen, V. K., and Lesemann, J.-E. (2009). Glacial effects limiting mountain height. *Nature* 460 (7257), 884. doi:10.1038/nature08263

England, P., and Molnar, P., (1990). Surface uplift, uplift of rocks, and exhumation of rocks. *Geology* 18 (12), 1173–1177. doi:10.1130/0091-7613(1990)018<1173:suuora>2.3.co;2

Ferrier, K. L., Huppert, K. L., and Perron, J. T. (2013). Climatic control of bedrock river incision. *Nature* 496, 206–209. doi:10.1038/nature11982

Fox, M. (2019). A linear inverse method to reconstruct paleo-topography. *Geomorphology* 337, 151–164. doi:10.1016/j.geomorph.2019.03.034

Fox, M., Bodin, T., and Shuster, D. L. (2015b). Abrupt changes in the rate of Andean Plateau uplift from reversible jump Markov chain Monte Carlo inversion of river profiles. *Geomorphology* 238, 1–14. doi:10.1016/j.geomorph.2015.02.022

Fox, M., Herman, F., Kissling, E., and Willett, S. D. (2015a). Rapid exhumation in the Western Alps driven by slab detachment and glacial erosion. *Geology* 43 (5), 379–382. doi:10.1130/g36411.1

Fox, M., Goren, L., May, D. A., and Willett, S. D. (2014). Inversion of fluvial channels for paleorock uplift rates in Taiwan. *J. Geophys. Res. Earth Surf.* 119 (9), 1853–1875. doi:10.1002/2014jf003196

Ge, Y., Liu-Zeng, J., Zhang, J., Wang, W., Tian, Y., Fox, M., et al. (2020). Spatio-temporal variation in rock exhumation linked to large-scale shear zones in the southeastern Tibetan Plateau. *Sci. China Earth Sci.* 63, 512–532. doi:110.1007/s11430-019-9567-y

Goren, L., Fox, M., and Willett, S. D. (2014). Tectonics from fluvial topography using formal linear inversion: theory and applications to the Inyo Mountains, California. *J. Geophys. Res. Earth Surf.* 119, 1651–1681. doi:10.1002/2014jf003079

Gourbet, L., Yang, R., Fellin, M. G., Paquette, J.-L., Willett, S. D., Gong, J., et al. (2020). Evolution of the Yangtze river network, southeastern Tibet: insights from thermochronology and sedimentology. *Lithosphere* 12 (1), 3–18. doi:10.1130/l1104.1

Hales, T. C., and Roering, J. J. (2007). Climatic controls on frost cracking and implications for the evolution of bedrock landscapes. *J. Geophys. Res. Earth Surf.* 112 (F2). doi:10.1029/2006jf000616

Hallet, B., and Molnar, P. (2001). Distorted drainage basins as markers of crustal strain east of the Himalaya. *J. Geophys. Res.* 106 (B7), 13697–13709. doi:10.1029/2000jb900335

Hansen, P. C. (1992). Analysis of discrete ill-posed problems by means of the L-curve. *SIAM Rev.* 34, 561–580. doi:10.1137/1034115

Henck, A. C., Huntington, K. W., Stone, J. O., Montgomery, D. R., and Hallet, B. (2011). Spatial controls on erosion in the three rivers region, southeastern Tibet and southwestern China. *Earth Planet Sci. Lett.* 303 (1-2), 71–83. doi:10.1016/j.epsl.2010.12.038

Howard, A. D. (1994). A detachment-limited model of drainage basin evolution. *Water Resour. Res.* 30, 2261–2285. doi:10.1029/94wr00757

Kirby, E., and Whipple, K. X. (2012). Expression of active tectonics in erosional landscapes. *J. Struct. Geol.* 44, 54–75. doi:10.1016/j.jsg.2012.07.009

Kirby, E., Whipple, K. X., Tang, W., and Chen, Z. (2003). Distribution of active rock uplift along the eastern margin of the Tibetan Plateau: inferences from bedrock channel longitudinal profiles. *J. Geophys. Res. Solid Earth* 108 (B4), 2217. doi:10.1029/2001jb000861

Lehner, B., Verdin, K., and Jarvis, A. (2008). New global hydrography derived from spaceborne elevation data. *Eos Trans. AGU* 89 (10), 93–94. doi:10.1029/2008eo100001

Li, Y., Liu, M., Li, Y., and Chen, L. (2019). Active crustal deformation in southeastern Tibetan Plateau: the kinematics and dynamics. *Earth Planet Sci. Lett.* 523, 115708. doi:10.1016/j.epsl.2019.07.010

Liu, F., Gao, H., Pan, B., Li, Z., and Su, H. (2019). Quantitative analysis of planation surfaces of the upper Yangtze River in the Sichuan-yunnan region, Southwest China. *Front. Earth Sci.* 13 (1), 55–74. doi:10.1007/s11707-018-0707-y

Liu-Zeng, J., Zhang, J., McPhillips, D., Reiners, P., Wang, W., Pik, R., et al. (2018). Multiple episodes of fast exhumation since Cretaceous in southeast Tibet, revealed by low-temperature thermochronology. *Earth Planet Sci. Lett.* 490, 62–76. doi:10.1016/j.epsl.2018.03.011

Ma, Z., Zhang, H., Wang, Y., Tao, Y., and Li, X. (2020). Inversion of Dadu River bedrock channels for the late cenozoic uplift history of the eastern Tibetan Plateau. *Geophys. Res. Lett.*

McPhillips, D., Hoke, G. D., Liu-Zeng, J., Bierman, P. R., Rood, D. H., and Niedermann, S. (2016). Dating the incision of the Yangtze River gorge at the First Bend using three-nuclide burial ages. *Geophys. Res. Lett.* 43 (1), 101–110. doi:10.1002/2015gl066780

Molnar, P., Boos, W. R., and Battisti, D. S. (2010). Orographic controls on climate and paleoclimate of Asia: thermal and mechanical roles for the Tibetan Plateau. *Annu. Rev. Earth Planet Sci.* 38, 77–102. doi:10.1146/annurev-earth-040809-152456

Mudd, S. M., Attal, M., Milodowski, D. T., Grieve, S. W. D., and Valters, D. A. (2014). A statistical framework to quantify spatial variation in channel gradients using the integral method of channel profile analysis. *J. Geophys. Res. Earth Surf.* 119, 138–152. doi:10.1002/2013jf002981

Mudd, S. M., Clubb, F. J., Gailleton, B., and Hurst, M. D. (2018). How concave are river channels? *Earth Surf. Dynam. Discuss.* 6 (2), 505–523. doi:10.5194/esurf-6-505-2018

Nie, J., Ruetenik, G., Gallagher, K., Hoke, G., Garzione, C. N., Wang, W., et al. (2018). Rapid incision of the Mekong River in the middle Miocene linked to monsoonal precipitation. *Nat. Geosci.* 11, 944–948. doi:10.1038/s41561-018-0244-z

Ouimet, W. B., Whipple, K. X., and Granger, D. E. (2009). Beyond threshold hillslopes: channel adjustment to base-level fall in tectonically active mountain ranges. *Geology* 37 (7), 579–582. doi:10.1130/g30013a.1

Ouimet, W., Whipple, K., Royden, L., Reiners, P., Hodges, K., and Pringle, M. (2010). Regional incision of the eastern margin of the Tibetan Plateau. *Lithosphere* 2, 50–63. doi:10.1130/l57.1

Pan, G. T., Ding, J., Yao, D. S., and Wang, L. Q. (2004). *Guidebook of 1: 1,500,000 geologic map of the Qinghai–Xizang (Tibet) plateau and adjacent areas*. Chengdu, China: Chengdu Cartographic Publishing House, 48.

Pan, Y., and Shen, W. B. (2017). Contemporary crustal movement of southeastern Tibet: constraints from dense GPS measurements. *Sci. Rep.* 7, 45348. doi:10.1038/srep45348

Perron, J. T., and Royden, L. (2012). An integral approach to bedrock river profile analysis. *Earth Surf. Process. Landf.* 38, 570–576. doi:10.1002/esp.3302

Replumaz, A., San José, M., Margirier, A., van der Beek, P., Gautheron, C., Leloup, P. H., et al. (2020). Tectonic control on rapid late Miocene—quaternary incision of the Mekong River Knickzone, southeast Tibetan Plateau. *Tectonics* 39 (2), e2019TC005782. doi:10.1029/2019tc005782

Richards, F. D., Hoggard, M. J., and White, N. J. (2016). Cenozoic epeirogeny of the Indian peninsula. *Geochem. Geophys. Geosyst.* 17, 4920–4954. doi:10.1002/2016gc006545

Roering, J. J., Marshall, J., Booth, A. M., Mort, M., and Jin, Q. (2010). Evidence for biotic controls on topography and soil production. *Earth Planet Sci. Lett.* 298 (1-2), 183–190. doi:10.1016/j.epsl.2010.07.040

Roberts, G. G., Paul, J. D., White, N., and Winterbourne, J. (2012). Temporal and spatial evolution of dynamic support from river profiles: a framework for Madagascar. *Geochem. Geophys. Geosyst.* 13 (4), 1087. doi:10.1029/2012gc004040

Roy, S. G., Tucker, G. E., Koons, P. O., Smith, S. M., and Upton, P. (2016). A fault runs through it: modeling the influence of rock strength and grain-size distribution in a fault-damaged landscape. *J. Geophys. Res. Earth Surf.* 121 (10), 1911–1930. doi:10.1002/2015jf003662

Royden, L., and Taylor Perron, J. (2013). Solutions of the stream power equation and application to the evolution of river longitudinal profiles. *J. Geophys. Res.: Earth Surface* 118 (2), 497–518

Rudge, J. F., Roberts, G. G., White, N. J., and Richardson, C. N. (2015). Uplift histories of Africa and Australia from linear inverse modeling of drainage inventories. *J. Geophys. Res. Earth Surf.* 120 (5), 894–914. doi:10.1002/2014jf003297

Schaller, M., Ehlers, T. A., Lang, K. A. H., Schmid, M., and Fuentes-Espoz, J. P. (2018). Addressing the contribution of climate and vegetation cover on hillslope denudation, Chilean Coastal Cordillera (26°-38°S). *Earth Planet Sci. Lett.* 489, 111–122. doi:10.1016/j.epsl.2018.02.026

Scherler, D., DiBiase, R. A., Fisher, G. B., and Avouac, J.-P. (2017). Testing monsoonal controls on bedrock river incision in the Himalaya and Eastern Tibet with a stochastic-threshold stream power model. *J. Geophys. Res. Earth Surf.* 122 (7), 1389–1429. doi:10.1002/2016jf004011

Schoenbohm, L. M., Whipple, K. X., Burchfiel, B. C., and Chen, L. (2004). Geomorphic constraints on surface uplift, exhumation, and plateau growth in the Red River region, Yunnan Province, China. *Geol. Soc. Am. Bull.* 116, 895–909. doi:10.1130/b25364.1

Schwanghart, W., and Scherler, D. (2020). Divide mobility controls knickpoint migration on the Roan Plateau (Colorado, USA). *Geology* 48, 698–702. 10.1130/G47054.1

Sklar, L. S., and Dietrich, W. E., (2001). Sediment and rock strength controls on river incision into bedrock. *Geology* 29 (12), 1087–1090. doi:10.1130/0091-7613(2001)029<1087:sarsco>2.0.co;2

Sternai, P., Herman, F., Champagnac, J.-D., Fox, M., Salcher, B., and Willett, S. D. (2012). Pre-glacial topography of the European Alps. *Geology* 40, 1067–1070. doi:10.1130/g33540.1

Styron, R. H., Garcia, J., and Pagani, M. (2017). "The GEM Global Active Faults Database: the growth and synthesis of a worldwide database of active structures for PSHA, research, and education," in AGU fall meeting abstracts, Washington, DC, December 11–15, 2017.

Suhail, H. A., Yang, R., Chen, H., and Rao, G. (2020). The impact of river capture on the landscape development of the Dadu River drainage basin, eastern Tibetan Plateau. *J. Asian Earth Sci.* 198, 104377. doi:10.1016/j.jseaes.2020.104377

Tan, X., Liu, Y., Lee, Y.-H., Lu, R., Xu, X., Suppe, J., et al. (2019). Parallelism between the maximum exhumation belt and the Moho ramp along the eastern Tibetan Plateau margin: coincidence or consequence? *Earth Planet Sci. Lett.* 507, 73–84. doi:10.1016/j.epsl.2018.12.001

Tapponnier, P., Peltzer, G. L. D. A. Y., Le Dain, A. Y., Armijo, R., and Cobbold, P. (1982). Propagating extrusion tectonics in Asia: new insights from simple experiments with plasticine. *Geology* 10 (12), 611–616. doi:10.1130/0091-7613(1982)10<611:petian>2.0.co;2

Whipple, K. X., DiBiase, R. A., Ouimet, W. B., and Forte, A. M. (2017a). Preservation or piracy: diagnosing low-relief, high-elevation surface formation mechanisms. *Geology* 45, 91–94. doi:10.1130/g38490.1

Whipple, K. X., DiBiase, R. A., Ouimet, W. B., and Forte, A. M. (2017b). Preservation or piracy: diagnosing low-relief, high-elevation surface formation mechanisms: reply. *Geology* 45, e422. doi:10.1130/g39252y.1

Whipple, K. X., Forte, A. M., DiBiase, R. A., Gasparini, N. M., and Ouimet, W. B. (2017c). Timescales of landscape response to divide migration and drainage capture: implications for the role of divide mobility in landscape evolution. *J. Geophys. Res. Earth Surf.* 122 (1), 248–273. doi:10.1002/2016jf003973

Willett, S. D. (2017). Preservation or piracy: diagnosing low-relief, high-elevation surface formation mechanisms: comment. *Geology* 45, e421. doi:10.1130/g38929c.1

Willett, S. D., McCoy, S. W., Perron, J. T., Goren, L., and Chen, C. Y. (2014). Dynamic reorganization of river basins. *Science* 343. 1248765. doi:10.1126/science.1248765

Yang, R., Suhail, H. A., Gourbet, L., Willett, S. D., Fellin, M. G., Lin, X., et al. (2020). Early Pleistocene drainage pattern changes in Eastern Tibet: constraints from provenance analysis, thermochronometry, and numerical modeling. *Earth Planet Sci. Lett.* 531, 115955. doi:10.1016/j.epsl.2019.115955

Yang, R., Willett, S. D., and Goren, L. (2015). *In situ* low-relief landscape formation as a result of river network disruption. *Nature* 520, 526–529. doi:10.1038/nature14354

Zhang, H., Oskin, M. E., Liu-Zeng, J., Zhang, P., Reiners, P. W., and Xiao, P. (2016). Pulsed exhumation of interior eastern Tibet: implications for relief generation mechanisms and the origin of high-elevation planation surfaces. *Earth Planet Sci. Lett.* 449, 176–185. doi:10.1016/j.epsl.2016.05.048

Zheng, H., Clift, P. D., He, M., Bian, Z., Liu, G., Liu, X., et al. (2020). Formation of the first bend in the late Eocene gave birth to the modern Yangtze River, China. *Geology* 48. 10.1130/G48149.1

Conflict of Interest: The authors declare that the research was conducted in the absence of any commercial or financial relationships that could be construed as a potential conflict of interest.

frontiers in Earth Science

ORIGINAL RESEARCH
published: 12 January 2021
doi: 10.3389/feart.2020.587022

A Middle to Late Miocene Trans-Andean Portal: Geologic Record in the Tatacoa Desert

C. Montes[1], C. A. Silva[2], G. A. Bayona[3], R. Villamil[4], E. Stiles[2,5], A. F. Rodriguez-Corcho[6], A. Beltran-Triviño[7], F. Lamus[1], M. D. Muñoz-Granados[4], L. C. Perez-Angel[8], N. Hoyos[1], S. Gomez[2,7], J. J. Galeano[1], E. Romero[7,2], M. Baquero[3], A. L. Cardenas-Rozo[7] and A. von Quadt[9]*

[1]Universidad del Norte, Barranquilla, Colombia, [2]Center for Tropical Paleoecology and Archaeology, Smithsonian Tropical Research Institute, Ancón, Panamá, [3]Corporación Geologica Ares, Bogotá, Colombia, [4]Departamento de Geociencias, Universidad de Los Andes, Bogotá, Colombia, [5]Department of Biology, University of Washington, Seattle, WA, United States, [6]Schoool of Earth Sciences, University of Melbourne, Melbourne, VIC, Australia, [7]Departamento de Ciencias de la Tierra, Universidad EAFIT, Medellín, Colombia, [8]Department of Geological Sciences, Cooperative Institute for Research in Environmental Sciences (CIRES), Institute of Arctic and Alpine Research (INSTAAR), University of Colorado Boulder, Boulder, CO, United States, [9]Institute of Geochemistry and Petrology, Department of Earth Sciences, ETH Zurich, Zürich, Switzerland

OPEN ACCESS

Edited by:
Paolo Ballato, Roma Tre University, Italy

Reviewed by:
Cristina Maria Pinto Gama, University of Evora, Portugal
Fabio Matano, National Research Council (CNR), Italy

***Correspondence:**
C. Montes
camilomontes@uninorte.edu.co

Specialty section:
This article was submitted to Quaternary Science, Geomorphology and Paleoenvironment, a section of the journal Frontiers in Earth Science

Received: *24 July 2020*
Accepted: *20 November 2020*
Published: *12 January 2021*

Citation:
Montes C, Silva CA, Bayona GA, Villamil R, Stiles E, Rodriguez-Corcho AF, Beltran-Triviño A, Lamus F, Muñoz-Granados MD, Perez-Angel LC, Hoyos N, Gomez S, Galeano J J, Romero E, Baquero M, Cardenas-Rozo AL and von Quadt A (2021) A Middle to Late Miocene Trans-Andean Portal: Geologic Record in the Tatacoa Desert. Front. Earth Sci. 8:587022. doi: 10.3389/feart.2020.587022

Integration of several geologic lines of evidence reveals the prevalence of a lowland trans-Andean portal communicating western Amazonia and the westernmost Andes from at least middle Miocene until Pliocene times. Volcanism and crustal shortening built up relief in the southernmost Central and Eastern Cordilleras of Colombia, closing this lowland gap. Independent lines of evidence consist first, of field mapping in the Tatacoa Desert with a coverage area of ~381 km^2, 1,165 km of geological contact traces, 164 structural data points, and 3D aerial digital mapping models. This map documents the beginning of southward propagation of the southernmost tip of the Eastern Cordillera's west-verging, fold-and-thrust belt between ~12.2 and 13.7 Ma. Second, a compilation of new and published detrital zircon geochronology in middle Miocene strata of the Tatacoa Desert shows three distinctive age populations: middle Miocene, middle Eocene, and Jurassic; the first two sourced west of the Central Cordillera, the latter in the Magdalena Valley. Similar populations with the three distinctive peaks have now been recovered in western Amazonian middle Miocene strata. These observations, along with published molecular and fossil fish data, suggest that by Serravallian times (~13 Ma), the Northern Andes were separated from the Central Andes at ~3°N by a fluvial system that flowed into the Amazon Basin through the Tatacoa Desert. This paleogeographic configuration would be similar to a Western Andean, or Marañon Portal. Late Miocene flattening of the subducting Nazca slab caused the eastward migration of the Miocene volcanic arc, so that starting at ~4 Ma, large composite volcanoes were built up along the axis of today's Central Cordillera, closing this lowland Andean portal and altering the drainage patterns to resemble a modern configuration.

Keywords: Northern Andes, Andes, miocene, drainages, La Venta, portal, Magdalena valley

INTRODUCTION

Located between two major cordilleras in the Northern Andes (**Figure 1**), the Miocene deposits of the Tatacoa Desert, collectively known as "La Venta", have provided key insights into the paleogeography and the biodiversity of the Neogene in South America. La Ventan deposits contain the record of the Eastern Cordilleran uplift (Guerrero, 1993, Guerrero, 1997; Lundberg et al., 1998; Anderson et al., 2016), span a section of the Mid-Miocene Climatic Optimum—one of the most notable Cenozoic global warming events (Flower and Kennett, 1994; Zachos et al., 2001), and are the source of one of the best-studied Neotropical terrestrial vertebrate assemblages in South America (Kay et al., 1997; Carrillo et al., 2015). The rich paleontological record of La Venta deposits has shed light on the evolution and biogeography of vertebrate lineages and the development of major drainage basins in South America. Arguably, one of the most relevant geological insights has been gained from fossil fish faunas preserved in La Ventan strata of the Tatacoa Desert. These fossils are evidence of a direct lowland connection between the Amazonian and the Magdalena drainage systems (i.e. an Andean portal) during middle Miocene times (Lundberg and Chernoff, 1992). This insight places tight constraints on the mode and timing of mountain growth, specially the presence

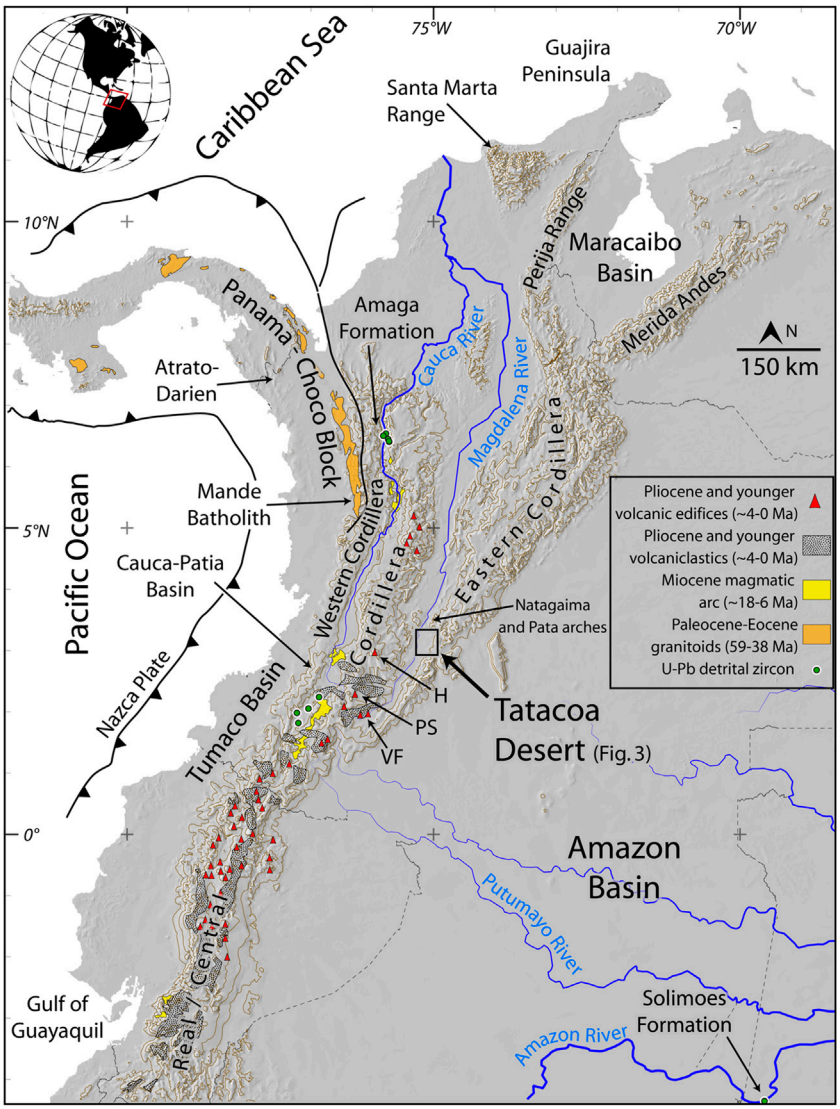

FIGURE 1 | General location map of the Northern Andes (the Andean block of Pennington, 1981), contour lines every 1,000 m. Green dots represent U-Pb detrital zircon samples: middle Miocene strata of the Amaga Formation (Montes et al., 2015), the Cauca-Patia Basin (Echeverri et al., 2015), and the Amazon Basin (Kern et al., 2020). The Miocene magmatic arc consists of hypabyssal porphyritic granitoids, while the Panama-Choco Eocene arc consists mostly of granitoids (Leal-Mejia, 2011; Montes et al., 2012; Bineli-Betsi et al., 2017; Leal-Mejia et al., 2019). Pliocene (~4 Ma) and younger ignimbrites and volcanoclastic rocks (Barberi et al., 1988; Torres-Hernandez, 2010; Egüez et al., 2017) represent the initial magmatic pulses in the construction of large composite active today in the Northern Andes (H: Huila Volcano, PS: Purace-Sotara volcanoes, VF: Villalobos-La Fragua volcanic center).

and timing of lowland portals that segmented the Andean cordillera of the past.

Equatorial lowland portals through the Andes have long been proposed to exist, variably called the Marañon, or Western Andean Portal (Hoorn et al., 1995; Lundberg et al., 1998; Antonelli et al., 2009; Hoorn et al., 2010). Such a lowland passage would have allowed equatorial (**Figure 1**) westward flow of major South American rivers (Hurtado et al., 2018), separating mountain-specific taxa between Central and Northern Andes (Antonelli et al., 2009), and joining lowland taxa of the Pacific and the Amazon (Haffer, 1967; Slade and Moritz, 1998; Miller et al., 2008; Weir and Price, 2011). Vanishing of such Late Cretaceous to middle Miocene times portal took place as a result of Andean topographic growth, as the raising orogen joined formerly isolated high Andean elevations, simultaneously segmenting formerly connected lowland drainage basins. There is however, little geologic data that more precisely pinpoint the location, and corroborate the presence of a lowland portal in the Northern Andes, and the time it remained opened.

In an attempt to better constrain Andean paleotopography, we focused our study on the gaps, or lowland portals that allowed the flow of major rivers across the Northern Andes. In this contribution we document the prevalence of low topography in a segment of the Northern Andes (~3°N) during Miocene times. By updating the geologic map of the Tatacoa Desert (Guerrero, 1993, Guerrero, 1997), and adding geochronological constraints to the existing stratigraphic framework (Flynn et al., 1997; Anderson et al., 2016), we established cartographic and geochronological criteria that helped trace the evolution of a major cross-Andean drainage. These new data, along with a compilation of existing data in the Northern Andes and Amazonia, bring into better focus the Miocene drainage networks and therefore, the timing and location of topographic growth in this part of the Northern Andes.

PALEOGEOGRAPHY OF THE TATACOA DESERT

Today, the Magdalena Valley is a large, longitudinal inter-Andean depression with variable widths between 20 and 40 km, whose evolution has been controlled by tectonic processes (Schamel, 1991; Van der Wiel and Van den Bergh, 1992) while maintaining a low topography of around 400 m a.s.l. (**Figure 1**). The Tatacoa Desert is located at the southern termination of the Magdalena Valley (**Figure 1**), loosely called a desert despite having precipitations of ~1,100 mm/yr and a dry forest cover (Hermelin, 2016). Its location in a leeward position with respect to the Eastern Cordillera, and bedrock geology characterize the Tatacoa Desert as badlands (Dill et al., 2020) with bedrock freshly exposed with no intervening regolith, extensive soil development or thick vegetation. It is in these badlands with nearly continuously exposed bedrock, long dip slopes, and frequent gullies, that the paleontological richness of La Venta strata has been abundantly documented within the stratigraphic framework defined by Guerrero (1993), Guerrero (1997).

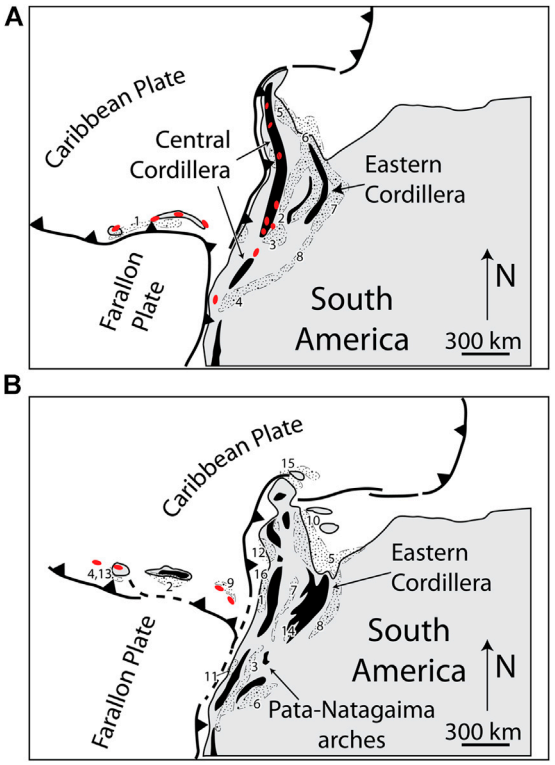

FIGURE 2 | Palinspastic reconstruction of the Northern Andes and southern Caribbean modified after Montes et al. (2019) showing significant relief in black, magmatic centers in red, and coarse-grained deposits (stippled pattern), tracking the presence and approximate location of relief, but not its magnitude. Numbers represent the location of known clastic units of that age. **(A)** Schematic paleogeography of late Paleocene-early Eocene times (1: Woodring, 1957; 2: Guerrero et al., 2000; 3: Montes et al., 2003; 4: Ruiz et al., 2004; Martin-Gombojav and Winkler, 2008; 5: Bayona et al., 2011; 6: Ayala-Calvo et al., 2012; 7: Bayona et al., 2013; 8: Bayona, 2018). **(B)** Schematic paleogeography (Ayala-Calvo et al., 2012; Cardona et al., 2014) of latest Eocene-early Oligocene times (1: Grosse, 1926; 2: Woodring, 1957; 3: Caicedo and Roncancio, 1994; 4: Kolarsky et al., 1995; 5: Parnaud et al., 1995; 6: Christophoul et al., 2002; 7: Gomez et al., 2005a; 8: Bayona et al., 2008; 9: Rodriguez and Sierra, 2010; 10: Xie et al., 2010; 11: Borrero et al., 2012; 12: Cardona et al., 2012; 13: Herrera et al., 2012; 14: Ochoa et al., 2012; 15: Zapata et al., 2014; Moreno et al., 2015; 16: Manco-Garces et al., 2020).

In the following paragraphs, we review the landscape history of the southern Magdalena Valley in light of the Cretaceous and younger regional development of northwestern South America. The inception of a Cretaceous passive margin can be taken as a convenient starting point to review the history of landscape development in the Northern Andes. Regionally continuous Cretaceous strata document the persistence of a west-facing oceanic margin (Etayo-Serna, 1994; Moreno-Sanchez and Pardo-Trujillo, 2003), with source areas located to the east, in the Guiana shield (Villamil, 1998; Horton, 2018; Sarmiento-Rojas, 2018).

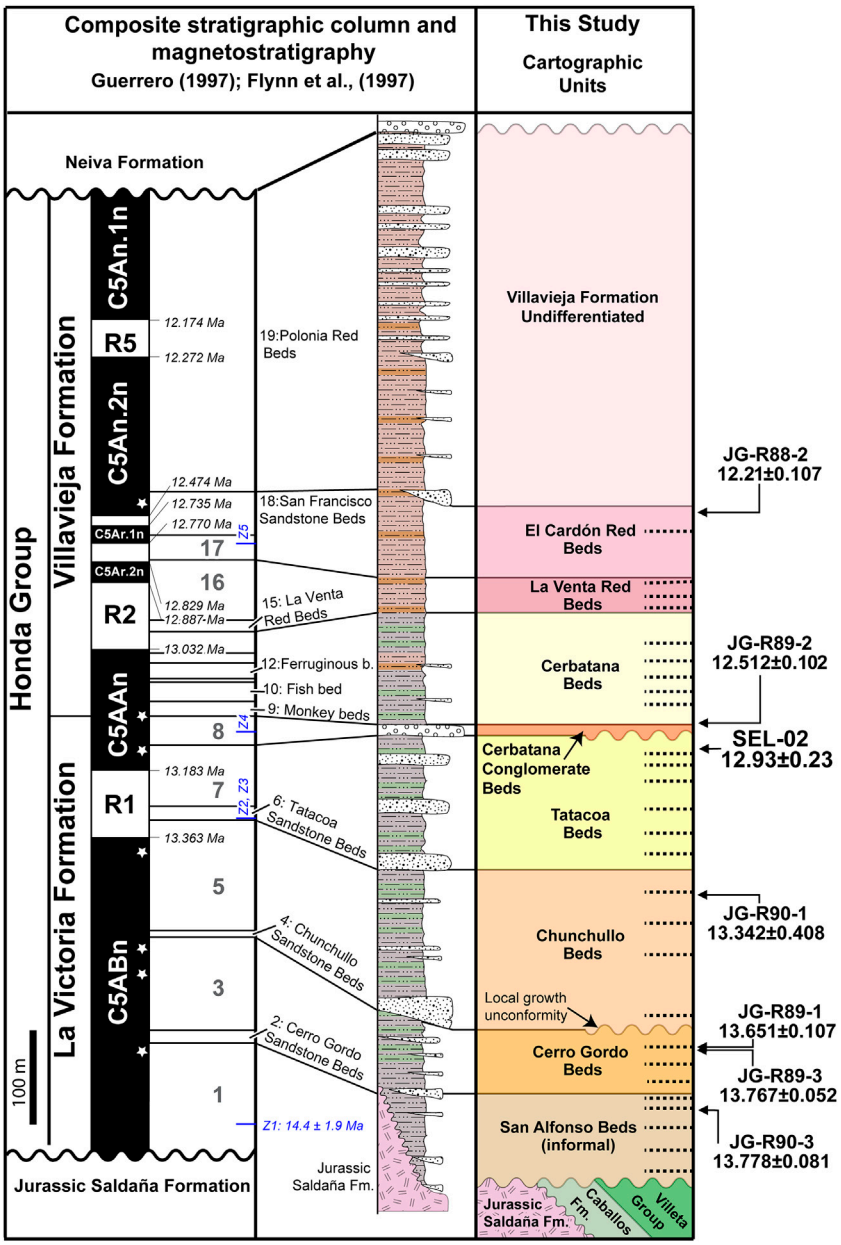

FIGURE 3 | Updated stratigraphic scheme for the Honda Group in the Tatacoa Desert. The original columns of Guerrero (1993, 1997), were consolidated into a single composite column where lenticular beds represent discontinuous sandstone units (i.e. found in only one stratigraphic column), and mudstones according to their color (Anderson et al., 2016). Magnetostratigraphy covers the C5An.1n-C5ABn interval, showing updated ages after Hilgen et al. (2012). Black arrows represent geochronological samples from Flynn et al. (1997), blue arrows represent maximum depositional ages of Anderson et al., (2016). All samples were re-located (stars) in the stratigraphic column following the lithostratigraphic marker beds (horizontal dashed lines) of the geologic map (**Figure 4**).

Latest Cretaceous-Early Eocene

Collision of oceanic terranes against the Cretaceous passive margin of northwestern South America marked the start of a regional marine regression, and gradual installation of swampy environments where locally thick coal beds were deposited (Bayona et al., 2011). These swamps were bound to the west by a primordial, probably discontinuous, eastwardly-tilted Central/Real Cordillera (**Figure 2A**), and to the east by isolated intra-plate uplifts (Villamil, 1999; Gomez et al., 2003; Gomez et al., 2005b; Bayona et al., 2011; Bayona et al., 2020). This tectonically-forced marine regression may have started as early as latest Cretaceous to the south in the Oriente Basin, reaching the northern end of the orogen in the Guajira region in middle Paleocene times, taking ~10 million years to propagate from south to north (Jaimes and de Freitas, 2006; Martin-Gombojav and Winkler, 2008; Weber et al.,

2009a; Weber et al., 2009b; Bayona et al., 2011; Cardona et al., 2011; Hurtado et al., 2018). Upper Cretaceous coarse-grained clastic deposits track the location of this orogen to segments of today's Central Cordillera (Schamel, 1991; Montes et al., 2019), a mountain range that would have constricted most westward-directed drainages in northern South America, spawning the first north- or northeastward-directed Orinoco style drainages (Hoorn et al., 1995; Lundberg et al., 1998; Hoorn et al., 2010; Bande et al., 2012; Horton, 2018; Hurtado et al., 2018).

Middle Eocene-Oligocene

In middle Eocene to Oligocene times, contractional deformation concentrated along the eastern foothills of the Central Cordillera, or internal uplifts in the Magdalena Valley, where conglomerate units (Tesalia/Chicoral, in the south, and La Paz formations in the north) unconformably accumulated upon Cretaceous and Jurassic sequences (Ramon and Rosero, 2006). By late Eocene times contractional deformation propagates eastward, to the domains of the Eastern Cordillera where westward-verging, north-trending thrust faults started defining a north-south, en-echelon fold belt that defines a young—yet incomplete—Magdalena Valley north of ~4°N (Reyes-Harker et al., 2015). The Magdalena Valley would have been defined by a topographic depression between two flanking, linear, probably discontinuous mountain ranges (**Figure 2B**): a primordial Central Cordillera to the west (Gomez et al., 2003; Gomez et al., 2005a; Nie et al., 2010; Nie et al., 2012; Horton et al., 2015) and the young Eastern Cordillera to the east (Mora et al., 2006; Bande et al., 2012; Bayona et al., 2013; Lamus et al., 2013). South of ~4°N, near the latitude of the Tatacoa Desert, the mountainous highland terrain of the Eastern Cordillera would have gently eased into the lowlands of the Amazon/Orinoco (Mora et al., 2013), only interrupted by isolated intra-basin uplifts.

In the area centered around the Tatacoa Desert, the entire 2.3 km thick, Cretaceous-Paleocene regional succession of the southern Magdalena Valley (Amezquita and Montes, 1994), is missing (see Figure 5B in Caballero et al., 2013). The Lower to Middle Jurassic volcanic, volcanoclastic mechanical basement of the Saldaña Formation (Cediel et al., 1980; Mojica and Franco, 1990) is covered by the middle Miocene strata of the Honda Group in a marked angular unconformity. This unconformity has been variably mapped as the arch of Natagaima, or Pata (**Figure 1**), resulting from a period of deformation, exhumation and erosion that removed the passive margin succession sometime between Eocene and early Miocene times (Schamel, 1991; Amezquita and Montes, 1994; Villarroel et al., 1996; Ramon and Rosero, 2006), correlative to the middle Eocene unconformity to the north in the middle Magdalena Valley (Gomez et al., 2005b). The Jurassic basement of the Natagaima Arch indeed records cooling peaks at 30 and 50 Ma (apatite fission-track in Saltaren-1 well, Reyes-Harker et al., 2015), consistent with exhumation and erosion removing most of the Cretaceous strata in the area now occupied by the Tatacoa Desert.

Miocene

By middle Miocene times the area formerly undergoing exhumation and erosion in the arches of Natagaima and Pata began subsiding, opening accommodation space to accumulate fluvial strata of the ~1,000 m thick Honda Group (Guerrero, 1993, 1997).

Stratigraphy of the Honda Group

In general terms, the Honda Group is a monotonous stratigraphic unit dominated by fining-upward, gray lithic sandstone beds (**Figure 3**), that can be easily recognized all along the southern Magdalena Valley between the ~2° and ~5°N latitude, but never in the surrounding Eastern and Central Cordilleras. Large faults of the bounding cordilleras thrust crystalline basement on to strata of the Honda Group, deforming it, and making it the youngest significantly deformed strata in the southern Magdalena Valley (Van der Hammen, 1958). West-verging, low-angle crystalline thrust sheets of the Eastern Cordillera place the Jurassic volcanoclastic Saldaña Formation (~3°N, Prado Fault, Cossio et al., 1995), and metamorphic rocks of the Garzon Massif (~2°N, Iskana-1 well, Saeid et al., 2017), on top of strata of the Honda Group. East-verging, low-angle thrust faults place Jurassic intrusives on top of strata of the Honda Group along the eastern flank of the Central Cordillera (~3°N, Amezquita and Montes, 1994).

The base of the Honda Group is marked by either an angular unconformity atop Jurassic-Cretaceous strata, or a paraconformity on strata of the Oligocene Gualanday Group, or La Cira Formation (Van der Hammen, 1958; Guerrero, 1997). The upper Miocene/Pliocene Neiva/Gigante formations rest in angular unconformity atop strata of the Honda Group (Van der Hammen, 1958; Guerrero, 1997) in the south of the Magdalena Valley (~2°N), or the Pliocene Mesa Formation to the north (~5°N).

From bottom to top the Honda Group was divided by Guerrero (1993, 1997) into two units: the La Victoria Formation, and the Villavieja Formation. The same author discriminated nineteen different horizons within the ~1,000 m thick sequence (**Figure 3**), mapping seven of them throughout parts of the Tatacoa Desert (**Figure 4**), and giving informal names of important paleontological localities to three of them: the Monkey, Fish, and Ferruginous beds (**Figure 3**). Within the La Victoria Formation, Guerrero (1993, 1997) recognized four conspicuous horizons, from bottom to top: the Cerro Gordo, Chunchullo, Tatacoa, and Cerbatana, the first three made up by sandstone beds and bedsets, and the last one a conglomerate bed, also marking the top of the La Victoria Formation. The intervening stratigraphic horizons were left unnamed.

Age of the Honda Group

The age of the Honda Group in the Tatacoa Desert was tightly constrained using magneto-stratigraphy (intervals C5An.1n - C5ABn of Cande and Kent, 1992) tied to six Ar/Ar ages in plagioclase and hornblende crystals from pumice fragments within eight "volcanic units" (Flynn et al., 1997). Although no truly volcanic ash beds were identified in strata of the Honda Group, the upsection decrease in youngest detrital zircon ages

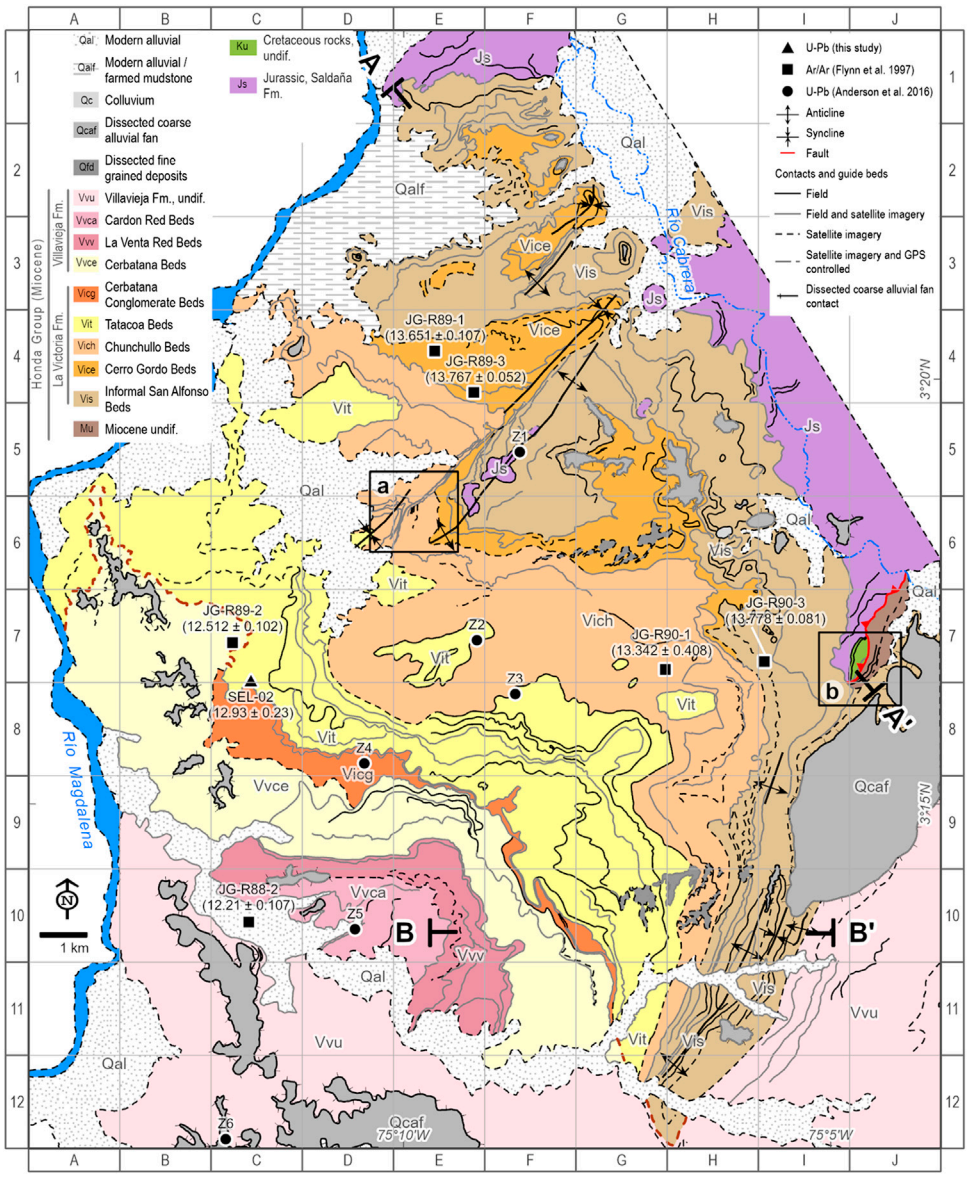

FIGURE 4 | Geologic map of the Tatacoa Desert expanded from original mapping by Guerrero (1993, 1997). The Tataoca Desert is bound to the west by the Magdalena River, to the east by the first ranges of the Eastern Cordillera, to the north by the volcaniclastic outcrops of the Jurassic Saldaña Formation in the Natagaima Arch, and to the south by strata of the overlying Neiva Formation. A larger-scale, printable at 1:25.000 version available of the map also available (Supplementary Figure S1), as well as an electronic .kml version with contacts and data stations in the Supplementary Materials.

was taken as evidence of syndepositional volcanism within the drainage basin (Anderson et al., 2016). Pumice fragments within volcanoclastic sandstones of the Honda Group show evidence of reworking since the time of eruption, but the lag time between eruption and sediment deposition was considered to be short, so Ar/Ar ages were used as near-depositional ages, and as tie points for magneto-stratigraphic reversal matching assuming no major hiatuses within the sequence (210 samples, yielding an interval between 11.6 and 13.5 Ma, Flynn et al., 1997). Despite updates to the chronology of intervals C5An.1n - C5ABn (Hilgen et al., 2012), the correlation of the magnetic polarity stratigraphy of the Honda Group of Flynn et al. (1997) remains unchanged (**Figure 3**). More recent U-Pb detrital zircon geochronology suggests an earlier start for the accumulation of the Honda Group (14.4 ±1.9 Ma) using the cluster of youngest detrital zircon grains from five samples of Honda Group sandstone in the Tatacoa Desert (samples Z1 to Z5 of Anderson et al., 2016).

Fluvial strata within the lower Villavieja Formation contain fossil fish with Amazonian affinities like the giant Pirarucu,

Arapaima gigas, and many others riverine fish. These findings imply that at the time of deposition of these strata, large meandering river systems (Guerrero, 1997) were connected to the Amazonian drainage system (i.e., no continuous southernmost Eastern Cordillera, Lundberg and Chernoff, 1992; Albert et al., 2006; Ballen and Moreno-Bernal, 2019). This connection would have been severed by topographic growth of the Eastern Cordillera as west-verging structures (Schamel, 1991; Saeid et al., 2017) built topography after accumulation of strata of the Honda Group, and seem to have definitely established the Eastern Cordillera south of 4°N.

In summary, the area now occupied by the Tatacoa Desert preserves a record of most episodes in the growth and evolution of the Northern Andes. First, it contains the record of a stable Late Cretaceous passive margin in an embayment open to the north. Then, deformation, exhumation and erosion formed an isolated intrabasin uplift in Eocene-Oligocene times. Later in Miocene times, subsidence formed a sub-Andean sedimentary basin open to the lowlands of the Amazon to the east. This Miocene basin contains the record of the last lowland hydrologic connection between the Caribbean and the Amazon before forming the fully inter-Andean valley of today.

METHODOLOGY

Field Mapping

Traditional geologic mapping was performed at 1:25.000 scale using Brunton compass, colored pencils, and paper maps (IGAC topo sheets: 303-III-A and C, 303-I-C, 302-IV-B and D, and 302-II-D). Because the low dips, monotonous sequence, and nearly complete absence of conspicuous marker beds, it is often difficult to establish the stratigraphic position of individual beds within the Miocene sequence of the Tatacoa Desert. Additionally, local relief in the Tatacoa Desert is subtle, with changes in elevation along field transects rarely exceeding 50 m. Field mapping was focused on deciphering superposition relations amongst beds and bed sets by following prominent cliff-forming strata along-strike for several kilometers. These cliffs, often less than 20 m high, are defined by sandstone or conglomerate beds more resistant to erosion, while gentler topography represents massive mudstone. By repeating this exercise in multiple transects, it was possible to construct a framework of superposed cliff-forming beds, and bed sets that allows lateral lithostratigraphic correlation to the stratigraphic succession of units defined by Guerrero (1993, 1997). In the northern third of the mapping area, topography is more subdued, dips are lower, with less prominent sandstone beds, so the approach described above was combined with a systematic collection of control points using hand-held GPS units.

Once the field map was completed, the contacts were digitized in QGIS and their location accuracy was checked using Google Earth satellite imagery (2013 and newer imagery). All contacts, control points and dip data are contained in .kml files (see Supplementary Material). Each geologic contact contains an attribute that indicates its origin, and the nature of post-processing, if any. Contacts mapped in the field, with no changes made during post-processing have the attribute "*Obs.field*"; contacts adjusted during post-processing are coded as "*Obs.field+i*". New contacts added during post-processing are identified as "*imagery*" and usually needed to map alluvial deposits, or extend beds mapped in the field. Contacts needed to topologically close polygons were labeled as "*border*".

We measured dip data on sandy beds, avoiding cross beds, channelized beds and clinoforms. Although it would have been preferable to measure dip data on fine-grained sediments, the massive nature, and poorer exposure of most mudstone sections prevented a systematic collection of dip data in these lithologic types. Whenever possible, we averaged out local irregularities on sandstone tops by selecting a view of a planar bedding surface, moving laterally until the two-dimensional surface appeared as a line, taking a level sight to the trace of the planar surface, and then the strike of the same sight line, later converted to dip direction (Compton, 1985).

We used oblique ortho-photos to document changing dip domains in selected, low relief, key areas of the Tatacoa Desert. We collected 338 vertical photographs at 60 m-altitude to generate a detailed 3D model of 7.83 Ha using Agisoft Metashape software. We then converted a 131-million-point cloud into a 2.8-million faces mesh with photographic texture. In order to detect beds in the 2.74 cm/pix 3D image, we employed the original 1.37 cm/pix image resolution using a textured tiled model. We used OpenPlot (Tavani et al., 2011) in 101 triangles joining single bed points to measure attitudes.

Detrital Zircon U-Pb Geochronology

Detrital zircon separation was performed at EAFIT University facilities following standard procedures such as those proposed by Mange and Maurer (1991). Rock samples were crushed in a conventional jaw-breaker and sieved various fractions. Heavy minerals were concentrated by panning the 400–63 μm fraction. Zircon grains were randomly picked-out by hand using a binocular lens from the heavy mineral concentrates, mounted in epoxy resin and polished down to be coated by carbon at ETH Zurich. Cathodoluminescence (CL) images of zircon grains were acquired to evaluate magmatic zoning, metamorphic origin or inherited cores in a Vega 3 scanning electron microscope (SEM) at the scientific center for optical and electron microscopy (ScopeM) at ETH Zurich. *In situ* U-Pb geochronology were conducted by laser ablation inductively coupled plasma mass spectrometry (LA-ICP-MS) at the Institute of Geochemistry and Petrology at ETH Zurich using a 193 nm Resolution (S155) ArF excimer laser coupled to a Element SF ICPMS (Guillong et al., 2014; Von Quadt et al., 2014). Laser ablation spots (19 microns) were selected in both cores and rims when it was possible. The full analytical dataset is reported in Table SM-1. Age uncertainties (at 2σ) for individual grains in the data table include only measurement errors. Interpreted ages are based on $^{206}Pb/^{238}U$ for grains younger than 800 Ma and $^{206}Pb/^{207}Pb$ for grains older than 800 Ma. Analyses that were >30% discordant (by comparison of $^{206}Pb/^{238}U$ and $^{206}Pb/^{207}Pb$ ages), or >5% reverse discordant, or >4% error age were not considered

FIGURE 5 | Field photographs of strata of the Honda Group. **(A)** Trough cross-stratified (arrows) medium-grained sandstone with imbricated pebbles of the Cerbatana Conglomerate Beds (quadrangle G11 in **Figure 4**). **(B)** Mudstone at the base of the San Alfonso Beds, near Cerro Gordo (quadrangle F5 in **Figure 4**). **(C)**, **(D)** Mud-cracks and erosive contact respectively, in red muddy/sandy strata of the San Alfonso Beds (quadrangle H10 in **Figure 4**). **(E)** Sharp basal contact (arrow) of the Cerbatana Conglomerate Beds (quadrangle D8 in **Figure 4**). **(F)** Gently dipping strata in the Chunchullo Beds in quadrangle H9 in **Figure 4**, notice the mappable sandstone beds and bed sets within the sequence (arrows). **(G)** Dissected alluvial deposits (black arrow) capping strata of the Cerro Gordo Beds marked by white arrow (quadrangle G5 in **Figure 4**). Inset shows close up of alluvial deposits showing the typical size distribution.

further. Uranium-Pb Concordia diagrams are constructed using Isoplot4.15 (Ludwig, 2012). We show the Tera and Wassergburg (1972) concordia diagram ($^{238}U/^{206}Pb$ - $^{207}Pb/^{206}Pb$) to focus on Mesozoic and Cenozoic zircon ages.

We calculated detrital zircon MDA (maximum depositional age) using the method of the weighted average of the youngest concordant three zircons (Y3Z), in our case, the date overlaps within 2σ uncertainty. An assessment of detrital zircon MDA estimation methods (Coutts et al., 2019) suggests that the Y3Z method is more successful and accurate than other methods such as the young grain cluster at 2σ uncertainty (YGC 2σ; Dickinson and Gehrels, 2009). The weighted average MDA was calculated by using the algorithm in Isoplot 4.15 (Ludwig, 2012).

RESULTS

Geologic Map

The updated geologic map of the Tatacoa Desert covers an area of 381 km^2, contains 1,165 km of contact traces, and 164 structural control points. This map (**Figure 4**) broadens the distribution of strata within the La Victoria and Villavieja formations of Guerrero (1993, 1997) to the entire extent of the Tatacoa Desert. We keep existing stratigraphic and structural nomenclature, using the name of the seven most prominent (**Figure 3**) sets of beds identified in Guerrero's map (1993, 1997). Our map documents the presence of two growth unconformities within the Honda Group discussed in the following paragraphs.

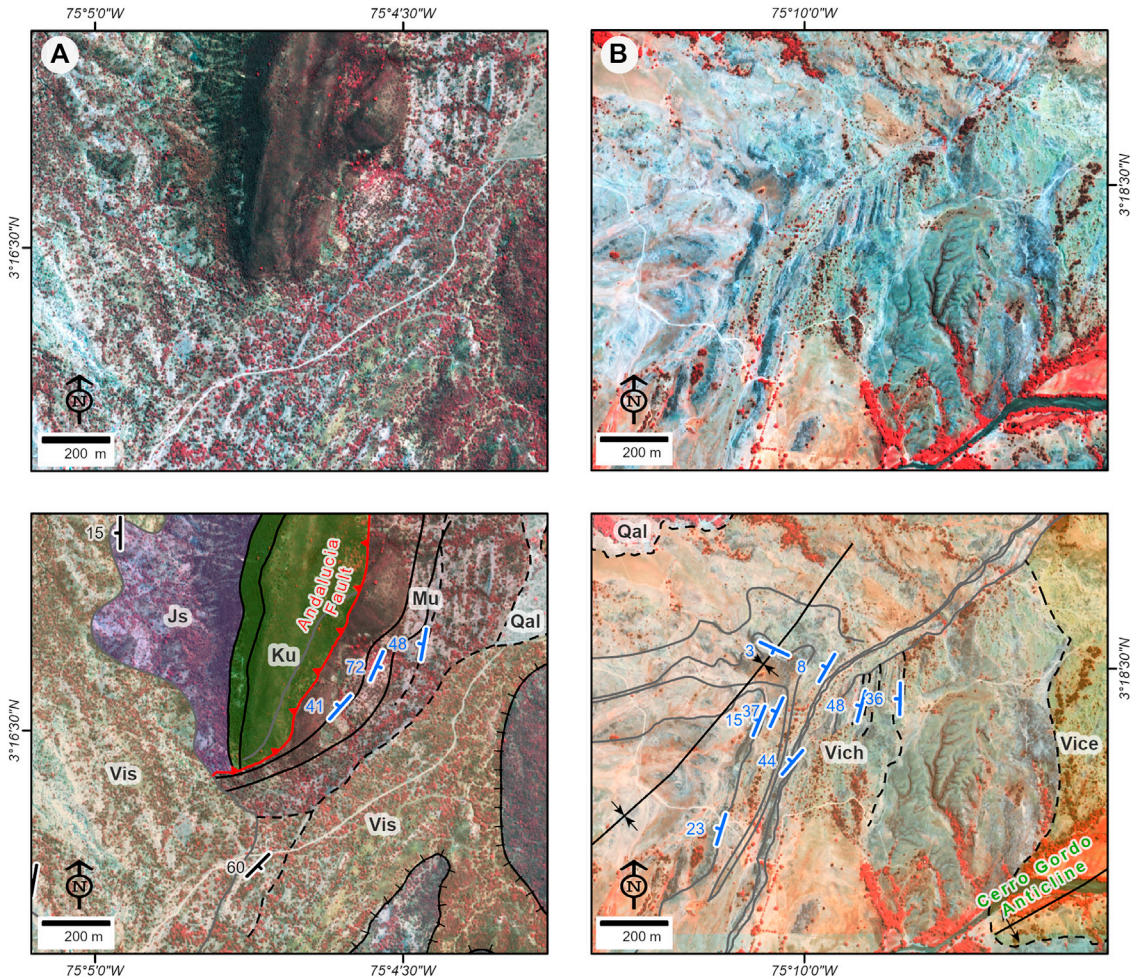

FIGURE 6 | Close ups of the geologic map (**Figure 4**) to highlight key crosscutting field relationships. **(A)** Satellite image **(top)** and geologic contacts **(bottom)** showing the trace of the Andalucia Fault fossilized by strata of the San Alfonso Beds. **(B)** Satellite image **(top)** and geologic contacts **(bottom)** showing the truncation of strata (growth unconformity) near the axis of the Cerro Gordo growth anticline. Images are Pleiades natural color composite images. All symbols as in **Figure 4**.

Being a characteristically fining-upwards unit, we decided to use each one of the horizons defined and mapped by Guerrero (1993, 1997), to name the strata above each one (**Figure 3**). This way, we separated the Honda Group in the Tatacoa Desert from bottom to top on the Cerro Gordo Beds, Chunchullo Beds (**Figure 5F**), Tatacoa Beds, Cerbatana Beds, La Venta Red Beds (**Figure 5A**), and El Cardon Red Beds. The Cerbatana Beds corresponds to the base of the Villavieja Formation and includes the Monkey Beds, Fish Beds and Ferruginous Beds. We kept the conglomerate as a separate unit (Cerbatana Conglomerate Beds, **Figures 5A,E**) as it is the most conspicuous unit in the region, which also extends laterally ~10 km, and marks the top of the La Victoria Formation (Guerrero, 1993, Guerrero, 1997). In naming the map units by the horizons at their bases, the unit at the base of the Honda Group would have been left unnamed. We therefore modified the original stratigraphic scheme by informally adding the San Alfonso Beds (**Figures 5B–D**) at the base of the La Victoria Formation to refer to those beds below the Cerro Gordo Beds (horizon 1 of Guerrero (1993, 1997)), and directly above the mechanical basement (**Figure 3**). Additionally, we report the presence of strata seemingly older than the San Alfonso Beds. We additionally refined the mapped extent of younger alluvial deposits (**Figure 5G**).

The geologic map (**Figure 4**) defines a very gently folded, south- and southeast-dipping stratigraphic succession, resting in angular unconformity on Jurassic volcanoclastic basement of the Saldaña Formation (Cediel et al., 1981). This unconformity, defining the Natagaima Arch (Mojica and Franco, 1990; Schamel, 1991; Ramon and Rosero, 2006), beheads the hanging wall anticline of the east-verging Andalucia thrust fault (Villarroel et al., 1996). Erosion did not entirely remove the Cretaceous sequence near the easternmost edge of this hanging wall anticline. Here (quadrangle I7 in **Figures 4**, **6A**, **7** section A-A'), the Albian Caballos Formation (**Figure 3**, sensu Florez and Carrillo, 1994) rests unconformably on the Saldaña Formation near the fault zone, which is marked by a sliver of black fossiliferous limestone less than 50 m across, probably part

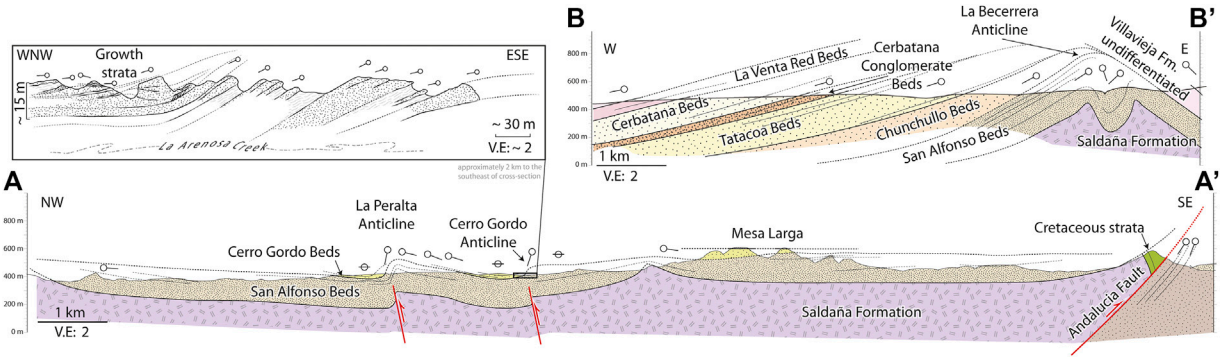

FIGURE 7 | Cross-sections of the Tatacoa Desert. **(A–A')** Cross-section highlighting growth strata associated to the relatively small La Peralta and Cerro Gordo anticlines (quadrangle F3-G4 in **Figure 4**). Inset: field drawing of growth strata along the Arenosa creek ~ 2km to the southeast of the cross-section along the axis of the Cerro Gordo Anticline. **(B–B')** Cross-section showing the growth unconformity below the La Venta Red Beds inferred from the map (**Figure 4**) where strata in the northwestern flank of La Becerrera Anticline may also represent growth strata.

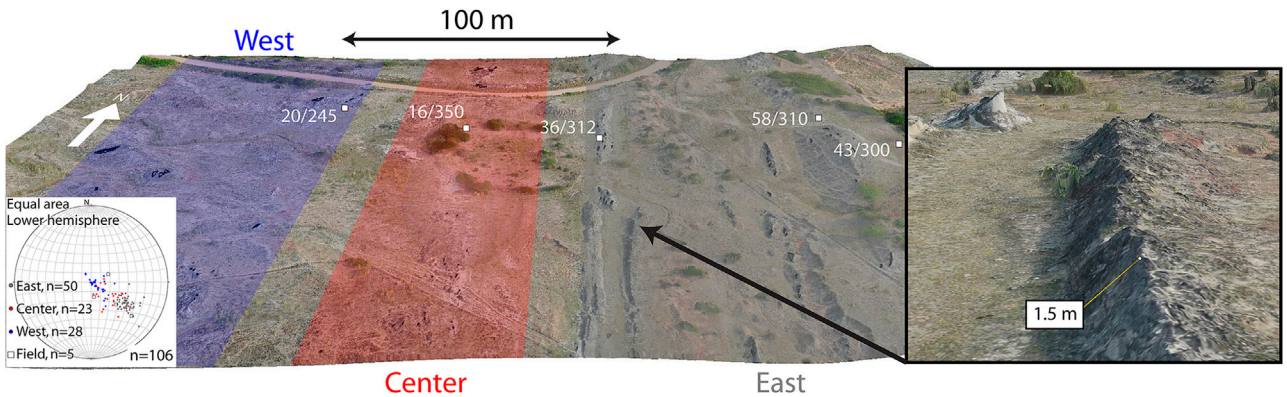

FIGURE 8 | Spatial attitude of bedding in the western flank of La Peralta Anticline showing three northwestern-dipping domains display progressively higher dips (quadrangle F3 in **Figure 4**). Field data (red dots) corroborates 3D model measurements (black dots). Inset shows render of steeply dipping strata.

of the Cenomanian–Turonian Villeta Group (**Figure 3**, Villamil and Arango, 1998). The footwall of this fault contains a sequence of northwest-dipping, massive mudstone and medium-grained sandstone, lithologically indistinguishable from strata typical of the La Victoria, and parts of the Villavieja formations (indeed mapped as such by Villarroel et al., 1996; Ingeominas, 2002). Crucially, the trace of the Andalucia Fault is fossilized by strata of the San Alfonso Beds, as these beds can be followed covering undisturbed the fault trace (**Figure 6A**). Lithic sandstone/mudstone strata in the footwall of the Andalucia Fault are therefore older than the oldest strata fossilizing the fault trace (San Alfonso Beds of La Victoria Formation) and left as an undifferentiated Miocene unit below the Honda Group (**Figure 6A**), perhaps correlative to the La Cira Formation (De Porta and De Porta, 1962).

The geologic map (**Figure 4**) also reveals two growth unconformities within strata of La Victoria Formation. In the northern third of the mapping area, strata of the Chunchullo and Tatacoa Beds are folded in two en-echelon, left-stepping, west- and northwest-verging anticlines (Cerro Gordo and La Peralta anticlines, Guerrero (1993, 1997). Dips and thickness of strata define a fan-like pattern on the northwestern flanks of these folds (**Figure 7**, inset), with thickening strata dipping much more steeply near the axis of the anticline, suddenly thinning and flattening to regain low dips less than 250 m westwards (**Figure 8**). Satellite imagery and the geologic map (**Figure 6B**) show the truncations of strata near the southern tip of the Cerro Gordo anticline, diagnostic of growth unconformities. Another, larger growth unconformity is suggested by the contrasting structural attitude of strata towards the southeastern edge of the mapping area (**Figure 7**, section B–B'). Here, strata of the San Alfonso Beds are folded in an upright, tight NNE-trending, asymmetrical anticline (La Becerrera Anticline, Guerrero (1993, 1997). The Cerbatana, Tatacoa and Chunchullo Beds are thick, and well developed in the western flank of the anticline, but they are missing or severely thinned on the eastern flank (**Figure 4**, quadrangles H12 to I10).

The geologic map (**Figure 4**) also shows a deeply dissected, unconsolidated deposit with well-rounded, quartzite cobble and

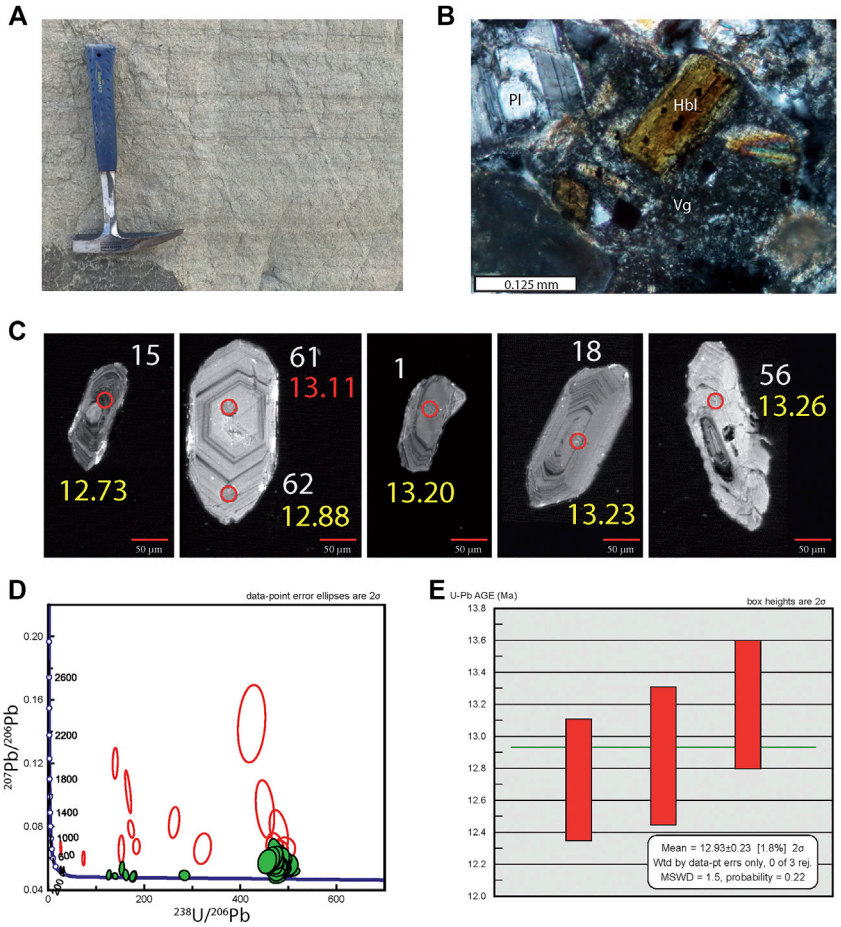

FIGURE 9 | Sample SEL-02 (coordinates: 3.27419 N, 75.1965 W). **(A)** Sampled strata in a plane parallel-bedded volcanoclastic unit near the top of the Tatacoa Beds (**Figure 3**). **(B)** Photomicrograph showing fresh detrital components, plagioclase (PL), hornblende (Hbl), surrounded by volcanic glass (Vg). **C)** Cathodo-luminescence of the five youngest zircons, note youngest ages in overgrowths (number in yellow: best age, number in red: discordant age). See SM2 for all images. **(D)** Tera–Wasserburg concordia diagram showing concordant (green, $n = 47$) and discordant (red, $n = 15$) U-Pb ages. **(E)** Detrital zircon maximum depositional age (MDA) calculated using weighted average of the youngest three U-Pb ages (Y3Z method of Coutts et al., 2019).

boulder clasts, within a characteristically red, muddy/sandy matrix (**Figure 5G**). This is typically preserved at hilltops, making them conspicuously flat, with steep, reddish edges (**Figure 5G**). The quartzite cobbles and pebbles, more resistant to erosion, act as a carapace protecting the sequence below from erosion, so these alluvial remains usually occupy the highest areas throughout the Tatacoa Desert. Differential removal of the finer-grained matrix of the coarse-grained deposit leaves behind reddish, cobble and pebble float that still protects the underlying strata from erosion, usually along the slopes of flat-topped hills. Remains of this unconsolidated deposit, and leftover float cobbles are ubiquitous. A thin, fine-grained unconsolidated deposit was also discriminated in the geologic map, and although much less prominent, it can be seen as flat terrain on top of dipping strata. It is unclear what is its relationship to the coarse-grained unconsolidated deposit, but being finer-grained, and located in lower topographic positions, it should be younger than the coarse-grained deposit. Near the eastern edge of the map, the coarse-grained deposit is found tilted to the east (**Figure 4**, quadrangle I10).

Geochronology

We actively sought volcanic ash beds interbedded within the sequence to place tighter constraints on depositional ages. Having found none, we settled for clastic beds nearly 30 m below the base of the Cerbatana Conglomerate Beds that contained the most volcanic components to extract detrital zircon grains and perform U-Pb LA-ICP-MS geochronology. We chose sample SEL-02 from a sandstone bed in banks of internally massive to plane-parallel bedded, laterally continuous beds, composed of fine-to medium-grained lithic arkose (quartz = 25%; feldspar = 47%; lithics = 28%) with flat lamination, and horizontal stratification structures at top and bottom, massive in between (**Figure 9A**). Sand-size fragments include non-altered angular clasts of plagioclase, K-feldspar, and hornblende with trace amounts of silt-size matrix (**Figure 9B**). Below this bed, the sequence shows a more typical La Victoria Formation sedimentary pattern characterized by fine-grained grey lithic sandstones interlayered with pinkish mudstones. Anderson et al. (2016) identified a similar lithic arkose in a sandstone unit also below

the Cerbanata Conglomerate Beds (their sample S5), and we recognized similar lithofacies in other localities in roughly the same stratigraphic position.

In our sample SEL-2 we performed 62 U-Pb, LA-ICPMS measurements on 61 zircon grains (**Figure 9C**). Fifteen of those measurements were rejected because they yielded high discordance or a large error age percentage (**Figure 9D**). Miocene ages are recorded in 24 grains (51%), where 23 grains (49%) yield ages younger than 20 Ma. The youngest age obtained in this analysis is 12.7 ± 0.38 Ma (see SM-2). All zircon grains younger than 14 Ma show elongated morphologies, while the youngest grain is fully prismatic (grain 62 in **Figure 9C**). Because we are seeking to constrain depositional ages, we use the three youngest zircons, including the external rim of grain 62, or 12.93 ± 0.23 Ma (**Figure 9E**, MSWD: 1.5).

DISCUSSION

The updated geologic map of the Tatacoa Desert (**Figure 4**) and additional geochronological work (**Figure 9**) help refine the Miocene drainages and paleogeography of this crucial paleontological locality. In the following paragraphs we document that active deformation was taking place during accumulation of strata of the La Victoria Formation, with the resulting growth unconformities. We then review new and existing detrital zircon geochronology in light of the updated geologic map, and suggest that the river system that transported the sediments of the Honda Group was sourced in active volcanic centers in today's Cauca Valley and the eastern flank of the Western Cordillera, draining eastward to the Amazon lowlands. We then use published data to document the time at which this Andean portal was closed.

Growth Strata

The northeast-trending, northwest-verging, fault-related Cerro Gordo and La Peralta anticlines were growing at the time of accumulation of the San Alfonso and Cerro Gordo Beds. These folds display a classic fan-like, cross-sectional geometry in their northwestern flanks (**Figures 6B**,**7** inset, **8**), typical of growth strata (e.g., Suppe et al., 1997). These relatively minor structures (only ~5 km long), caused strata of the Chunchullo and Cerro Gordo Beds to be thicker in their northwestern flanks, and thin, or pinch out entirely in their southeastern flanks (**Figure 7**). A growth unconformity is well developed near the southwestern tip of the Cerro Gordo Anticline, where steeply-dipping strata within the Chunchullo beds are truncated by gently-dipping strata to the northwest (**Figure 6B**, quadrangle E6 in **Figure 4**). Geochronological data indicates that these strata were accumulated between ~13.3 and 13.7 Ma (Flynn et al., 1997), and therefore date deformation and propagation of structures to this time interval (**Figure 4**).

A larger, and more significant unconformity developed as the NNE-trending La Becerrera Anticline grew. The Chunchullo, Tatacoa and Cerbatana Beds are well developed in its northwestern flank, but thin, or absent in its southeastern flank (**Figure 7**, section B–B'). By analogy to the smaller structures described above, this anticline grew at the time of deposition of the Chunchullo, Tatacoa and Cerbatana Beds, served as the eastern limit for their extent, and only tighten after the accumulation of the La Venta Red Beds, which overlaps it. This growth unconformity therefore documents the propagation of deformation to between ~12.2 and 13.3 Ma (Flynn et al., 1997).

Geochronological Constraints

The updated geologic map (**Figure 4**) helps re-evaluate published geochronological data points (**Figure 3**). Consistent with its stratigraphic position, the lowest sample is also the oldest maximum depositional age in the sequence, in the San Alfonso Beds (sample Z1 14.4 ± 1.9 Ma, U-Pb, Anderson et al., 2016), albeit with a low fraction of zircons younger than 20 Ma (only 8%), and an analytical error large enough to overlap all other age determinations. Sample JG-R90-3 was also re-located to the lowest unit of La Victoria Formation (San Alfonso Beds) yielding the second oldest age within the sequence (13.778 ± 0.081 Ma, Ar/Ar in biotite, Flynn et al., 1997). In ascending stratigraphic order, Ar/Ar samples JG-R89-1 (13.651 ± 0.107 Ma) and JG R89-3 (13.767 ± 0.052 Ma) with overlapping analytical errors (Flynn et al., 1997), were both re-located near the top of the Cerro Gordo Beds, and suggest rapid accumulation rates. Sample JG-R90-1 (13.342 ± 0.408 Ma, Ar/Ar in hornblende, Flynn et al., 1997) in the upper part of the Chunchullo Beds shows maximum depositional ages (**Figure 3**) younger than detrital zircon samples Z2 and Z3 at the base of the overlying Tatacoa Beds with U-Pb age of 13.75 Ma (±0.9 and 0.4 Ma, respectively, Anderson et al., 2016). However, samples Z2 and Z3, besides having large analytical errors, plot stratigraphically above in the geologic map (**Figure 4**), and must therefore rework older volcanic units, and should not be taken as near-depositional ages. Further up stratigraphically, near the top of Cardon Red Beds, sample JG-R88-2 yielded a 12.21 ± 0.107 Ma (Ar/Ar in hornblende, Flynn et al., 1997), being the youngest age of the Villavieja Formation. While this sample plots in recent alluvial deposits (**Figure 4**), it was more likely collected in strata exposed along spotty outcrops along a creek bed. Other U-Pb detrital zircon samples with older detrital ages, and low fractions of young (less than 20 Ma) detrital populations (Z4 = 27%; Z5 to Z9 = 0–9%, Anderson et al., 2016), are most likely reworking older volcanic deposits and provide maximum accumulation ages far removed from a true depositional age.

Our U-Pb detrital zircon sample SEL-02 (12.93 ± 0.23 Ma, MSWD: 1.5, **Figure 9E**), collected in strata just 30 m below the base of the Cerbatana Conglomerate Beds is consistent with sample JG-R89-2 (12.512 ± 0.102 Ma in plagioclase and hornblende, Flynn et al., 1997), collected just above it (**Figure 3**). Both of these ages bracket the age of the conglomerate, and suggest fast accumulation rates (between 0.75 and 0.086 Ma), as suggested by Flynn et al. (1997), to explain the slightly discordant age of sample JG-R89-2 (**Figure 3**) with respect to the magnetostratigraphic data.

We interpreted the volcanic-rich bed where sample SEL-02 was collected, as the record of a diluted lahar deposit which may

FIGURE 10 | Huila Volcano, a massive ~5,600 m a.s.l. active composite volcano as seen from the Tatacoa Desert, looking west (see **Figure 1** for location). Eastward migration of a Miocene magmatic arc built these volcanic edifices (**Figure 1**) starting at ~4 Ma (Barberi et al., 1988; Ujueta, 1999; Torres-Hernandez, 2010), that along with contractional deformation along the flanks of the Central and Eastern cordilleras (Alfonso et al., 1994; Saeid et al., 2017), severed any fluvial communication between the Cauca and Magdalena valleys. Ridges in the foreground correspond to Oligocene molasse deposits involved in the east-vergent, fold-and-thrust belt at the toe of the Central Cordillera.

be the response of a major change in the hydraulic regime in the basin. The presence of almost fresh volcanic fragments, plagioclase, and hornblende (**Figure 9B**) suggests a short lag time between crystallization, exhumation erosion and deposition (e.g. Cawood et al., 2012), and requires volcanic sources located near the Tatacoa Desert (less than ~200 km, Johnsson et al., 1991; Amorocho et al., 2011).

Volcanic activity in the age range of the Honda Group strata (~12–14 Ma) is restricted in the Northern Andes to a northward-propagating, post-collisional magmatic arc that lit up as Nazca lithosphere subducted behind the accreted Panama arc. This magmatic arc extended from about 3°S (Bineli-Betsi et al., 2017), up to ~7°N along an axis located west of today's Central Cordillera (Wagner et al., 2017). The Upper Cauca–Patia magmatic center is part of this arc, with crystallization ages between 17 and 9 Ma (Leal-Mejia, 2011; Echeverri et al., 2015; Leal-Mejia et al., 2019). This magmatic center is located ~130 km to the west of the Tatacoa Desert (**Figure 1**), making it the only candidate for unstable volcanic fragments (e.g. hornblende, **Figure 9B**) to arrive unweathered (Johnsson et al., 1991; Amorocho et al., 2011) to the depositional basin of the Tatacoa Desert. This possible source however, is today located west of the axis of the Central Cordillera (**Figure 10**).

Paleogeography

Fossil fish fragments found in Honda Group strata firmly establish a middle Miocene connection between the fluvial systems of the Magdalena and Amazon basins before the rise of the southernmost Eastern Cordillera (Lundberg, 1997; Lundberg et al., 1998; Ballen and Moreno-Bernal, 2019). Paleocurrents measured in the Honda Group strata indicate an east-southeastward directed paleoflow (Guerrero, 1993; Guerrero, 1997; Anderson et al., 2016), resembling drainages in today's eastern Andean foothills (**Figure 1**). Detrital zircon geochronology in middle and late Miocene strata of both the southern Magdalena Valley and the Amazon Basin (**Figure 11**) is consistent with this paleogeographic configuration. Very similar middle Miocene, middle Eocene, and Jurassic detrital zircon age populations are found in Miocene strata of both basins (~11–12 Ma, Solimoes Formation, Kern et al., 2020).

Other sites with similar Miocene and Eocene detrital zircon populations include the middle to upper Miocene strata of the Amaga Formation (Montes et al., 2015), and the Cauca-Patia Basin (Echeverri et al., 2015). Both sites are located west of today's Central Cordillera (**Figure 1**), and both are derived from sources west of the Central Cordillera: 1) the Panama block (docked by ~15 Ma, Montes et al., 2015; Leon et al., 2018), as no other area of the Northern Andes contains such U-Pb zircon sources (Leal-Mejia, 2011; see discussion in; Jaramillo et al., 2017b; Leal-Mejia et al., 2019); and 2) the Miocene magmatic centers in the Cauca-Patia Basin (Echeverri et al., 2015; Wagner et al., 2017). Detrital zircon populations in the Tatacoa Desert and the Amazon Basin (**Figure 11**, and Fig. SM2) could have been sourced in the Cauca–Patia, and northwestern Andes, suggesting that these sites were once connected by the same fluvial system through today's Central and Eastern cordilleras.

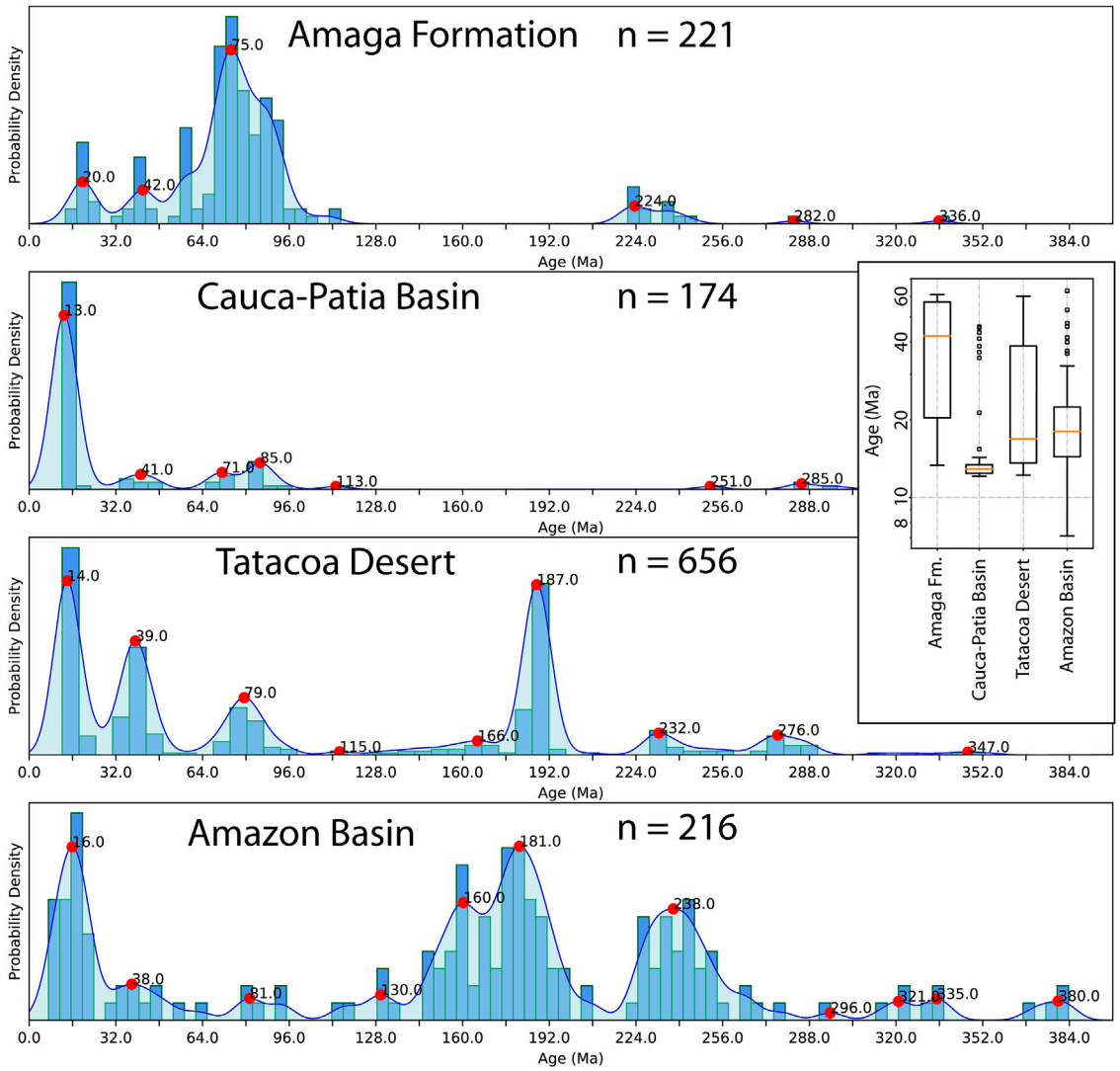

FIGURE 11 | Histograms and probability density plots of detrital zircon populations in four different middle Miocene localities in the Northern Andes showing only the last 400 Ma. From top to bottom: Amaga Formation, Cauca-Patia Basin, Tatacoa Desert, and Amazon Basin (Echeverri et al., 2015; Montes et al., 2015; Anderson et al., 2016; Kern et al., 2020), see **Figure 1** for locations. All contain a distinctive middle Eocene and middle Miocene populations, with a Jurassic peak only present downstream from the Tatacoa Desert. Inset shows box and whisker plots comparing Cenozoic detrital zircon populations in the same localities.

We therefore propose a paleogeographic interpretation where a river drained the docked Panama-Choco block, and the active volcanic centers in the Cauca Valley into the Tatacoa Desert, to reach the western Amazon Basin (**Figure 12**). This drainage would have not been impeded by either the Central or Eastern cordilleras at this time. Drainage connectivity across the Central Cordillera like the one we suggest here, is consistent with phylogeographic concordance factors of co-occurring groups of fresh water fish (*Hemibrycon*) between the Atrato-Darien (**Figure 1**) and southern Magdalena Valley drainages (Rincon-Sandoval et al., 2019). This lowland corridor would have therefore segmented the Andes at about 3°N, and further south (Cadena and Casado-Ferrer, 2019), in a fashion similar to a Marañon, or Western Andean Portal (Lundberg et al., 1998; Antonelli et al., 2009), during middle Miocene times.

The northernmost Central Andes, positive since at least latest Cretaceous times (Witt et al., 2017; Hurtado et al., 2018) would have defined the southern tip of this lowland portal (**Figure 2A**). Intense volcanic activity after ~4 Ma (Barberi et al., 1988; Van der Wiel, 1991; Ujueta, 1999; Torres-Hernandez, 2010) along the axis of the Real/Central Cordillera (**Figures 1**,**10**) resulted from flattening of the subducting Nazca slab (Wagner et al., 2017), and eastward migration of the Miocene magmatic arc. This Pliocene activity, and continued fault propagation (Alfonso et al., 1994; Saeid et al., 2017) built the final highland connection between the Central and Northern Andes, as well as between the Eastern and Central cordilleras (Ujueta, 1999), severing any connections to Amazonian drainages, and between the Cauca and Magdalena valleys (**Figure 1**).

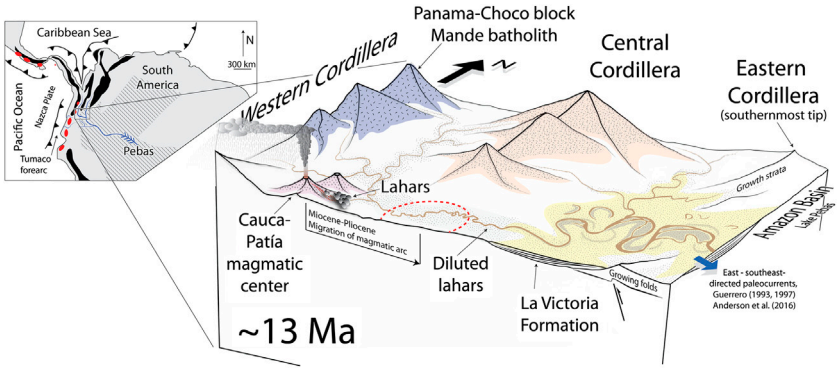

FIGURE 12 | Block-diagram illustrating a possible paleogeographic scenario for middle Miocene times (~13 Ma) in the Tatacoa Desert. Light yellow represent areas where subsidence and sediment accumulation took place. Dashed red line represents the future location of the Pliocene and younger magmatic arc of the Central Cordillera (**Figure 10**). Detrital geochronology (**Figure 11**), paleocurrent data (Guerrero, 1997; Anderson et al., 2016), and molecular fish data (Rincon-Sandoval et al., 2019) suggest connection of the volcanically active Cauca-Patia Basin (Leal-Mejia, 2011; Echeverri et al., 2015; Leal-Mejia et al., 2019), the recently accreted Panama-Choco block (Montes et al., 2015; Leon et al., 2018), with the Tatacoa Desert, itself connected to westernmost Amazonia's Pebas system. Dominant wind directions according to Sepulchre et al. (2009). Inset shows palinspastic reconstruction of the margin at the same time (Montes et al., 2019), showing significant relief in black (Montes et al., 2015; Witt et al., 2017), Pebas system extent and drainages in diagonal pattern (Lundberg and Chernoff, 1992; Wesselingh et al., 2001; Jaramillo et al., 2017a; Kern et al., 2020), and active magmatic centers in red (Echeverri et al., 2015; Bineli-Betsi et al., 2017; Wagner et al., 2017).

CONCLUSIONS

(1) Miocene strata preserved in the Tatacoa Desert contain the record of tectonic activity during the time that La Victoria and the base of Villavieja formations were accumulated ~12.2–13.7 Ma. NNE-trending anticlines (Cerro Gordo and La Peralta) grew at the time that the San Alfonso Beds and Cerro Gordo Beds (base of La Victoria Formation) accumulated. Similarly, the larger La Becerrera Anticline developed contemporaneously with the deposition of the Cerro Gordo Beds to Cerbatana Beds, generating significant growth unconformities.

(2) Possible sources for the detrital zircon grains (**Figure 11**) recovered in middle Miocene (Serravallian) strata of the Honda Group are located west today's Central Cordillera. This includes the Eocene magmatic rocks of the Panama-Choco block, and the middle Miocene magmatic rocks of the Cauca Valley (**Figure 12**). A matching detrital zircon signature (**Figure 11**) has been recovered from upper Miocene strata in the Amazon Basin to the east (Kern et al., 2020) suggesting that Amazon-like drainages may have operated since ~12 Ma.

(3) A Serravallian trans-Andean passage at ~3°N across the Central Cordillera (**Figure 11**) may have existed to allow both the Eocene and the Miocene detrital zircon populations to mix and accumulate in strata of the Tatacoa Desert. This lowland passage would have therefore communicated the late Pebas system (Wesselingh et al., 2001) in the western Amazonian Basin, to at least the Cauca Valley to the west (**Figure 12**).

(4) This Andean portal would have been open since at least 13–14 Ma, until a combination of fault propagation and intense volcanic activity during Pliocene times built the final connection joining the highlands of the Eastern and Central cordilleras.

DATA AVAILABILITY STATEMENT

The original contributions presented in the study are included in the article/**Supplementary Material**, further inquiries can be directed to the corresponding author.

AUTHOR CONTRIBUTIONS

Geologic mapping: CM, CS, RV, ES, FL, DM, LP-A, and JG. Geochronology: AB-T, ER, AvQ, AR-C; GIS: CM, SG and NH. Stratigraphy: GB, ER and AC. Geological background and writing of the paper: CM, GB, ES, AB and AC.

FUNDING

The authors would like to thank Carlos Rosero, doña Orfanda, Natalia Pardo, DIDI (Dirección de Investigación, Desarrollo e Innovación) of Universidad del Norte-Alianza 4U, Semillero Paleontología EAFIT, Smithsonian Tropical Research Institute, Uniandes P12 160422.002/001, Anders Foundation, 1923 Fund, Gregory D. and Jennifer Walston Johnson, and Uniandes field students 2013 to 2017 for their enthusiastic help. N. Hoyos was partially funded by The Canadian Queen Elizabeth II Diamond Jubilee Scholarships (QES), a partnership among Universities in Canada, the Rideau Hall Foundation (RHF), Community Foundations of Canada (CFC). The QES-AS is made possible with financial support from IDRC and SSHRC. N Hoyos was also partially supported by the Fulbright Visiting Scholar Program. In memory of Javier Maldonado, instigator of this work.

SUPPLEMENTARY MATERIAL

The Supplementary Material for this article can be found online at: https://www.frontiersin.org/articles/10.3389/feart.2020.587022/full#supplementary-material.

REFERENCES

Albert, J. S., Lovejoy, N. R., and Crampton, W. G. (2006). Miocene tectonism and the separation of cis-and trans-Andean river basins: evidence from Neotropical fishes. *J. South Am. Earth Sci.* 21 (1), 14–27.

Alfonso, C., Sacks, P., Secor, D., Rine, J., and Pérez, V. (1994). A Tertiary fold and thrust belt in the Valle del Cauca Basin, Colombian Andes. *J. South Am. Earth Sci.* 7 (3–4), 387–402.

Amezquita, F., and Montes, C. (1994). "Seccion geologica El Maco-Buenavista: estructura en el sector Occidental del Valle Superior del Magdalena," in *Estudios geologicos del Valle Superior del Magdalena: Bogota*. Editor F. Etayo-Serna (Bogotá:Universidad Nacional de Colombia-Ecopetrol), 601–636.

Amorocho, R., Bayona, G., and Reyes-Harker, A. (2011). Controles en la composición de arenas fluviales en la zona proximal de una cuenca de Antepais Tropical (Colombia). *Geol. Colomb.* 36, 163–178. doi:10.18257/raccefyn.632

Anderson, V. J., Horton, B. K., Saylor, J. E., Mora, A., Teson, E., Breecker, D. O., et al. (2016). Andean topographic growth and basement uplift in southern Colombia: implications for the evolution of the Magdalena, Orinoco, and Amazon river systems. *Geosphere*. 12 (4), 1–22. doi:10.1130/GES01294.1

Antonelli, A., Nylander, J. A., Persson, C., and Sanmartín, I. (2009). Tracing the impact of the Andean uplift on Neotropical plant evolution. *Proc. Natl. Acad. Sci. USA*. 106 (24), 9749–9754. doi:10.1073/pnas.0811421106

Ayala-Calvo, R., Bayona, G., Cardona, A., Ojeda, C., Montenegro, O., Montes, C., et al. (2012). The paleogene synorogenic succession in the northwestern Maracaibo block: tracking intraplate uplifts and changes in sediment delivery systems. *J. South Am. Earth Sci.* 39, 93–111. doi:10.1007%2F978-3-319-76132-9_7

Ballen, G. A., and Moreno-Bernal, J. W. (2019). New records of the enigmatic neotropical fossil fish *Acregoliath rancii* (Teleostei Incertae sedis) from the middle Miocene Honda group of Colombia. *Ameghiniana*. 56 (6), 431–440. doi:10.5710/AMGH.17.09.2019.3266

Bande, A., Horton, B. K., Ramírez, J. C., Mora, A., Parra, M., and Stockli, D. F. (2012). Clastic deposition, provenance, and sequence of Andean thrusting in the frontal Eastern Cordillera and Llanos foreland basin of Colombia. *Geol. Soc. Am. Bull.* 124 (1–2), 59–76. doi:10.1029/2011TC003089

Barberi, F., Coltelli, M., Ferrara, G., Innocenti, F., Navarro, J. M., and Santacroce, R. (1988). Plio-quaternary volcanism in Ecuador. *Geol. Mag.* 125 (1), 1–14.

Bayona, G. A., Montes, C., Cardona, A., Jaramillo, C., Ojeda, G., Valencia, V., et al. (2011). Intraplate subsidence and basin filling adjacent to an oceanic arc-continent collision: a case from the southern Caribbean-South America plate margin. *Basin Res.* 23, 403–422. doi:10.1111/j.1365-2117.2010.00495.x

Bayona, G., Baquero, M., Ramírez, C., Tabares, M., Salazar, A. M., Nova, G., et al. (2020). *Unravelling the widening of the earliest Andean northern orogen: Maastrichtian to early Eocene intra-basinal deformation in the northern Eastern Cordillera of Colombia: basin Research*.

Bayona, G., Cardona, A., Jaramillo, C., Mora, A., Montes, C., Caballero, V., et al. (2013). Onset of fault reactivation in the eastern Cordillera of Colombia and proximal Llanos basin; response to Caribbean south American convergence in early Palaeogene time. *Geol. Soc. Lond.* 377, 285–314.

Bayona, G., Cortes, M., Jaramillo, C., Ojeda, G., Aristizabal John, J., and Reyes-Harker, A. (2008). An integrated analysis of an orogen-sedimentary basin pair; latest Cretaceous-Cenozoic evolution of the linked Eastern Cordillera Orogen and the Llanos foreland basin of Colombia, *Geol. Soc. Am. Bull.* 120, 9–10. doi:10.1111/j.1365-2117.2009.00459.x

Bayona, G. (2018). El inicio de la emergencia de los Andes del norte: una perspectiva a partir del registro tectónico-sedimentológico del Coniaciano al Paleoceno. *Revista de la Academia Colombiana de Ciencias*. 42 (165), 364–378. doi:10.18257/raccefyn.632

Bineli-Betsi, T., Ponce, M., Chiaradia, M., Ulianov, A., and Camacho, A. (2017). Insights into the genesis of the epithermal Au-Ag mineralization at Rio Blanco in the Cordillera Occidental of southwestern Ecuador: constraints from U-Pb and Ar/Ar geochronology. *J. South Am. Earth Sci.* 80, 353–374. doi:10.1016/j.jsames.2017.10.004

Borrero, C., Pardo, A., Jaramillo, C. M., Osorio, J. A., Cardona, A., Flores, A., et al. (2012). Tectonostratigraphy of the Cenozoic Tumaco forearc basin (Colombian Pacific) and its relationship with the northern Andes orogenic build up. *J. South Am. Earth Sci.* 39, 75–92. doi:10.1007/s13202-019-0660-7

Caballero, V., Parra, M., Mora, A., Lopez, C., Rojas, L. E., and Quintero, I. (2013). Factors controlling selective abandonment and reactivation in thick-skin orogens: a case study in the Magdalena Valley, Colombia, *Geol. Soc. Lond.* 377, 343–367. doi:10.1144/SP377.4

Cadena, E.-A., and Casado-Ferrer, I. (2019). Late Miocene freshwater mussels from the intermontane Chota basin, northern ecuadorean Andes. *J. South Am. Earth Sci.* 89, 39–46. doi:10.1016/j.jsames.2018.10.012

Caicedo, J., and Roncancio, J. (1994). "El Grupo Gualanday como ejemplo de acumulacion sintectonica, en el Valle Superior del Magdalena, durante el Paleogeno," in *Estudios geologicos del Valle Superior del Magdalena*. Editor F. Etayo Serna (Bogota: Universidad Nacional de Colombia-Ecopetrol), 1001–1019.

Cande, S. C., and Kent, D. V. (1992). A new geomagnetic polarity time scale for the Late Cretaceous and Cenozoic. *J. Geophys. Res. Solid Earth*. 97 (B10), 13917–13951.

Cardona, A., Montes, C., Ayala, C., Bustamante, C., Hoyos, N., Montenegro, O., et al. (2012). From arc-continent collision to continuous convergence, clues from Paleogene conglomerates along the southern Caribbean-South America plate boundary. *Tectonophysics*. 580, 58–87. doi:10.1016/J.TECTO.2012.08.039

Cardona, A., Valencia, V., Bayona, G., Duque, J., Ducea, M., Gehrels, G., et al. (2011). Early subduction-€related orogeny in the northern Andes: Turonian to Eocene magmatic and provenance record in the Santa Marta Massif and Rancheria basin, northern Colombia. *Terra Nova*. 23 (1), 26–34. doi:10.1111/j.1365-3121.2010.00979.x

Cardona, A., Weber, M., Valencia, V., Bustamante, C., Montes, C., Cordani, U., et al. (2014). Geochronology and geochemistry of the Parashi granitoid, NE Colombia: tectonic implication of short-lived Early Eocene plutonism along the SE Caribbean margin. *J. South Am. Earth Sci.* 50, 75–92. doi:10.1590/2317-488920160030294

Carrillo, J. D., Forasiepi, A., Jaramillo, C., and Sánchez-Villagra, M. R. (2015). Neotropical mammal diversity and the Great American Biotic Interchange: spatial and temporal variation in South America's fossil record. *Front. Genet.* 5, 451. doi:10.3389/fgene.2014.00451

Cawood, P. A., Hawkesworth, C., and Dhuime, B. (2012). Detrital zircon record and tectonic setting. *Geology*. 40 (10), 875–878. doi:10.1130/G32945.1

Cediel, F., Mojica, J., and Macia, C. (1980). Definicion estratigrafica del Triasico en Colombia, Suramerica; formaciones Luisa, Payande y Saldana. Translated Title: stratigraphic definition of the Triassic in Colombia, South America; Luisa, Payande and Saldana formations. *Newsl. Stratigr.* 9 (2), 73–104. doi:10.1016/j.tecto.2004.12.024

Cediel, F., Mojica, J., and Macia, C. (1981). Las formaciones Luisa, Payandé y Saldaña sus columnas estratigráficas características. *Geol. Norandina*. 3 (1), 11–19.

Christophoul, F., Baby, P., and Davila, C. (2002). Stratigraphic responses to a major tectonic event in a foreland basin: the Ecuadorian Oriente Basin from Eocene to Oligocene times. *Tectonophysics*. 345 (1–4), 281–298. doi:10.1016/S0040-1951(01)00217-7

Compton, R. R. (1985). *Geology in the field*. New Jersey: John Wiley & Sons.

Cossio, U., Rodriguez, G., and Rodriguez, M. (1995). *Geología de la Plancha 283 Purificación: Inegominas, scale 1:100.000*.

Coutts, D. S., Matthews, W. A., and Hubbard, S. M. (2019). Assessment of widely used methods to derive depositional ages from detrital zircon populations. *Geosci. Front.* 10, 1421–1435. doi:10.1016/j.gsf.2018.11.002

De Porta, J., and De Porta, N. S. (1962). Discusion sobre las edades de las formaciones Hoyon, Gualanday y La Cira en la region de Honda-San Juan de Rioseco. *Boletin de geologia UIS*. 9 (1), 69–85.

Dickinson, W. R., and Gehrels, G. E. (2009). Use of U–Pb ages of detrital zircons to infer maximum depositional ages of strata: a test against a Colorado Plateau Mesozoic database. *Earth Planet Sci. Lett.* 288 (1), 115–125. doi:10.1016/j.gsf.2018.11.002

Dill, H. G., Buzatu, A., Balaban, S.-I., Ufer, K., Gomez, J., Birgaoanu, D., et al. (2020). The "badland trilogy" of the Desierto de la Tatacoa, upper Magdalena Valley, Colombia, a result of geodynamics and climate: with a review of badland landscapes. *Catena*. 194, 1–20.

Echeverri, S., Cardona, A., Pardo, A., Monsalve, G., Valencia, V. A., Borrero, C., et al. (2015). Regional provenance from southwestern Colombia fore-arc and intra-arc basins: implications for Middle to Late Miocene orogeny in the Northern Andes. *Terra Nova*. 27 (5), 1–8. doi:10.1111/ter.12167

Egüez, A., Gaona, M., and Albán, A. (2017). Mapa Geológico de la República del Ecuador, *Scale*. 21, 2881–2903. doi:10.1016/S0022-1694(02)00283-4

Etayo-Serna, F. (1994). "Epilogo; a modo de historia geológica del Cretacico en el valle superior del Magdalena," in *Estudios Geológicos del Valle Superior del Magdalena: Bogotá*. Editor F. Etayo-Serna (Bogotá: Universidad Nacional de Colombia), 1–4.

Florez, J. M., and Carrillo, G. A. (1994). "Estratigrafia de la sucesion litológica basal del Cretacico del valle superior del Magdalena," in *Estudios Geológicos del Valle Superior del Magdalena: Bogotá*. Editor F. Etayo-Serna (Bogotá: Universidad Nacional de Colombia), 1–26.

Flower, B. P., and Kennett, J. P. (1994). The middle Miocene climatic transition: east Antarctic ice sheet development, deep ocean circulation and global carbon cycling. *Palaeogeogr. Palaeoclimatol. Palaeoecol.* 108 (3-4), 537–555.

Flynn, J., Guerrero, J., and Swisher, C. (1997). "Geochronology of the Honda group," in *Vertebrate Paleontology in the Neotropics: the Miocene fauna of La Venta, Colombia*. Editors R. Kay, C. Madden, R. L. Cifelli, and J. Flynn (Washington, DC: Smithsonian Institution Press), 44–60.

Gomez, E., Jordan, T. E., Allmendinger, R. W., and Cardozo, N. (2005a). Development of the Colombian foreland-basin system as a consequence of diachronous exhumation of the northern Andes. *Geol. Soc. Am. Bull.* 117 (9), 1272–1292. 10.1306/06181411110.

Gomez, E., Jordan, T. E., Allmendinger, R. W., Hegarty, K., Kelley, S., and Heizler, M. (2003). Controls on architecture of the late Cretaceous to Cenozoic southern middle Magdalena valley basin, Colombia. *Geol. Soc. Am. Bull.* 115, 131–147. doi:10.1111/j.1365-3121.2010.00979.x

Gomez, E., Jordan, T. E., Allmendinger, R. W., Hegarty, K., and Kelley, S. (2005b). Syntectonic Cenozoic sedimentation in the northern middle Magdalena valley basin of Colombia and implications for exhumation of the northern Andes. *Geol. Soc. Am. Bull.* 117 (5-6), 547–569.

Grosse, E. (1926). *Estudio Geológico del Terciario Carbonífero de Antioquia en la parte Occidental de la Cordillera Central de Colombia entre el rio Arma y Sacaojal*. Berlin: Dietrich Reimer (Ernst Vohsen), 361.

Guerrero, J. (1993). *Magnetostratigraphy of the upper part of the Honda group and Neiva formation: miocene uplift of the Colombian Andes*. Durham: Duke University.

Guerrero, J., Sarmiento, G., and Navarrete, R. E. (2000). The stratigraphy of the W side of the Cretaceous Colombian Basin in the Upper Magdalena Valley. Reevaluation of selected areas and type localities including Aipe. *Guaduas, Ortega, and Piedras: Geol. Colomb*. 25, 45–110.

Guerrero, J. (1997). "Stratigraphy, sedimentary environments, and the Miocene uplift of the Colombian Andes," in *Vertebrate Paleontology in the Neotropics: the Miocene fauna of La Venta, Colombia*. Editors R. Kay, R. Madden, R. Cifelli, and J. Flynn (Washington DC: Smithsonian Institution Press), 15–43.

Guillong, M., vonvon Quadt, A., Sakata, S., Peytcheva, I., and Bachmann, O. (2014). LA-ICP-MS Pb–U dating of young zircons from the Kos–Nisyros volcanic centre, SE Aegean arc. *J. Anal. Atom. Spectrom*. 29 (6), 963–970. doi:10.1016/j.dib.2018.03.100

Haffer, J. (1967). Speciation in Colombian forest birds west of the Andes. *Am. Mus. Novit*. 2294, 1–57.

Hermelin, M. (2016). *Geomorphological landscapes and Landforms of Colombia, landscapes and Landforms of Colombia*. New York, NY: Springer, 1–21.

Herrera, F., Manchester, S., and Jaramillo, C. (2012). Permineralized fruits from the late Eocene of Panama give clues of the composition of forests established early in the uplift of Central America. *Rev. Paleobot. Palynol*. 175, 10–24. doi:10.1016/j.revpalbo.2012.02.007

Hilgen, F., Lourens, L., and van Dam, J. A. (2012). "*The neogene period*.," in *The geologic time scale 2012*. Editors F. M. Gradstein, J. G. Ogg, M. Schmitz, and G. Ogg (Netherlands: Elsevier), 923–978.

Hoorn, C., Wesselingh, F., Ter Steege, H., Bermudez, M., Mora, A., Sevink, J., et al. (2010). Amazonia through time: Andean uplift, climate change, landscape evolution, and biodiversity. *Science*. 330, 927–931. doi:10.1126/science.1194585

Hoorn, C., Guerrero, J., Sarmiento Gustavo, A., and Lorente Maria, A. (1995). Andean tectonics as a cause for changing drainage patterns in Miocene northern South America. *Geology Boulder*. 23 (3), 237–240.

Horton, B. K., Anderson, V. J., Caballero, V., Saylor, J. E., Nie, J., Parra, M., et al. (2015). Application of detrital zircon U-Pb geochronology to surface and subsurface correlations of provenance, paleodrainage, and tectonics of the Middle Magdalena Valley Basin of Colombia. *Geosphere*. 11 (6), 1790–1811. doi:10.1130/GES01251.1

Horton, B. K. (2018). Sedimentary record of Andean mountain building. *Earth Sci. Rev*. 178, 279–309. doi:10.3389/feart.2019.00353

Hurtado, C., Roddaz, M., Santos, R. V., Baby, P., Antoine, P.-O., and Dantas, E. L. (2018). Cretaceous-early Paleocene drainage shift of Amazonian rivers driven by Equatorial Atlantic Ocean opening and Andean uplift as deduced from the provenance of northern Peruvian sedimentary rocks (Huallaga basin). *Gondwana Res*. 63, 152–168. doi:10.1590/1982-0224-20180033

Ingeominas (2002). *Geologia de la plancha 303, Colombia, 1:100.000.Ingeominas, scale*.

Jaimes, E., and de Freitas, M. (2006). An Albian–Cenomanian unconformity in the northern Andes: evidence and tectonic significance. *J. South Am. Earth Sci*. 21 (4), 466–492. doi:10.1016/j.jsames.2006.07.011

Jaramillo, C., Romero, I., D'Apolito, C., Bayona, G., Duarte, E., Louwye, S., et al. (2017a). Miocene flooding events of western Amazonia. *Sci Adv*. 3 (5), e1601693. doi:10.1126/sciadv.1601693

Jaramillo, C. A., Montes, C., Cardona, A., Silvestro, D., Antonelli, A., and Bacon, C. D. (2017b). Conclusions by O'Dea et al. regarding formation of the Isthmus of Panama are not supported. *Sci. Adv*. 3 (6), e1602321. doi:10.1126/sciadv.1602321

Johnsson, M. J., Stallard, R. F., and Lundberg, N. (1991). Controls on the composition of fluvial sands from a tropical weathering environment: sands of the Orinoco River drainage basin, Venezuela and Colombia. *Geol. Soc. Am. Bull.* 103, 1622–1647.

Kay, R. F., Madden, R. H., Cifelli, R. L., and Flynn, J. J. (1997). *Vertebrate paleontology in the neotropics: the Miocene fauna of La Venta*. (Washington, Colombia: Smithsonian Institution Press).

Kern, A. K., Gross, M., Galeazzi, C. P., Pupim, F. N., Sawakuchi, A. O., Almeida, R. P., et al. (2020). Re-investigating Miocene age control and paleoenvironmental reconstructions in western Amazonia (northwestern Solimões Basin, Brazil). *Palaeogeogr. Palaeoclimatol. Palaeoecol*. 545, 109652. doi:10.1016/j.palaeo.2020.109652

Kolarsky, R. A., Mann, P., and Monechi, S. (1995). "Stratigraphic development of southwestern Panama as determined from integration of marine seismic data and onshore geology," in *Geologic and Tectonic Development of the Caribbean Plate boundary in southern Central America*. Editor P. Mann (Boulder, Colorado: Geological Society of America), Volume 295, 159–200.

Lamus, F., Bayona, G., Cardona, A., and Mora, A. (2013). Procedencia de las unidades Cenozoicas del sinclinal de Guaduas: Implicación en la evolución tectónica del sur del valle medio del Magdalena y orógenos adyacentes. *Bol. Geol*. 35, 1. doi:10.1016/j.earscirev.2019.102903

Leal-Mejia, H. (2011). *Phanerozoic gold metallogeny in the Colombian Andes: a tectono-magmatic approach*. Ph.D.: Universitat de Barcelona, 989.

Leal-Mejia, H., Shaw, R. P., and Melgarejo i Draper, J. C. (2019). "Spatial-Temporal migration of granitoid magmatism and the Phanerozoic Tectono-magmatic evolution of the Colombian Andes," in *Geology and tectonics of northwestern South America: the Pacific-Caribbean-Andean Junction: Cham*. Editors F. Cediel and R. P. Shaw (Springer International Publishing), 253–410.

Leon, S., Cardona, A., Parra, M., Jaramillo, J. S., Valencia, V., Chew, D., et al. (2018). Transition from collision to subduction: an example from Panama-Nazca Neogene interactions. *Tectonics*. 37, 1–21. doi:10.1002/2017TC004785

Ludwig, K. (2012). *User's manual for Isoplot 3.75—a geochronology toolkit for Microsoft Excel*., Berkeley Geochronology Center Special Publication, 5, 75.

Lundberg, J. (1997). "Freshwater fishes and their paleobiotic implications," in *Vertebrate Paleontology in the Neotropics: the Miocene fauna of La Venta*. Editors R. Kay, R. Madden, R. Cifelli, and J. Flynn (ColombiaWashington: Smithsonian Isntitution), 67–91.

Lundberg, J. G., and Chernoff, B. (1992). *A miocene fossil of the Amazonian fish Arapaima (Teleostei, Arapaimidae) from the Magdalena River region of Colombia—Biogeographic and evolutionary Implications: Biotropica*., 2–14.

Lundberg, J. G., Marshall, L. G., Guerrero, J., Horton, B., and Malabarba, M. (1998). *The stage for Neotropical fish diversification: a history of tropical South American rivers*.

Manco-Garces, A., Marin-Ceron, M. I., Sanchez-Plazas, C. J., Escobar-Arenas, L. C., Beltran-Triviño, A., and Von Quadt, A. (2020). Provenance of the Cienaga de Oro formation: unveiling the tectonic evolution of the Colombian Caribbean

margin during the Oligocene-early Miocene. *Bol. Geol*. 42 (3), 205–226. doi:10.18273/revbol.v42n3-2020009

Mange, M. A., and Maurer, H. (1991). *Heavy minerals in Colour*. New York, NY: Springer.

Martin-Gombojav, N., and Winkler, W. (2008). Recycling of Proterozoic crust in the Andean Amazon foreland of Ecuador: implications for orogenic development of the northern Andes. *Terra Nova*. 20 (1), 22–31. doi:10.1111/j.1365-3121.2007.00782.x

Miller, M. J., Bermingham, E., Klicka, J., Escalante, P., do Amaral, F. S., Weir, J. T., et al. (2008). Out of Amazonia again and again: episodic crossing of the Andes promotes diversification in a lowland forest flycatcher. *Proc. Biol. Sci*. 275 (1639), 1133–1142. doi:10.1098/rspb.2008.0015

Mojica, J., and Franco, R. (1990). Estructura y evolución tectónica del valle medio y superior del Magdalena, Colombia. *Geol. Colomb*. 17, 41–64.

Montes, C., Cardona, A., Jaramillo, C., Pardo, A., Silva, J., Valencia, V., et al. 2015). Middle Miocene closure of the Central American Seaway. *Science*. 348 (6231), 226–229. doi:10.1126/science.aaa2815

Montes, C., Bayona, G., Cardona, A., Buchs, D., Silva, C., Moron, S. E., et al. (2012). Arc-continent collision and orocline formation: closing of the Central American Seaway. *J. Geophys. Res*. 12, 156. doi:10.1029/2011JB008959

Montes, C., Restrepo-Pace Pedro, A., and Hatcher Robert, D., Jr. (2003). Three-dimensional structure and kinematics of the Piedras-Girardot fold belt; surface expression of transpressional deformation in the Northern Andes, *AAPG Memoir*. 79, 849–873.

Montes, C., Rodriguez-Corcho, A. F., Bayona, G., Hoyos, N., Zapata, S., and Cardona, A. (2019). Continental margin response to multiple arc-continent collisions: the northern Andes-Caribbean margin. *Earth Sci. Rev*. 198, 102903. doi:10.1016/j.earscirev.2019.102903

Mora, A., Parra, M., Strecker, M. R., Kammer, A., Dimate, C., and Rodriguez, F. (2006). Cenozoic contractional reactivation of Mesozoic extensional structures in the Eastern Cordillera of Colombia. *Tectonics*. 25, 20. doi:10.1029/2005TC001854

Mora, A., Reyes-Harker, A., Rodriguez, G., Teson, E., Ramirez-Arias, J. C., Parra, M., et al. (2013). *Inversion tectonics under increasing rates of shortening and sedimentation: Cenozoic example from the Eastern Cordillera of Colombia*. Geological Society, London, Special Publications, 377.

Moreno, F., Hendy, A., Quiroz, L., Hoyos, N., Jones, D., Zapata, V., et al. (2015). Revised stratigraphy of neogene strata in the Cocinetas basin, La Guajira, Colombia. *Swiss J. Palaeontol*. 28, 1–39. doi:10.1007/s13358-015-0071-4

Moreno-Sanchez, M., and Pardo-Trujillo, A. (2003). "Stratigraphical and sedimentological constraints on western Colombia: implications on the evolution of the Caribbean plate," *He Circum-Gulf of Mexico and the Caribbean: hydrocarbon habitats, basin formation, and plate tectonics*. Editors C. Bartolini, R. Buffler, and J. Blickwede (AAPG), Volume Memoir 79, 891–924.

Nie, J., Horton, B. K., Mora, A., Saylor, J. E., Housh, T. B., Rubiano, J., et al. (2010). Tracking exhumation of Andean ranges bounding the middle Magdalena valley basin. *Colomb. Geol*. 38 (5), 451–454. doi:10.1130/G30775.1

Nie, J., Horton, B. K., Saylor, J. E., Mora, A. s., Mange, M., Garzione, C. N., et al. (2012). Integrated provenance analysis of a convergent retroarc foreland system: U/Pb ages, heavy minerals, Nd isotopes, and sandstone compositions of the Middle Magdalena Valley basin, northern Andes, Colombia. *Earth Sci. Rev*. 110 (1), 111–126. doi:10.1016/j.jsames.2016.06.003

Ochoa, D., Hoorn, C., Jaramillo, C., Bayona, G., Parra, M., and De la Parra, F. (2012). The final phase of tropical lowland conditions in the axial zone of the Eastern Cordillera of Colombia: evidence from three palynological records. *J. S. Am. Earth Sci*. 39, 157–169. doi:10.1029/JB086iB11p10753

Parnaud, F., Gou, Y., Pacual, J.-C., Capello, M. A., Truskowski, I., and Passalacqua, H. (1995). "Stratigraphic synthesis of western Venezuela," Editors A. J. Tankard, S. Suarez, and H. J. Welsink (Petroleoum Basins of South AmericaAAPG), 62, 681–698.

Pennington, W. D. (1981). Subduction of the eastern Panama basin and Seismotectonics of northwestern South America. *J. Geophys. Res*. 86 (B11), 10753–10770.

Ramon, J. C., and Rosero, A. (2006). Multiphase structural evolution of the western margin of the Girardot subbasin, Upper Magdalena Valley, Colombia. *J. S. Am. Earth Sci*. 21 (4), 493–509. doi:10.1016/j.jsames.2006.07.012

Reyes-Harker, A., Ruiz-Valdivieso, C. F., Mora, A., Ramirez-Arias, J. C., Rodriguez, G., De La Parra, F., et al. (2015). Cenozoic paleogeography of the Andean foreland and retroarc hinterland of Colombia. *AAPG (Am. Assoc. Pet. Geol.) Bull*. 99 (8), 1407–1453. 10.1126/sciadv.1601693.

Rincon-Sandoval, M., Betancur-R, R., and Maldonado-Ocampo, J. A. (2019). Comparative phylogeography of trans-Andean freshwater fishes based on genome-wide nuclear and mitochondrial markers. *Mol. Ecol*. 28 (5), 1096–1115. doi:10.1111/mec.15036

Rodriguez, G., and Sierra, M. I. (2010). Las Sedimentitas de Tripogadi y las Brechas de Trigana: Un registro de Volcanismo de Arco, Corrientes de Turbidez y Levantamiento Rapido Eoceno en el noroccidente de Sur America, *Geol. Colomb*. 35, 74–86. doi:10.1016/j.earscirev.2019.102903

Ruiz, G., Seward, D., and Winkler, W. (2004). Detrital thermochronology a new perspective on hinterland tectonics, an example from the Andean Amazon Basin, Ecuador. *Basin Res*. 16 (3), 413–430. doi:10.1111/j.1365-2117.2004.00239.x

Saeid, E., Bakioglu, K., Kellogg, J., Leier, A., Martinez, J., and Guerrero, E. (2017). Garzón Massif basement tectonics: structural control on evolution of petroleum systems in upper Magdalena and Putumayo basins, Colombia. *Mar. Petrol. Geol*. 88, 381–401. doi:10.1016/B978-0-12-816009-1.00006-X

Sarmiento-Rojas, L. F. (2018). "Cretaceous stratigraphy and Paleo-facies maps of northwestern South America," in *Geology and tectonics of northwestern South America: Medellin*. Editors F. Cediel and H. Shaw John, 673–747.

Schamel, S. (1991). "*Middle and upper Magdalena basins, Colombia*.," *Active margin basins*. Editor K. T. Biddle (Tulsa, OK: AAPG), 52, 283–301.

Sepulchre, P., Sloan, L. C., Snyder, M., and Fiechter, J. (2009). Impacts of Andean uplift on the Humboldt Current system: a climate model sensitivity study. *Paleoceanography and Paleoclimatology*. 24 (4), 1–11. doi:10.1029/2008PA001668

Slade, R., and Moritz, C. (1998). Phylogeography of Bufo marinus from its natural and introduced ranges. *Proc. Biol. Sci*. 265, 769–777. doi:10.1098/rspb.1998.0359

Suppe, J., Sàbat, F., Munoz, J. A., Poblet, J., Roca, E., and Vergés, J. (1997). Bed-by-bed fold growth by kink-band migration: Sant Llorenç de Morunys, eastern Pyrenees. *J. Struct. Geol*. 19 (3–4), 443–461.

Tavani, S., Arbues, P., Snidero, M., Carrera, N., and Muñoz, J. (2011). Open Plot Project: an open-source toolkit for 3-D structural data analysis. *Solid Earth*. 2, 53–63. doi:10.5194/se-2-53-2011

Tera, F., and Wasserburg, G. (1972). U-Th-Pb systematics in three Apollo 14 basalts and the problem of initial Pb in lunar rocks. *Earth Planet Sci. Lett*. 14 (3), 281–304.

Torres-Hernandez, M. P. (2010). *Petrografía, geocronología y geoquímica de las ignimbritas de la formación Popayán, en el contexto del vulcanismo del suroccidente de Colombia [M.Sc. Universidad EAFIT]*., 132.

Ujueta, G. (1999). La Cordillera Oriental colombiana no se desprende de la Cordillera Central. *Geol. Colomb*. 24, 3–28.

Van der Hammen, T. (1958). Estratigrafía del Terciario y Maastrichtiano continentales y tectogénesis de los Andes colombianos. *Bol. Geol*. 6 (1–3), 1–56.

Van der Wiel, A. (1991). *Uplift and volcanism of the SE Colombian Andes in relation to Neogene sedimentation in the upper Magdalena valley [PhD. Agricultural University of Wageningen*., 208.

Van der Wiel, A., and Van den Bergh, G. (1992). Uplift, subsidence, and volcanism in the southern Neiva basin, Colombia, Part 1: Influence on fluvial deposition in the Miocene Honda formation. *J. South Am. Earth Sci*. 5 (2), 153–173.

Villamil, T., and Arango, C. (1998). "Integrated stratigraphy of latest Cenomanian and early Turonian facies of Colombia," *Paleogeographic evolution and non-glacial Eustacy*. Editors L. Pindell James and L. Drake Charles (Tulsa, OK: Northern South AmericaSEPM), 58, 129–159.

Villamil, T. (1999). Campanian–Miocene tectonostratigraphy, depocenter evolution and basin development of Colombia and western Venezuela. *Palaeogeogr. Palaeoclimatol. Palaeoecol*. 153 (1), 239–275.

Villamil, T. (1998). "Chronology, relative sea-level history and a new sequence stratigraphic model for basinal Cretaceous facies of Colombia," in *Paleogeographic evolution and non-glacial Eustacy*. Editors L. Pindell James and L. Drake Charles (Tulsa, OK: Northern South AmericaSEPM), 58, 161–216.

Villarroel, C., Setoguchi, T., Brieva, J., and Macia, C. (1996). Geology of the La Tatacoa "desert" (Huila, Colombia): Precisions on the stratigraphy of the Honda group, the evolution of the" Pata high" and the presence of the La Venta fauna:

Memoirs of the Faculty of science. *Kyoto University, Series of Geology and Mineralogy*. 58, 41–66.

Von Quadt, A., Gallhofer, D., Guillong, M., Peytcheva, I., Waelle, M., and Sakata, S. (2014). U–Pb dating of CA/non-CA treated zircons obtained by LA-ICP-MS and CA-TIMS techniques: impact for their geological interpretation. *J. Anal. Atom. Spectrom*. 29 (9), 1618–1629. doi:10.1039/c4ja00102h

Wagner, L., Jaramillo, J., Ramirez-Hoyos, L., Monsalve, G., Cardona, A., and Becker, T. (2017). Transient slab flattening beneath Colombia. *Geophys. Res. Lett*. 44 (13), 6616–6623. doi:10.1002/2017GL073981

Weber, M., Cardona, A., Paniagua, F., Cordani, U., Sepúlveda, L., and Wilson, R. (2009a). The Cabo de la Vela Mafic-ultramafic Complex, northeastern Colombian Caribbean region: a record of multistage evolution of a late Cretaceous intra-oceanic arc. *Geol. Soc. Lond*. 328, 549–568.

Weber, M., Cardona, A., Wilson, R., Gomez, J., and Zapata, G. (2009b). High-pressure rocks from the Colombian Caribbean; record of a changing convergent margin. *Geochem. Cosmochim. Acta*. 71, A1095.

Weir, J. T., and Price, M. (2011). Andean uplift promotes lowland speciation through vicariance and dispersal in Dendrocincla woodcreepers. *Mol. Ecol*. 20 (21), 4550–4563. doi:10.1111/j.1365-294X.2011.05294.x

Wesselingh, F., Räsänen, M., Irion, G., Vonhof, H., Kaandorp, R., Renema, W., et al. (2001). Lake Pebas: a palaeoecological reconstruction of a Miocene, long-lived lake complex in western Amazonia. *Cainozoic Res*. 1 (1/2), 35–68. doi:10.1371/journal.pone.0199201

Witt, C., Rivadeneira, M., Poujol, M., Barba, D., Beida, D., Beseme, G., et al. (2017). Tracking ancient magmatism and Cenozoic topographic growth within the Northern Andes forearc: Constraints from detrital U-Pb zircon ages. *Bulletin*. 129 (3–4), 415–428. doi:10.1029/2019TC005967

Woodring, W. P. (1957). Geology and description of Tertiary mollusks (gastropods; trochidae to Turritellidae). Geology and paleontology of Canal Zone and adjoining parts of Panama. *U. S. Geol. Surv. Prof. Pap*. 306-A, 145.

Xie, X. Y., Mann, P., and Escalona, A. (2010). Regional provenance study of Eocene clastic sedimentary rocks within the South America-Caribbean plate boundary zone using detrital zircon geochronology. *Earth Planet Sci. Lett*. 291 (1–4), 159–171. doi:10.1086/668683

Zachos, J., Pagani, M., Sloan, L., Thomas, E., and Billups, K. (2001). Trends, rhythms, and aberrations in global climate 65 Ma to present. *Science*. 292 (5517), 686–693. doi:10.1126/science.1059412

Zapata, S., Cardona, A., Montes, C., Valencia, V., Vervoort, J., and Reiners, P. (2014). Provenance of the Eocene soebi blanco formation, Bonaire, Leeward Antilles: Correlations with post-Eocene tectonic evolution of northern South America. *J. South Am. Earth Sci*. 52, 179–193. doi:10.1007%2F978-3-319-55787-8_18

Conflict of Interest: The authors declare that the research was conducted in the absence of any commercial or financial relationships that could be construed as a potential conflict of interest section.

frontiers in Earth Science

ORIGINAL RESEARCH
published: 12 February 2021
doi: 10.3389/feart.2021.635181

High-Resolution Stable Isotope Paleotopography of the John Day Region, Oregon, United States

Tyler Kukla[1], Daniel Enrique Ibarra[1,2,3], Jeremy K. Caves Rugenstein[4], Jared T. Gooley[1,5], Casey E. Mullins[6], Samuel Kramer[7], Danielle Y. Moragne[7,8] and C. Page Chamberlain[1]*

[1]Department of Geological Sciences, Stanford University, Stanford, CA, United States, [2]Institute at Brown for Environment and Society and the Department of Earth, Environmental and Planetary Science, Brown University, Providence, RI, United States, [3]Department of Earth and Planetary Science, University of California, Berkeley, Berkeley, CA, United States, [4]Department of Geosciences, Colorado State University, Fort Collins, CO, United States, [5]Currently at United States Geological Survey, Reston, VA, United States, [6]Earth Systems Program, Stanford University, Stanford, CA, United States, [7]Department of Earth System Science, Stanford University, Stanford, CA, United States, [8]Department of Earth Sciences, Dartmouth College, Hanover, NH, United States

OPEN ACCESS

Edited by:
Heiko Pingel,
University of Potsdam, Germany

Reviewed by:
Gregory Retallack,
University of Oregon, United States
John Bershaw,
Portland State University,
United States

***Correspondence:**
Tyler Kukla
tykukla@stanford.edu

Specialty section:
This article was submitted to Quaternary Science, Geomorphology and Paleoenvironment, a section of the journal Frontiers in Earth Science

Received: *30 November 2020*
Accepted: *14 January 2021*
Published: *12 February 2021*

Citation:
Kukla T, Ibarra DE, Rugenstein JKC, Gooley JT, Mullins CE, Kramer S, Moragne DY and Chamberlain CP (2021) High-Resolution Stable Isotope Paleotopography of the John Day Region, Oregon, United States. Front. Earth Sci. 9:635181. doi: 10.3389/feart.2021.635181

The John Day region of central Oregon, United States contains ~50 million years of near-continuous, fossiliferous sedimentation, representing one of the world's richest archives of Cenozoic terrestrial ecosystems and climate. Stable isotope proxy data from this region are commonly used to infer the elevation history of the Cascades, which intercept westerly moisture in transit to the John Day region. However, the Blue Mountains, which accreted in the Mesozoic, create a region of local high topography that can confound signals of Cascades uplift. John Day deposits, including the John Day Formation, are divided into an eastern facies located within the Blue Mountains and a western facies in the adjacent plains. As a result, the Blue Mountains may have supported gradients in climate and ecology between the eastern and western facies, and constraining these gradients is necessary for reconstructing past topography and ecosystem change. In order to define the Cenozoic extent and magnitude of Blue Mountains topography we use oxygen isotopes in authigenic clay minerals to construct a spatially resolved map of local elevation. We find that the oxygen isotope composition of clay minerals within the Blue Mountains is ~3‰ lower than in the adjacent high plains, and this offset is mostly constant throughout our record (spanning ~50 – 5 Ma). We attribute this offset to Blue Mountains topography, either directly from upslope rainout or indirectly through the effect of elevation on local variations in precipitation seasonality. Our results highlight the importance of local topographic features in regional paleotopography reconstructions and provide important biogeographical context for the rich paleo-floral and -faunal records preserved in John Day sediments.

Keywords: paleotopography, John Day, Blue Mountains, oxygen isotopes, biogeography, clay minerals

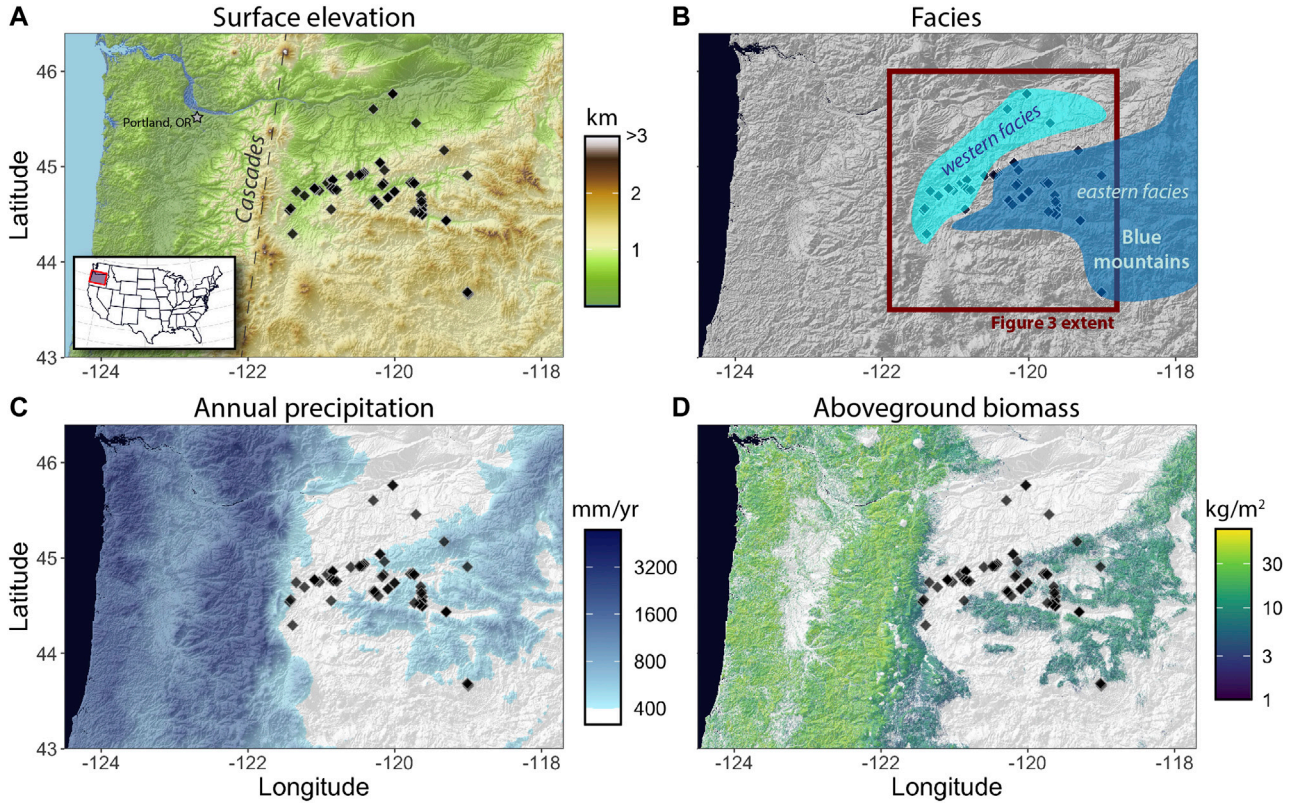

FIGURE 1 | (A) Surface elevation (km) map of study region. Light blue represents ocean, diamond symbols are authigenic clay sample locations. Inset indicates the location of the study area within the United States. Elevation data collected with the elevatr package in R. **(B)** Approximate extent of the western (light blue polygon) and eastern (dark blue polygon) facies. Eastern facies follows the extent of the Blue Mountains region. Polygons based on Albright et al. (2008); Graham (2014); Robinson et al. (1984); Takeuchi (2007). Red box denotes the areal extent of maps in **Figure 3**. **(C)** Annual precipitation map (mm/yr). White area receives less than 400 mm of precipitation per year and characterizes the Cascades rainshadow. Data from the PRISM Climate Group (2012). **(D)** Aboveground biomass (kg/m^2; live, dry). White area denotes no or negligible aboveground biomass. Data from Kellndorfer et al. (2012).

INTRODUCTION

The John Day region lies in the High Desert of central Oregon with the Cascades Range to the west and the Blue Mountains province to the east (**Figures 1A,B**). The region, denoted here as the extent of the eastern and western facies (**Figure 1B**), is known for its near-continuous, fossil-rich terrestrial sedimentation, making it one of the planet's most complete records of Cenozoic environments and climate. Over one hundred years of extensive study has built a foundation ripe for disentangling the co-evolution of local climate, landscapes, and life (Bestland and Retallack, 1994; Clark, 1989; Dillhoff et al., 2009; Merriam and Sinclair, 1906; Retallack et al., 2004; Robinson et al., 1984; Robson et al., 2019; Samuels et al., 2015; Sinclair, 1905; Swanson and Robinson, 1968). In addition to providing an ideal case study for paleo-biogeographical change (Kohn and Fremd, 2007; Retallack, 2004), John Day proxy data have been used to unravel the tectonic history of the Cascades, which serve as a barrier between Oregon's High Desert and moisture-laden winter westerly winds originating in the Pacific (Bershaw et al., 2019; Kohn et al., 2002; Takeuchi et al., 2010). Due to the strong rainshadow cast by the Cascades today (**Figure 1C**), the range's uplift history is considered an important driver of Cenozoic precipitation and vegetation change in the John Day region and across the northwestern United States (Retallack, 2004; Takeuchi and Larson, 2005; Kohn and Fremd, 2007; Takeuchi et al., 2010).

However, the Cascades Range is not the only topographic feature of consequence in the John Day region. The Blue Mountains province, which accreted in the Mesozoic (Dickinson and Thayer, 1978; Dickinson, 1979; Dickinson, 2004; Schwartz et al., 2010; LaMaskin et al., 2015), contains the eastern facies of deposition in the John Day region, separating it from the western facies in the adjacent high plains (Robinson et al., 1984) (**Figure 1B**). Today, the Blue Mountains create local gradients in precipitation and vegetation, with higher precipitation and a denser canopy in the mountain slopes (eastern facies) compared to the surrounding plains (western facies; **Figures 1C,D**). This significant local variability in hydroclimate and ecology may confound regional-scale interpretations of paleo archives if similar gradients existed in the past. For example, spatial variability

can be misinterpreted as temporal variability if outcrop or sampling locations shift along these gradients with age. Similarly, changes in environmental parameters due to changes in local high elevation can be mis-attributed to the height of the Cascades if local topography is not accounted for.

There is some evidence that precipitation and vegetation gradients in the Blue Mountains have been present as far back as the Eocene. Near the western tip of the eastern facies Bestland and Retallack (1994) identified two different plant assemblages in the same stratigraphic horizon that point to distinct elevation regimes, perhaps related to Blue Mountain topography or local stratovolcanoes (White and Robinson, 1992). The floras are interpreted to reflect a wetter, more densely vegetated tropical lowland forest and an adjacent temperate, early successional highland forest (Bestland and Retallack, 1994; Bestland et al., 2002). In contrast, wetter conditions with denser vegetation appear in the highlands today while the lowlands are drier and sparsely vegetated (**Figures 1C,D**). Thus, while ecological gradients surrounding the Blue Mountains may be long-lived, their magnitude and even their direction may have changed with time.

In this study we present spatial and temporal oxygen isotope data from authigenic clay minerals, a proxy for past precipitation $\delta^{18}O$, to constrain the spatial expression of Blue Mountains topography and its effect on regional precipitation patterns. Isotopes of authigenic clays have been widely applied to studying tectonic and climatic change in Cenozoic western North America (Takeuchi and Larson, 2005; Mulch et al., 2006; Sjostrom et al., 2006; Mix et al., 2011, Mix et al., 2016, Mix et al., 2019; Chamberlain et al., 2012; Mix and Chamberlain, 2014) and they are particularly useful in places like John Day where soil carbonates—a more commonly used paleo-$\delta^{18}O$ proxy—are not continuously present through the sedimentary record (Bestland et al., 2002). Here, we document a ~3‰ offset in authigenic clay $\delta^{18}O$ between the western and eastern facies, with lower values in the east. This offset is best explained by the influence of the Blue Mountains on local precipitation patterns, indicating the range has supported local precipitation gradients since at least the Eocene.

GEOLOGIC SETTING

Prior to the deposition of Cenozoic sediment in the John Day region, the Mesozoic accretion of the Wallowa and Olds Ferry arcs created the Blue Mountains province (Dickinson and Thayer, 1978; Dickinson, 1979; Schwartz et al., 2010; LaMaskin et al., 2015). The province accreted along the Salmon River suture zone, likely sometime before 130 Ma (Dickinson, 1979, Dickinson, 2004; Schwartz et al., 2010; LaMaskin et al., 2015). After accretion, deformation of the suture zone is thought to have ended around 90 Ma, setting the stage for Cenozoic deposition within the John Day region.

Deposition in the John Day region occurred throughout the Eocene to the Pliocene and sediment was predominantly derived from air-fall ash and some ash-flow sheets with evidence for minor reworking by alluvial and lacustrine processes (Swanson and Robinson, 1968; Robinson et al., 1984; Graham, 2014). Volcanism appears frequent throughout the depositional record and likely shifted westward from the Blue Mountains province to the proto-Cascades ~37–40 million years ago, possibly due to "flat slab" detachment and a steepening of western North American subduction (Lipman et al., 1972; Noble, 1972; Robinson et al., 1984; Heller et al., 1987). This shift may be linked to the start of Western Cascades uplift, but early volcanism in the Western Cascades was likely associated with isolated stratovolcanoes along a low-lying coastal plain that may not have intercepted westerly moisture as effectively as today's Cascades Range (White and Robinson, 1992; Dillhoff et al., 2009). The timing of the onset of the Cascades rainshadow is still debated, and likely varies north-south (Priest, 1990; Kohn et al., 2002; Takeuchi and Larson, 2005; Takeuchi et al., 2010; Bershaw et al., 2020; Pesek et al., 2020), but drier, rainshadow-like conditions appear to emerge in Oregon in the late Oligocene to early Miocene (Woodburne and Robinson, 1977; MacFadden and Hulbert, 1988; Retallack, 2004).

The eastern and western facies of John Day deposition are separated by the Blue Mountains but they share some lithologic similarities (Swanson and Robinson, 1968; Robinson et al., 1984). The facies share the same formations for most of the Cenozoic, from the lower-mid Eocene Clarno Formation to the upper Eocene–lower Miocene John Day Formation. After deposition of the John Day Formation, the western facies contains the Ellensburg, Simtustus, Dalles, and Deschutes Formations while the eastern facies contains the Mascall and Rattlesnake Formations (Smiley, 1963; Farooqui et al., 1981; Smith, 1986; Graham, 2014). Both facies are primarily comprised of claystones and air-fall tuffs. The western facies contains more ash-flows and lava-flows than the eastern facies, suggesting a volcanic source west of the Blue Mountains and indicating the topographic barrier of the Blue Mountains may have limited the eastern extent of these deposits (Swanson and Robinson, 1968; Robinson et al., 1984). A third unit, referred to as the southern facies, also exists within the Blue Mountains region and shares lithological similarities with the eastern facies, but was not sampled in this study. The western facies, especially after the westward shift in volcanism at ~40 Ma, generally hosts coarser grained volcaniclastic material with thicker sedimentary packages, further supporting a western source of volcanic material (Robinson et al., 1984).

Paleobotanical evidence in the John Day region points to a long-term aridification trend beginning about 30 million years ago with the expansion of open-habitat grasslands. Paleosols at this time contain evidence for grassy root textures, and mammal fossils reveal adaptations for running ("cursoriality," a common indicator of open vegetation) and eating tougher foods like grasses ("hypsodonty") (MacFadden and Hulbert, 1988; Janis et al., 2002; Retallack, 2004). This transition to drier conditions, lasting until ~19 Ma, is generally interpreted to reflect strengthening of the Cascades rainshadow and/or a shift in the seasonality of precipitation from summer-dominated to the

winter-dominated regime that exists today (Retallack, 2004; Retallack, 1997).

METHODS

Authigenic Clay Sample Preparation and Isotopic Analysis

We analyzed the oxygen isotope composition of 29 samples spanning 15 localities to build on existing data from Takeuchi (2007). Clay-rich paleosol samples were gently ground with a mortar and pestle and centrifuged to separate the <0.5 μm size fraction. The separated material was dried and gently ground with a mortar and pestle into a powder. Samples with indication of organic matter (dark coloration) were treated with a 3% hydrogen peroxide (H_2O_2) solution for 24–48 h before being rinsed at least 5 times with de-ionized water in a centrifuge.

At least one sample from each sedimentary package at each locality was run for X-ray diffraction to identify the clay mineralogy and screen for quartz. X-ray diffractometry was run at the Stanford University Environmental Measurements Facility using a Rigaku MiniFlex 600 Benchtop X-ray Diffraction System. The diffractometer is equipped with a copper (Cu) anode set at the maximum power of 600 W. Powdered samples were first suspended in isopropanol and left to air-dry on a zero-background quartz sample holder. Once dried, each sample was run twice with the 2-theta angle ranging from 2 to 90°. Samples were untreated in the first run and glycolated in the second run. To glycolate the samples, dried powders were placed in a sealed desiccator with 1 cm of ethylene glycol at the base and left overnight in an oven set to 65°C. The Rigaku PDXL software was used to aid in mineral identification for each sample. Samples identified to have quartz and/or illite peaks were not analyzed for oxygen isotopes.

After screening for quartz and illite, 1–2 mg of sample powder was mixed with lithium flouride (*LiF*; ~1:1 by mass) and pressed into pellets. The *LiF* pellets prevent dispersion of clay powder during laser ablation. Samples were brought to a vacuum to remove atmospheric vapor in the *LiF*. Any remaining vapor and any sorbed water in smectite minerals was removed through 2–4 pre-flourinations where samples were exposed to bromine pentaflouride (BrF_5) for ~90 s. Afterward, samples were laser ablated with a New Wave Research MIR10-25 infrared laser ablation system in the presence of BrF_5 to liberate O_2 gas (Sharp, 1990; Sjostrom et al., 2006; Mix and Chamberlain, 2014; Mix et al., 2016). Oxygen isotope analyses on O_2 gas were performed in dual-inlet mode at the Stanford University Stable Isotope Biogeochemistry Laboratory on a Thermo Finnigan MAT 252 or 253+, depending on the date of acquisition (Abruzzese et al., 2005; Hren et al., 2009; Mix et al., 2016; Chamberlain et al., 2020). We purified O_2 gas from samples run on the MAT 252 with two liquid nitrogen cold traps and one potassium bromide (*KBr*) trap before freezing O_2 on a liquid nitrogen-temperature zeolite and subsequently equilibrating it with the mass spectrometer sample bellows. On the MAT 253+, O_2 gas was purified with three liquid nitrogen traps and one sodium chloride (*NaCl*) trap, frozen on a zeolite at liquid nitrogen temperature, passed over a room temperature flow-through zeolite with high purity He as the carrier gas, and finally frozen in a zeolite trap and equilibrated with the mass spectrometer sample bellows. Repeated analyses of in-house standard DS069 were made during each day of analysis to correct for drift. Precision of DS069 replicates was 0.26‰ (n = 43). All isotopic ratios are reported relative to Vienna Standard Mean Ocean Water (VSMOW).

Comparing Oxygen Isotope Values of the Eastern and Western Facies

In order to map out the spatial pattern of authigenic clay $\delta^{18}O$ through the Cenozoic we calculate the residual of all data points relative to the Cenozoic trend. We build this Cenozoic trend by taking the average of the eastern and western facies trends, each defined by a loess smooth curve. This approach ensures that the Cenozoic trend is not biased toward one facies or the other when its sample density is relatively higher for a given point in time. After establishing the Cenozoic trend we calculate the residual $\delta^{18}O$ value for each sample ($\delta^{18}O_{sample} - \delta^{18}O_{trend}$). This represents a detrended record of $\delta^{18}O$ that allows for a spatial comparison of samples from different times of the record.

RESULTS

Most clay-size separates were comprised of smectite or mixed smectite/kaolinite with few kaolinite samples. Samples containing illite and/or quartz were not analyzed for $\delta^{18}O$. Kaolinite-rich samples are mostly found in the Eocene when conditions were likely wetter, consistent with the findings of Takeuchi (2007). Typical diffraction patterns for smectite, kaolinite, and excluded (illite/quartz) samples can be found in **Supplementary Figure S1**. We plot oxygen isotope data of kaolinite and smectite samples together because their fractionation factors are similar for at environmental temperatures (Sheppard and Gilg (1996); **Supplementary Figure S3**). We note that a recent database for oxygen isotope fractionation suggests a 2–3‰ offset between kaolinite and smectite fractionation at environmental temperatures (Vho et al., 2019), but the database is not recommended for use at low, environmental temperatures because a key approximation does not hold in this range Eq. 5 of Vho et al. (2019)).

Oxygen isotope values of our composite record range from 8.3 to 16.9‰ with an average value of 12.5‰ (±2.2‰, 1 σ). In the eastern facies the average $\delta^{18}O$ value is 11.1‰ (±1.9‰, 1 σ) and in the western facies mean $\delta^{18}O$ is 13.7‰ (±1.6‰, 1 σ). Throughout the record, oxygen isotope values in the eastern facies (the Blue Mountains province) are ~3‰ lower than those from the western facies, while $\delta^{18}O$ values in both facies follow similar trends. Specifically, eastern and western facies $\delta^{18}O$ values both show a ~3‰ increase between 30 and 20 Ma (**Figure 2A**).

DISCUSSION

Oxygen Isotopes of the Eastern and Western Facies

Lower oxygen isotope values in the Blue Mountains province (eastern facies) suggests this local topographic feature has

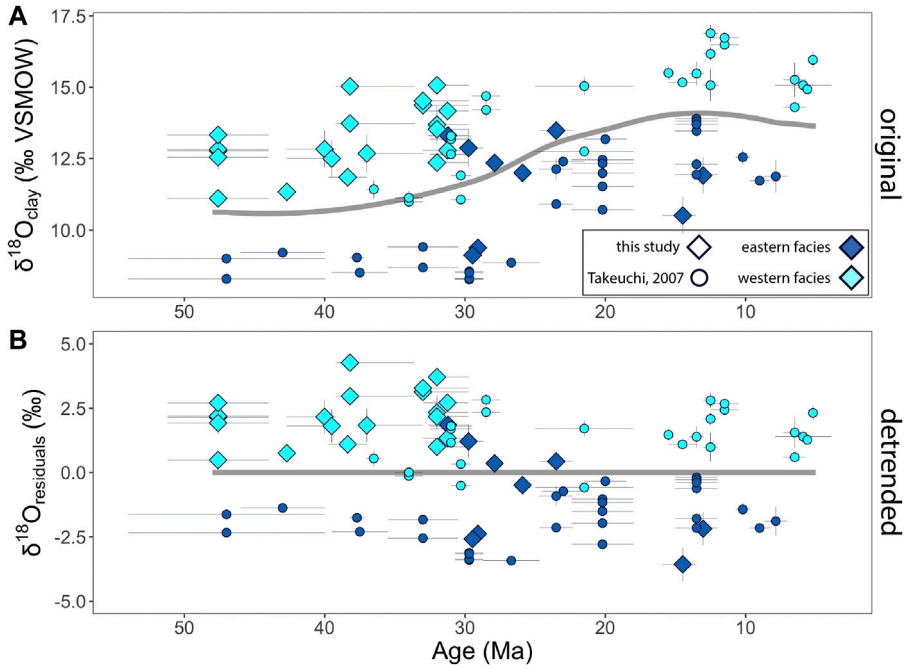

FIGURE 2 | (A) Oxygen isotope values of authigenic clay samples (‰ VSMOW) in the eastern (dark blue) and western (light blue) facies. Diamonds denote data from this study and circles are from Takeuchi (2007). In both panels the thin, horizontal and vertical gray lines are age uncertainty and $\delta^{18}O$ uncertainty, respectively. Thick, gray line denotes the average of the eastern and western facies trends, representing a regional trend. **(B)** Residual $\delta^{18}O$ values relative to the regional trend (gray line). Eastern facies $\delta^{18}O$ values are ~3‰ lower than the western facies throughout the record.

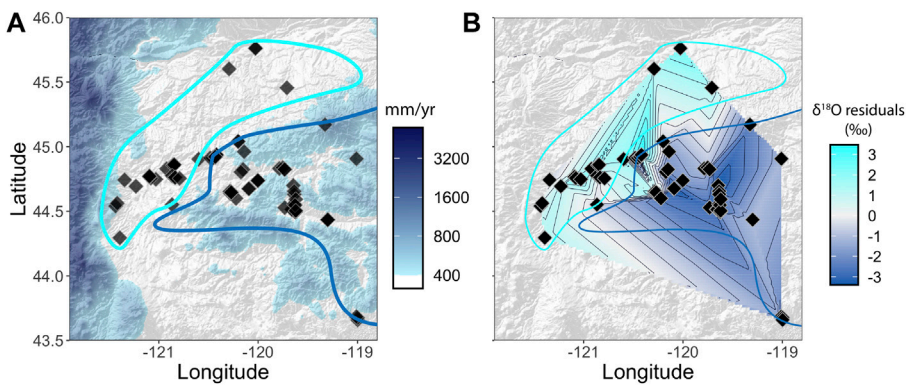

FIGURE 3 | (A) Zoomed-in panel (see **Figures 1B,C**) of sample locations (black diamonds) and mean annual precipitation. Light and dark blue polygon outlines reflect the approximate spatial extent of the western and eastern facies, respectively (after Albright et al. (2008); Graham (2014); Robinson et al. (1984); Takeuchi (2007)). **(B)** Spatially interpolated map of $\delta^{18}O$ residuals overlain with eastern and western facies extents.

influenced regional precipitation patterns for at least the last ~50 million years (Dickinson and Thayer, 1978; Dickinson, 1979; Schwartz et al., 2010; LaMaskin et al., 2015). Based on spatial interpolation of oxygen isotope residuals (**Figure 2B**) we find that the boundary between negative (lower $\delta^{18}O$) and positive (higher $\delta^{18}O$) residuals closely tracks the modern boundary of the eastern and western facies (which is, itself, defined by the extent of the Blue Mountains) (**Figure 3**). This close correspondence with the modern extent of the Blue Mountains suggests the possibility that authigenic clay $\delta^{18}O$ values reflect modern conditions due to diagenetic alteration or overprinting by modern waters instead of reflecting changes in past precipitation $\delta^{18}O$. However, $\delta^{18}O$ values from the eastern and western facies both increase by ~3‰ between 30 and 20 Ma, and this shift likely would not be coherent if all samples have been similarly altered by modern waters. Thus, we interpret $\delta^{18}O$ values to represent the oxygen isotope composition of water at the time of clay mineral formation.

Today, the windward slopes of the Blue Mountains capture more annual precipitation than the adjacent high plains (see

Figure 1C) and receive a larger fraction of annual precipitation during the winter months (**Supplementary Figure S2**). Both of these observations support lower $\delta^{18}O$ values in the Blue Mountains than in the adjacent plains. First, increased rainout over mountains is often explained by topography forcing air upward, leading to adiabatic cooling and moisture condensation and precipitation (Aristotle, 1931; Smith, 1979; Smith and Barstad, 2004; Roe, 2005). Higher precipitation due to Blue Mountains orography implies more rainout and a decrease in $\delta^{18}O$ values as precipitation preferentially removes $\delta^{18}O$. Alternatively, lower $\delta^{18}O$ values in the Blue Mountains region may be related to precipitation seasonality as, compared to the plains, the Blue Mountains receive a greater fraction of total precipitation in the winter months when precipitation $\delta^{18}O$ values are lower. It is possible that upslope rainout and precipitation seasonality both contribute to lower $\delta^{18}O$ values in the Blue Mountains. However, disentangling the effect of seasonality from upslope rainout on precipitation $\delta^{18}O$ is difficult because most modern $\delta^{18}O$ data in the John Day region are sampled in warmer months or from rivers that integrate seasonal precipitation (e.g., Bershaw et al. (2019)).

Despite the close link between residual $\delta^{18}O$ values and the extent of the Blue Mountains, $\delta^{18}O$ residuals do not correlate strongly with modern elevation or fraction of winter precipitation (**Supplementary Figure S4**). Residual $\delta^{18}O$ values generally decrease with elevation by ~3.3‰ per kilometer, similar to the regional lapse rate of ~3.2‰ Bershaw et al. (2020) per kilometer, but the correlation is weak ($R^2 = 0.17$). There is no significant correlation between residual $\delta^{18}O$ and the fraction of annual precipitation occurring in winter. The weak relationships between past clay $\delta^{18}O$ and modern conditions is not unexpected since some clays likely formed in contact with local meteoric water (tracking local elevation and precipitation seasonality) while others formed in floodplains in contact with upstream runoff (tracking the upstream hypsometric mean elevation and precipitation seasonality). Without reliable constraints on past floodplain extents and local drainage divides it is difficult to determine the relative importance of elevation, precipitation seasonality, or other factors in eastern and western facies $\delta^{18}O$ values. Additionally, modern winter precipitation and topography may differ from that of most samples in our record. Thermochronometry and geochronology data from the western Cascades in the latitude range of our samples points to exhumation between 20 and 10 Ma (Pesek et al., 2020), and there is abundant evidence that the timing of Cascades uplift and exhumation varied north-to-south (Reiners et al., 2002; Takeuchi and Larson, 2005; Pesek et al., 2020). If spatially variable topographic changes affected the spatial pattern of $\delta^{18}O$, a direct comparison of past John Day data with modern conditions may be invalid.

Implications for Regional Climate and Tectonics

Our results suggest that a regional gradient in precipitation amount and/or seasonality has existed around the Blue Mountains for most of the last 50 million years. If the Blue Mountains did not increase rainout or were not elevated above the plains, we would expect no difference in clay $\delta^{18}O$ values between the eastern and western facies. While the Blue Mountains are generally wetter than the adjacent plains today, lower $\delta^{18}O$ values in the eastern facies does not require that the Blue Mountains were wetter in the past. For example, it is possible that the Blue Mountains and the plains received similar amounts of annual precipitation, but summer (winter) precipitation made up a larger fraction of annual precipitation in the plains (mountains). However, summer and winter precipitation both increase with elevation in the Blue Mountains (and across the western United States; **Supplementary Figure S5**) today, and there is no clear reason why topography would not have the same effect on precipitation in the past. We suggest the Blue Mountains have received more precipitation than the surrounding plains for at least the last ~50 million years. Thus, a possible Eocene boundary between tropical lowland and temperate highland vegetation (Bestland and Retallack, 1994; Bestland et al., 2002) is likely driven by colder temperatures or topographic relief, but not drier conditions in the Blue Mountains.

Despite a long-lived precipitation gradient associated with the Blue Mountains, both the Blue Mountains and the plains record an increase in $\delta^{18}O$ values that tracks independent evidence for regional aridification. This $\delta^{18}O$ increase is probably not driven by temperature since the shift is unidirectional while global climate both warmed and cooled between 30 and 20 Ma (Zachos et al., 2001). Meanwhile, the onset of drier conditions between 30 and 20 million years ago is evidenced by the expansion of open-habitat grasslands and mammals adapted to running and eating tougher vegetation like grasses (Woodburne and Robinson, 1977; MacFadden and Hulbert, 1988; Jacobs et al., 1999; Janis et al., 2002; Retallack, 2004), although this transition may also be explained by grassland-grazer coevolution, independent of climate (Retallack, 2001; Retallack, 2013). The ~3‰ increase in authigenic clay $\delta^{18}O$ may be related to drying, but the interpretation is not straightforward. For example, Retallack (2004) suggests that drying is related to 1) the uplift of the Cascades and 2) a decrease in summer (high-$\delta^{18}O$) precipitation. But both of these effects would likely decrease $\delta^{18}O$ values rather than increase them. Further, marine $\delta^{18}O$ values vary by just 1‰ from 30 to 20 Ma and do not show a systematic increase capable of overprinting the effects of Cascades uplift and less summer precipitation (Zachos et al., 2001). Increased upstream (westward) moisture recycling in drier climates can also increase $\delta^{18}O$ (Salati et al., 1979; Sonntag et al., 1983; Mix et al., 2013; Chamberlain et al., 2014; Winnick et al., 2014; Kukla et al., 2019), but this effect is negligible in near-coastal settings where upstream land area is minimal (Mix et al., 2013; Winnick et al., 2014; Kukla et al., 2019).

Instead, we speculate that the $\delta^{18}O$ increase in our data reflects the onset of the Cascades rainshadow driving a decrease in winter (low-$\delta^{18}O$) precipitation. Today, the Cascades represent a much stronger rainshadow in the winter than in the summer (e.g., Siler and Durran (2016); **Supplementary Figure S6**), suggesting the possibility that their uplift would disproportionately decrease winter precipitation inland. Still, it is not clear that the increase in $\delta^{18}O$ from less winter precipitation could outweigh any decrease in $\delta^{18}O$ from Cascades uplift. It is possible that other factors associated with drier conditions, like surface water and subcloud evaporation, could also increase $\delta^{18}O$. Thus, more work is needed

to test the hypothesis that drying in the John Day region is owed to disproportionate drying in the winter.

The distinct isotopic signature of the Blue Mountains emphasizes the importance of local elevation in regional tectonic reconstructions. Even though the eastern and western facies lie leeward (east) of the Cascades, lower $\delta^{18}O$ values in the eastern facies (the Blue Mountains) may be misinterpreted to reflect the height of the Cascades instead of local topography. For example, using hydrogen isotopes of a volcanic glass sample from the Blue Mountains, Bershaw et al. (2019) suggests the Cascades may have been higher than present as early as ~32 million years ago. Alternatively, we suggest that low hydrogen isotope ratios in the Oligocene reflect the local topography of the Blue Mountains rather than upstream elevation of the Cascades. Interestingly, the hydrogen isotope data of Bershaw et al. (2019) reveal an increase in δD of ~16‰ (~2‰ in $\delta^{18}O$) that happens near the mid-Miocene, between ~16 and 8 Ma, significantly later than the increase of ~3‰ between 30 and 20 Ma found in our data. Due to sparse hydrogen isotope data east of the Cascades older than 20 Ma, it is not clear whether volcanic glass δD also records an increase from 30 to 20 Ma. Further, while there are few coeval glass samples from the eastern and western facies to test for a spatial pattern, the existing data do not show a systematic difference in δD between the two regions. If the spatial and temporal trends of authigenic clay and volcanic glass isotopes differ, it is likely that the proxies are forming under different conditions and may be seasonally biased relative to one another. Such information would provide increasingly nuanced insight to the uplift history of the Cascades and its effect on leeward precipitation seasonality. However, at present there is not enough overlap between our authigenic clay data and the volcanic glass data to determine whether the results truly reflect distinct trends.

CONCLUSION

The Blue Mountains have likely supported local (<100 km) gradients in precipitation for much of the Cenozoic with more precipitation reaching the Blue Mountains than the surrounding plains. Distinct floral assemblages from the same stratigraphic interval provided the first hint that the John Day region may have hosted multiple biomes as early as the Eocene (Bestland and Retallack, 1994; Bestland et al., 2002), and our stable isotope results suggest these biomes could co-exist due to distinct elevation and climate regimes. We also find no evidence that regional drying from 30 to 20 million years ago was driven by a shift from summer-dominated to winter-dominated precipitation (Retallack, 2004).

Our high spatial resolution constraints on Blue Mountains topography provides a benchmark for future paleo -floral and -faunal work in the John Day region. Efforts to compare floral and faunal assemblages from the eastern and western facies will constrain how the Blue Mountains influenced local ecosystem dynamics through time. Additionally, our results suggest that the comparison of authigenic clay $\delta^{18}O$ and mammal tooth enamel $\delta^{18}O$ may allow for constraints on local mammal migration patterns. For example, comparing tooth enamel $\delta^{18}O$ from mammals of the same site may inform whether the range of some animals was more local than others (living in the eastern facies, western facies, or traveling between both). Further, changes in the inferred seasonal amplitude of tooth enamel $\delta^{18}O$ could reflect changes in seasonal migration between the two facies. Overall, our constraints on the spatial pattern of Blue Mountains topography and its possible influence over regional precipitation opens new opportunities for biogeography research on the relationship between landscapes and life in John Day through the Cenozoic.

DATA AVAILABILITY STATEMENT

The original contributions presented in the study are included in the article/**Supplementary Material**, further inquiries can be directed to the corresponding author.

AUTHOR CONTRIBUTIONS

TK, DI, JR, SK, and CC conceptualized the study. TK, DI, and CM performed laboratory analysis. TK, DI, JR, JG, DM, and CC performed fieldwork. JG and DM led field-based observation. TK analyzed data and wrote the original draft. All authors contributed to editing and revising.

FUNDING

This research was funded by NSF EAR-1322084 and Heising-Simons grants to CPC.

ACKNOWLEDGMENTS

The authors acknowledge J. Bershaw and Gregory Retallack for comments that improved the manuscript. We also acknowledge Joshua X. Samuels, Nicholas Famoso, Shelley Hall, and Patrick Gamman for assistance obtaining research permits at John Day Fossil Beds National Monument. We also thank Joshua X. Samuels for assistance with field stratigraphy and sampling, and Nicholas Famoso for further guidance on sampling and our age model. Elevation data are sourced from Terrain Tiles hosted on Amazon Web Services. Terrain Tiles data combines Global ETOPO1 and 3DEP datasets. Global ETOPO1 terrain data is courtesy of the U.S. National Oceanic and Atmospheric Administration. United States 3DEP (formerly NED) and global GMTED2010 and SRTM terrain data are courtesy of the U.S. Geological Survey. Research at John Day Fossil Beds National Monument was conducted under Study Number JODA-00033 with Permit Numbers JODA-2017-SCI-001 and JODA-2018-SCI-002, issued by John Day Fossil Beds and the United States Department of the Interior National Park Service.

SUPPLEMENTARY MATERIAL

The Supplementary Material for this article can be found online at: https://www.frontiersin.org/articles/10.3389/feart.2021.635181/full#supplementary-material.

REFERENCES

Abruzzese, M. J., Waldbauer, J. R., and Chamberlain, C. P. (2005). Oxygen and hydrogen isotope ratios in freshwater chert as indicators of ancient climate and hydrologic regime. *Geochem. Cosmochim. Acta* 69, 1377–1390. doi:10.1016/j.gca.2004.08.036

Albright, L. B., III, Woodburne, M. O., Fremd, T. J., Swisher, C. C., III, MacFadden, B. J., and Scott, G. R. (2008). Revised chronostratigraphy and biostratigraphy of the John Day Formation (Turtle cove and kimberly members), Oregon, with implications for updated calibration of the Arikareean North American land mammal age. *J. Geol.* 116, 211–237. doi:10.1086/587650

Aristotle (c 350 B.C.E., translated) (1931). *Meteorologica* Editor W. D. Ross Translated by E.W. Webster) (Oxford, UK: Oxford: Clarendon Press).

Bershaw, J., Cassel, E. J., Carlson, T. B., Streig, A. R., and Streck, M. J. (2019). Volcanic glass as a proxy for Cenozoic elevation and climate in the Cascade Mountains, Oregon, United States. *J. Volcanol. Geoth. Res.* 381, 157–167. doi:10.1016/j.jvolgeores.2019.05.021

Bershaw, J., Hansen, D. D., and Schauer, A. J. (2020). Deuterium excess and ^{17} O-excess variability in meteoric water across the Pacific Northwest, United States. *Tellus B* 72, 1–17. doi:10.1080/16000889.2020.1773722

Bestland, E., and Retallack, G. J. (1994). Geology and Palaeoenvironments of the Clarno unit (John Day Fossil Beds National Monument, Oregon: US National Park Service Open-File Report).

Bestland, E. A., Hammond, P. E., Blackwell, D. L. S., Kays, M. A., Retallack, G. J., and Stimac, J. (2002). Geologic framework of the Clarno unit, John Day fossil Beds National monument, Central Oregon (Oregon Department of Geology and Mineral Industries Open-File Report), 1–39.

Chamberlain, C., Ibarra, D., Lloyd, M., Kukla, T., Sjostrom, D., Gao, Y., et al. (2020). Triple oxygen isotopes of meteoric hydrothermal systems – implications for palaeoaltimetry. *Geochem. Perspect. Lett.* 15, 6–9. doi:10.7185/geochemlet.2026

Chamberlain, C. P., Mix, H. T., Mulch, A., Hren, M. T., Kent-Corson, M. L., Davis, S. J., et al. (2012). The cenozoic climatic and topographic evolution of the western north American Cordillera. *Am. J. Sci.* 312, 213–262. doi:10.2475/02.2012.05

Chamberlain, C. P., Winnick, M. J., Mix, H. T., Chamberlain, S. D., and Maher, K. (2014). The impact of neogene grassland expansion and aridification on the isotopic composition of continental precipitation. *Global Biogeochem. Cycles* 28, 992–1004. doi:10.1002/2014GB004822

Clark, R. D. (1989). *The Odyssey of Thomas Condon: Irish immigrant: frontier missionary: oregon geologist*. 1st Edn. Portland, OR: Oregon Historical Society.

Dickinson, W. R. (2004). Evolution of the North American Cordillera. *Annu. Rev. Earth Planet Sci.* 32, 13–45. doi:10.1146/annurev.earth.32.101802.120257

Dickinson, W. R. (1979). Mesozoic forearc basin in central Oregon. *Geology* 7, 166–170. doi:10.1130/0091-7613(1979)7<166:mfbico>2.0.co;2

Dickinson, W. R., and Thayer, T. P. (1978). "Paleogeographic and paleotectonic implications of Mesozoic stratigraphy and structure in the John Day Inlier of Central Oregon," in *Mesozoic paleogeography of the Western United States* (Los Angeles, California: Pacific Section: Society of Economic Paleontologists and Mineralogists), 147–161, no. 2 in Pacific Coast Paleogeography Symposium.

Dillhoff, R. M., Dillhoff, T. A., Dunn, R. E., Myers, J. A., and Stromberg, C. A. (2009). Cenozoic paleobotany of the John Day Basin, Central Oregon. *Geol. Soc. America Field Guide* 15, 165–185. doi:10.1130/2009.fl

Farooqui, S. M., Beaulieu, J. D., Bunker, R. C., Stensland, D. E., and Thoms, R. E. (1981). Dalles Group: neogene formations overlying the Columbia River Basalt Group in north-central Oregon. *Oregon Geol.* 43, 131–140.

Graham, J. P. (2014). John Day Fossil Beds national monument geologic resources inventory report, 117.

Heller, P. L., Tabor, R. W., and Suczek, C. A. (1987). Paleogeographic evolution of the United States Pacific Northwest during Paleogene time. *Can. J. Earth Sci.* 24, 1652–1667. doi:10.1139/e87-159

Hren, M. T., Tice, M. M., and Chamberlain, C. P. (2009). Oxygen and hydrogen isotope evidence for a temperate climate 3.42 billion years ago. *Nature* 462, 205–208. doi:10.1038/nature08518

Jacobs, B. F., Kingston, J. D., and Jacobs, L. L. (1999). The origin of grass-dominated ecosystems. *Ann. Mo. Bot. Gard.* 86, 590. doi:10.2307/2666186

Janis, C. M., Damuth, J., and Theodor, J. M. (2002). The origins and evolution of the North American grassland biome: the story from the hoofed mammals. *Palaeogeogr. Palaeoclimatol. Palaeoecol.* 177, 183–198. doi:10.1016/S0031-0182(01)00359-5

Kellndorfer, J., Walker, W., Kirsch, K., Fiske, G., Bishop, J., LaPoint, L., et al. (2012). NACP aboveground biomass and carbon baseline data (NBCD 2000). ORNL DAAC.

Kohn, M. J., and Fremd, T. J. (2007). Tectonic controls on isotope compositions and species diversification, John Day Basin, central Oregon. *PaleoBios* 27, 14.

Kohn, M. J., Miselis, J. L., and Fremd, T. J. (2002). Oxygen isotope evidence for progressive uplift of the Cascade Range, Oregon. *Earth Planet Sci. Lett.* 204, 151–165. doi:10.1016/S0012-821X(02)00961-5

Kukla, T., Winnick, M. J., Maher, K., Ibarra, D. E., and Chamberlain, C. P. (2019). The sensitivity of terrestrial δ^{18} O gradients to hydroclimate evolution. *J. Geophys. Res.: Atmos.* 124, 563–582. doi:10.1029/2018JD029571

LaMaskin, T. A., Dorsey, R. J., Vervoort, J. D., Schmitz, M. D., Tumpane, K. P., and Moore, N. O. (2015). Westward growth of Laurentia by Pre–Late jurassic terrane accretion, Eastern Oregon and Western Idaho, United States. *J. Geol.* 123, 233–267. doi:10.1086/681724

Lipman, P. W., Prostka, H. J., and Christiansen, R. L. (1972). Cenozoic volcanism and plate-tectonic evolution of the Western United States. I. Early and middle cenozoic. *Phil. Trans. Math. Phys. Eng. Sci.* 271, 217–248. doi:10.1098/rsta.1972.0008

MacFadden, B. J., and Hulbert, R. C. (1988). Explosive speciation at the base of the adaptive radiation of Miocene grazing horses. *Nature* 336, 466–468. doi:10.1038/336466a0

Merriam, J. C., and Sinclair, W. J. (1906). *Tertiary faunas of the John Day region*. University of California Publications on Geological Sciences, Vol. 5, 171–205.

Mix, H. T., and Chamberlain, C. P. (2014). Stable isotope records of hydrologic change and paleotemperature from smectite in Cenozoic western North America. *Geochem. Cosmochim. Acta* 141, 532–546. doi:10.1016/j.gca.2014.07.008

Mix, H. T., Caves Rugenstein, J. K., Reilly, S. P., Ritch, A. J., Winnick, M. J., Kukla, T., et al. (2019). Atmospheric flow deflection in the late Cenozoic Sierra Nevada. *Earth Planet Sci. Lett.* 518, 76–85. doi:10.1016/j.epsl.2019.04.050

Mix, H. T., Ibarra, D. E., Mulch, A., Graham, S. A., and Page Chamberlain, C. (2016). A hot and high Eocene Sierra Nevada. *Bull. Geol. Soc. Am.* 128, 531–542. doi:10.1130/B31294.1

Mix, H. T., Mulch, A., Kent-Corson, M. L., and Chamberlain, C. P. (2011). Cenozoic migration of topography in the North American Cordillera. *Geology* 39, 87–90. doi:10.1130/G31450.1

Mix, H. T., Winnick, M. J., Mulch, A., and Page Chamberlain, C. (2013). Grassland expansion as an instrument of hydrologic change in Neogene western North America. *Earth Planet Sci. Lett.* 377–378, 73–83. doi:10.1016/j.epsl.2013.07.032

Mulch, A., Graham, S. A., and Chamberlain, C. P. (2006). Hydrogen isotopes in Eocene river gravels and paleoelevation of the Sierra Nevada. *Science* 313, 87–89. doi:10.1126/science.1125986

Noble, D. (1972). Some observations of the cenezoic volcano-tectonic evolution of the great Basin, Western United States. *Earth Planet Sci. Lett.* 17, 142–150. doi:10.1016/0012-821x(72)90269-5

Pesek, M. E., Perez, N. D., Meigs, A., Rowden, C. C., and Giles, S. M. (2020). Exhumation timing in the Oregon cascade range decoupled from deformation, magmatic, and climate patterns. *Tectonics* 39, e2020TC006078. doi:10.1029/2020TC006078

Priest, G. R. (1990). Volcanic and tectonic evolution of the cascade volcanic Arc, Central Oregon. *J. Geophys. Res.* 95, 19583–19599. doi:10.1029/JB095iB12p19583

Reiners, P. W., Ehlers, T. A., Garver, J. I., Mitchell, S. G., Montgomery, D. R., Vance, J. A., et al. (2002). Late Miocene exhumation and uplift of the Washington cascade range. *Geology* 30, 767–770. doi:10.1130/0091-7613(2002)030<0767:lmeauo>2.0.co;2

Retallack, G. J. (2001). Cenozoic expansion of grasslands and climatic cooling. *J. Geol.* 109, 407–426. doi:10.1086/320791

Retallack, G. J. (2013). Global cooling by grassland soils of the geological past and near future. *Annu. Rev. Earth Planet Sci.* 41, 69–86. doi:10.1146/annurev-earth-050212-124001

Retallack, G. J. (2004). Late Oligocene bunch grassland and early Miocene sod grassland paleosols from central Oregon, United States. *Palaeogeogr., Palaeoclimatol., Palaeoecol.* 207, 203–237. doi:10.1016/S0031-0182(04)00042-2

Retallack, G. J. (1997). Neogene expansion of the North American Prairie. *Palaios* 12, 380–390. doi:10.2307/3515337

Retallack, G. J., Wynn, J. G., and Fremd, T. J. (2004). Glacial-interglacial-scale paleoclimatic change without large ice sheets in the Oligocene of central Oregon. *Geology* 32, 297–300. doi:10.1130/G20247.1

Robinson, P. T., Brem, G. F., Mckee, E. H., Survey, U. S. G., Road, M., Park, M., et al. (1984). John Day Formation of Oregon: a distal record of early cascade volcanism. *Geology* 12, 229–232. doi:10.1130/0091-7613(1984)12<229

Robson, S., Famoso, N., Davis, E., and Hopkins, S. (2019). First mesonychid from the Clarno Formation (Eocene) of Oregon, United States. *Palaeontol. Electron.* 22, 1–13. doi:10.26879/856

Roe, G. H. (2005). Orographic precipitation. *Annu. Rev. Earth Planet Sci.* 33, 645–671. doi:10.1146/annurev.earth.33.092203.122541

Salati, E., Dall'Olio, A., Matsui, E., and Gat, J. R. (1979). Recycling of water in the Amazon Basin: an isotopic study. *Water Resour. Res.* 15, 1250–1258. doi:10.1029/WR015i005p01250

Samuels, J. X., Albright, L. B., and Fremd, T. J. (2015). The last fossil primate in North America, new material of the enigmatic Ekgmowechashala from the Arikareean of Oregon. *Am. J. Phys. Anthropol.* 158, 43–54. doi:10.1002/ajpa.22769

Schwartz, J. J., Snoke, A. W., Frost, C. D., Barnes, C. G., Gromet, L. P., and Johnson, K. (2010). Analysis of the Wallowa-Baker terrane boundary: implications for tectonic accretion in the Blue Mountains province, northeastern Oregon. *Geol. Soc. Am. Bull.* 122, 517–536. doi:10.1130/B26493.1

Sharp, Z. D. (1990). A laser-based microanalytical method for the *in situ* determination of oxygen isotope ratios of silicates and oxides. *Geochem. Cosmochim. Acta* 54, 1353–1357. doi:10.1016/0016-7037(90)90160-M

Sheppard, S., and Gilg, H. (1996). Stable isotope geochemistry of clay minerals. *Clay Miner.* 31, 1–24. doi:10.1180/claymin.1996.031.1.01

Siler, N., and Durran, D. (2016). What causes weak orographic rain shadows? insights from case studies in the Cascades and idealized simulations. *Am. Meteorol. Soc.* 73, 4077–4099. doi:10.1175/JAS-D-15-0371.1

Sinclair, W. J. (1905). *New or imperfectly known rodents and ungulates from the John Day Series*. Berkeley, CA: University of California Publications on Geological Sciences, Vol. 4, 125–143.

Sjostrom, D. J., Hren, M. T., Horton, T. W., Waldbauer, J. R., and Chamberlain, C. P. (2006). Stable isotopic evidence for a pre–late Miocene elevation gradient in the Great Plains–Rocky Mountain region, United States. *Geol. Soc. Am. Spec. Pap.* 398, 309–319. doi:10.1130/2006.2398(19)

Smiley, C. (1963). *The Ellensburg flora of Washington*. Berkeley, CA University of California Publications on Geological Sciences, Vol. 35, 159–276.

Smith, G. A. (1986). Simtustus Formation: paleogeographic and stratigraphic significance of a newly defined Miocene unit in the Deschutes basin, central Oregon. *Oregon Geol.* 48, 63–72.

Smith, R. B. (1979). "The influence of mountains on the atmosphere," in *Advances in geophysics*, Editor B. Saltzman (New York, NY: Elsevier).

Smith, R. B., and Barstad, I. (2004). A linear theory of orographic precipitation. *J. Atmos. Sci.* 61, 1377–1391. doi:10.1175/1520-0469(2004)061<1377:altoop>2.0.co;2

Sonntag, C., Rozanski, K., Münnich, K., and Jacob, H. (1983). "Variations of deuterium and oxygen-18 in continental precipitation and groundwater and their causes," in *Variations in the Global Water Budget*, Editors A. Street-Perrott, M. Beran, and R. Ratcliffe (D. Reidel Publishing Company), 107–124.

Swanson, D., and Robinson, P. (1968). *Base of the John Day Formation in and near the Horse Heaven mining district, north-central Oregon*. Washington, D.C.: U.S. Geological Survey Professional Paper, 154–161.

Takeuchi, A. (2007). Decoupling the ancient hydrologic system from the modern. Thesis.

Takeuchi, A., and Larson, P. B. (2005). Oxygen isotope evidence for the late Cenozoic development of an orographic rain shadow in eastern Washington, United States. *Geology* 33, 313–316. doi:10.1130/G21335.1

Takeuchi, A., Hren, M. T., Smith, S. V., Chamberlain, C. P., and Larson, P. B. (2010). Pedogenic carbonate carbon isotopic constraints on paleoprecipitation: evolution of desert in the Pacific Northwest, United States, in response to topographic development of the Cascade Range. *Chem. Geol.* 277, 323–335. doi:10.1016/j.chemgeo.2010.08.015

Vho, A., Lanari, P., and Rubatto, D. (2019). An internally-consistent database for oxygen isotope fractionation between minerals. *J. Petrol.* 60, 2101–2129. doi:10.1093/petrology/egaa001

White, J. D., and Robinson, P. T. (1992). Intra-arc sedimentation in a low-lying marginal arc, Eocene Clarno Formation, central Oregon. *Sediment. Geol.* 80, 89–114. doi:10.1016/0037-0738(92)90034-O

Winnick, M. J., Chamberlain, C. P., Caves, J. K., and Welker, J. M. (2014). Quantifying the isotopic 'continental effect'. *Earth Planet Sci. Lett.* 406, 123–133. doi:10.1016/j.epsl.2014.09.005

Woodburne, M. O., and Robinson, P. T. (1977). A new late hemingfordian mammal fauna from the John Day Formation, Oregon, and its stratigraphic implications. *J. Paleontol.* 51, 750–757.

Zachos, J., Pagani, M., Sloan, L., Thomas, E., and Billups, K. (2001). Trends, rhythms, and aberrations in global climate 65 Ma to present. *Science* 292, 686–693. doi:10.1126/science.1059412

Conflict of Interest: The authors declare that the research was conducted in the absence of any commercial or financial relationships that could be construed as a potential conflict of interest.

frontiers in Earth Science

MINI REVIEW
published: 18 February 2021
doi: 10.3389/feart.2021.624542

How Can Climate Models Be Used in Paleoelevation Reconstructions?

Svetlana Botsyun and Todd A. Ehlers*

Department of Geosciences, University of Tübingen, Tübingen, Germany

Paleoelevation reconstructions derived from proxy data such as stable oxygen isotope records in terrestrial archives have been determined for Cenozoic mountain ranges around the world. Recent studies have highlighted that a variety of paleoclimate processes can contribute to the isotopic composition of a measured precipitation ($\delta^{18}O_p$) signal used in elevation reconstructions. These processes can include: regional, global, and topographic variations in paleotemperature; environmental conditions of an air mass before orographic ascent; evapotranspiration; water vapor recycling; and changes in the vapor source. In some cases, these processes can overprint the elevation signal sought in proxy data and preclude robust elevation reconstructions. Recent advances in isotope tracking climate models allow us to estimate paleoclimate changes during orogen development and associated changes in paleo $\delta^{18}O_p$ due to both climate and topographic changes. These models account for adiabatic and non-adiabatic temperature changes, relative humidity variations, changing continental evapotranspiration, vapor recycling, vapor source changes, etc. Modeling strategies using high-resolution isotopes-enabled General Circulation Models (iGCMs) together with time-specific boundary conditions and variable topography provide a powerful tool for enhancing elevation reconstructions from $\delta^{18}O_p$ proxy data. In this review, we discuss the principles, benefits and caveats of using iGCMs for interpreting isotopic records from natural archives for paleoelevation reconstructions. We also highlight future challenges for the application of iGCMs to paleoaltimetry proxy data that open up new avenues for research on tectonic-climate interactions.

Keywords: paleoaltimetry, oxygen isotopes ($\delta^{18}O$), isotope-enabled GCM, paleoelevation reconstruction, stable oxygen isotope composition, tectonic-climatic interaction, proxy interpretation, atmosphere circulation modeling

OPEN ACCESS

Edited by:
Heiko Pingel,
University of Potsdam, Germany

Reviewed by:
Gilles Ramstein,
UMR8212 Laboratoire des Sciences du Climat et de l'Environnement, France
Michael Hren,
University of Connecticut, United States

****Correspondence:***
Svetlana Botsyun
botsyun.svetlana@gmail.com

Specialty section:
This article was submitted to Quaternary Science, Geomorphology and Paleoenvironment, a section of the journal Frontiers in Earth Science

Received: *31 October 2020*
Accepted: *13 January 2021*
Published: *18 February 2021*

Citation:
Botsyun S and Ehlers TA (2021) How Can Climate Models Be Used in Paleoelevation Reconstructions?. Front. Earth Sci. 9:624542. doi: 10.3389/feart.2021.624542

INTRODUCTION

Quantitative paleoelevation techniques based on proxy data include approaches such as stable isotopes (e.g., $\delta^{18}O$, δD) measured in terrestrial deposits, paleofloral and faunal findings and their physiognomic characteristics, and clumped isotope (Δ_{47}) paleothermometry. These techniques (and others) have been extensively applied to various mountain ranges such as the Himalayas and Tibetan Plateau (Rowley and Currie, 2006; Gébelin et al., 2013; Ding et al., 2014), the North America Cordillera (Chamberlain et al., 2012; Gébelin et al., 2012; Cassel et al., 2014), the Andes and Andean Plateau (Mulch et al., 2010; Garzione et al., 2017) for elevation reconstructions throughout the Cenozoic, ranging from the Paleocene and Eocene (e.g., Ding et al., 2014) up to the Pleistocene (e.g., Hoke et al., 2014). Oxygen isotope paleoaltimetry is one of the most widely applied techniques and is based on a progressive decrease in the $\delta^{18}O$ value of precipitation ($\delta^{18}O_p$) with elevation during the

topographic (i.e., orographic) ascent of an air mass. This technique assumes Rayleigh distillation of an air mass under equilibrium conditions and without local evaporation or advection of additional vapor from outside the system (Rozanski et al., 1993; Gat, 1996).

Oxygen isotope paleoaltimetry uses $\delta^{18}O$ preserved in pedogenic or lacustrine carbonates (hereafter referred to as $\delta^{18}O_c$) as a proxy for paleoelevation. Interpretation of measured $\delta^{18}O_c$ generally requires two steps. For the first step, the reconstruction of paleoprecipitation $\delta^{18}O$ ($\delta^{18}O_{pp}$) using the calcite-water fractionation coefficients depend on the carbonate formation temperature as described through the equilibrium between calcite and water $\delta^{18}O$ (Kim and O'Neil, 1997). Paleoaltimetry estimates based on $\delta^{18}O$ alone, without independent information on paleotemperatures from other proxies or a paleoclimate model, depend on assumptions made about the paleoelevation and temperature (global and regional) changes relative to the modern. Knowledge of these paleo-conditions is challenging to come by. Moreover, if a surface temperature is assumed, then the calculation of paleoelevation from the proxy involves circular reasoning. This is because the temperature used at the point of interest depends on the elevation through the temperature lapse rate and often the chosen coefficients from the equations in Kim and O'Neil (1997) already implies high elevations.

For the second step, the reconstructed $\delta^{18}O_{pp}$ must be attributed to a paleoelevation using a $\delta^{18}O_{pp}$-elevation relationship (the "isotopic lapse rate") in a reference to low-elevation $\delta^{18}O$. A common approach (largely due to it's simplicity) is to assume that the modern isotopic lapse rate measured from precipitation in an elevation-transect of stations (e.g., Gonfiantini et al., 2001; Fiorella et al., 2015), or simulated using a one-dimensional thermodynamic model for $\delta^{18}O_p$ composition based on the Rayleigh distillation, can be used to predict changes in the $\delta^{18}O_p$ response to changes in temperature, and the relative humidity of air parcels during orographic ascent (Rowley et al., 2001; Rowley and Garzione, 2007). This approach assumes the isotopic lapse rate at the time of carbonate formation not to change over millions of years. Thus, both of the previous steps rely on several assumptions regarding the contribution (if any) of global and regional climate change to $\delta^{18}O$ and the stationarity of the $\delta^{18}O_{pp}$-elevation relationship throughout geologic time.

However, numerous recent studies have shown that a range of atmospheric processes are important for the interpretation of $\delta^{18}O_{pp}$. For example, hemispheric-scale atmospheric circulation and associated teleconnections (Schneider and Noone, 2007; Takahashi and Battisti, 2007; Pausata et al., 2011), moisture transport changes (Ehlers and Poulsen, 2009; Poulsen et al., 2010), evapotranspiration and water vapor recycling within continental interiors (Risi et al., 2013; Chamberlain et al., 2014), and shifts in precipitation amount and ratios of convective-to-large-scale precipitation (Lee and Fung, 2008; Feng et al., 2013; Botsyun et al., 2019a) all can affect $\delta^{18}O_{pp}$. The effect of these complicating processes on isotopic lapse rates range from insignificant to major, up to the extent of flattening or inverting the paleo isotopic lapse rate relative to the modern (e.g., Moran et al., 2007). Thus, despite the intriguing potential of proxy records to reconstruct the paleoelevation history of orogens, the interpretation of the data requires several assumptions about the congruence between modern and paleo atmospheric processes and climate which may, or may not, be correct (e.g., Starke et al., 2020). Therefore, a rigorous interpretation of paleoelevations requires evaluating these assumptions on a case-by-case basis, which in practice is not always simple. One promising methods to address these concerns is an application of climate models for reconstructing time-specific temperatures, $\delta^{18}O_p$ and isotopic lapse rates for adequate interpretation of $\delta^{18}O_c$ signal.

Basic Principles of Isotope Tracking Climate Models. . . in a Nutshell

Climate (and paleoclimate) models are typically based on a set of governing primitive equations for conservation of mass, energy, and momentum. These equations are solved simultaneously by discretizing (gridding) the surface of the earth and atmosphere and applying a numerical model. If only an atmospheric General Circulation Model (GCM) is used (as opposed to a coupled ocean-atmosphere GCM) then solving these equations also requires application of boundary conditions such as sea-surface temperatures, solar radiation, and also material properties of the atmosphere and land surface such as greenhouse gas concentrations, topography, vegetation/ice cover, sea-ice extent, soil properties, etc. Given the physics-based approach of these models, they can be used for diverse purposes including weather prediction/forecasts, future climate predictions, or paleoclimate predictions so long as the appropriate boundary conditions, and land surface properties are known. Thus, paleoclimate modeling studies that are applied to paleoelevation proxy data interpretation are "simply" applying well used and tested climate models from the atmospheric sciences community, with the caveat that they require a means for predicting the isotopic composition of precipitation, discussed next.

Isotopic Modeling and (Non-)stationarity of $\delta^{18}O_p$-Lapse Rate

Climate modeling has been extensively applied to study the impact of mountain surface uplift on atmospheric physics and dynamics (Ruddiman and Kutzbach, 1989; Broccoli and Manabe, 1992; Sepulchre et al., 2006). The implementation of water isotope tracking in simple climate models (Dansgaard, 1964) and further into GCMs (Joussaume et al., 1984) enabled calculation of the atmospheric, land surface, and topographic processes impacting $\delta^{18}O_p$. Since the development of iGCMs, a diverse range of studies have been conducted documenting the sensitivity of $\delta^{18}O_p$ to climate change resulting from variations in pCO_2 (Poulsen et al., 2007; Poulsen and Jeffery, 2011), sea surface temperatures (SSTs) (Sturm et al., 2007), sea level variations (Poulsen et al., 2007), and paleogeography (Sewall and Fricke, 2013; Roe et al., 2016; Botsyun et al., 2019a), and much more (Risi, 2009; Sturm et al., 2010 and references herein).

The previous iGCM based studies have shown, among other things, that present-day isotopic lapse rates are not always suitable for paleoelevation reconstructions. First, modeling studies have shown spatial non-stationarity of the isotopic lapse rates. For example, Galewsky (2009) uses an idealized, fully nonlinear atmospheric model to evaluate the effects of stratified atmospheric flows on orographic precipitation isotopic ratios, with the aim of improving the foundation for interpreting proxy records used for paleoelevation studies. He showed that existing Rayleigh condensation models are strictly applicable for paleoaltimetry studies only when the atmosphere is not stratified. Changes in climate or the horizontal terrain aspect ratio can change precipitation isotopic ratios at least as much as changes in surface elevation (Galewsky, 2009), suggesting that proxy records must be interpreted within a broad context of climate variability and landscape evolution.

Second, iGCMs have demonstrated the impact of global climate change on $\delta^{18}O_p$ and the non-stationarity of isotopic lapse rates through time. For example, in climate simulations with elevated CO_2 concentrations, the middle troposphere undergoes preferential moistening and warming, which weakens vertical stratification and gives rise to shallower lapse rates (Poulsen and Jeffery, 2011). Li et al. (2016) identified spatial and temporal variations in simulated isotopic lapse rates for different high relief zones along the flanks of the Tibetan plateau during Late Quaternary climates. They found that the precipitation weighted annual mean $\delta^{18}O_p$ lapse rate at the Himalaya is about 0.4‰/km larger during the Middle Holocene and 0.2‰/km smaller during the Last Glacial Maximum than during pre-industrial times. These changes are large enough to impact the interpretation of proxy data (Li et al., 2016). Furthermore, results from Botsyun et al. (2020) predict a similar magnitude (4–5‰ relative to present day) of change in $\delta^{18}O_p$ resulting from the topographic development of the European Alps and paleoclimate change during the Pliocene and the Last Glacial Maximum.

Third, modeling studies show that regional (e.g. continental or subcontinental scale) climate changes result from mountain surface uplift and also have a potential impact on $\delta^{18}O_p$. For example, previous work has shown that Andean Plateau surface uplift resulted in the onset of convective precipitation (Poulsen et al., 2010) following a switch of the prevalent moisture source and associated transport paths from the South Pacific to the Equatorial Atlantic and initiation/strengthening of the South American Low Level Jet (Ehlers and Poulsen, 2009; Insel et al., 2010). These studies suggest that high precipitation rates enhance the isotope amount effect, leading to more negative $\delta^{18}O_p$ at high elevations and, thus, increases in the isotopic lapse rate. In agreement with this result, experiments with reduced elevations of the Andean Plateau by Insel et al. 2012 show that use of present-day isotopic lapse rate can lead to an underestimation of surface elevation by 2,000 m.

Regional climate changes associated with surface uplift have also been shown to impact $\delta^{18}O_p$ across the North American Cordillera (Feng et al., 2013) and Tibetan Plateau (Botsyun et al., 2016; Shen and Poulsen, 2019). For both these areas it was suggested that neither the common assumption that isotopic fractionation occurs primarily through rainout following Rayleigh distillation, nor the application of modern empirical $\delta^{18}O_p$ lapse rates to past environments, are valid. Shifts in atmospheric processes, including shifts in local precipitation type between convective and large-scale rain and between rain and snow, intensification of low-level vapor recycling particularly on leeward slopes, development of air mass mixing and changes in wind direction and moisture source changes all contributed to the deviations of the isotopic signal.

Finally, the robustness of applying the present-day isotopic lapse rate to interpret Eocene Tibetan Plateau proxy data was recently tested in work of Botsyun et al. (2019a). In this study, an iGCM with time specific Eocene boundary conditions was applied to assess the influence of changing Eocene paleogeography on climate and $\delta^{18}O_p$ signals. The authors found that a combination of increased convective precipitation, a mixture of air masses of different origin, widespread aridity, and an intensified water recycling resulted in a reversed isotopic lapse rate across the southern flank of the Tibetan Plateau. These processes resulted in the most negative $\delta^{18}O_p$ occurring over northern India and increased $\delta^{18}O_p$ northward (**Figure 1**). Taken together, these results indicate that standard stable isotope paleoaltimetry methods are not applicable in Eocene Asia and an alternative method, which takes into account paleo isotopic lapse rates, should be developed.

In recent years, iGCMs have been extensively applied for $\delta^{18}O$ proxy interpretation by using model-derived: 1) $\delta^{18}O_p$ lapse rates for various elevation scenarios; and 2) $\delta^{18}O_c$ and soil temperatures for time-specific simulations including various paleogeographies and paleotopographies. Fan et al. (2017) and Gao and Fan (2018) used an iGCM-derived $\delta^{18}O_p$-elevation gradient from Feng et al. (2013) to constrain the paleoelevations of the Cordillera orogenic system (Uinta Mountains, United States). This approach allows them to consider vapor mixing in the mountain flank and the warm climate during the Paleogene. Sundell et al. (2019) interpreted observed $\delta^{18}O_p$ across the Peruvian central Andes using different lapse rates including the thermodynamically-derived non-linear model from Rowley et al. (2001), an empirical approach from Quade et al. (2007), and reconstructed isotopic lapse rate using a climate model. Experiments with 25, 50, 75, and 100% of Andean elevations from Insel et al. (2012) and experiments with 50 and 100% Andean elevation from Poulsen et al. (2010) together with climate correction are used for the data interpretation.

Botsyun et al. (2019a) designed experiments with variable Tibetan Plateau elevations and Eocene paleogeography to compare simulated $\delta^{18}O_c$ values with previously published data. These sensitivity tests identified that the best model-data fit corresponds to a low Tibetan Plateau in the Eocene. The authors showed that quantitative estimates of paleoaltimetry from stable isotopes depend on the outcome of a climate model, which in turn used paleoaltimetry, as input. This means that paleoaltimetry and paleoclimate models need to be iteratively tuned until the input elevation and the output relations

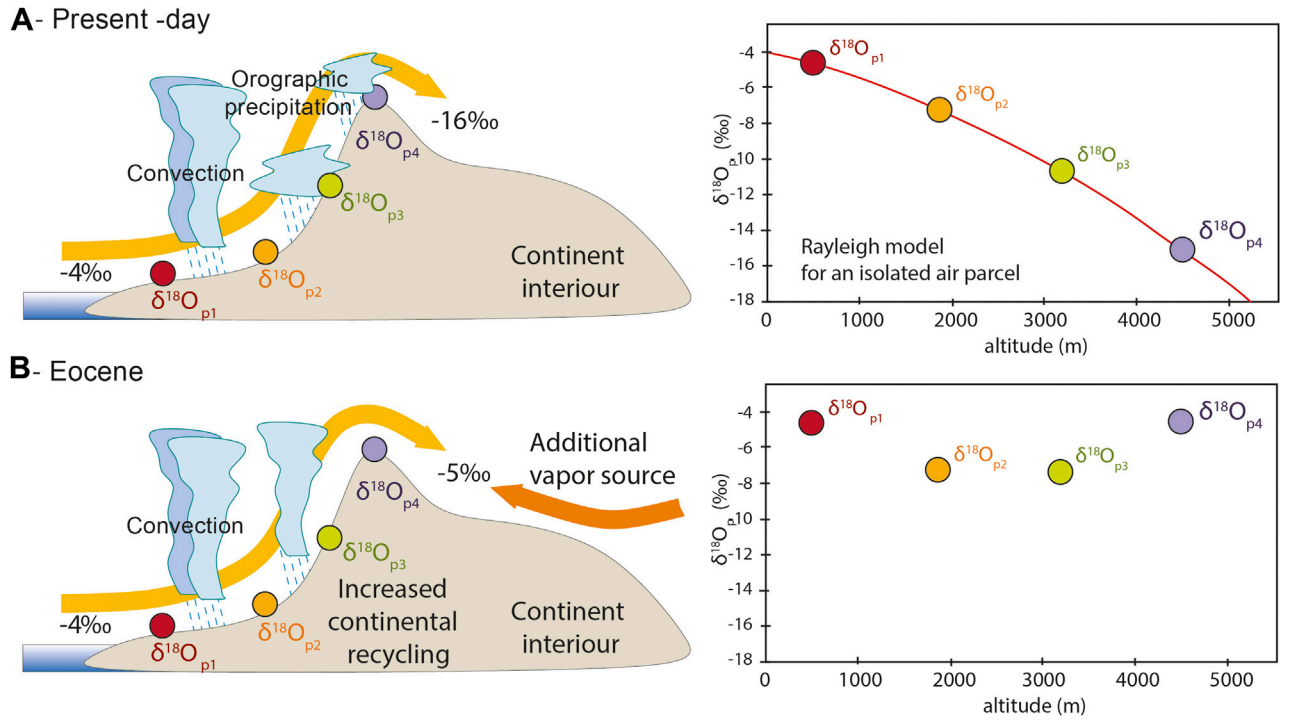

FIGURE 1 | Schematic representation of the processes in the atmosphere and over land that potentially contribute to a $\delta^{18}O_p$ signal resulting in: **(A)** an isotopic lapse rate according to a Rayleigh distillation model for an isolated air parcel; and **(B)** flattened or inversed isotopic lapse rate. Examples of proxy data interpretations based on iGCM results.

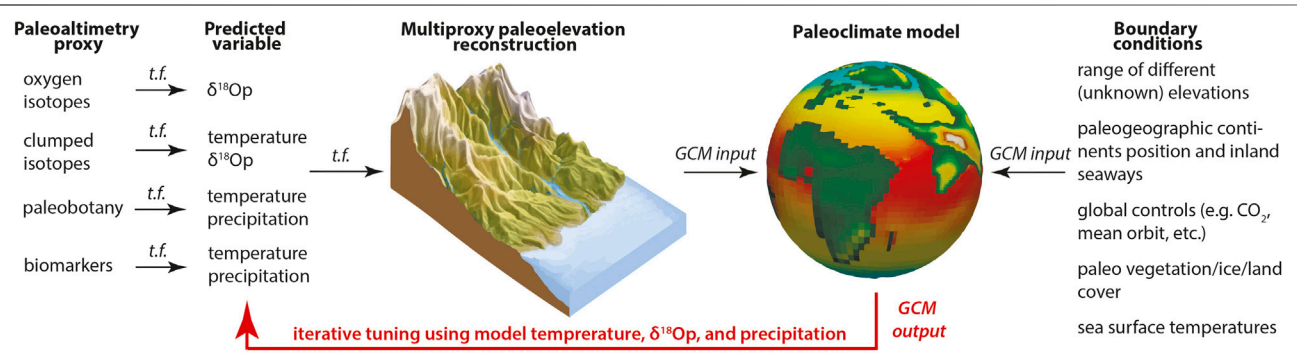

FIGURE 2 | Principal scheme showing application of a paleoclimate model for paleoelevation reconstructions. *t.f.*—transfer function.

between isotopic ratio and elevation are mutually consistent (**Figure 2**).

Limits of climate modeling technique to paleoaltimetry studies

From a stable isotope paleoaltimetry point of view the application of iGCMs have several limitations. The key caveats of climate modeling approach are linked to: 1) the limited ability of the model to simulate $\delta^{18}O$ patterns over regions with complex topography due to the complexity of natural processes and limited scope of model parameterizations; 2) uncertainties in precipitation and $\delta^{18}O$ changes in monsoonal areas; 3) limited computational resources for high-resolution fully-coupled ocean-atmosphere simulations; 4) uncertainties in the choice of boundary conditions (e.g. **Figure 2**), 5) relatively low model spatial resolution, and 6) a "social" challenge whereby the most fruitful applications involve a collaboration between proxy-oriented and model-oriented scientists.

Examples supporting the first point are as follows. Convective processes are known to have a significant imprint on the stable oxygen isotope composition of precipitation, especially in the tropics (Risi et al., 2008). However, convective processes in a iGCM strongly depend on the parameterization applied (Hourdin et al., 2006). Large uncertainties also exist in iGCMs

depending on the representation of water stable isotopes parameterizations used for the isotopic exchanges between vapor and rain droplets during descent and the degree of partial reevaporation (Lee and Fung, 2008; Risi et al., 2010). Risi et al. (2010) demonstrated a sensitivity of modeling results to evaporation, especially in dry regions where this process is prevalent. In addition, the isotopic equilibration time of raindrops is drop-size dependent, with smaller equilibration time for small raindrops (Lee and Fung, 2008). Given this, if raindrop size is not taken into account an underestimation of equilibration times for heavy rains with big raindrops could be expected. Additional potential limitations of using iGCMs include complexity associated with realistic representation of soils, evapotranspiration schemes, geochemistry, vegetation, and clouds (Risi et al., 2010; Haese et al., 2013; Rio and Hourdin, 2015). These challenges are active areas of research in the climate modeling community and improvements in model parameterizations are always occurring.

The response of the hydrologic cycle to the climate forcing in monsoon areas vary depending on the model applied and, even for future climates, monsoons amplification has not been shown as a strong feature (Wang et al., 2020). Furthermore, the interpretation of water isotope variations and their link to monsoon is not straightforward even for recent climates (e.g., Middle Holocene) when there is no problem of mountain elevation change (Lin et al., 2019). Further uncertainties are associated with the application of atmosphere-only climate model with no feedbacks between the atmosphere, vegetation and the ocean. Use of modeling techniques with SSTs and sea ice extension prescribed from coupled simulations to run a separate high resolution atmospheric model suffer from not taking into account ocean variability and its feedback to the atmosphere. Moreover, vegetation can also play an important role in isotopic changes through not only evapotranspiration changes, but also through changing surface albedo feedback. Given this coupled high-resolution ocean-atmosphere and dynamic vegetation modeling approaches are preferred, but extremely challenging to conduct. However, usage of high-resolution atmosphere-only iGCMs that use previous coarser resolution coupled ocean-atmosphere models for boundary conditions have been shown to be a good trade-off between the high-resolution necessary to capture observed spatial, seasonal, and daily variations of $\delta^{18}O_p$ and computation resources required (Botsyun et al., 2019b).

Furthermore, paleoclimate studies are sensitive to the paleogeographical reconstruction used (e.g., Baatsen et al., 2016). Producing paleogeographic reconstructions for climate models is time-consuming and elaborate. For example, paleoclimate models frequently use reconstructions where the latest state-of-the-art of plate tectonic, crustal and paleomagnetic reconstructions, paleotopography, paleobathymetry, or vegetation distribution have not yet been incorporated. The availability of realistic Cenozoic boundary conditions, such as sea-surface temperatures, is also limited, unless a time-consuming coupled ocean-atmosphere model is used. Finally, coarse model resolutions used in iGCMs to reduce simulation time often prevent accurate representation of smaller-scale topographic features such that explicit simulation of air masses ascending mountain topography are only grossly represented (Hourdin et al., 2006; Haese et al., 2013). Despite the above caveats, numerous studies have applied iGCMs to capture regional changes in $\delta^{18}O_p$ through time, and comparison of model predicted $\delta^{18}O_p$ to observations (e.g., Global Network of Isotopes in Precipitation (GNIP) stations data) to understand model limitations are commonly conducted when applying models to new locations.

When are state-of-the-art climate models useful and when can simpler approaches be applied?

Despite the previously mentioned limitations associated with iGCMs, applications of climate models to enhance proxy interpretations are gaining success (e.g., van Hinsbergen and Boschman, 2019). Modeling studies have shown that simpler (i.e., non-iGCM based) paleoaltimetry approaches are valid when the Rayleigh distillation process is dominant. However, iGCMs have provided several examples of when atmospheric processes lead to $\delta^{18}O_p$ variations that are different, and sometimes opposite, of those estimated using Rayleigh distillation models of moist adiabatic condensation. For example, Shen and Poulsen (2019) used the ECHAM5-wiso model to show that Rayleigh distillation is only prevailing in the monsoonal regions of the Himalayas when the mountains are high. In contrast, when orogen topography is lower, local surface recycling and convective processes become important. This is due to weakened forced ascent causing weaker Asian monsoons. In this example, applying a standard paleoaltimetry approach is not valid. Similarly, over the North America Cordillera changes in atmospheric processes have been shown to impact $\delta^{18}O_p$ and violate the common assumption that isotopic fractionation occurs through rainout following Rayleigh distillation (Feng et al., 2013). In this example, the atmospheric changes included shifts in local precipitation type between convective and large-scale rain and also between rain and snow, intensification of low-level vapor recycling on leeward slopes, and development of air mass mixing and changes in wind direction and moisture source. Given the uncertainty of when, or when not, a one-dimensional Rayleigh distillation model adequately represents moisture transport, the significance of lateral vapor mixing, or temporal changes in the isotopic lapse rate, the application of iGCMs is recommended (e.g., Li et al., 2016) as an initial step to characterize these processes rather than assuming they are insignificant.

There are, however, observational (non-iGCM based) techniques that have emerged to help circumvent the effects of changing atmospheric processes on paleoaltimetry data. One such technique is the δ-δ approach. This approach assumes that a baseline sets of samples collected from a low elevation stratigraphic succession provides a reference frame for interpreting higher elevation samples. The implicit assumption is that any regional or global climate change will affect stable isotopes records from both (low and high elevation) localities equally if looking at the same time interval. If true, then the difference between the two records can be interpreted as

resulting from elevation change, thereby enabling a paleoelevation reconstruction (e.g., Campani et al., 2012; Gébelin et al., 2012; Mulch, 2016; Pingel et al., 2020). While the δ-δ approach holds promise and there are geographic locations where this may work well, the approach does require that a suitable baseline location has been chosen–which is difficult to do without prior knowledge. In recent work by Botsyun et al. (2020), an iGCM was used to explore the $\delta^{18}O_p$ signal of Cenozoic topographic and paleoclimatic change in the European Alps. The results of their study suggest that the δ-δ approach is applicable for the case of the European Alps under the condition that the low-elevation reference section measured hasn't experienced climate change, and that it is located far enough away and upwind from the area of interest to not experience climate changes associated with orogenic uplift.

In summary, when working with proxy records from "non-simple" locations where Rayleigh distillation assumptions may not be valid, the modern paleoelevation community is well equipped to make a step forward to more advanced reconstructions involving isotope enabled climate modeling. However, doing this requires a collaboration between proxy and climate modeling communities to evaluate how simple, or complex, the $\delta^{18}O_p$ response is to changing atmospheric processes. In this review, we have highlighted how application of climate models in conjunction with geological/geochemical data provides a powerful tool to incorporate climatic change effects into the analysis of paleoaltimetry work. Moreover, paleobotanic data and stable oxygen isotope paleoaltimetry can be reconciled using climate models. Further model-data comparison studies that combine multiple proxy types, together with iGCM modeling efforts testing the impact of complex topography structures as well as atmospheric parameterizations on $\delta^{18}O$ are paving the way for more accurate and robust paleoelevation estimates in the decades to come.

AUTHOR CONTRIBUTIONS

SB and TAE conceived and wrote the manuscript.

FUNDING

This study was supported as part of the German priority research program Mountain Building Processes in 4D (MB4D) grant (EH329/18-1 and 23-1) to TAE.

REFERENCES

Baatsen, M., van Hinsbergen, D. J. J., von der Heydt, A. S., Dijkstra, H. A., Sluijs, A., Abels, H. A., et al. (2016). Reconstructing geographical boundary conditions for palaeoclimate modelling during the Cenozoic. *Clim. Past* 12, 1635–1644. doi:10.5194/cp-12-1635-2016

Botsyun, S., Sepulchre, P., Risi, C., and Donnadieu, Y. (2016). Impacts of Tibetan Plateau uplift on atmospheric dynamics and associated precipitation $\delta^{18}O$. *Clim. Past* 12, 1401–1420. doi:10.5194/cp-12-1401-2016

Botsyun, S., Sepulchre, P., Donnadieu, Y., Risi, C., Licht, A., and Caves Rugenstein, J. K. (2019a). Revised paleoaltimetry data show low Tibetan Plateau elevation during the Eocene. *Science* 363 (6430), eaaq1436. doi:10.1126/science.aaq1436

Botsyun, S., Sepulchre, P., Donnadieu, Y., Risi, C., Licht, A., and Caves Rugenstein, J. K. (2019b). Response to comment on "Revised paleoaltimetry data show low Tibetan Plateau elevation during the Eocene". *Science*, 365 (6459), eaax8990. doi:10.1126/science.aax8990

Botsyun, S., Ehlers, T. A., Mutz, S. G., Methner, K., Krsnik, E., and Mulch, A. (2020). Opportunities and challenges for paleoaltimetry in "small" orogens: Insights from the European Alps. *Geophys. Res. Lett.*, e2019GL086046. doi:10.1029/2019GL086046

Broccoli, A. J., and Manabe, S. (1992). The effects of orography on midlatitude northern hemisphere dry climates. *J. Clim.* 5, 1181–1201. doi:10.1175/1520-0442(1992)005<1181:TEOOOM>2.0.CO;2

Campani, M., Mulch, A., Kempf, O., Schlunegger, F., and Mancktelow, N. (2012). Miocene paleotopography of the Central Alps. *Earth Planet. Sci. Lett.* 337–338, 174–185. doi:10.1016/j.epsl.2012.05.017

Cassel, E. J., Breecker, D. O., Henry, C. D., Larson, T. E., and Stockli, D. F. (2014). Profile of a paleo-orogen: High topography across the present-day basin and range from 40 to 23 Ma. *Geology* 42, 1007–1010. doi:10.1130/G35924.1

Chamberlain, C. P., Mix, H. T., Mulch, A., Hren, M. T., Kent-Corson, M. L., Davis, S. J., et al. (2012). The Cenozoic climatic and topographic evolution of the western North American Cordillera. *Am. J. Sci.* 312, 213–262. doi:10.2475/02.2012.05

Chamberlain, C. P., Winnick, M. J., Mix, H. T., Chamberlain, S. D., and Maher, K. (2014). The impact of Neogene grassland expansion and aridification on the isotopic composition of continental precipitation. *Global Biogeochem. Cycles* 28, 992–1004. doi:10.1002/2014GB004822

Dansgaard, W. (1964). Stable isotopes in precipitation. *Tellus* 16, 436–468. doi:10.1111/j.2153-3490.1964.tb00181.x

Ding, L., Xu, Q., Yue, Y., Wang, H., Cai, F., and Li, S. (2014). The Andean-type Gangdese Mountains: Paleoelevation record from the Paleocene-Eocene Linzhou Basin. *Earth Planet Sci. Lett.* 392, 250–264. doi:10.1016/j.epsl.2014.01.045

Ehlers, T. A., and Poulsen, C. J. (2009). Influence of Andean uplift on climate and paleoaltimetry estimates. *Earth Planet Sci. Lett.* 281, 238–248. doi:10.1016/j.epsl.2009.02.026

Fan, M., Constenius, K. N., and Dettman, D. L. (2017). Prolonged high relief in the northern Cordilleran orogenic front during middle and late Eocene extension based on stable isotope paleoaltimetry. *Earth Planet Sci. Lett.* 457, 376–384. doi:10.1016/j.epsl.2016.10.038

Feng, R., Poulsen, C. J., Werner, M., Chamberlain, C. P., Mix, H. T., and Mulch, A. (2013). Early Cenozoic evolution of topography, climate, and stable isotopes in precipitation in the North American Cordillera. *Am. J. Sci.* 313, 613–648. doi:10.2475/07.2013.01

Fiorella, R. P., Poulsen, C. J., Zolá, R. S. P., Barnes, J. B., Tabor, C. R., and Ehlers, T. A. (2015). Spatiotemporal variability of modern precipitation $\delta^{18}O$ in the central Andes and implications for paleoclimate and paleoaltimetry estimates. *J. Geophys. Res. Atmos.*, 1–27. doi:10.1002/2014JD022893

Galewsky, J. (2009). Orographic precipitation isotopic ratios in stratified atmospheric flows: Implications for paleoelevation studies. *Geology* 37, 791–794. doi:10.1130/G30008A.1

Gao, M., and Fan, M. (2018). Depositional environment, sediment provenance and oxygen isotope paleoaltimetry of the early Paleogene greater Green River Basin, southwestern Wyoming, U.S.A. *Am. J. Sci.* 318, 1018–1055. doi:10.2475/10.2018.02

Garzione, C. N., McQuarrie, N., Perez, N. D., Ehlers, T. A., Beck, S. L., Kar, N., et al. (2017). Tectonic evolution of the Central Andean plateau and implications for the growth of plateaus. *Annu. Rev. Earth Planet Sci.* 45, 529–559. doi:10.1146/annurev-earth-063016-020612

Gat, J. R. (1996). Oxygen and hydrogen isotopes in the hydrologic cycle. *Annu. Rev. Earth Planet Sci.* 24, 225–262. doi:10.1146/annurev.earth.24.1.225

Gébelin, A., Mulch, A., Teyssier, C., Page Chamberlain, C., and Heizler, M. (2012). Coupled basin-detachment systems as paleoaltimetry archives of the western North American Cordillera. *Earth Planet Sci. Lett.* 335–336, 36–47. doi:10.1016/j.epsl.2012.04.029

Gébelin, A., Mulch, A., Teyssier, C., Jessup, M. J., Law, R. D., and Brunel, M. (2013). The Miocene elevation of mount everest. *Geology* 41, 799–802. doi:10.1130/G34331.1

Gonfiantini, R., Roche, M. A., Olivry, J. C., Fontes, J. C., and Zuppi, G. M. (2001). The altitude effect on the isotopic composition of tropical rains. *Chem. Geol.* 181, 147–167. doi:10.1016/S0009-2541(01)00279-0

Haese, B., Werner, M., and Lohmann, G. (2013). Stable water isotopes in the coupled atmosphere-land surface model ECHAM5-JSBACH. *Geosci. Model Dev. (GMD)* 6, 1463–1480. doi:10.5194/gmd-6-1463-2013

Hoke, G. D., Liu-Zeng, J., Hren, M. T., Wissink, G. K., and Garzione, C. N. (2014). Stable isotopes reveal high southeast Tibetan Plateau margin since the Paleogene. *Earth Planet Sci. Lett.* 394, 270–278. doi:10.1016/j.epsl.2014.03.007

Hourdin, F., Musat, I., Bony, S., Braconnot, P., Codron, F., Dufresne, J. L., et al. (2006). The LMDZ4 general circulation model: climate performance and sensitivity to parametrized physics with emphasis on tropical convection. *Clim. Dynam.* 27, 787–813. doi:10.1007/s00382-006-0158-0

Insel, N., Poulsen, C. J., and Ehlers, T. A. (2010). Influence of the Andes Mountains on South American moisture transport, convection, and precipitation. *Clim. Dynam.* 35, 1477–1492. doi:10.1007/s00382-009-0637-1

Insel, N., Poulsen, C. J., Ehlers, T. A., and Sturm, C. (2012). Response of meteoric δ18O to surface uplift - implications for Cenozoic Andean Plateau growth. *Earth Planet. Sci. Lett.* 317–318, 262–272. doi:10.1016/j.epsl.2011.11.039

Joussaume, S., Sadourny, R., and Jouzel, J. (1984). A general circulation model of water isotope cycles in the atmosphere. *Nature* 311, 24–29. doi:10.1038/311024a0

Kim, S. T., and O'Neil, J. R. (1997). Equilibrium and nonequilibrium oxygen isotope effects in synthetic carbonates. *Geochem. Cosmochim. Acta* 61, 3461–3475. doi:10.1016/S0016-7037(97)00169-5

Lee, J. E., and Fung, I. (2008). "Amount effect" of water isotopes and quantitative analysis of post-condensation processes. *Hydrol. Process.* 22, 1–8. doi:10.1002/hyp.6637

Li, J., Ehlers, T. A., Werner, M., Mutz, S. G., Steger, C., and Paeth, H. (2016). Late quaternary climate, precipitation $\delta^{18}O$, and Indian monsoon variations over the Tibetan Plateau. *Earth Planet Sci. Lett.* doi:10.1016/j.epsl.2016.09.031

Lin, Y., Ramstein, G., Wu, H., Rani, R., Braconnot, P., Kageyama, M., et al. (2019). Mid-Holocene climate change over China: model–data discrepancy. *Clim. Past*, 15 (4), 1223–1249. doi:10.5194/cp-15-1223-2019

Moran, T. A., Marshall, S. J., Evans, E. C., and Sinclair, K. E. (2007). Altitudinal gradients of stable isotopes in lee-slope precipitation in the Canadian rocky mountains. *Arctic Antarct. Alpine Res.* 39, 455–467. doi:10.1657/1523-0430(06-022)[MORAN]2.0.CO;2

Mulch, A. (2016). Stable isotope paleoaltimetry and the evolution of landscapes and life. *Earth Planet. Sci. Lett.* 433, 180–191. doi:10.1016/j.epsl.2015.10.034

Mulch, A., Uba, C. E., Strecker, M. R., Schoenberg, R., and Chamberlain, C. P. (2010). Late Miocene climate variability and surface elevation in the central Andes. *Earth Planet Sci. Lett.* 290, 173–182. doi:10.1016/j.epsl.2009.12.019

Pausata, F. S. R., Li, C., Wettstein, J. J., Kageyama, M., and Nisancioglu, K. H. (2011). The key role of topography in altering North Atlantic atmospheric circulation during the last glacial period. *Clim. Past* 7, 1089–1101. doi:10.5194/cp-7-1089-2011

Pingel, H., Strecker, M. R., Mulch, A., Alonso, R. N., Cottle, J., and Rohrmann, A., (2020). Late Cenozoic topographic evolution of the Eastern Cordillera and Puna Plateau margin in the southern Central Andes (NW Argentina). *Earth Planet Sci. Lett.* 535, 116112. doi:10.1016/j.epsl.2020.116112

Poulsen, C. J., and Jeffery, M. L. (2011). Climate change imprinting on stable isotopic compositions of high-elevation meteoric water cloaks past surface elevations of major orogens. *Geology* 39, 595–598. doi:10.1130/G32052.1

Poulsen, C. J., Pollard, D., and White, T. S. (2007). General circulation model simulation of the $\delta^{18}O$ content of continental precipitation in the middle Cretaceous: a model-proxy comparison. *Geology* 35, 199–202. doi:10.1130/G23343A.1

Poulsen, C. J., Ehlers, T. A., and Insel, N. (2010). Onset of convective rainfall during gradual late Miocene rise of the central Andes. *Science* 328 (5977), 490–493. doi:10.1126/science.1185078

Quade, J., Garzione, C., and Eiler, J. (2007). Paleoelevation reconstruction using pedogenic carbonates. *Rev. Mineral. Geochem.* 66, 53–87. doi:10.2138/rmg.2007.66.3

Rio, C., and Hourdin, F. (2015). A thermal plume model for the convective boundary layer: Representation of cumulus clouds. *J. Atmos. Sci.* 72. doi:10.1175/2007JAS2256.1

Risi, C., Bony, S., and Vimeux, F. (2008). Influence of convective processes on the isotopic composition ($\delta^{18}O$ and δD) of precipitation and water vapor in the tropics: 2. Physical interpretation of the amount effect. *J. Geophys. Res. Atmos.* 113, 1–12. doi:10.1029/2008JD009943

Risi, C., Bony, S., Vimeux, F., and Jouzel, J. (2010). Water-stable isotopes in the LMDZ4 general circulation model: Model evaluation for present-day and past climates and applications to climatic interpretations of tropical isotopic records. *J. Geophys. Res. Atmos.* 115, 1–27. doi:10.1029/2009JD013255

Risi, C., Noone, D., Frankenberg, C., and Worden, J. (2013). Role of continental recycling in intraseasonal variations of continental moisture as deduced from model simulations and water vapor isotopic measurements. *Water Resour. Res.* 49, 4136–4156. doi:10.1002/wrcr.20312

Risi, C.. (2009). *Les isotopes stables de l'eau: applications à l'étude du cycle de l'eau et des variations du climat*. PhD thesis. Université Pierre et Marie Curie.

Roe, G. H., Ding, Q., Battisti, D. S., Molnar, P., Clark, M. K., and Garzione, C. N. (2016). A modeling study of the response of Asian summertime climate to the largest geologic forcings of the past 50 Ma. *J. Geophys. Res. Atmos.* 121, 5453–5470. doi:10.1002/2015JD024370

Rowley, D. B., and Currie, B. S. (2006). Palaeo-altimetry of the late Eocene to Miocene Lunpola basin, central Tibet. *Nature* 439, 677–681. doi:10.1038/nature04506

Rowley, D. B., and Garzione, C. N. (2007). Stable isotope-based paleoaltimetry. *Annu. Rev. Earth Planet Sci.* 35, 463–508. doi:10.1146/annurev.earth.35.031306.140155

Rowley, D. B., Pierrehumbert, R. T., and Currie, B. S. (2001). A new approach to stable isotope-based paleoaltimetry: implications for paleoaltimetry and paleohypsometry of the High Himalaya since the Late Miocene. *Earth Planet Sci. Lett.* 188, 253–268. doi:10.1016/S0012-821X(01)00324-7

Rozanski, K., Araguás-Araguás, L., and Gonfiantini, R. (1993). Isotopic patterns in modern global precipitation. *Clim. Change Cont. Isot. Rec.*, 1–36. doi:10.1029/GM078p0001

Ruddiman, W. F., and Kutzbach, J. E. (1989). Forcing of late Cenozoic northern hemisphere climate by plateau uplift in southern Asia and the American West. *J. Geophys. Res. Atmos.* 94, 18409–18427.

Schneider, D. P., and Noone, D. C. (2007). Spatial covariance of water isotope records in a global network of ice cores spanning twentieth-century climate change. *J. Geophys. Res. Atmos.* 112. doi:10.1029/2007JD008652

Sepulchre, P., Ramstein, G., Fluteau, F., Schuster, M., Tiercelin, J. J., and Brunet, M. (2006). Tectonic uplift and Eastern Africa aridification. *Science* 313, 1419–1423. doi:10.1126/science.1129158

Sewall, J. O., and Fricke, H. C. (2013). Andean-scale highlands in the Late Cretaceous Cordillera of the North American western margin. *Earth Planet Sci. Lett.* 362, 88–98. doi:10.1016/j.epsl.2012.12.002

Shen, H., and Poulsen, C. J. (2019). Precipitation $\delta^{18}O$ on the Himalaya–Tibet orogeny and its relationship to surface elevation. *Clim. Past* 15, 169–187. doi:10.5194/cp-15-169-2019

Starke, J., Ehlers, T. A., and Schaller, M. (2020). Latitudinal effect of vegetation on erosion rates identified along western South America. *Science* 367, 1358–1361. doi:10.1126/science.aaz0840

Sturm, C., Hoffmann, G., and Langmann, B. (2007). Simulation of the stable water isotopes in precipitation over South America: Comparing regional to global circulation models. *J. Clim.* 20, 3730–3750. doi:10.1175/JCLI4194.1

Sturm, C., Zhang, Q., and Noone, D. (2010). An introduction to stable water isotopes in climate models: benefits of forward proxy modelling for paleoclimatology. *Clim. Past* 6, 115–129.doi:10.5194/cp-6-115-2010

Sundell, K. E., Saylor, J. E., Lapen, T. J., and Horton, B. K. (2019). Implications of variable late Cenozoic surface uplift across the Peruvian central Andes. *Sci. Rep.* 9, 1–12. doi:10.1038/s41598-019-41257-3

Takahashi, K., and Battisti, D. S. (2007). Processes controlling the mean tropical pacific precipitation pattern. Part I: The Andes and the eastern Pacific ITCZ. *J. Clim.* 20, 3434–3451. doi:10.1175/JCLI4198.1

van Hinsbergen, D. J. J., and Boschman, L. M. (2019). How high were these mountains? *Science* 363, 928–929. doi:10.1126/science.aaw7705

Wang, B., Jin, C., and Liu, J. (2020). Understanding future change of global monsoons projected by CMIP6 models. *J. Clim.* 33 (15), 6471–6489. doi:10.1175/JCLI-D-19-0993.1

Conflict of Interest: The authors declare that the research was conducted in the absence of any commercial or financial relationships that could be construed as a potential conflict of interest.

frontiers in Earth Science

PERSPECTIVE
published: 25 February 2021
doi: 10.3389/feart.2021.623982

Tools for Comprehensive Assessment of Fluid-Mediated and Solid-State Alteration of Carbonates Used to Reconstruct Ancient Elevation and Environments

Miquela Ingalls[1]* *and Kathryn E. Snell*[2]

[1]Department of Geosciences, The Pennsylvania State University, University Park, PA, United States, [2]Department of Geological Sciences, University of Colorado, Boulder, CO, United States

Carbonates are ubiquitous in the rock record and provide a broad array of stable isotope-based paleoclimatic proxies (i.e., $\delta^{18}O$, $\delta^{13}C$, $\Delta^{17}O$, Δ_{47}, Δ_{48}) that provide information on stratigraphy, carbon cycling, temperature, hydrology, and the altitude of ancient land surfaces. Thus, carbonates are an essential archive of environmental and topographic histories of continental terranes. However, carbonate minerals are highly susceptible to post-depositional alteration of primary isotopic values via fluid-mediated and solid-state reactions. We propose a hierarchical suite of techniques to comprehensively assess alteration in carbonates, from essential and readily accessible tools to novel, high-resolution techniques. This framework provides a means of identifying preserved textures in differentially altered samples that contain high-value environmental information. To illustrate this progressive approach, we present a case study of Tethyan nearshore carbonates from the Paleocene Tso Jianding Group (Tibet). We demonstrate the utility of each technique in identifying chemical and crystallographic indicators of post-depositional alteration at progressively finer spatial scales. For example, secondary ionization mass spectrometry (SIMS) oxygen isotope maps of micrite and bioclasts reveal significant isotopic heterogeneity due to grain-scale water-rock exchange in textures that were labeled "primary" by optical inspection at coarser spatial resolution. Optical and cathodoluminescence microscopy should be the minimum required assessment of carbonate samples used in stable isotope analyses, but supplemented when necessary by SIMS, PIC mapping, and other yet untapped technologies that may allow distinction of primary and altered fabrics at finer spatial resolutions.

Keywords: carbonate alteration, carbonate diagenesis, oxygen isotope (δ18O), paleoaltimetry, petrography, clumped isotope thermometry

OPEN ACCESS

Edited by:
Alexis Licht,
University of Washington,
United States

Reviewed by:
David Bajnai,
University of Cologne, Germany
Justine Briard,
Université de Bourgogne, France
Fuyun Cong,
China University of Geosciences
Wuhan, China

***Correspondence:**
Miquela Ingalls
ingalls@psu.edu

Specialty section:
This article was submitted to Sedimentology, Stratigraphy and Diagenesis, a section of the journal Frontiers in Earth Science

Received: *30 October 2020*
Accepted: *07 January 2021*
Published: *25 February 2021*

Citation:
Ingalls M and Snell KE (2021) Tools for Comprehensive Assessment of Fluid-Mediated and Solid-State Alteration of Carbonates Used to Reconstruct Ancient Elevation and Environments. Front. Earth Sci. 9:623982. doi: 10.3389/feart.2021.623982

INTRODUCTION

Carbonate rocks provide an archive of geochemical information related to the climatic and tectonic setting of their depositional environment. In particular, oxygen isotopes of terrestrial carbonates ($\delta^{18}O_c$) have been used as a proxy for ancient rainwater ($\delta^{18}O_w$) in the field of stable isotope paleoaltimetry. The relationship between altitude and meteoric water composition is defined by the

orogressive distillation of the heavy isotopes of water (^{18}O, D) as a moisture source rains out over mountains ($\Delta\delta^{18}O_w = \delta^{18}O_{w,sample\ altitude} - \delta^{18}O_{w,sea\ level}$; Chamberlain and Poage, 2000; Rowley et al., 2001). This approach has enabled reconstructions of the tectonic evolution of the Andes, western North American Cordillera, Tibetan Plateau and other continental terranes (e.g., Rowley and Currie, 2006; Garzione, 2008; Chamberlain et al., 2012). Clumped isotope thermometry (T (Δ_{47})) advanced the use of carbonates for stable isotope paleoaltimetry by 1) facilitating direct calculations of $\delta^{18}O_w$ from primary $\delta^{18}O_c$ values, which reduces uncertainties on traditional $\delta^{18}O$ paleoaltimetry estimates by accounting for mineral formation temperature (e.g., Snell et al., 2014; Huntington et al., 2015; Ingalls et al., 2017; Ingalls et al., 2020), and 2) providing temperatures that can be used with lapse rates to provide an additional estimate of elevation that is independent of ancient precipitation isotopes (e.g., Huntington et al., 2010).

The paradox of carbonate stable isotope paleoaltimetry is the need for preservation of primary isotopic signatures in rocks that experienced the complex burial and thermal histories associated with regions of active tectonics. Carbonate minerals are highly susceptible to both water-rock and solid-state isotopic exchange during burial (e.g., Banner and Hanson, 1990; Passey and Henkes, 2012). This susceptibility led Quade et al. (2020) to question whether burial alteration reactions, driven by the very tectonic activity stable isotope paleoaltimetry intends to reconstruct, erases the original elevation signal in the proxy record. Samples that have been inferred to retain primary information based on minimal assessment of diagenetic histories have been used to reconstruct paleoaltitudes. Conversely, entire stratigraphic packages are dismissed as problematic recorders of primary environments when alteration is suspected based on burial and thermal histories (e.g., stratigraphic thickness, vitrinite reflectance, thermochronology) or alteration fabrics. To enable reconstructions of previously unsolvable tectonic histories, we sought to answer the questions: can analyses at high spatial resolution identify zones of preserved primary carbonate within high-value samples that have been previously classified as altered? Are there finer-scale textural or geochemical indicators of isotopic exchange in the absence of classic alteration fabrics at coarse resolution?

Here, we present a tool kit to guide rigorous assessment of alteration in carbonates at cm-to μm-scales. We intend for this hierarchical framework to improve stable isotope paleoaltimetry through critical assessment of the signs of diagenetic alteration at a range of spatial resolutions. We review textures and chemical signatures indicative of primary, early diagenesis, and burial alteration identifiable by standard optical petrography and cathodoluminescence (CL) microscopy. We suggest complementary analyses commonly employed in diagenesis research, e.g., electron probe microanalyses (EPMA) and scanning electron microscopy electron backscatter diffraction (SEM-EBSD). These techniques provide chemical and crystallographic indicators of post-depositional alteration at <20 μm resolution. Additionally, we propose the use of novel analytical techniques with order of magnitude higher spatial resolution (e.g., secondary ionization mass spectrometry [SIMS] and polarization-dependent imaging contrast [PIC] mapping) to identify textural and chemical alteration that can occur at a finer scale than achievable by standard optical techniques. If primary domains identified by these high-resolution techniques exceed the size of a drill bit, primary isotopic values from key samples previously dismissed as altered by coarser optical techniques could now be attainable. More rigorous and comprehensive assessment of isotopic alteration should ultimately improve and expand our carbonate records of ancient climate and tectonics, and improve our understanding of carbonate alteration mechanisms. Finally, to provide an example of the utility of the analytical framework presented herein, we apply the framework to Tethyan shallow marine carbonates from the Paleocene Jialazi Formation of southern Tibet to characterize the extent of textural and chemical alteration.

Hierarchical Framework for Alteration Assessment Techniques

The assessment techniques are categorized by spatial resolution, which generally coincides with ease of access and cost (**Table 1**). Category one techniques should be applied in all carbonate proxy research, whereas Category three techniques, which are costlier and/or available at a limited number of institutions, are meant to be reserved for assessing and obtaining high-value geochemical information not available by other means. Our intention is to provide a brief overview of the techniques that illustrates their primary utility and caveats for assessing diagenesis, and to show how they can be used hierarchically to holistically. Further information about the techniques can be found in the Supplement and in the references herein.

It is important to note that terrestrial carbonates are typically more variable geochemically than marine carbonates, and are generally less well characterized than marine carbonates. To maximize the ability to interpret data from any of the techniques mentioned below, it will be helpful to measure modern analogs of specific terrestrial carbonates or biogenic material to establish an informative baseline for a given sample.

Category 1—mm- to μm-Scale

Optical Petrography

Optical microscopy of carbonate thin sections is the most essential and accessible method for qualitative assessment of alteration. With plane polar (PPL) and cross polarized light (XPL), one can identify mineralogy, crystal domains and habit, and textures that can be associated with primary formation or water-rock alteration. Some features that may indicate water-rock alteration are secondary porosity, microfractures, meteoric and vadose zone blocky or meniscus cements, pressure dissolution stylolites, dolomitization and microspar or spar-filled veins crosscutting the host rock (Wanless, 1979; Buxton and Sibley, 1981; Moore, 1989; Budd and Land, 1990; Budd et al., 2002; Moore, 2002).

Optical identification of primary domains allows for fabric-specific subsampling from the corresponding slab for geochemical analyses (**Table 1**). In marine or lacustrine limestones, a dense micritic fabric is often considered a primary fabric, and commonly preferred in stable isotope studies. However, micrite can also represent diagenesis via

TABLE 1 | A toolbox of optical and microanalytical techniques for studying the alteration history of a carbonate sample. Spatial resolutions and optimal spot sizes are dependent on the analytical conditions, materials analyzed, and instrumentation, but commonly accepted resolutions are given. Examples of necessary instrumentation are given, although there are often multiple options from different companies for a given instrument. Similarly, we present relative data acquisition time for one datum, but this will vary significantly depending on whether the analysis is a single point or a compositional map, and with user-determined measurement resolution. The techniques are categorized by increasing spatial resolution, which typically coincides with decreasing accessibility and increasing fees.

Ranked accessibility	Technique	Spatial resolution or spot size	Sample preparation	Destructive?	Relevant information obtainable	Instrumentation	Analytical time
1	**Optical petrography**	~30 μm	Thin sections	Non-destructive	• Preservation of primary texture/fabric • Mineralogy • Alteration fabrics (e.g., veins, grain ripening)	Petrographic binocular microscope	Immediate
	Cathodoluminescence	~30 μm	Thin section or other polished surface	Non-destructive	• Details of internal structures in fossils • Compositional variation between crystal domains or fabrics, indicative of different formation fluids • Microtextures and compositional variation not evident in light microscopy	Petrographic microscope and cathodoluminescence system (i.e., cold cathode electron gun, vacuum chamber) OR CL detector with SEM	Immediate
2	**SEM-EDS**	50–100 nm	Cut and polished or raw surface with conductive coating	Minorly destructive (no volume loss)	• Mineralogy of secondary phases often indicative of water-rock alteration (e.g., clays) • Element composition maps	Scanning electron microscope with EDS detector and carbon or gold coater	Seconds to hours
	SEM-EBSD	50–100 nm	Extra-fine polish and conductive coating of flat surface (thin section or billet)	Minorly destructive (no volume loss)	• 3D orientations of individual crystals • Enlarged crystal domains, potentially from dissolution-precipitation at grain boundaries • Statistical distributions of orientations of individual grains of a given phase in pole figures • Preferred orientations of altered crystal domains	Same as above, + EBSD detector	Hours
	Electron microprobe	10–20 μm	Extra-fine polish and conductive coating of flat surface	Minorly destructive (no volume loss)	• Concentration mapping of elements; partitioning or gradients of elements at grain boundaries • Chemical analysis of microns-sized spot; transects to identify elemental variability tied to source waters	Field-emission electron probe micro-analyzer with wavelength dispersive spectrometers (WDS) and EDS	Minutes (spot analyses) to hours (compositional maps)

(Continued on following page)

TABLE 1 | (*Continued*) A toolbox of optical and microanalytical techniques for studying the alteration history of a carbonate sample. Spatial resolutions and optimal spot sizes are dependent on the analytical conditions, materials analyzed, and instrumentation, but commonly accepted resolutions are given. Examples of necessary instrumentation are given, although there are often multiple options from different companies for a given instrument. Similarly, we present relative data acquisition time for one datum, but this will vary significantly depending on whether the analysis is a single point or a compositional map, and with user-determined measurement resolution. The techniques are categorized by increasing spatial resolution, which typically coincides with decreasing accessibility and increasing fees.

Ranked accessibility	Technique	Spatial resolution or spot size	Sample preparation	Destructive?	Relevant information obtainable	Instrumentation	Analytical time
3	**Synchrotron PIC mapping**	>20 nm	Extra-fine polish and conductive coating of flat surface	Destructive (radiation damage)	• Redox states of individual elements • Crystallographic orientation on finer scale than EBSD	Synchrotron beamline capable of x-ray photoelectron emission spectromicroscopy (X-PEEM) and x-ray absorption near-edge structure spectroscopy (XANES)	Hours
	SIMS	>10 μm	Extra-fine polish and conductive coating; 1″ round set in epoxy[a]	Essentially non-destructive	• *in situ* trace element abundances and isotopic ratios at ppb levels • Isotopic spatial variability at orders of magnitude smaller scale than bulk analyses • Depth profiling for subsurface variability that may be integrated while drilling for bulk analyses	SIMS and gold coater	Minutes (spot analyses) to hours (compositional maps)

Note: Spatial resolutions and optimal spot sizes are dependent on analytical conditions, material analyzed, and instrumentation.
[a]*Technique is sensitive to composition of epoxy; always check with lab technician prior to sample preparation.*

micritization. Biogenic carbonates (e.g., shells, foraminifera tests) have clade-specific growth habits that are typically optically identifiable, which makes bioclasts a good starting point in assessing water-rock alteration of fossiliferous samples. However, some alteration is fabric retentive, and thus, during mineral replacement and isotopic exchange, the crystal domain can retain its internal structure (e.g. fabric-retentive dolomitization). Further, some materials are more reticent to water-rock exchange (e.g., brachiopods; Grossman et al., 1996). Thus, careful fabric-specific sampling combined with isotopic analyses of the different fabrics in a sample can aid in discerning altered vs. primary values.

Optical Cathodoluminescence

Cold-cathode optical-CL allows one to pair textural information to geochemical information inaccessible via light microscopy alone. Luminescence is the response of a material to bombardment of high energy electrons generated by the discharge between a negative high voltage cathode and an anode at ground potential in ionized gas under vacuum ($\sim 10^{-2}$ Torr), and requires only a well-polished surface. Impurity ions and lattice defects are common in carbonate minerals (Nielsen et al., 2013) and act as electron traps, resulting in increased CL (Boggs and Krinsley, 2006). Trace metals can be incorporated into carbonate by sorption onto growing crystal surfaces, occlusion into lattice defects, substitution for a major element, and as impurity ions (Sun and Hanson, 1975). Mn^{2+} is an "activator" that increases CL emission and appears yellow to orange-red, whereas Fe^{2+} in the presence of Mn^{2+} is a "quencher" resulting in dull to non-luminescence (Gorobets and Walker, 1995). CL has long been a popular tool for identifying carbonate components least altered by recrystallization (dull to non-luminescence; e.g., Lohmann and Walker, 1989), and overprinting of primary chemical zonation within calcite crystals (mottled or blotchy luminescence; Budd et al., 2002; Machel, 2000). An additional benefit of optical-CL is the ability to directly compare CL to PPL and XPL images of the same crystal domains in a thin section (**Table 1**). Observations of larger, geochemically distinct domains of dull luminescence, such as within a shell or micrite, would signal an ideal location for microdrilling or further investigation by microbeam techniques (e.g., Snell et al., 2013).

Category 2—μm-to 100s of nm-scale

Scanning Electron Microscopy–Secondary Electron and Energy Dispersive X-Ray Spectroscopy (SEM—SE and -EDS)

The interactions between carbonate surfaces and a focused electron beam reveal chemical and morphological information by detection of secondary electrons (SE) and energy dispersive x-ray spectroscopy (EDS). A benefit of SEM imaging is the achievement of up to 30,000x magnification with 50–100 nm spatial resolution (**Table 1**). Chemical point analyses and maps enable *qualitative* identification of carbonate alteration, such as changes in elemental distribution in multiphase systems, phase replacement or neomorphism, and high-resolution characterization of chemical relationships at grain boundaries tied to the high-resolution textural information provided by the SEM images themselves (**Figure 1**).

SEM–Electron Backscatter Diffraction (EBSD)

SEM electron beams can be diffracted by atomic layers within a carbonate crystal to generate visible backscatter patterns as they pass through a phosphor screen. The backscatter patterns are projections of the lattice plane geometry of individual carbonate crystals. These data are used to generate misorientation maps and pole figures displaying statistical distributions of crystallographic c-axis orientations of all individual grains of a given phase (**Figure 1**), superimposed on the SE and/or EDS images. The statistical data can be used to test alteration hypotheses and reconstruct the history of crystal reorientation related to water-rock alteration, including processes like grain ripening, calcite zonation, and overprinting of a unified c-axis orientation during reprecipitation. For example, micrite in a lacustrine limestone from the Lunpola basin had no preferred c-axis orientation, as seen in the pole figure in **Figure 1**. Following EBSD and optical petrographic observations, Ingalls et al. (2020) interpreted that this sample likely preserved primary fabrics and isotope values, since alteration would likely produce greater alignment of c-axis orientations within the micrite (e.g., Ryb et al., 2017).

Electron Probe Microanalysis (EPMA)

EPMA is a non-destructive tool that operates by the same principles as SEM, but is capable of quantitative, spatially resolved elemental analyses by wavelength dispersive spectroscopy (WDS). These 2D element maps can be overlaid on SE, BSE, and CL images to directly compare chemical variability between textural, mineralogical, crystallographic, and redox domains. Element maps and <10 μm spot analyses can reveal micron-scale chemical variability (**Table 1**), thereby serving as a test for subsurface water-rock interaction that may occur from pore fluids at a fine spatial scale. Quantitative analyses of major, minor and trace element ratios (e.g., Mg/Ca, Sr/Ca, Mn/Sr) provide evidence for carbonate formation from a different fluid composition than primary Earth surface water (**Figure 1**).

Category 3—μm-to 10s of nm-scale

Secondary Ionization Mass Spectrometry (SIMS)

SIMS and nanoSIMS provide one of the highest spatial resolution, *in situ* isotopic and elemental measurements currently available. SIMS provides oxygen and carbon isotope values at <20 μm scale (**Table 1**), similar to the spatial resolution of EPMA, while nanoSIMS can provide geochemical information on spots as small as 10s of nanometers. A primary positive ($^{133}Cs^{+}$) or negative ($^{16}O^{2-}$) ion beam focused on a sample surface generates secondary ions of specific elements that are measured by a mass spectrometer. SIMS analyses enable isotopic differentiation between microtextures and observation of isotopic gradients over areas that are integrated during bulk sample drilling. SIMS could open doors to characterizing extent of water-rock alteration and paragenesis from pore fluids, as well as potentially revealing residual primary carbonate material in differentially altered samples.

Polarization-dependent Imaging Contrast (PIC) Mapping

PIC mapping is an outgrowth of X-ray absorption near-edge structure (XANES) spectroscopy, in which spectra vary depending on the orientation of a carbonate mineral's c-axis due to X-ray linear dichroism (Gilbert, 2012; DeVol et al., 2014). Crystallographic orientations can be quantified for domains >20 nm (DeVol et al., 2014), which is why this technique is commonly applied to biogenic carbonates to investigate biomineralization. Different modes of alteration result in different distributions of reoriented c-axes, which can then be explicitly tied to geochemical data from nanoSIMS on a comparable spatial scale. This is analogous to pairing EBSD-derived maps with SIMS on even finer spatial scales. A recent application of PIC mapping revealed reorientations of c-axes in individual nacre within fossil values, which demonstrated that altered biogenic aragonite can preserve original biomineral structures and mineralogy (Gilbert et al., 2017). This type of alteration would not be detectable at the scale of optical petrography, which could result in isotope values from altered material being used erroneously to reconstruct paleoenvironmental conditions. In the future, nanoSIMS analyses could reveal whether geochemical changes correspond to this nacre-scale alteration.

Modeling Potential Extent of Solid-State Bond Reordering in Clumped Isotope applications

At high temperatures, atoms can migrate within the carbonate lattice by solid-state diffusion, thereby randomizing the distribution of ^{13}C–^{18}O pairs and altering Δ_{47}, and in turn, the inferred formation temperature (Passey and Henkes, 2012; Stolper and Eiler, 2015; Henkes et al., 2018). Importantly, solid-state alteration retains primary fabrics *and* bulk $\delta^{13}C$ and $\delta^{18}O$ while reducing Δ_{47} via diffusion. Samples experiencing solid-state alteration would pass all previously described assessments of textural and isotopic alteration, making it difficult to identify. Thus, it is critical to sufficiently rule out effects of fluid-based alteration before inferring that solid-state reordering is responsible for erroneous Δ_{47} temperatures.

Fluid-mediated recrystallization also resets T (Δ_{47}) to the recrystallization temperature. However, the extent of Δ_{47} alteration by solid-state ^{13}C–^{18}O reordering is dependent on the integrated time above a mineral-specific threshold. For example, calcite held at 75°C for 100 My would only increase T (Δ_{47}) by < 1 °C, but would increase T (Δ_{47}) by ~40 °C if held at 120 °C for 100 My (Stolper and Eiler, 2015). Independent constraints on the burial histories of sedimentary basins and application of mineral-specific kinetic parameters in reordering models provide means for assessing the potential extent of solid-state reordering (e.g., Lawson et al., 2018; Lloyd et al., 2018; Lacroix and Niemi, 2019), for samples that show no other signs of fluid-based alteration that could account for erroneous Δ_{47} values.

Case Study: Differential Alteration of Tethyan Shallow Marine carbonate

The shallow marine Paleocene-Eocene Jialazi Formation of the Tso Jianding Group (southern Tibet) is ideal for investigating the expression of water-rock and solid-state alteration in micritic and biogenic carbonate at a variety of spatial scales because of the incongruity of its isotope values and textural characteristics. The Jialazi Formation records the transition from marine to terrestrial

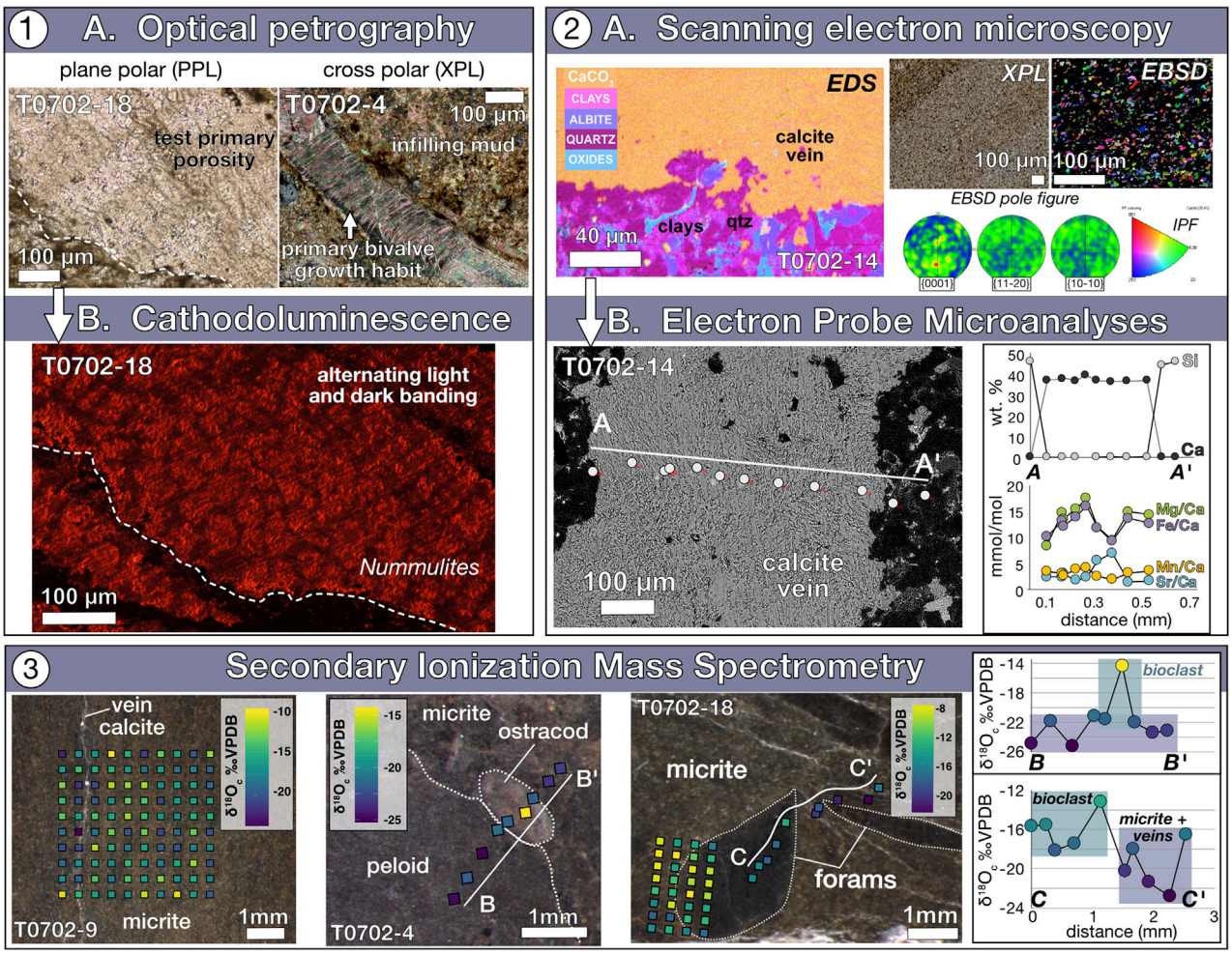

FIGURE 1 | Optical and geochemical investigations of carbonate alteration increasing in spatial resolution (1→3). (1) Preservation of primary porosity in a foram test (T0702-18) in plane polar light; secondary carbonate precipitation within the test microporosity can be identified by the brighter red luminescence, indicative of elemental chemistry different from the water in which the foram grew. The test walls preserve alternating light and dark banding in CL, although it is patchier than is likely for the original fabric. Preserved primary bivalve growth habit (T0702-4) can be identified in cross polar light. (2) Scanning electron microscopy (SEM) energy dispersive spectroscopy (EDS) of a calcite vein cutting through a mudstone (T0702-14) displays phase mixing on the 10s of microns scale. Electron probe microanalysis (EPMA) shows elevated Sr/Ca at the core of the same vein (T0702-14), potentially indicative of two episodes of water-rock alteration. A sample from the Lunpola basin analyzed by EBSD demonstrates the expected no preferred c-axis orientation for a primary lacustrine limestone composed of micrite. IPF = inverse pole figure. (3) On the finest scale, ~10 to 15‰ variability in carbonate δ18O values are seen within limestones (T0702-9), and across abiotic and biotic carbonate components (T0702-4 and -18). Generally, micrite and allochems yielded lower δ18O values than bioclasts. Overall, in this study, bioclasts were more fabric retentive and less divergent from expected values of marine carbonate than other carbonate components.

deposition within the Xigaze forearc basin following the India-Asia collision (Orme et al., 2014; Orme, 2017). Currently, no low-altitude $\delta^{18}O_w$ or δD_w estimate of precipitation south of Tibet exists for Paleogene $\Delta\delta^{18}O_w$-based reconstructions during a critical period of Tibetan tectonics. Ingalls (2019) aimed to provide a low-altitude δD_w from terrestrially derived organics preserved within the nearshore sediments if effects of alteration could be more concretely assessed.

Ingalls (2019) found that textural and isotopic data presented contradictory cases for the preservation of primary information in the Jialazi Formation. While primary biofabrics of shells and foraminifera were identified by traditional optical techniques (**Figure 1**), $\delta^{18}O_c$ values were ~10–20‰ lower than any primary marine carbonate, and similar to carbonates that precipitate from Tibetan meteoric water today (Ingalls, 2019). Specifically, optical petrography showed preserved primary foraminifera test porosity in plane polarized light and primary bivalve growth habit with banding perpendicular to growth laminae crossed polars (T0702–4; **Figure 1**). Contrary to these indicators of textural preservation, test edges appeared to be partially dissolved or weathered and pores were infilled with cements with increased luminescence (T0702–18; **Figure 1**; **Supplementary Figure S1**). The dull luminescence of the tests and micritic matrix

suggested those domains may preserve geochemical information of the depositional environment, but the red luminescence within pore spaces indicated carbonate precipitation from a fluid with different redox chemistry. Subsampling material from the *Nummulites* tests without integrating altered pore-filling carbonate is beyond the spatial capability of a micromill, so traditional isotope analysis would likely integrate primary and altered material.

Instead, using EPMA, we identified secondary carbonate formed from two generations of alteration fluids in sample T0702–14. Across a ~500 μm transect with 12 elemental spot analyses (10–20 μm diameter; **Figure 1**), we identified two populations: 1) a primary trend of increasing Mg/Ca and Fe/Ca away from the vein-mudstone interface on both sides, and 2) consistently low Mn/Ca and Sr/Ca that later overprinted via dissolution-precipitation. This is seen in a spike in Sr/Ca paired with a relative decrease in Mg/Ca and Fe/Ca along the central axis of the vein. We suspect that interaction with a subsurface brine caused Sr/Ca enrichment in the second alteration event because saline burial fluids typically carry significantly higher Sr concentrations than seawater (Banner, 1995).

The clumped isotope-derived temperatures ranged from ~80 ° to 10 °C (Ingalls, 2019), reflecting the complex water-rock and solid-state alteration history. Ingalls (2019) assessed the potential extent of solid-state reordering using thermochronologic data from the Xigaze forearc (Orme, 2017) in an exchange-diffusion model (Lloyd, 2020) partnered with fabric-specific analyses. The model results suggest that late-stage, low-temperature, fluid-based alteration superseded partial solid-state reordering in the Jialazi Formation, overprinting the deep burial history with low T (Δ_{47}) values. Perhaps most importantly for paleoenvironmental reconstruction, the extent to which $\delta^{18}O$ values departed from original marine compositions varied in the Jialazi Formation (e.g., $\delta^{18}O_c$ values of ~ −10 to −25‰ VPDB; **Figure 1**). Additionally, transects in samples T0702-4 and -18 revealed a trend of higher $\delta^{18}O_c$ values (~−12 to −18‰) in bioclasts than in micrite (>−26‰; **Figure 1**). Although the Jialazi Formation as a whole was altered beyond use for palaeoenvironmental reconstruction, we determined that biogenic materials were either more reticent to water-rock exchange than micritic carbonate or were altered by a different fluid than the micrite. SIMS analyses of micrite, bioclasts and diagenetic cements in the Paris Basin yielded similar magnitude $\delta^{18}O$ variability (Vincent et al., 2017), demonstrating that intrasample geochemical variability on a finer scale than can be resolved by micromilling is not unique to the Jialazi Formation. Thermal maturation indices of organic matter and benchmark values for marine carbonate $\delta^{18}O$ (~0‰ VPDB) clearly identified these rocks as strongly impacted by isotopic exchange reactions. Had these samples been derived from a terrestrial environment whose expected values could have been similar to the values obtained, and only screened by optical petrography, the altered $\delta^{18}O$ values might have been used erroneously to make stable isotope-based calculations of ancient elevations.

To demonstrate the magnitude of error that can arise from misinterpretation of altered $\delta^{18}O$ values, we performed $\Delta(\delta^{18}O_w)$-based calculations using the endmember Jialazi Fm $\delta^{18}O_w$ values for sea level estimates (−19.1, −12.8‰ VSMOW, noting that seawater $\delta^{18}O_w$, recorded by marine carbonate, is typically higher than meteoric $\delta^{18}O_w$), and both Paleocene (−13.6‰; Ingalls et al., 2017) and modern compositions (−18.1‰; Bershaw et al., 2012) from the high-altitude margin of Tibet (see Supplement). Using Jialazi Fm $\delta^{18}O_w$ values as the sea level proxy, we calculated Paleocene elevations of −5,288 and 548 m. a.s.l. for the southern Tibetan margin, with the former being physically implausible (**Supplementary Table S1**). Differencing Jialazi Fm values with modern precipitation yielded elevations of −755 and 2,874 m. a.s.l. for a land surface currently >4,000 m. a.s.l. Therefore, incorrectly using altered $\delta^{18}O$ values as an estimate for low elevation meteoric water in paleoaltimetry calculations can underestimate elevations by several kilometers (**Supplementary Table S1**). By the same logic, alteration of high-altitude samples can result in inaccurate paleo-elevations by similar magnitudes.

SUMMARY

We present a hierarchical framework for assessing alteration in carbonates used for environmental and tectonic reconstructions. As an example, we built on the exchange-diffusion modeling and texture-specific isotopic measurements of Ingalls (2019) to construct a more detailed alteration history for the Jialazi Formation. We demonstrated that apparent textural preservation can coincide with differential alteration of primary isotopic values, which can lead to significant errors in paleoaltimetric reconstructions. Had the Jialazi Formation been nonmarine, the application of the full suite of screening techniques and consideration of thermal history would have been essential to ruling out the use of $\delta^{18}O$ and Δ_{47} for paleoaltimetry. The adoption of this hierarchical framework for assessing carbonate alteration could improve our understanding of the carbonate record and processes of carbonate isotopic alteration, as well as resolve previously unsolvable tectonic problems by enabling access to finite domains of preserved primary carbonate.

DATA AVAILABILITY STATEMENT

The datasets presented in this study can be found in online repositories. The names of the repository/repositories and accession numbers can be found below: https://osf.io/34k8y doi: 10.17605/OSF.IO/34K8Y.

AUTHOR CONTRIBUTIONS

MI conceived of the hierarchical assessment framework, performed analyses, interpreted data and wrote the manuscript. KS contributed to the conception of the alteration

framework, and contributed writing and feedback on the manuscript.

FUNDING

This work was funded by NSF EAR 2040145 to MI and KS, and funding to KS from the University of Colorado.

ACKNOWLEDGMENTS

MI thanks Chi Ma and Yunnan Guan for assistance with SEM and SIMS microanalyses at the California Institute of Technology, Julien Allaz for assistance with EPMA at the University of Colorado, and David Budd for discussions of primary and diagenetic fabrics in large foraminifera. We thank the editors for the invitation to contribute to Reaching New Heights: Recent Progress in Paleotopography, and constructive comments from three reviewers.

SUPPLEMENTARY MATERIAL

The Supplementary Material for this article can be found online at: https://www.frontiersin.org/articles/10.3389/feart.2021.623982/full#supplementary-material.

REFERENCES

Banner, J. L. (1995). Application of the trace element and isotope geochemistry of strontium to studies of carbonate diagenesis. *Sedimentology* 42, 805–824. doi:10.1111/j.1365-3091.1995.tb00410.x

Banner, J. L., and Hanson, G. N. (1990). Calculation of simultaneous isotopic and trace element variations during water-rock interaction with applications to carbonate diagenesis. *Geochem. Cosmochim. Acta.* 54, 3123–3137. doi:10.1016/0016-7037(90)90128-8

Bershaw, J., Penny, S., and Garzione, C. N. (2012). Stable isotopes of modern water across the Himalaya and eastern Tibetan Plateau: implications for estimates of paleoelevation and paleoclimatic. *J. Geophys. Res.* 117, D02110. doi:10.1029/2011JD016132

Boggs, S., and Krinsley, D. (2006). *Application of cathodoluminescence imaging to the study of sedimentary rocks*. Cambridge University Press.

Budd, D. A., and Land, L. S. (1990). Geochemical imprint of meteoric diagenesis in holocene ooid sands, schooner cays, bahamas: correlation of calcite cement geochemistry with extant groundwaters. *J. Sediment. Petrol.* 60, 361–378. doi:10.1007/s00204-003-0469-4

Budd, D. A., Pack, S. M., and Fogel, M. L. (2002). The destruction of paleoclimatic isotopic signals in Pleistocene carbonate soil nodules of Western Australia. *Palaeogeogr. Palaeoclimatol. Palaeoecol.* 188, 249–273.

Buxton, T. M., and Sibley, D. F. (1981). Pressure solution features in a shallow buried limestone. *J. Sediment. Res.* 51, 19–26. doi:10.1306/212F7BF8-2B24-11D7-8648000102C1865D

Chamberlain, C. P., Mix, H. T., Mulch, A., Hren, M. T., Kent-Corson, M. L., Davis, S. J., et al. (2012). The Cenozoic climatic and topographic evolution of the western North American cordillera. *Am. J. Sci.* 312, 213–262. doi:10.2475/02.2012.05

Chamberlain, C. P., and Poage, M. A. (2000). Reconstructing the paleotopography of mountain belts from the isotopic composition of authigenic minerals. *Geology.* 28, 115–118. doi:10.1130/0091-7613(2000)28<115:RTPOMB>2.0.CO;2

DeVol, R. T., Metzler, R. A., Kabalah-Amitai, L., Pokroy, B., Politi, Y., Gal, A., et al. (2014). Oxygen spectroscopy and polarization-dependent imaging contrast (PIC)- mapping of calcium carbonate minerals and biominerals. *J. Phys. Chem. B.* 118, 8449–8457. doi:10.1021/jp503700g

Gilbert, C. N. (2008). Surface uplift of Tibet and Cenozoic global cooling. *Geology.* 36, 1003–1004. doi:10.1130/focus122008.1

Gilbert, P. U. P. A., Bergmann, K. D., Myers, C. E., Marcus, M. A., DeVol, R. T., Sun, C.-Y., et al. (2017). Nacre tablet thickness records formation temperature in modern and fossil shells. *Earth Planet Sci. Lett.* 460, 281–292. doi:10.1016/j.epsl.2016.11.012

Gilbert, P. U. P. A. (2012). Polarization-dependent imaging contrast (PIC) mapping reveals nanocrystal orientation patterns in carbonate biominerals. *J. Electron. Spectrosc. Relat. Phenom.* 185, 395–405. doi:10.1016/j.elspec.2012.06.001

Gorobets, B. S., and Walker, G. (1995). "Origins of luminescence in minerals: a summary of fundamental studies and applications," in *Advanced mineralogy*. Berlin: Springer-Verlag, 124–135.

Grossman, E. L., Mii, H.-S., Zhang, C. L., and Yancey, T. E. (1996). Chemical variation in pennsylvanian brachiopod shells; diagenetic, taxonomic, microstructural, and seasonal effects. *J. Sediment. Res.* 66, 1011–1022. doi:10.1306/D4268469-2B26-11D7-8648000102C1865D

Henkes, G. A., Passey, B. H., Grossman, E. L., Shenton, B. J., Yancey, T. E., and Pérez-Huerta, A. (2018). Temperature evolution and the oxygen isotope composition of phanerozoic oceans from carbonate clumped isotope thermometry. *Earth Planet Sci. Lett.* 490, 40–50. doi:10.1016/j.epsl.2018.02.001

Huntington, K. W., Saylor, J., Quade, J., and Hudson, A. M. (2015). High late Miocene-Pliocene elevation of the Zhada Basin, southwestern Tibetan Plateau, from carbonate clumped isotope thermometry. *Geol. Soc. Am. Bull.* 127, 181–199. doi:10.1130/B31000.1

Huntington, K. W., Wernicke, B. P., and Eiler, J. M. (2010). Influence of climate change and uplift on colorado plateau paleotemperatures from carbonate clumped isotope thermometry. *Tectonics* 29, TC3005. doi:10.1029/2009TC002449

Ingalls, M. (2019). Reconstructing carbonate alteration histories in orogenic sedimentary basins: Xigaze forearc, southern Tibet. *Geochem. Cosmochim. Acta.* 251, 284–300. doi:10.1016/j.gca.2019.02.005

Ingalls, M., Rowley, D. B., Currie, B. S., and Colman, A. S. (2020). Reconsidering the uplift history and peneplanation of the northern lhasa terrane. *Tibet.* 320, 479–532. doi:10.2475/06.2020.01

Ingalls, M., Rowley, D. B., Olack, G., Currie, B. S., Li, S., Schmidt, J., et al. (2017). Paleocene to Pliocene low-latitude, high-elevation basins of southern Tibet: implications for tectonic models of India-Asia collision, Cenozoic climate, and geochemical weathering. *Geol. Soc. Am. Bull.* 130, 307–330. doi:10.1130/B31723.1

Lacroix, B., and Niemi, N. A. (2019). Investigating the effect of burial histories on the clumped isotope thermometer: an example from the Green River and Washakie Basins, wyoming. *Geochem. Cosmochim. Acta.* 247, 40–58. doi:10.1016/J.GCA.2018.12.016

Lawson, M., Shenton, B. J., Stolper, D. A., Eiler, J. M., Rasbury, E. T., Becker, T. P., et al. (2018). Deciphering the diagenetic history of the El Abra formation of eastern Mexico using reordered clumped isotope temperatures and U-Pb dating. *Bull. Geol. Soc. Am.* 130, 617–629. doi:10.1130/B31656.1

Lloyd, M. (2020). Clumpycool. open science framework. *ClumpyCool* doi:10.17605/OSF.IO/JYHSW

Lloyd, M., Ryb, U., and Eiler, J. M. (2018). Experimental determination of the preserve- tion potential of the dolomite clumped isotope thermometer. *Geochem. Cosmochim. Acta.* 242, 1–20.

Lohmann, K. C., and Walker, J. C. G. (1989). The $\delta^{18}O$ record of phanerozoic abiotic marine calcite cements. *Geophys. Res. Lett.* 16, 319–322. doi:10.1029/GL016i004p00319

Machel, H. G. (2000). "Application of cathodoluminescence to carbonate diagenesis," in *Cathodoluminescence in Geosciences*. Berlin, Heidelberg: Springer, 271–301.

Moore, C. H. (1989). "Carbonate diagenesis and porosity," in *Developments in Sedimentology*. Elsevier, 337.

Moore, C. H. (2002). Marine and petroleum geology carbonate reservoirs porosity evolution and diagenesis in a sequence stratigraphic framework. *Marine Petrol. Geology* doi:10.1016/S0264-8172(03)00037-0

Nielsen, L. C., De Yoreo, J. J., and DePaolo, D. J. (2013). General model for calcite growth kinetics in the presence of impurity ions. *Geochem. Cosmochim. Acta.* 115, 100–114. doi:10.1016/j.gca.2013.04.001

Orme, D. A. (2017). Burial and exhumation history of the xigaze forearc basin, yarlung suture zone, Tibet. *Geosci. Front.* 1–15. doi:10.1016/j.gsf.2017.11.011

Orme, D. A., Carrapa, B., and Kapp, P. (2014). Sedimentology, provenance and geochronology of the upper cretaceous-lower eocene western xigaze forearc basin, southern Tibet. *Basin Res.* 27, 387–411. doi:10.1111/bre.12080

Passey, B. H., and Henkes, G. A. (2012). Carbonate clumped isotope bond reordering and geospeedometry. *Earth Planet Sci. Lett.* 351–352, 223–236. doi:10.1016/j.epsl.2012.07.021

Quade, J., Leary, R., Dettinger, M. P., Orme, D., Krupa, A., DeCelles, P. G., et al. (2020). Resetting southern tibet: the serious challenge of obtaining primary records of paleoaltimetry. *Global Planet. Change.* 191, 103194. doi:10.1016/j.gloplacha.2020.103194

Rowley, D. B., and Currie, B. S. (2006). Palaeo-altimetry of the late eocene to miocene lunula basin, central Tibet. *Nature.* 439, 677–681. doi:10.1038/nature04506

Rowley, D. B., Pierrehumbert, R. T., and Currie, B. S. (2001). A new approach to stable isotope-based paleoaltimetry: implications for paleoaltimetry and paleohypsometry of the high himalaya since the late miocene. *Earth Planet Sci. Lett.* 5836, 1–17. doi:10.1016/S0012-821X(01)00324-7

Ryb, U., Lloyd, M. K., Stolper, D. A., and Eiler, J. M. (2017). The clumped-isotope geochemistry of exhumed marbles from Naxos, Greece. *Earth Planet Sci. Lett.* 470, 1–12. doi:10.1016/j.epsl.2017.04.026

Snell, K. E., Koch, P. L., Druschke, P., Foreman, B. Z., and Eiler, J. M. (2014). High elevation of the "nevadaplano" during the late cretaceous. *Earth Planet Sci. Lett.* 386, 52–63. doi:10.1016/j.epsl.2013.10.046

Snell, K. E., Thrasher, B. L., Eiler, J. M., Koch, P. L., Sloan, L. C., and Tabor, N. J. (2013). Hot summers in the bighorn basin during the early Paleogene. *Geology.* 41, 55–58. doi:10.1130/G33567.1

Stolper, D. A., and Eiler, J. M. (2015). The kinetics of solid-state isotope-exchange reactions for clumped isotopes: a study of inorganic calcites and apatites from natural and experimental samples. *Am. J. Sci.* 315, 363–411. doi:10.2475/05.2015.01

Sun, S. S., and Hanson, G. N. (1975). Origin of Ross Island basanitoids and limitations on the heterogeneity of mantle sources of alkali basalts and nephelinites. *Contrib. Mineral. Petrol.* 54, 77–106. doi:10.1007/BF00395006

Vincent, B., Brigaud, B., Emmanuel, L., and Loreau, J.-P. (2017). High resolution ion microprobe investigation of the δ18O of carbonate cements (Jurassic, Paris Basin, France): new insights and pending questions. *Sediment. Geol.* 350, 42–54. doi:10.1016/j.sedgeo.2017.01.008

Wanless, H. R. (1979). Limestone response to stress; pressure solution and dolomitization. *J. Sediment. Res.* 49, 437–462. doi:10.1306/212F7766-2B24-11D7-8648000102C1865D

Conflict of Interest: The authors declare that the research was conducted in the absence of any commercial or financial relationships that could be construed as a potential conflict of interest.

frontiers in Earth Science

ORIGINAL RESEARCH
published: 25 March 2021
doi: 10.3389/feart.2021.628868

Reconstructing Past Elevations From Triple Oxygen Isotopes of Lacustrine Chert: Application to the Eocene Nevadaplano, Elko Basin, Nevada, United States

Daniel E. Ibarra[1,2,3], Tyler Kukla[2], Katharina A. Methner[2], Andreas Mulch[4,5] and C. Page Chamberlain[2]*

[1] Department of Earth and Planetary Science, University of California, Berkeley, Berkeley, CA, United States, [2] Department of Geological Sciences, Stanford University, Stanford, CA, United States, [3] The Department of Earth, Environmental and Planetary Science, Institute at Brown for Environment and Society, Brown University, Providence, RI, United States, [4] Senckenberg Biodiversity and Climate Research Centre, Frankfurt am Main, Germany, [5] Institute of Geosciences, Goethe University Frankfurt, Frankfurt am Main, Germany

OPEN ACCESS

Edited by:
Michaël Hermoso, UMR 8187 Laboratoire d'océanologie et de géosciences (LOG), France

Reviewed by:
Naomi E. Levin, University of Michigan, United States
Julia Kelson, University of Michigan, United States

***Correspondence:**
Daniel E. Ibarra
dibarra@berkeley.edu;
daniel_ibarra@brown.edu

Specialty section:
This article was submitted to Quaternary Science, Geomorphology and Paleoenvironment, a section of the journal Frontiers in Earth Science

Received: *13 November 2020*
Accepted: *25 February 2021*
Published: *25 March 2021*

Citation:
Ibarra DE, Kukla T, Methner KA, Mulch A and Chamberlain CP (2021) Reconstructing Past Elevations From Triple Oxygen Isotopes of Lacustrine Chert: Application to the Eocene Nevadaplano, Elko Basin, Nevada, United States. Front. Earth Sci. 9:628868. doi: 10.3389/feart.2021.628868

Triple oxygen isotope measurements are an emerging tool in paleoclimate reconstructions. In this contribution we develop the application of triple oxygen isotope measurements to lacustrine sediments to reconstruct past elevations. We focus on a well-constrained sample set from the Eocene North American Cordillera (Cherty Limestone Formation, Elko Basin, NV, United States, 42–43.5 Ma) on the east side of the elevated Nevadaplano. We present triple oxygen isotope measurements on freshwater lacustrine chert samples from the Cherty Limestone Formation. Across an evaporation trend spanning 6.5‰ in $\delta^{18}O$ values we observe a negative correlation with $\Delta'^{17}O$ ranging from −0.066 to −0.111‰ (λ_{RL} = 0.528), with an empirical slope (λ_{chert}, $\delta'^{17}O$ vs. $\delta'^{18}O$) of 0.5236. Additionally, we present new carbonate clumped isotope (Δ_{47}) temperature results on the overlying fluvial-lacustrine Elko Formation, which indicate an error-weighted mean temperature of 32.5 ± 3.8°C (1σ), and evaporatively enriched lake water spanning $\delta^{18}O$ values of −3.7 to +3.5‰ (VSMOW). Paired chert and carbonate $\delta^{18}O$ values demonstrate that co-equilbrium among the carbonate and chert phases is unlikely. Thus, as also previously suggested, it is most likely that Elko Basin chert formed during early diagenesis in equilbirium with pore waters that reflect evaporatively ^{18}O-enriched lake water. Using this scenario we apply a model for back-calculating unevaporated water composition to derive a source water of $\delta'^{18}O$ = −16.1‰ (VSMOW), similar to modern local meteoric waters but lower than previous work on paired $\delta^{18}O$- δD measurements from the same chert samples. Further, this back-calculated unevaporated source water is higher than those derived using δD measurements of Late Eocene hydrated volcanic glass from the Elko Basin (average $\delta'^{18}O$ equivalent of approximately −18.4‰, VSMOW). This suggests, assuming Eocene meteoric water $\Delta'^{17}O$ values similar to today (∼0.032‰), either that: (1) the hypsometric mean elevation recorded by the lacustrine Cherty Limestone was lower than that derived

from the average of the volcanic glass δD measurements alone; or (2) there was hydrogen exchange in volcanic glass with later low δD meteoric fluids. Nonetheless, our new findings support a relatively high (∼2.5–3 km) plateau recorded in the Elko Basin during the mid-Eocene.

Keywords: paleoaltimetry, triple oxygen isotopes, lacustrine chert, lakes, Eocene, carbonate clumped isotopes

INTRODUCTION AND GEOLOGIC SETTING

Reconstructing the topographic history of mountain belts relies heavily upon the oxygen ($\delta^{18}O$) and hydrogen (δD) isotopes of authigenic minerals in paleosols and paleolake sediments (e.g., Chamberlain et al., 1999; Poage and Chamberlain, 2002; Takeuchi and Larson, 2005; Ghosh et al., 2006a; Garzione et al., 2006; Davis et al., 2009; Takeuchi et al., 2010; Mulch et al., 2010, 2015; Gébelin et al., 2013; Schwartz et al., 2019; Pingel et al., 2020; Ingalls et al., 2020a; Quade et al., 2020; San Jose et al., 2020; Kukla et al., 2021). Rainout causes systematic monotonic depletion in $\delta^{18}O$ and δD with elevation (e.g., Rowley et al., 2001), which can be exploited to reconstruct past elevations of ancient mountain belts. However, the interpretation of these isotopic data as signals of past elevation is often complicated by evaporation in soils and lakes that will enrich waters in ^{18}O and D (e.g., Abruzzese et al., 2005; Davis et al., 2009; Mulch et al., 2015; Mulch, 2016; Ingalls et al., 2020a). These evaporitic effects are particularly problematic in semi-arid to arid settings that often form in the rain shadow of uplifting mountains. Thus, methods to determine the pre-evaporative isotopic composition of meteoric waters are needed to isolate the signal of surface uplift from progressive drying.

One way of assessing evaporative trends is to use combined δD and $\delta^{18}O$ values of chert deposits in the paleolake sediments. Abruzzese et al. (2005) used this approach in their study of the Eocene chert found in foreland lake deposits of the Rocky Mountains. Despite recording strong evaporitic signals, the trends in δD and $\delta^{18}O$ values of chert were used to extrapolate to the isotopic composition of original un-evaporative meteoric waters (Abruzzese et al., 2005). Oxygen isotope ratios of the hydroxyl ions of chert are likely a robust indicator of waters from which they form (Knauth, 1973) since hydroxyl ions appear to resist post-depositional exchange (Micheelsen, 1966). However, it is strongly material dependent how resilient hydrogen isotopes are to later diagenesis and exchange particularly given that other minerals (clays and micas) can exhibit some degree of later exchange of hydrogen (O'Neil and Kharaka, 1976; Chamberlain et al., 2020). For this reason, we explore the triple oxygen system (^{16}O, ^{17}O, and ^{18}O) of chert to determine meteoric water compositions. Complementary to triple oxygen isotopes, carbonate clumped isotope analyses are needed to constrain the effect of evaporation on the $\delta^{18}O$ values of the minerals by assessing the carbonate formation temperatures and the $\delta^{18}O$ values of (evaporatively enriched) lake water from which the carbonate mineral formed.

In this study we present the first lacustrine chert triple oxygen isotope dataset from a Cenozoic basin in western North America and use this data set, with carbonate clumped isotope measurements from overlying strata, to derive an elevation estimate for the Eocene Nevadaplano. Our study site in the vicinity of Elko, Nevada (United States) hosts well-studied sections from the Eocene eastern Nevadaplano. We focused on the Eocene sections in the Elko Basin because of the controversy concerning the timing and extent of surface uplift in this region [contrasting Smith et al. (2017) and Cassel et al. (2018) with Mulch et al. (2015) as well as Lund Snee et al. (2016)]. In essence the controversy revolves around the timing and amount of surface uplift of this region that was first discovered through the stable isotopic studies of Horton et al. (2004). These authors argued that ∼2 km of surface uplift occurred between the middle Eocene and the early Oligocene based on oxygen isotope changes in paleosol and lacustrine carbonate. These data are important as they are one of the few basins with somewhat continuous Cenozoic sedimentation providing a key datum on the progressive north to south topographic response associated with the removal of the Farallon slab or piecemeal remove of the mantle lithosphere (Carroll et al., 2008; Mix et al., 2011; Chamberlain et al., 2012). However, at the time of the Horton et al. (2004) paper there was insufficient age control to know with any certainty when this uplift occurred. New ages and stable isotope data provided by Mulch et al. (2015) suggested that the surface uplift of 2 km occurred in the late Eocene between 43 and 38 Ma. Yet, this has recently been challenged by Smith et al. (2017) who argues that the Mulch et al. (2015) data for pre-uplift isotope values are from lacustrine samples that have been strongly affected by evaporation and they argue that surface uplift likely occurred after the formation of the Eocene lakes, possibly during the Oligocene (Cassel et al., 2018). However, very low $\delta^{18}O$ values in the full isotopic record are consistent with high elevations occurring during the Eocene (Mulch et al., 2015). To place new constraints on this issue we focused on the Eocene lacustrine cherts because the triple oxygen isotopes allow us to quantitatively assess evaporative effects and previous work demonstrated significant spread in the $\delta^{18}O$ of the chert samples from the Elko Formation (Abruzzese et al., 2005).

Our findings suggest that paleoelevation estimates using volcanic glass δD values (Smith et al., 2017; Cassel et al., 2018) give higher elevations than the data derived here from the basin depocenter indicating lower hypsometric mean elevations. Nonetheless, the findings presented below suggest a >2.5 km elevation in the Elko Basin region during the middle Eocene and surface uplift of about 1–1.5 km between deposition of the Cherty Limestone at 42–43.5 Ma and the late Eocene, ∼38–40 Ma.

ISOTOPE NOTATION AND SYSTEMATICS

We summarize the isotope notation used in this study and define the nomenclature and fractionation factors used for the

triple oxygen and carbonate clumped isotope measurements as well as the subsequent calculations. Isotopic abundance ratio is reported here in both standard and linear notation. The standard δ-notation is defined as (McKinney et al., 1950):

$$\delta^{x}Y = \left(\frac{{}^{x}R_{sample}}{{}^{x}R_{standard}} - 1\right) \times 1000 \quad (1)$$

where x is the heavier mass of interest, Y is oxygen (O), carbon (C) and R is the ratio of interest (i.e., $^{18}O/^{16}O$, $^{17}O/^{16}O$, $^{13}C/^{12}C$). We report chert oxygen isotopes ($\delta^{18}O$ and $\delta^{17}O$) relative to the VSMOW2-SLAP2 scale via primary standards (Wostbrock et al., 2020; see section "Materials and Methods"), and the carbonate oxygen and carbon isotopes ($\delta^{18}O$ and $\delta^{13}C$) relative to the VSMOW and VPDB standards, respectively, normalized via carbonate standards. Equilibrium fractionation (α) between two phases (A and B) is:

$$\alpha_{A-B} \equiv \frac{R_A}{R_B} = \frac{\delta_A - 1000}{\delta_B - 1000} \quad (2)$$

We are interested in oxygen isotope fractionation between water and minerals ($CaCO_3$-H_2O and SiO_2-H_2O), as well as oxygen isotope fractionation between liquid and vapor water during lake water evaporation.

Following the recent triple oxygen isotope literature (e.g., Pack and Herwartz, 2014; Passey et al., 2014; Sharp et al., 2018; Barkan et al., 2019; Passey and Ji, 2019; Liljestrand et al., 2020; Bindeman, 2021; Herwartz, 2021; Zakharov et al., 2021), we report our oxygen isotope data using linear notation, which removes curvature when comparing $\delta^{18}O$ and $\delta^{17}O$ variations (Hulston and Thode, 1965; Miller, 2002):

$$\delta'^{x}O \equiv 1000ln\left(\frac{\delta^{x}O}{1000} + 1\right) \quad (3)$$

where *x* is either 17 or 18 (as in ^{17}O or ^{18}O). In linearized notation the equilibrium fractionation equation between two phases (A and B) is:

$$1000ln\,(\alpha_{A-B}) = \delta'^{x}O_A - \delta'^{x}O_B \quad (4)$$

The fractionation of ^{17}O relative to ^{18}O is given by the following equations [standard (eq. 5) and linearized (eq. 6) forms]:

$$\alpha^{17}O_{A-B} = \left(\alpha^{18}O_{A-B}\right)^{\theta} \quad (5)$$

$$ln\left(\alpha^{17}O_{A-B}\right) = \theta \times ln(\alpha^{18}O_{A-B}) \quad (6)$$

where θ is ∼0.5 and is defined, for the triple oxygen isotopes, as

$$\theta_{A-B} = \frac{\delta'^{17}O_A - \delta'^{17}O_B}{\delta'^{18}O_A - \delta'^{18}O_B} \quad (7)$$

representing the mass law associated with physical processes (e.g., mineral precipitation, evaporation, etc.). Originally, variations in θ were observed to be close to ∼0.5, and thus it was thought that the measurement of $\delta^{17}O$ provided no new additional information (Craig, 1957). Recent high-precision work and theory demonstrates measurable (10 s of ppm level) variations in θ for Earth-surface processes like the temperature dependence of equilibrium fractionation during mineral precipitation (θ = 0.5237–0.5255 for SiO_2-H_2O fractionation from 0 to 100°C; Cao and Liu, 2011; Sharp et al., 2016; Hayles et al., 2017; Wostbrock et al., 2018), equilibrium condensation and evaporation of water vapor (θ = 0.529; Barkan and Luz, 2005), and water vapor diffusion (θ = 0.5185; Barkan and Luz, 2007; θ = 0.5194; Yeung et al., 2018), all of which are lower than the theoretical infinite-temperature end-member (θ = 0.5305; Matsuhisa et al., 1978; Young et al., 2002). To visualize variations graphically and normalize to a specific process (Meijer and Li, 2006; Passey et al., 2014; Sharp et al., 2016, 2018; Barkan et al., 2019; Passey and Ji, 2019; Sha et al., 2020; Bindeman, 2021; Herwartz, 2021; Miller and Pack, 2021; Zakharov et al., 2021) we define a reference slope λ_{RL} to look at small deviations in $\delta'^{17}O$ relative to $\delta'^{18}O$ using $\Delta'^{17}O$ notation (sometimes also denoted ^{17}O-excess):

$$\Delta'^{17}O = \delta'^{17}O - \lambda_{RL} \times \delta'^{18}O + \gamma \quad (8)$$

where γ is the y-intercept (zero in this and most work) in $\delta'^{17}O$ vs. $\delta'^{18}O$ space.

We choose a λ_{RL} value of 0.528 to normalize for variations related to meteoric water processes (Luz and Barkan, 2010). Passey and Ji (2019) recently demonstrated modern waters in western North America also fall along this slope (see also Li et al., 2015) with an intercept of $\Delta'^{17}O = 0.032 \pm 0.015‰$. This choice is similar to using a global or local slope of ∼8 for δD vs. $\delta^{18}O$ measurements (i.e., the "Global Meteoric Water Line"; Craig, 1961; Rozanski et al., 1993). Water vapor diffusion from evaporation into an undersaturated atmosphere (i.e., relative humidity below 100%) yields a slope between 0.529 and 0.5185, thus negative deviations from our reference slope of 0.528 can indicate evaporative lacustrine processes like those observed in modern and Quaternary lake systems (e.g., Passey et al., 2014; Surma et al., 2015, 2018, 2021; Herwartz et al., 2017; Gázquez et al., 2018; Evans et al., 2018; Passey and Ji, 2019; Aron et al., 2020). For the calculations carried out in this work we use the model presented by Passey and Ji (2019) (see their Table 1 and "Materials and Methods" section "Back-Calculation of Unevaporated Waters and Paleoaltimetry Calculations" below). Further, we use here the temperature-dependent equilibrium oxygen isotope fractionation (α) and mass law exponent (θ) for SiO_2 (quartz or opaline phases) and water derived empirically by Sharp et al. (2016) and Wostbrock et al. (2018).

Carbonate clumped isotope thermometry on lacustrine deposits allow for the deconvolution of temperature (via carbonate mineral formation temperatures determined by Δ_{47}, defined below) and water $\delta^{18}O$ values (from which carbonate minerals form) (e.g., Ghosh et al., 2006a; Affek et al., 2008; Passey et al., 2010; Huntington et al., 2010; Eiler, 2011; Lechler et al., 2013; Huntington and Lechler, 2015; Petryshyn et al., 2015; Methner et al., 2016). Given isotopic equilibrium, the tendency of heavier isotopes to "clump" together is only temperature dependent (Eiler, 2007, 2011), and requires only a single mineral phase that can be accurately and precisely measured as Δ_{47},

defined as (Ghosh et al., 2006b; Huntington et al., 2009):

$$\Delta_{47} = \left[\left(\frac{^{47}R}{^{47}R^*} - 1\right) - \left(\frac{^{46}R}{^{46}R^*} - 1\right) - \left(\frac{^{45}R}{^{45}R^*} - 1\right)\right] \times 1000 \quad (9)$$

where ^{x}R is for CO_2 relative to mass 44 (i.e., $^{47}R = [^{47}CO_2]/[^{44}CO_2]$), and the superscript * is the R value for a system with a stochastic distribution (i.e., high-temperature) for the same bulk composition calculated from the abundance of ^{13}C and ^{18}O in the sample.

Lastly, combinations of temperatures derived from Δ_{47} values along with the $\delta^{18}O$ values of carbonates allow the $\delta^{18}O$ of the formation fluid, in this case lake water, to be calculated (e.g., Came et al., 2007; Huntington et al., 2010; Lechler et al., 2013). For the calculations carried out here we use the temperature-dependent equilibrium oxygen isotope fractionation of Kim and O'Neil (1997) (and updated by Kim et al., 2007) for inorganic calcite and the temperature calibration of Petersen et al. (2019).

MATERIALS AND METHODS

Chert Triple Oxygen Isotope Measurements

Chert samples analyzed in this study were 2–4 mg chips of hand samples from Horton et al. (2004) and Abruzzese et al. (2005). Chips were tested for carbonate using HCl, and only those without carbonate were analyzed. We performed triple oxygen isotope measurements using a Thermo Scientific^{TM} 253 Plus 10kV Isotope Ratio Mass Spectrometer (IRMS) on chert samples at Stanford University with O_2 as the analyte. We generated O_2 gas from silicates using the laser fluorination method after Sharp (1990), on the setup described in Chamberlain et al. (2020) (see also Sharp et al., 2016; Wostbrock et al., 2018, 2020; Lowe et al., 2020; Kukla et al., 2021). This setup is similar to recent studies from other labs producing triple oxygen isotope measurements of chert and silica (Pack and Herwartz, 2014; Levin et al., 2014; Liljestrand et al., 2020; Sengupta et al., 2020; Zakharov et al., 2021). Two to four micrograms of samples are loaded into the vacuum line sample chamber. For a given set of analyses, we generally load 2–3 standards and 3–4 samples. Following loading, samples were pumped down to <10 mbar using a turbopump and then pre-fluorinated with 30 Torr BrF_5 in order to remove absorbed water before analysis. This pre-fluorination step is repeated until it generates <2 mbar of non-condensible gas in a liquid nitrogen trap. When possible, the samples and standards were loaded and vacuumed by turbopump overnight or over several days prior to pre-fluorination.

Following pre-fluorinations, we add 130 mbar BrF_5 to the sample chamber and heat the sample using a 50 W CO_2 infrared laser (Elemental Scientific Lasers/New Wave Research MIR10-25). Consistent with the results of Sharp (1990), we found that we achieve better reproducibility for isotopic measurements and sample yields if the laser fluorination of samples is completed within 5 min. Following laser fluorination, excess BrF_5 is frozen into a liquid nitrogen trap and the evolved O_2 gas is passed over a heated NaCl trap to remove produced waste gases (such as F_2) and then frozen onto a 5 Å mol sieve immersed in liquid nitrogen. The sample is then thawed at room temperature, entrained in a high purity He stream, and passed through a through a GC column to remove NF_3 and other contaminants and refrozen in another 5 Å mole sieve trap immersed in liquid nitrogen. Helium is then pumped away (with the trap still immersed in liquid nitrogen) and the 5 Å mol sieve is heated using heat tape and a heat gun to release the trapped O_2. This purified O_2 is then introduced to and equilibrated with the IRMS sample-side bellow for 6 min. During this equilibration step, the bellow is cycled from 25 and 75% compression ~6 times.

Samples are measured against an O_2 reference tank ($\delta^{18}O$ = 24.067) with an oxygen isotope composition similar to air and chert samples analyzed in this study. Mass 32, 33, and 34 ion beams are collected on faraday cups, slit widths of 4.5, 1.5, and 4.5 mm, respectively, with a 3×10^{13} Ω amplifier for mass 33. Samples are measured at a mass 32 ion-beam intensity of 5–7 volts in blocks that consistent of 10 sample-standard brackets with 36 second integrations and 30 s of equilibration. Between 4 and 7 acquisitions are measured per sample (1.5–3 h) until $\Delta'^{17}O$ precision is <0.01‰ (SE) for an individual dual inlet measurement on gas from a single fluorination. We applied a pressure baseline correction following methods similar to Yeung et al. (2018) to account for $\Delta'^{17}O$ variations due to mass spectrometer and source conditions (see also Yeung and Hayles, 2021). Specifically, we measured the negative voltage to the left of the mass 33 peak and calibrated this baseline correction (additional or missing voltage) against the mass $^{32}O_2$ intensity every session (2 weeks to 1 month). All of our reported sample and standard analyses are relative to the mean published high-precision L1/UNM_Q ($\delta^{18}O$ = 18.070; $\Delta'^{17}O$ = −0.076) values reported in Wostbrock et al. (2020) on the VSMOW2-SLAP2 scale adjusted for a new calibration of SCO, UWG-2, and NBS 28 (Sharp and Wostbrock, 2020), which are also measured regularly in our laboratory (Chamberlain et al., 2020; Lowe et al., 2020). Both $\delta^{18}O$ and $\Delta'^{17}O$ values are measured here relative to L1/UNM_Q. For $\delta^{18}O$ measurements, we correct the data to the measured standards from a given day's batch of measured samples. For $\Delta'^{17}O$, values were standardized based on the average values of standards measured in a given session. In this case all samples were measured during one session over several weeks in 2019 that amounted to 10 total analysis days. Two samples were measured in replicate and we report the number of acquisitions measured as well as the (SE) for each individual dual inlet measurement on gas from a single fluorination.

During the session of analyses presented here, we also measured two secondary SiO_2 standards. One of these is a low $\delta^{18}O$ quartz (Sandia quartz; $\delta^{18}O$ = 0.72 ± 0.05, n = 3) also used as an internal standard at University of New Mexico, and the other secondary standard is an in-house chert standard (CH-1; $\delta^{18}O$ = 22.87 ± 0.04, n = 2) previously analyzed in the Stanford laboratory (e.g., Abruzzese et al., 2005; Hren et al., 2009). CH-1 has not been previous measured for $\Delta'^{17}O$. The Sandia quartz has previously been measured at the University of New Mexico ($\delta^{18}O$ = 0.78 and $\Delta'^{17}O$ = −0.016; *Personal Communication*, Wostbrock et al., 2018), within error of our measurements ($\Delta'^{17}O$ = −0.012 ± 0.022, n = 3; **Table 1**).

TABLE 1 | Lacustrine chert triple oxygen isotope measurements.

Sample ID	Height (m from top)	Chert $\delta^{18}O$ (VSMOW2-SLAP2)	Chert $\delta'^{18}O$ (VSMOW2-SLAP2)	Chert $\delta'^{17}O$ (VSMOW2-SLAP2)	Chert $\Delta'^{17}O$ (λ_{RF} = 0.528)	Chert $\Delta'^{17}O$ SE	No. of acquisitions	Lake water $\delta'^{18}O$ (32°C; scenario 1)	Lake water $\Delta'^{17}O$ (32°C; scenario 1)	Lake water $\delta'^{18}O$ (60°C; scenario 2)	Lake water $\Delta'^{17}O$ (60°C; scenario 2)
CL03	10	20.137	19.937	10.441	−0.086	0.007	5	−14.224	0.035	−7.999	−0.001
CL04	30	21.602	21.372	11.173	−0.111	0.006	7	−12.789	0.010	−6.565	−0.026
CL05	50	22.901	22.643	11.870	−0.085	0.007	5	−11.518	0.036	−5.293	0.000
CL05 rep	50	23.328	23.060	12.075	−0.101	0.007	5	−11.100	0.020	−4.876	−0.016
CL06	80	20.583	20.374	10.649	−0.108	0.008	5	−13.786	0.013	−7.562	−0.023
CL09	120	18.911	18.735	9.810	−0.082	0.008	5	−15.426	0.040	−9.201	0.003
CL10	125	n.m.									
CL11	140	16.987	16.844	8.823	−0.070	0.006	7	−17.316	0.051	−11.092	0.015
CL12	155	23.414	23.145	12.119	−0.102	0.007	5	−11.016	0.020	−4.792	−0.016
CL13	170	17.617	17.464	9.139	−0.082	0.007	5	−16.697	0.039	−10.472	0.003
CL14	180	n.m									
CL15	200	n.m									
CL17	210	22.146	21.904	11.456	−0.109	0.007	5	−12.256	0.012	−6.032	−0.024
CL18	220	n.m									
CL19	250	18.677	18.505	9.689	−0.082	0.008	5	−15.656	0.040	−9.431	0.003
CL21	255	n.m									
CL22	270	22.779	22.523	11.788	−0.104	0.009	4	−11.638	0.017	−5.413	−0.019
CL23	290	17.861	17.704	9.250	−0.097	0.007	6	−16.457	0.024	−10.232	−0.012
CL23 rep	290	16.909	16.768	8.787	−0.066	0.006	7	−17.393	0.055	−11.168	0.019
CL24	295	n.m									

Sample ID	Age (Ma) H2004	Chert $\delta^{18}O$ (VSMOW) H2004/A2005	Carbonate $\delta^{18}O$ (VSMOW) H2004/A2005	Carbonate $\delta^{13}C$ (VPDB) H2004/A2005	Carbonate $\delta^{18}O$ (VSMOW) M2015	Carbonate $\delta^{13}C$ (VPDB) M2015
CL03	42.0	18.9	19.2	−4.4		
CL04	42.1	21.8	20	−3.9		
CL05	42.2	23.0	20.1	−2.0		
CL05 rep	42.2					
CL06	42.5	18.0	23.0	−3.8		
CL09	42.6	19.5	17.8	−3.4		
CL10		15.6	21.2	−2.8	21.8	−2.1
CL11	42.8	15.6	18.3	−2.5	18.9	−2.5
CL12	42.9	21.5			19.2	−2.0
CL13	42.9	18.4	20.3	−4.1		
CL14		15.6	16.9			
CL18		14.9	17.2	−2.7	21.1	−4.4
CL19	43.2	20.9				
CL21		15.9	29.9	−3.0		

(Continued)

TABLE 1 | Continued

Sample ID	Age (Ma) H2004	Chert $\delta^{18}O$ (VSMOW) H2004/A2005	Carbonate $\delta^{18}O$ (VSMOW) H2004/A2005	Carbonate $\delta^{13}C$ (VPDB) H2004/A2005	Carbonate $\delta^{18}O$ (VSMOW) M2015	Carbonate $\delta^{13}C$ (VPDB) M2015
CL22	43.3	23.1	20.2	−5.5		
CL23	43.4	18.1	19.2	−5.6		
CL23 rep	43.4					
CL24	43.5	19.8	17.4			
Quartz standards	**n**	**$\delta'^{18}O$ (VSMOW2-SLAP2)**	**$\delta^{18}O$ SD**	**$\delta'^{17}O$ (VSMOW2-SLAP2)**	**$\Delta'^{17}O$ (λ_{RF} = 0.528)**	**$\Delta'^{17}O$ SD**
UNM_Q	13	17.903	0.073	9.378	−0.075	0.016
Sandia	3	0.721	0.059	0.369	−0.012	0.022
CH-1	2	22.873	0.036	12.000	−0.077	0.019

H2004—Horton et al. (2004); A2005—Abruzzese et al. (2005); M2015—Mulch et al. (2015). The dataset is normalized to UNM_Q values given in Wostbrock et al. (2020) ($\delta'^{18}O$ = 17.909; $\Delta'^{17}O$ = −0.076) corrected to VSMOW2-SLAP2 via SCO, UWG-2, and NSB-28 in Sharp and Wostbrock (2020). The standard error (SE) of $\Delta'^{17}O$ measurements is from individual dual inlet analyses of the gas produced from a single fluorination, with the number of acquisitions listed in the adjacent column, where one acquisition is 10 sample-standard brackets with 36 s integrations per side. See section "Materials and Methods" for more information. n.m., not measured.

Carbonate Clumped Isotope Measurements

Carbonate clumped (Δ_{47}) and stable ($\delta^{13}C$, $\delta^{18}O$) isotope measurements from the Elko Formation were performed on three lake carbonate samples originally reported in Mulch et al. (2015). Carbonate clumped isotope analyses were conducted at the Goethe University-Senckenberg BiK-F Stable Isotope Facility Frankfurt, Germany, following methods outlined in detail in Wacker et al. (2013) and Fiebig et al. (2016). Carbonate powder (8–12 mg) was digested in >106% phosphoric acid at 90°C ± 0.1°C for 30 min in a common acid bath. In brief, the evolved CO_2 gas was purified through cryogenic traps before and after passing through a Porapak Q-packed gas chromatography column with He carrier gas. Measurements of the cleaned CO_2 gas were made in dual inlet on a Thermo Scientific^{TM} MAT 253 IRMS for 10 acquisitions consisting of 10 cycles with an ion integration time of 20 s per cycle. CO_2 gases equilibrated at 1,000 and 25°C were measured along with the samples to establish the empirical transfer function and the Δ_{47} values reported here are in the "absolute reference frame" (ARF) (Dennis et al., 2011), also referred to in the literature as the "carbon dioxide equilibrated scale" (CDES). All data was processed using the IUPAC parameters (Daëron et al., 2016). We applied the 25−90°C acid fractionation factor of 0.088‰ and the temperatures calibration of Petersen et al. (2019).

One or two carbonate reference materials were analyzed each measurement day, including Carrara marble, *Arctica islandica* (also referred to as MuStd, a well-homogenized shell material of an aragonitic cold water bivalve), ETH-1, and ETH-3. During the measurement period, we obtained a mean Δ_{47} value of 0.205‰ ± 0.004‰ (SE, n = 6) for ETH-1 and of 0.614‰ ± 0.005‰ (SE, n = 7) ETH-3, which are similar to the long-term values reported in Bajnai et al. (2020). We use the Gonfiantini parameters and apply a 25−90°C acid fractionation factor of 0.069‰ to the Δ_{47} measurements of Carrara marble and *Arctica islandica* in order to compare them to previously reported Δ_{47} values of these carbonates. The mean Δ_{47} value of Carrara marble is 0.390‰ ± 0.005‰ (SE, n = 6), which is just greater than the long-term in-house mean Δ_{47} value of Carrara marble of 0.376‰ ± 0.002‰ (SE, n = 58) (Methner et al., 2020). The mean Δ_{47} value of *Arctica islandica* is 0.722‰ ± 0.007‰ (SE, n = 7), which is indistinguishable from the 0.724‰ ± 0.004‰ (SE, n = 28) reported by Wacker et al. (2013). All carbonate clumped data are provided in a comprehensive clumped isotope results and calculations **Supplementary Material**.

In addition to the new carbonate clumped isotope data we report the complete $\delta^{13}C$ values associated with the legacy $\delta^{18}O$ measurements (n = 15) originally made by Abruzzese et al. (2005) (see their Table 1 and "Materials and Methods" section for details), some of which (n = 6) were also remeasured in the dataset reported in Mulch et al. (2015).

Back-Calculation of Unevaporated Waters and Paleoaltimetry Calculations

In this study we follow the approach of Passey and Ji (2019) to back-calculate the unevaporated source water $\delta^{18}O$

value. Passey and Ji (2019) use a simple steady state model for throughflow and closed basin (terminal) lakes first developed by Criss (1999) modified for triple oxygen isotopes (e.g., Herwartz et al., 2017; Gázquez et al., 2018; Surma et al., 2018; Aron et al., 2020) to describe the isotopic composition of the lake water (R_W):

$$R_W = \frac{\alpha_{eq}\alpha_{diff}\left(1-h\right)R_I h X_E R_A}{X_E + \alpha_{eq}\alpha_{diff}\left(1-h\right)\left(1-X_E\right)} \quad (10)$$

where R_I and R_A are the isotope ratios of inflowing river water and ambient atmospheric water, respectively, h is the relative humidity, α_{eq} and α_{diff} are the equilibrium and kinetic fraction factors associated with lake water evaporation, and X_E is the volumetric fraction of inflowing water lost to evaporation. Applying this model to triple oxygen isotopes, and calibrating using four Quaternary lake systems in the western United States, Passey and Ji (2019) derive a model-based approach for inferring the isotopic composition of the incoming source water ($\delta'^{18}O_{source}$) as a function of lake water $\delta'^{18}O$ and $\Delta'^{17}O$:

$$\delta'^{18}\,O_{source} = \frac{\Delta'^{17}O_{MWL} - \Delta'^{17}\,O_{lake} + (\lambda_{lake} - \lambda_{RL})\delta'^{18}\,O_{l}ake}{\lambda_{lake} - \lambda_{RL}} \quad (11)$$

$$\lambda_{lake} = 1.985 \times \left(\Delta'^{17}O_{lake}\right)^3 + 0.5730 \times \left(\Delta'^{17}O_{lake}\right)^2 + 0.0601 \times \Delta'^{17}O_{lake} + 0.5236 \quad (12)$$

where $\Delta'^{17}O_{MWL}$ is the intercept of the meteoric water line (0.032 ± 0.015), $\delta'^{18}O_{lake}$ and $\Delta'^{17}O_{lake}$ are the isotopic composition of the lake, λ_{RL} is the reference slope (defined above as 0.528) and λ_{lake} was determined empirically using Monte Carlo simulations of all parameters in Eq. 10 to determine the polynomial shown in Eq. 12 (see Passey and Ji (2019), their Figure 2 and Table 1). The intercept of the meteoric water line may not be stationary in time due to changes in climate (e.g., humidity, moisture recycling over continents, etc.: Aron et al., 2020; Surma et al., 2021), though modeling studies suggest that Eocene $\delta^{18}O$-δD have been relatively stationary with respect to slope and intercept, with a significantly compressed global range (Speelman et al., 2010), though it is still unknown how $\delta^{18}O$-δD relationships map onto $\delta'^{18}O$–$\Delta'^{17}O$ in space and time, and as constrained by modern datasets (Passey and Levin, 2021). In our primary calculations we fix the $\Delta'^{17}O_{MWL}$ intercept; however, because this is an uncertainty and factors controlling the $\Delta'^{17}O_{MWL}$ intercept today are still to be worked out in subsequent sensitivity tests we demonstrate the effect of this assumption to our calculations across the full range of plausible meteoric water line intercepts for the western United States (see **Figure 3B**). In this study, following transfer of chert $\delta'^{18}O$ and $\Delta'^{17}O$ measurements to $\delta'^{18}O_{lake}$ and $\Delta'^{17}O_{lake}$ values using the appropriate empirically derived SiO_2-H_2O fractionation factors (Sharp et al., 2016; Wostbrock et al., 2018; Wostbrock and Sharp, 2021; see also theoretical fractionation factors derived by: Cao and Liu, 2011; Hayles et al., 2018; Schauble and Young, 2021; Yeung and Hayles, 2021) we directly apply Eqs. 11 and 12 to calculate the unevaporated source water when reconstructed lake waters are evaporative (i.e., $\Delta'^{17}O_{lake}$ values less than the MWL). We then assume that this $\delta'^{18}O_{source}$ value represents the basin's hypsometric mean elevation (i.e., the elevation hypsometry upslope of the basin) and apply the model of Rowley et al. (2001) to calculate Eocene paleoelevation of the deposits, similar to our approach recently employed in Chamberlain et al. (2020) for Eocene hydrothermal alteration of the Idaho Batholith.

RESULTS

Chert Oxygen Isotopes

Our triple oxygen isotope external reproducibility (1σ) during the session of analyses based on the primary standard used to correct $\delta^{18}O$ and $\Delta'^{17}O$ data (hydrothermal quartz standard L1/UNM_Q) is ±0.073‰ for $\delta^{18}O$ and 0.016‰ for $\Delta'^{17}O$ (± 1σ; n = 13). Replicates of two samples (CL05 and CL23) indicate similar reproducibility for $\Delta'^{17}O$ (±0.011 and ±0.022‰, respectively) but larger $\delta^{18}O$ variation (±0.295 and ±0.662‰). Comparison to previous measurements made on powders from Horton et al. (2004) and Abruzzese et al. (2005) indicate good agreement [$\delta^{18}O$ difference between the datasets of −0.1 ± 1.3‰ (n = 14)] though we note that we analyzed chips from the same hand samples, not the same sample powders as in the original studies.

Our dataset span 6.5‰ in $\delta^{18}O$ (16.9–23.4‰) and we observe a negative correlation with $\Delta'^{17}O$ ranging from −0.066 to −0.111‰ (**Figure 1A** and **Table 1**). We calculate an empirical slope (λ_{chert}, $\delta'^{17}O$ vs. $\delta'^{18}O$) of 0.5236, a value between the slopes expected for processes related to meteoric water and SiO_2 precipitation (0.528–0.524), and kinetic fractionation associated with evaporating water (>0.5185) (see section "Isotope Notation and Systematics").

Carbonate Oxygen, Carbon, and Clumped Isotopes

New carbonate clumped isotope measurements from the Elko Formation yielded Δ_{47} values of 0.680–0.710‰, corresponding to temperatures (following Petersen et al., 2019) of 17.8 ± 8.8 °C to 39.9 ± 3.4°C (1σ, **Table 2**). The Elko Formation carbonates are younger than the Cherty Limestone chert. However, as described below, given the existing age constraints, and the overlap in carbonate $\delta^{18}O$ and $\delta^{13}C$ values, the Elko Formation measurements provide a useful constraint on the triple oxygen isotope chert dataset. We calculate an error weighted mean temperature of 32.5 ± 3.8°C (MSWD = 3.9; **Table 2**). The error of this mean temperature is propagated in our subsequent calculations (see Scenario 1 in the section "Discussion"). Our calculated MSWD value for the error weighted mean temperature greater than 1 indicates over-dispersion of the dataset unrelated to analytical precision, which is likely a result of geologic scatter. These values are similar to the average temperatures (28.5 and 35°C) to Early Eocene stromatolites from the Rife Bed, Tipton Shale Member of the Green River Formation reported by Frantz et al. (2014). Similar to carbonate clumped isotope datasets from Quaternary lake systems (e.g., Hudson et al., 2017; Santi et al., 2020) this spread is indicative of

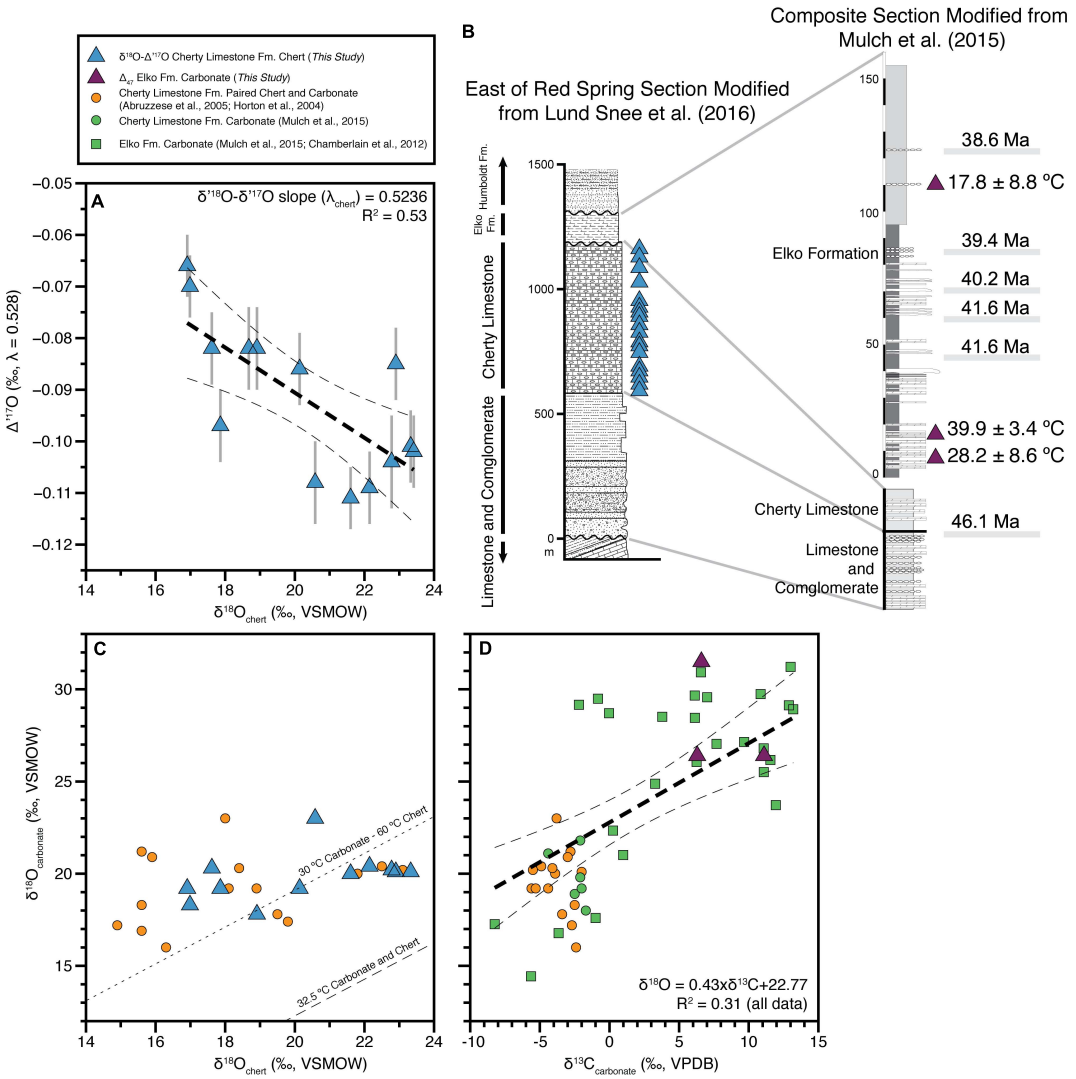

FIGURE 1 | Cross plots of isotope datasets from the Elko Basin. **(A)** $\delta^{18}O$ and $\Delta'^{17}O$ of chert from the Cherty Limestone (*This Study*). The λ_{chert} slope of 0.5236 was calculated in $\delta'^{18}O$ vs. $\delta'^{17}O$ space (not shown). $\Delta'^{17}O$ error bars are 1 SE of the analytical measurements (see section "Materials and Methods"). **(B)** Stratigraphic sections simplified from Lund Snee et al. (2016) and modified from Mulch et al. (2015) summarizing the Elko Basin stratigraphy and sample locations (vs. stratigraphic height) within the Cherty Limestone and Elko Formations. Ages are from $^{40}Ar/^{39}Ar$ geochronology (Mulch et al., 2015). The reader is referred to Lund Snee et al. (2016) for sampling localities (see their Figure 1B). **(C)** $\delta^{18}O$ of chert vs. carbonate in the Cherty Limestone Formation [*This Study*, Horton et al. (2004) and Abruzzese et al. (2005)]. Contours are for assumed co-equilibrium at 32.5°C [carbonate formation temperature (Δ_{47}) weighted mean = 32.5 ± 3.8°C (1σ, MSWD = 3.9)] and 30°C carbonate paired with 60°C chert using the fractionation factors of Kim and O'Neil (1997) and Sharp et al. (2016) (following Abruzzese et al., 2005). **(D)** Carbonate $\delta^{18}O$ and $\delta^{13}C$ in both the Cherty Limestone and Elko Formations [*This Study* ($n = 3\times\Delta_{47}$ measurements), Horton et al. (2004), Abruzzese et al. (2005), Chamberlain et al. (2012) and Mulch et al. (2015)]. The linear regression and confidence intervals are calculated through all data from both formations. As shown in the legend triangles are new measurements from this study, circles are previous measurements of paired carbonate and chert samples from the Cherty Limestone Fm. and squares are previous carbonate measurements from the Elko Fm.

a seasonally evaporitic lake system forming carbonates year around, though the climate system (e.g., the seasonality of temperature, precipitation and humidity) was likely quite different in the Eocene (e.g., Hyland et al., 2018). Based on modern lapse rates (Huntington et al., 2010) these temperatures would put our lake basin and the Green River Formation in Wyoming (Frantz et al., 2014) at <500 m, much lower than the oxygen and hydrogen isotope-based methods would suggest (see section "Discussion"). We propose that these temperatures are likely biased toward seasonal summer/warm month carbonate formation, evidenced by a reduced range in the carbonate $\delta^{18}O$ values relative to the chert $\delta^{18}O$ values (**Figure 1C**). Given the hotter mean annual temperature, and a proposed similar seasonality in temperature in the continental interior during the Eocene (Hyland et al., 2018), the temperature range and magnitude are reasonable, though clearly further work is necessary to better constrain temperatures via clumped isotopes in the Elko Basin and possibly, in combination with

TABLE 2 | Carbonate stable ($\delta^{18}O$ and $\delta^{13}C$) and clumped isotope (Δ_{47}) results and calculated oxygen isotopic ratios of lake water ($\delta^{18}O$).

Sample ID	Stratigraphic Height (m) M2015	Age (Ma) M2015	Replicates	Carbonate $\delta^{18}O$ (VSMOW) M2015	Carbonate $\delta^{13}C$ (VPDB) M2015	$\Delta_{47,ARF}$ (‰)	Δ_{47} SD	Δ_{47} SE	Temperature (°C)	Temperature SD	Lake Water $\delta^{18}O$ (VSMOW)	Lake Water $\delta^{18}O$ SD
NV-EF-05	8	42.5	4	31.5	6.6	0.680	0.024	0.019	28.2	8.6	3.45	2.42
NV-EF-08	17.5	42.0	3	26.4	11.1	0.649	0.008	0.011	39.9	3.4	0.67	0.88
NV-EF-24	110	39.9	3	26.4	6.3	0.710	0.027	0.034	17.8	8.8	−3.67	2.63
									Error weighted average (°C)	SD	MSWD	
									32.5	3.8	3.9	

Temperatures are calculated using an acid fractionation factor of +0.088‰ and the Petersen et al. (2019) calibration. Lake water $\delta^{18}O$ values are calculated by using pairs of Δ_{47} temperatures and carbonate $\delta^{18}O$ values and oxygen isotope fractionation coefficient of Kim and O'Neil (1997) (as updated by Kim et al., 2007). Carbonate $\delta^{18}O$ and $\delta^{13}C$ data are GasBench data originally reported by Mulch et al. (2015). Data produced during clumped isotope analyses differed by less than 1‰ in both $\delta^{18}O$ and $\delta^{13}C$. M2015—Mulch et al. (2015). ARF, AbsoLute Reference Frame, also referred to as the CDES (carbon dioxide equilibrated scale).

other sites, constrain and adjust the Eocene lapse rate for the western United States.

For the purposes of this work and because of our limited sample set, we use the carbonate clumped isotope data to interpret the triple oxygen isotope results from the lacustrine chert, since the chert formation temperature is itself unknown. Further, the carbonate clumped isotope data, in combination with the more extensive previous oxygen isotope measurements of both the Elko and Cherty Limestone Formations (Horton et al., 2004; Abruzzese et al., 2005; Chamberlain et al., 2012; Mulch et al., 2015), provide a target range for the plausible lake water $\delta^{18}O$ from which the carbonate formed assuming equilibrium fractionation and applying the $CaCO_3$-H_2O fractionation factor of Kim and O'Neil (1997). The target lake water $\delta^{18}O$ range is then a constraint on the lake water $\delta^{18}O$ from which the chert in the Cherty Limestone Formation may have formed.

The $\delta^{18}O$ and $\delta^{13}C$ values ($\delta^{18}O$ of 26.4–31.5‰ VSMOW, $\delta^{13}C$ of 6.3–11.1‰ VPDB) of the three clumped isotope measurements from the Elko Formation reflect evaporatively enriched values relative to the $\delta^{18}O$ and $\delta^{13}C$ values of incoming source water and dissolved inorganic carbon. These values are relatively high for Cenozoic lake basins in the western US, which range from approximately 10 to 32‰ VSMOW in $\delta^{18}O$ and approximately −6 to +12‰ VPDB in $\delta^{13}C$ values [see lacustrine samples in compilations by Davis et al. (2009) and Chamberlain et al. (2012)]. Further, these measurements are comparable to previous measurements from the Elko and Cherty Limestone Formations compiled in the box and whisker plots in **Figure 2B** (Horton et al., 2004; Abruzzese et al., 2005; Chamberlain et al., 2012; Mulch et al., 2015; with legacy $\delta^{13}C$ data reported for the first time in **Table 1**). Lake water $\delta^{18}O$ values derived from the three lacustrine carbonate clumped isotope measurements range from −3.7 to +3.5‰ VSMOW (**Table 1** and **Figure 2**). Applying the weighted mean formation temperature (32.5°C) to all samples from the Elko Formation and the Cherty Limestone Formation yields formation water $\delta^{18}O$ of approximately −13 to +5‰ VSMOW. In the $\delta^{13}C$-$\delta^{18}O$ crossplot shown in **Figure 1C** the stable isotope data of the two formations define a robust positive correlation, typical of evaporation trends for lacustrine systems (Li and Ku, 1997; Davis et al., 2009; Horton and Oze, 2012; Chamberlain et al., 2013; Ibarra et al., 2014; Ibarra and Chamberlain, 2015; Horton et al., 2016; Ingalls et al., 2020b). We note that in this limited carbonate dataset we do not see a systematic relationship between the enrichment of $\delta^{18}O$ and $\delta^{13}C$ in the positive evaporation trend and the carbonate clumped isotope derived temperatures.

DISCUSSION

Comparison of Oxygen Isotopes of Chert and Associated Carbonate

In the original work of Abruzzese et al. (2005) the oxygen isotope data of the chert nodules, the same samples as those re-measured here for $\delta^{18}O$ and $\Delta'^{17}O$, and their associated carbonate (carbonate and chert < 2 cm apart in hand sample) indicated a positive correlation. We pair our measurements

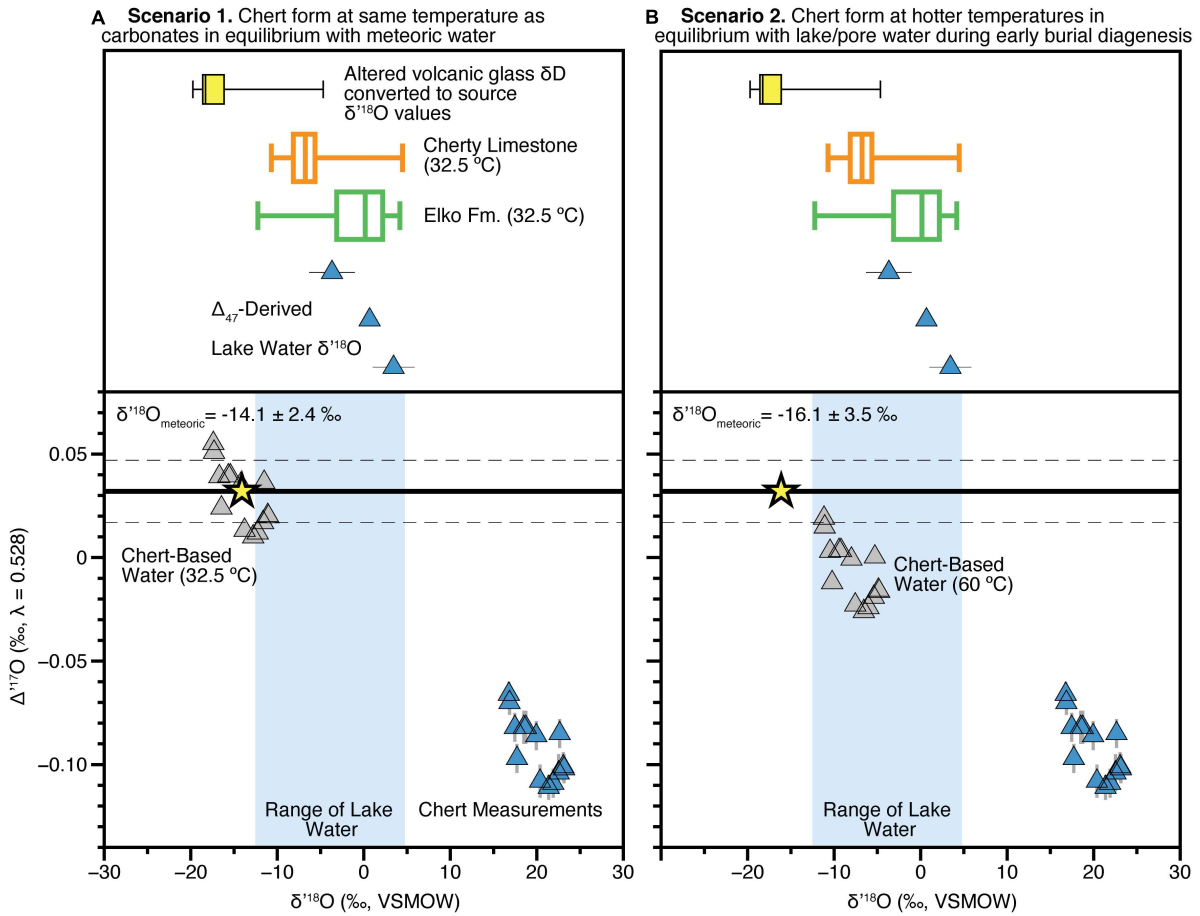

FIGURE 2 | Scenarios for interpreting chert triple oxygen isotope data. **(A)** In the upper panel we show the individual Δ_{47}-derived lake water $\delta^{18}O$ values (**Table 1**) from this study, as well as all data from the Elko (green) and Cherty Limestone (orange) Formations shown in **Figure 1** as box and whisker plots (Horton et al., 2004; Abruzzese et al., 2005; Chamberlain et al., 2012; Mulch et al., 2015). Yellow box and whisker plots are all Eocene volcanic glass δD data from the Elko Basin region measured by Cassel et al. (2014, 2018) assuming the glass-water fractionation factor determined by Friedman et al. (1993) and conversation to $\delta^{18}O$ using the global meteoric water line. The bottom panel shows the calculations assuming cherts formed at average carbonate formation temperature of 32.5°C (based on Δ_{47} measurements). Blue triangles are measurements, gray triangles are reconstructed lake water values (**Table 1**) and using the model equations of Passey and Ji (2019) with the reconstructed average meteoric source water value shown as a yellow star. The thick black line is the regional meteoric water (λ_{mwl} = 0.528, intercept = 0.032 ± 0.015) determined by Passey and Ji (2019), with the gray hashed horizontal lines representing the error. **(B)** As in **(A)** but using a chert formation temperature of 60°C, assumed to be in equilibrium with lake pore waters during early diagenesis.

with the associated carbonate measurements, as well as plot all data from the original study, and find the resulting trend is relatively unchanged (**Figure 1B**), though Abruzzese et al. (2005) did report some lower chert $\delta^{18}O$ values not measured here. Additionally, we rederive the temperature contours shown in Abruzzese et al. (2005) (see their **Figure 6**) by equating the fractionation factors from Kim and O'Neil (1997) and Sharp et al. (2016) assuming the samples formed from the same formation water (i.e., exhibiting identical $\delta^{18}O$ values) and in isotopic equilibrium. Importantly, the original fractionation factor for SiO_2-H_2O used by Abruzzese et al. (2005) from Knauth and Epstein (1976) has changed substantially at low (Earth surface) temperatures (see Sharp et al., 2016 for details), leading to a greater temperature sensitivity of chert $\delta^{18}O$ (a greater 1,000 lnα value). The 32.5°C contour (average Δ_{47}-temperature) does not pass through the samples shown on **Figure 1B** (lower right long dashed contour in the corner of **Figure 1B**). Assuming a ~30°C carbonate formation temperature, the best fit through our new data suggests a chert formation temperature of ~ 60°C (see dashed contour on **Figure 1B**), likely during early burial diagenesis, as originally suggested by Abruzzese et al. (2005). The total maximum overburden in the basin is less than 3,250 m; whereas the Eocene overburden is likely less than 1,250 m (Smith and Ketner, 1976; Abruzzese et al., 2005). The latter of which, given regional heat flow estimates (~65 mW/m^2) and thermal conductivities of similar sediments implemented in basin-scale modeling (e.g., Tong et al., 2017), makes 60°C a reasonable temperature estimate during early burial diagenesis. Using the old SiO_2-H_2O fractionation factors from Knauth and Epstein (1976) described above the paired $\delta^{18}O$-δD measurements of Abruzzese et al. (2005) originate from an equilibrium chert line of 40°C (see their **Figure 7**). As such, the new fractionation

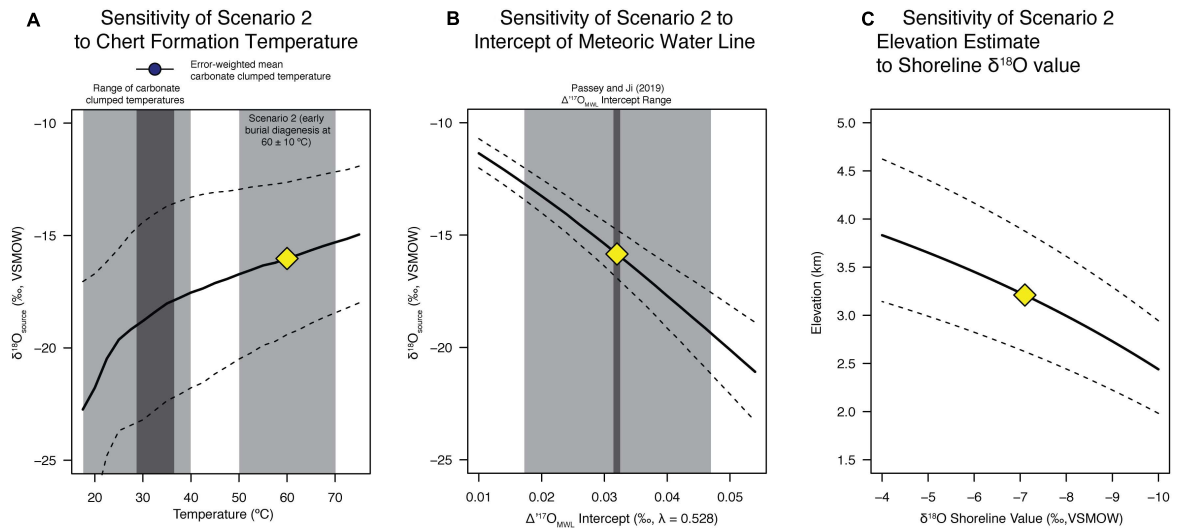

FIGURE 3 | Sensitivity of calculations to modeling assumptions. **(A)** Sensitivity of our scenario 2 results to the assumed chert formation temperature spanning 17.5–75°C in 2.5°C increments. The result for 60°C shown in **Figure 2B** is the yellow diamond. Monte Carlo uncertainty propagation (n = 50,000 iterations) using the measurement error (**Table 1**) and modeling uncertainty (Passey and Ji, 2019) is shown as dashed lines as 1σ uncertainty. **(B)** As in panel **(A)** but the sensitivity of our scenario 2 results to the assumed $\Delta'^{17}O_{MWL}$ intercept values. **(C)** Sensitivity of the calculated paleoelevation for scenario 2 based on the coastal shoreline precipitation $\delta^{18}O$ value, errors are the 95% confidence using the model of Rowley et al. (2001), as in **Figure 4**.

factors drive home the original interpretation that chert nodules and chert laminations of this type, with silica sourced from the weathering of volcanic glass and/or diatom blooms, commonly form from early burial diagenesis and/or dehydration of Opal A to microquartz. In marine settings the Opal A to microquartz transition has been found to occur between 50 and 70°C (Yanchilina et al., 2020), consistent with our estimate of Elko Basin chert formation at ∼60°C. However, given the freshwater nature of this system and the limited $\delta^{13}C$-$\delta^{18}O$ spread within the Cherty Limestone Formation, it also remains possible that the chert and coeval/associated carbonate did not form from waters of the same $\delta^{18}O$ value. To account for these alternative interpretations of our dataset, we propose two scenarios for deriving the $\delta^{18}O$ value of the basin source water. Both, however, allow for similar interpretations with respect to Eocene meteoric source water feeding the Elko Basin.

Estimates for Unevaporated Source Water $\delta^{18}O$ From Three Chert Formation Scenarios

First (Scenario 1), we evaluate the possibility that the Cherty Limestone Formation cherts precipitated at (Earth surface) temperatures similar to those suggested by Δ_{47} results from the overlying Elko Formation (**Figure 2**). This scenario is plausible given that the carbonate in the Cherty Limestone associated with the chert samples do overlap in $\delta^{18}O$ composition with some of the carbonate samples from the Elko Formation. This assumes that the climatic and hydrologic conditions were similar (i.e., a balance filled to overfilled lake system; Davis et al., 2009), though as described in the Results above, based on the absolute range of $\delta^{18}O$ values in the co-occurring Cherty Limestone carbonate vs. the chert (smaller vs. larger range, respectively in **Figure 1C**), it may be the case that the carbonates are warm season biased and chert formation is more annually distributed. Using the weighted mean clumped isotope derived temperature of 32.5°C and applying the SiO_2-H_2O triple oxygen isotope fractionation factor of Sharp et al. (2016) and Wostbrock et al. (2018) (θ = 0.5244 and α = 1.0348), we calculate from our chert samples water $\Delta'^{17}O$ values of 0.010–0.055‰ and an average source water value of $\delta'^{18}O$ of −14.1 ± 2.4‰ VSMOW (**Figure 2A**). These datapoints (gray triangles on **Figure 2A**) overlap the range of the meteoric water line for the western United States (Li et al., 2015; Passey and Ji, 2019), suggesting negligible evaporation of lake waters since evaporation leads to lower $\Delta'^{17}O$ values. Further, these $\delta'^{18}O$ values are significantly lower than those from coeval carbonate of the Cherty Limestone (shown as an orange box and whisker plot; **Figure 2A**). Thus, in this scenario we estimate a source $\delta'^{18}O$ of −14.1 ± 2.4‰ assuming that source and lake waters are isotopically indistinguishable.

Applying one single formation temperature is highly unlikely, given that we observe a spread of 6.5‰ in chert $\delta^{18}O$ values, and a negative correlation with $\Delta'^{17}O$ ranging from −0.066 to −0.111‰ with an empirical slope (λ_{chert}, $\delta'^{17}O$ vs. $\delta'^{18}O$) of 0.5236 (**Figure 1A**). As such, the negative correlation and spread would have to be explained by temperatures (assuming the mean value of 32.5°C) ranging from 21 to 47°C, a range comparable but larger than the range measured by the individual carbonate clumped isotope samples (note that this range is asymmetric because 1,000lnα is a function of 1/T with the largest fractionation factor at the coldest temperatures). However, the empirical slope of 0.5236 of our data set (λ_{chert}) is lower than the theoretical slopes for SiO_2-H_2O fractionation at this

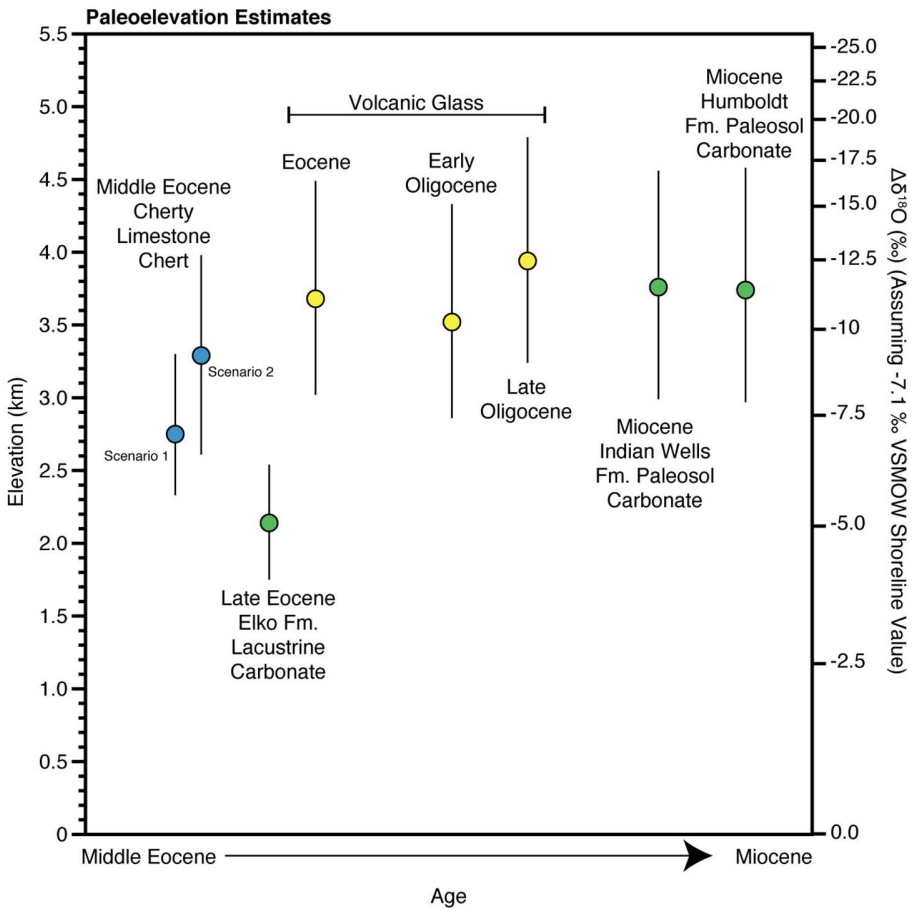

FIGURE 4 | Paleoelevations for this study and previous datasets (Horton et al., 2004; Mix et al., 2011; Chamberlain et al., 2012; Cassel et al., 2014, 2018; Mulch et al., 2015; Smith et al., 2017) as tabulated and calculated in **Table 3** using the model of Rowley et al. (2001). The volcanic glass samples include all samples east of the Eocene drainage divide to the west of the Elko Basin (Henry, 2008). Error bars are the 95% confidence (see **Table 3**).

temperature range (0.5242–0.5247), suggestive that evaporative processes must still influence a portion of the samples (lower $\Delta'^{17}O$ and higher $\delta^{18}O$) if this scenario was correct. Additionally, new measurements of carbonates presented by Passey and Ji (2019) from Quaternary lake systems, including the nearby Great Salt Lake, gave λ_{lake} ranging from 0.5219 to 0.5239, similar to that of the Cherty Limestone Formation chert samples analyzed here.

Thus, the alternative (Scenario 2) is that the chert formed during early diagenesis at higher temperatures from waters of a similar oxygen isotopic composition to the carbonates (**Figure 2**), as originally suggested by Abruzzese et al. (2005). Assuming 60 ± 10°C as the formation temperature places the primary (lake) water $\delta^{18}O$ recorded by the cherts in the range of expected values based on the carbonate clumped isotope constraints (blue vertical bar in **Figure 2B**), and with $\Delta'^{17}O$ values lower than the meteoric water line (as expected for evaporative systems). Thus, we take this population of data points (gray triangles) and calculate the unevaporated source water for the Cherty Limestone Formation chert samples using the equations present and derived by Passey and Ji (2019) (see also section "Back-Calculation of Unevaporated Waters and Paleoaltimetry Calculations"), accounting for the measurement uncertainty and the meteoric water line uncertainty. Doing so, and fully propagating errors via a distribution-based Monte Carlo sampling routine following that outlined in the original Matlab code of Passey and Ji (2019), we calculate a source water $\delta'^{18}O$ of −16.3 ± 3.5‰ VSMOW (**Figure 2B**), lower but within error of that that derived above in scenario 1.

This result is non-unique because the precise temperature of chert formation is (still) unknown despite the added constraint of carbonate clumped isotope temperatures and the third isotope of oxygen. In a sensitivity test we assume chert formation under a wide range of temperatures. Following the same methodology as scenario 2 (**Figure 2B**), we carried out Monte Carlo simulations at temperatures ranging from 17.5 to 75°C, with the full range of the clumped isotope measurements, the error-weighted mean carbonate clumped temperature and the scenario 2 range shown as gray bars (**Figure 3A**). Because the SiO_2-H_2O fractionation factor is greater at lower temperatures, the derived source water values are lower at lower temperatures (**Figure 3A**). Source water $\delta'^{18}O$ values across this broad temperature range span ∼−18 to −15‰. In addition, in **Figure 3B** we show the sensitivity of

our calculations to the intercept of the meteoric water line (i.e., the $\Delta'^{17}O_{MWL}$ intercept), a key uncertainty given the paucity of triple oxygen isotope data from modern settings and the question of whether the Eocene intercept was within the range used from Passey and Ji (2019) in our calculations. This sensitivity test shows that the source water $\delta'^{18}O$ value decreases with increasing $\Delta'^{17}O_{MWL}$ intercept (**Figure 3B**), a relationship that should be expected given that a higher $\Delta'^{17}O_{MWL}$ intercept places the reconstructed lake water $\delta'^{18}O$ and $\Delta'^{17}O$ points (gray points in **Figure 2**) further from the meteoric water line (i.e., a greater spacing between the MWL and the data points in the y-axis). In the next section we discuss the implications of this for the paleoelevation reconstruction if the $\Delta'^{17}O_{MWL}$ intercept was in fact higher.

Previously presented sedimentological data suggested that the chert nodules formed during early diagenesis at higher temperatures (Abruzzese et al., 2005; Davis et al., 2009), which likely lead to the shallow $\delta^{18}O$-δD slope of 2.7 for these samples (balance to underfilled evaporatively influenced lake systems typically have $\delta^{18}O$-δD slopes that fall between ∼4 and ∼7; Gonfiantini, 1986). As such, given the systematics explored above, including the empirical negative relationship of the chert data following a plausible evaporation trend, we prefer the results of scenario 2 as the most realistic and parsimonious. This includes the assumption that chert formed at temperatures greater than those recorded by the carbonate clumped isotope measurements of the overlying Elko Formation from lake water incorporated into the sediment pore water of a similar $\delta^{18}O$ composition range (light blue band in **Figure 2**) as both the coeval carbonate in the Cherty Limestone and the overlying Elko Formation.

Implications for Eocene Nevadaplano Paleoaltimetry and Comparison to Other Datasets

To determine the paleoelevation of the deposits in the Elko Basin we use the model of Rowley et al. (2001). This model assumes Rayleigh distillation whereby water parcel rainout is proportional to lifting due to orography producing a monotonic relationship between elevation and $\Delta\delta^{18}O$ or $\Delta\delta D$ (defined as coastal precipitation $\delta^{18}O$ value minus the inland $\delta^{18}O$ value). Assuming a shoreline (i.e., zero elevation) $\delta^{18}O$ value and that the air-mass lifting is proportional to the elevation difference between the coast and basin's hypsometric mean elevation, meteoric (source) $\delta^{18}O$ estimates can be converted to elevations (e.g., Rowley et al., 2001; Mulch et al., 2006). In **Figure 3** and **Table 3** we do so assuming the mean estimates for our new data accounting only for uncertainty in the Rayleigh distillation model of Rowley et al. (2001). A key limitation of this assumption is that upstream rainout due to orography higher than the study area of interest or due to continentality, which both lead to lower $\delta^{18}O$ values (Kukla et al., 2019), is negligible. Recent regional mapping work by Lund Snee et al. (2016) supports this assumption. Lund Snee et al. (2016) inferred that the Cretaceous to Eocene deposits in the Elko Basin represents a lake basin covered with volcanic rocks situated in relatively subdued topography, with regional rugged Basin and Range style topography only forming in the Miocene. However, upstream rainout could be due to either Eocene topography and associated rainout through the Sierra Nevada further west inferred by hydrogen and oxygen paleoaltimetry (Mulch et al., 2006; Cassel et al., 2009; Hren et al., 2010; Mix et al., 2016), or a drainage divide just west of the Elko Basin inferred from ash-flow tuffs (Henry, 2008), which are both likely and thus this possibility cannot be ruled out.

Assuming a coastal Eocene precipitation $\delta^{18}O$ value of −7.1‰ equivalent to previous studies (e.g., Mulch et al., 2006; Cassel et al., 2009; Hren et al., 2010; Mix et al., 2016), we calculate paleoelevation using the thermodynamic model of Rowley et al. (2001). The $\Delta\delta^{18}O$ for scenario 1 is −7.0‰, which for Eocene model results for the western United States give a mean elevation of 2.75 +0.55/−0.42 km (95% confidence). Alternatively, for scenario 2, the $\Delta\delta^{18}O$ value is −9.2‰, giving a mean elevation of 3.29 +0.69/−0.68 km. These estimates, not accounting for uncertainty in the meteoric water line shown in **Figure 3** are within error, indicating elevations of ∼3 km. In **Figure 3C** we show the sensitivity of our assumed coastal Eocene precipitation $\delta^{18}O$ value of −7.1‰, over a range of −4 to −10‰. Previous work in the Pacific Northwest and Idaho Batholith has suggested shoreline Eocene precipitation values of −6‰ (Methner et al., 2016; Chamberlain et al., 2020), which for scenario 2 would increase our elevation estimate to ∼2.9–4.2 km.

These estimates are within error of those derived by previous volcanic glass δD measurements made by Cassel et al. (2014, 2018) and Smith et al. (2017) (see Cassel et al., 2018; their **Figure 2**). However, putting the δD glass data into equivalent $\delta^{18}O$ values indicates a discrepancy. In **Figures 2A,B** we show a box and whisker plot (yellow) of all glass δD data from the Late Eocene sediments in and near the Elko Basin previously reported and converted to $\delta^{18}O$ using the fractionation factor of Friedman et al. (1993) to convert to environmental water values and the assumption that waters fall along the global meteoric water line. This approach is similar to assumptions relating δD and $\delta^{18}O$ data in clays (e.g., Poage and Chamberlain, 2002; Sjostrom et al., 2006; Mix and Chamberlain, 2014; Mix et al., 2016). The average $\delta^{18}O$ of the unevaporatively enriched samples reported by volcanic glass δD studies (Cassel et al., 2014, 2018; Smith et al., 2017), converted to $\delta^{18}O$, is -18.4 ± 1.0‰. This mean value is significantly (Student's t-test $p < 0.05$) lower than both estimates presented above in scenarios 1 and 2. We note however, that based on our sensitivity tests in **Figure 3**, associated with both formation temperature and the $\Delta'^{17}O_{MWL}$ intercept, it remains possible that the δD glass data and the chert-carbonate derived values presented here are actually in close agreement. For the latter, it would require that the mean value of the $\Delta'^{17}O_{MWL}$ intercept be higher, by 0.01–0.02‰ (i.e., approximately +1σ of the current modern water data), than the modern data from the western United States (Li et al., 2015; Passey and Ji, 2019).

An alternative possible reason for this discrepancy is hydrogen exchange in volcanic glass (noted previously by Chamberlain et al. (2020) for hydrothermally altered granite). Alternatively, and perhaps most parsimoniously, there are true differences in the depositional setting and thus elevation between the lower elevation lacustrine depocenter, where the thick Chery Limestone Formation (**Figure 1B**) was deposited, and the syn- and/or

TABLE 3 | Paleoelevation calculations for Scenarios 1 and 2 based on the Rowley et al. (2001) model and previous estimates recalculated.

	Formation temperature (°C)	Method for calculating source water	Source water $\delta'^{18}O$	Source water $\delta'^{18}O$ SD	Source water $\Delta'^{17}O$ (λ_{RF} = 0.528)	Source water $\Delta'^{17}O$ SD	$\Delta\delta^{18}O$ (−7.1‰ shoreline value)	Mean elevation (km)	95% confidence (±)
Cherty limestone scenario 1	32.5 ± 3.8°C (this study)	Average of all data (**Figure 2A**)	−14.09	2.39	0.029	0.015	−7.0	2.75	+0.55/−0.42
Cherty limestone scenario 2	60 ± 10°C in **Figure 2** (17.5–75°C in **Figure 3A**)	Passey and Ji (2019) back-trajectory method (**Figure 2B**)	−16.09	3.50	0.032	0.015	−9.2	3.29	+0.69/−0.68

	Formation temperature (°C)	$\Delta\delta^{18}O$ (−7.1‰ shoreline value)	Mean elevation (km)	95% confidence (±)	Data source
Paleosol or lacustrine carbonate data					
Elko Fm. lacustrine carbonate (lowest $\delta^{18}O$)	32.5°C (this study)	−5.1	2.14	+0.40/−0.39	H2004; C2012; M2015
Indian Wells Fm. paleosol carbonate (average $\delta^{18}O$)	13°C (Chase et al., 1998)	−11.6 ± 2.2	3.76	+0.80/−0.77	H2004; C2012; M2015
Humboldt Fm. paleosol carbonate (average $\delta^{18}O$)	13°C (Chase et al., 1998)	−11.5 ± 1.0	3.74	+0.84/−0.77	H2004; C2012; M2015
Hydrated volcanic glass data					
Volcanic glass—eocene, non-lacustrine samples	n/a	−11.2 ± 1.0	3.68	+0.81/−0.66	C2014; C2018
Volcanic glass—early oligocene	n/a	−10.3 ± 1.0	3.52	+0.81/−0.66	C2014; C2018
Volcanic glass—late oligocene	n/a	−12.7 ± 1.2	3.94	+0.85/−0.70	C2014; C2018

*Note that recent work (Lund Snee et al., 2016) recommends combining the Indian Wells Fm. with the Humboldt Fm. H2004—Horton et al. (2004); M2015—Mulch et al. (2015); C2012—Chamberlain et al. (2012); C2014—Cassel et al. (2014); C2018—Cassel et al. (2018). Note that the formation temperature used in Scenario 1 is the weighted average of the lacustrine carbonates (**Table 2**) from the Elko Fm.*

post-deposition Eocene fluvial sites of volcanic ash deposition associated with higher elevations. We note that Cassel et al. (2018) explicitly removed samples from their regional dataset from basin depocenters in lacustrine settings because they recorded δD values higher than other (nearby) samples from the same age and fluvial depositional settings. Further work to disentangle and systematically document the depositional settings, paleoelevations and geochronologic control of the individual localities for all of the proxies in the Elko Basin and regionally in northeastern Nevada is clearly necessary. One additional line of evidence is the $\delta^{18}O$ data of four chert samples from the Miocene Humboldt Formation ranging from 17.2 to 23.7‰ (Knauth and Epstein, 1976), thus, exhibiting a similar range to those of the Eocene Cherty Limestone Fm. (15.6–23.1‰) (**Table 1**; Horton et al., 2004; Abruzzese et al., 2005). Assuming similar formation temperatures, the Humboldt Formation chert data from Knauth and Epstein (1976) would yield similar paleoelevations to the Cherty Limestone Fm., but lower than nearby time equivalent (Miocene) volcanic glass data from Cassel et al. (2018), similar to our observations for the Eocene.

In **Figure 3** we summarize the paleoelevation estimates based on this work on triple oxygen isotopes of chert and those from other studies on younger rocks based on carbonates from paleolakes and paleosols and volcanic glasses of the Elko Basin. These data suggest a relatively simple uplift history of the Elko Basin with high elevations (∼3 km) in the mid to late Eocene in the oldest lake unit in the Elko Basin. Surface uplift of this region occurred at some point during the late Eocene to early Oligocene to elevations around 4 km and remained high throughout the Miocene. We do not think that the elevation estimates for the late Eocene Elko Formation reflect true low elevations as even the lowest $\delta^{18}O$ of carbonate have most likely been influenced by evaporation, as pointed out by Smith et al. (2017), and observed here in the positive correlation of $\delta^{18}O$ and $\delta^{13}C$ among even the lowest $\delta^{18}O$ samples (green squares in **Figure 1C**; see also discussion in Mulch et al., 2015). In addition, we see no evidence for the more complicated surface uplift history given in Cassel et al. (2018) who suggest high elevation in the Late Eocene to lower elevations in the Early Oligocene to the highest elevation in the Late Oligocene. However, this elevation history is largely based on rocks exposed just west of the Elko Basin as there are few to no substantial Oligocene sedimentary rocks exposed in the Elko Basin that allow paleoelevation constraints, based on the most recent mapping that indicates an angular unconformity (spanning ∼31–24 Ma) between the units mapped previously as the Indian Well Fm. and the Miocene Humboldt Fm (Lund Snee et al., 2016).

CONCLUSION

In this study we presented the first lacustrine chert triple oxygen isotope dataset from a Cenozoic basin in western North America and used this data, in conjunction with carbonate clumped isotope measurements to derive an elevation estimate for the eastern Eocene Nevadaplano. Future measurements on carbonates (e.g., Passey et al., 2014; Bergel et al., 2020; Fosu et al., 2020; Voarintsoa et al., 2020; Wostbrock et al., 2020) from the Elko Basin, specifically on the Elko Formation, would benefit from paired measurement of the carbonates from the Eocene to Miocene strata for both triple oxygen isotopes and carbonate clumped isotopes, allowing for issues for formation temperature associated with chert formation to be overcome. Nevertheless, state-of-the-art data sets presented here indicate that:

1. The empirical negative relationship in triple oxygen isotopes among the dataset is suggestive of evaporative enrichment of $\delta^{18}O$ values spanning 6.5‰.
2. Cherts in the Cherty Limestone Formation likely formed during early diagenesis at temperatures hotter than those recorded by coeval carbonate and carbonates in the overlying lacustrine portion of the Elko Formation as recorded by our new carbonate clumped isotope dataset.
3. Comparison to δD datasets (converted to water $\delta^{18}O$ values) from volcanic glass of similar age from the Elko Basin demonstrate that either the lacustrine carbonates and chert represent a lower hypsometric mean elevation of the basin depocenter or there exists later hydrogen exchange in the volcanic glass.
4. We calculate a relatively simple surface uplift history for Elko Basin with original deposition of lake sediments (Cherty Limestone Formation) at ∼3 km in the mid-Eocene. When compared to other paleoelevation studies in this area, we suggest that the was surface uplift of ∼1 km in the late Eocene to early Oligocene with elevations remaining high into the Miocene.

DATA AVAILABILITY STATEMENT

All datasets generated for this study are included in the article/**Supplementary Material**, further inquiries can be directed to the corresponding author/s.

AUTHOR CONTRIBUTIONS

DI wrote the initial draft of the manuscript with input from CC. DI made the figures. CC, TK, and DI made the triple oxygen isotope measurements. KM made the carbonate clumped isotope measurements. CC and AM provided the samples. DI and TK constructed the modeling framework. All authors provided input on the dataset interpretation and analysis and contributed to writing the manuscript.

FUNDING

This research was funded by NSF EAR-1322084 and Heising Simons grants to CC. KM and AM acknowledge support

through the LOEWE funding program of the Hessen State Ministry of Higher Education, Research, and the Arts as part of the LOEWE VeWa project. DI was supported by the UC Berkeley Miller Institute for Basic Research and UC President's Postdoctoral Fellowships, and KM was supported by the Feodor-Lynen-Fellowship of the Alexander von Humboldt Foundation.

ACKNOWLEDGMENTS

We thank NL and JK for thorough reviews and comments, and MH for handling our manuscript. We thank Peter Blisniuk for help with the isotope measurements at the Stanford University Stable Isotope Biogeochemistry Laboratory, Kristina Butler for providing feedback on a previous version of this manuscript, Max K. Lloyd with triple oxygen isotope data handling, as well as Yuan Gao, Zachary D. Sharp, Jordan A.G. Wostbrock, Max K. Lloyd, and Daniel A. Stolper for detailed discussions. We thank both reviewers of this manuscript for thorough and helpful comments and suggestions.

SUPPLEMENTARY MATERIAL

The Supplementary Material for this article can be found online at: https://www.frontiersin.org/articles/10.3389/feart.2021.628868/full#supplementary-material

REFERENCES

Abruzzese, M. J., Waldbauer, J. R., and Chamberlain, C. P. (2005). Oxygen and hydrogen isotope ratios in freshwater chert as indicators of ancient climate and hydrologic regime. *Geochim. Cosmochim. Acta* 69, 1377–1390. doi: 10.1016/j.gca.2004.08.036

Affek, H. P., Bar-Matthews, M., Ayalon, A., Matthews, A., and Eiler, J. M. (2008). Glacial/interglacial temperature variations in Soreq cave speleothems as recorded by "clumped isotope" thermometry. *Geochim. Cosmochim. Acta* 72, 5351–5360. doi: 10.1016/j.gca.2008.06.031

Aron, P. G., Levin, N. E., Beverly, E. J., Huth, T. E., Passey, B. H., Pelletier, E. M., et al. (2020). Triple oxygen isotopes in the water cycle. *Chem. Geol.* doi: 10.1016/j.chemgeo.2020.120026 [Epub ahead of print].

Bajnai, D., Guo, W., Spötl, C., Coplen, T. B., Methner, K., Löffler, N., et al. (2020). Dual clumped isotope thermometry resolves kinetic biases in carbonate formation temperatures. *Nat. Commun.* 11, 1–9.

Barkan, E., Affek, H. P., Luz, B., Bergel, S. J., Voarintsoa, N. R. G., and Musan, I. (2019). Calibration of δ17O and 17Oexcess values of three international standards: IAEA-603, NBS19 and NBS18. *Rapid Commun. Mass Spectrom.* 33:737. doi: 10.1002/rcm.8391

Barkan, E., and Luz, B. (2005). High precision measurements of 17O/16O and 18O/16O ratios in H2O. *Rapid Commun. Mass Spectrom.* 19, 3737–3742. doi: 10.1002/rcm.2250

Barkan, E., and Luz, B. (2007). Diffusivity fractionations of H216O/H217O and H218O/H218O in air and their implications for isotope hydrology. *Rapid Commun. Mass Spectrom.* 21, 2999–3005. doi: 10.1002/rcm.3180

Bergel, S. J., Barkan, E., Stein, M., and Affek, H. P. (2020). Carbonate 17O-excess as a paleo-hydrology proxy: Triple oxygen isotope fractionation between H2O and biogenic aragonite, derived from freshwater mollusks. *Geochim. Cosmochim. Acta* 275, 36–47. doi: 10.1016/j.gca.2020.02.005

Bindeman, I. N. (2021). Triple oxygen isotopes in evolving continental crust, granites, and clastic sediments. *Rev. Mineral Geochem.* 86, 241–290.

Came, R. E., Eiler, J. M., Veizer, J., Azmy, K., Brand, U., and Weidman, C. R. (2007). Coupling of surface temperatures and atmospheric CO_2 concentrations during the Palaeozoic era. *Nature* 449, 198–201. doi: 10.1038/nature06085

Cao, X., and Liu, Y. (2011). Equilibrium mass-dependent fractionation relationships for triple oxygen isotopes. *Geochim. Cosmochim. Acta* 75, 7435–7445. doi: 10.1016/j.gca.2011.09.048

Carroll, A. R., Doebbert, A. C., Booth, A. L., Chamberlain, C. P., Rhodes-Carson, M. K., Smith, M. E., et al. (2008). Capture of high altitude precipitation by a low-altitude Eocene lake, western U.S. *Geology* 36, 791–794. doi: 10.1130/g24783a.1

Cassel, E. J., Breecker, D. O., Henry, C. D., Larson, T. E., and Stockli, D. F. (2014). Profile of a paleo-orogen: High topography across the present-day Basin and Range from 40 to 23 Ma. *Geology* 42, 1007–1010. doi: 10.1130/g35924.1

Cassel, E. J., Graham, S. A., and Chamberlain, C. P. (2009). Cenozoic tectonic and topographic evolution of the northern Sierra Nevada, California, through stable isotope paleoaltimetry in volcanic glass. *Geology* 37, 547–550. doi: 10.1130/g25572a.1

Cassel, E. J., Smith, M. E., and Jicha, B. R. (2018). The impact of slab rollback on earth's surface: uplift and extension in the hinterland of the North American Cordillera. *Geophys. Res. Lett.* 45, 996–911.

Chamberlain, C. P., Ibarra, D. E., Lloyd, M. K., Kukla, T., Sharp, Z. D., Gao, Y., et al. (2020). Triple oxygen isotopes of meteoric hydrothermal system – implications for paleoaltimetry. *Geochem. Perspect. Lett.* 15, 6–9. doi: 10.7185/geochemlet.2026

Chamberlain, C. P., Mix, H. T., Mulch, A., Hren, M. T., Kent-Corson, M. L., Davis, S. J., et al. (2012). The Cenozoic climatic and topographic evolution of the western North American Cordillera. *Am. J. Sci.* 312, 213–262.

Chamberlain, C. P., Poage, M. A., Craw, D., and Reynolds, R. C. (1999). Topographic development of the Southern Alps recorded by the isotopic composition of authigenic clay minerals, South Island, New Zealand. *Chem. Geol.* 155, 279–294. doi: 10.1016/s0009-2541(98)00165-x

Chamberlain, C. P., Wan, X., Graham, S. A., Carroll, A. R., Doebbert, A. C., Sageman, B. B., et al. (2013). Stable isotopic evidence for climate and basin evolution of the Late Cretaceous Songliao basin, China. *Palaeogeogr. Palaeoclimatol. Palaeoecol.* 385, 106–124. doi: 10.1016/j.palaeo.2012.03.020

Chase, C. G., Gregory-Wodzicki, K. M., Parrish-Jones, J. T., and DeCelles, P. (1998). "Topographic history of the western Cordillera of North America and controls on climate", in *Tectonic Boundary Conditions for Climate Model Simulations*, eds T. J. Crowley and K. Burke (Oxford, UK: Oxford University Press, Oxford Monographs on Geology and Geophysics), 73–99.

Craig, H. (1957). Isotopic standards for carbon and oxygen and correction factors for mass-spectrometric analysis of carbon dioxide. *Geochim. Cosmochim. Acta* 12, 133–149. doi: 10.1016/0016-7037(57)90024-8

Craig, H. (1961). Isotopic variations in meteoric waters. *Science* 133, 1702–1703. doi: 10.1126/science.133.3465.1702

Criss, R. E. (1999). *Principles of Stable isotope Distribution*. Oxford: Oxford University Press.

Daëron, M., Blamart, D., Peral, M., and Affek, H. P. (2016). Absolute isotopic abundance ratios and the accuracy of Δ47 measurements. *Chem. Geol.* 442, 83–96. doi: 10.1016/j.chemgeo.2016.08.014

Davis, S. J., Mulch, A., Carroll, A. R., Horton, T. W., and Chamberlain, C. P. (2009). Paleogene landscape evolution of the central North American Cordillera: Developing topography and hydrology in the Laramide foreland. *Geol. Soc. Am. Bull.* 121, 100–116.

Dennis, K. J., Affek, H. P., Passey, B. H., Schrag, D. P., and Eiler, J. M. (2011). Defining an absolute reference frame for 'clumped' isotope studies of CO2. *Geochim. Cosmochim. Acta* 75, 7117–7131. doi: 10.1016/j.gca.2011.09.025

Eiler, J. M. (2007). "Clumped-isotope" geochemistry—The study of naturally-occurring, multiply-substituted isotopologues. *Earth Planet. Sci. Lett.* 262, 309–327. doi: 10.1016/j.epsl.2007.08.020

Eiler, J. M. (2011). Paleoclimate reconstruction using carbonate clumped isotope thermometry. *Quat. Sci. Rev.* 30, 3575–3588. doi: 10.1016/j.quascirev.2011.09.001

Evans, N. P., Bauska, T. K., Gázquez-Sánchez, F., Brenner, M., Curtis, J. H., and Hodell, D. A. (2018). Quantification of drought during the collapse of the classic Maya civilization. *Science* 361, 498–501. doi: 10.1126/science.aas9871

Fiebig, J., Hofmann, S., Löffler, N., Lüdecke, T., Methner, K., and Wacker, U. (2016). Slight pressure imbalances can affect accuracy and precision of dual inlet-based clumped isotope analysis. *Isotop. Environ. Health Stud.* 52, 12–28. doi: 10.1080/10256016.2015.1010531

Fosu, B. R., Subba, R., Peethambaran, R., Bhattacharya, S. K., and Ghosh, P. (2020). Developments and applications in triple oxygen isotope analysis of carbonates. *ACS Earth Space Chem.* 4, 702–710. doi: 10.1021/acsearthspacechem.9b00330

Frantz, C. M., Petryshyn, V. A., Marenco, P. J., Tripati, A., Berelson, W. M., and Corsetta, F. A. (2014). Dramatic local environmental change during the Early Eocene Climatic Optimum detected using high resolution chemical analyses of Green River Formation stromatolites. *Palaeogeogr. Palaeoclimatol. Palaeoecol.* 405, 1–15. doi: 10.1016/j.palaeo.2014.04.001

Friedman, I., Gleason, J., and Warden, A. (1993). "Ancient climate from deuterium content of water in volcanic glass: climate change in continental isotopic records," in *Climate Change in Continental Isotopic Records: American Geophysical Union Geophysical Monograph*, Vol. 78, eds P. K. Swart, K. C. Lohmann, J. Mckenzie, and S. Savin, (Washington, DC: American Geophysical Union), 309–319. doi: 10.1029/gm078p0309

Garzione, C. N., Molnar, P., Libarkin, J. C., and MacFadden, B. J. (2006). Rapid late Miocene rise of the Bolivian Altiplano: Evidence for removal of mantle lithosphere. *Earth Planet. Sci. Lett.* 241, 543–556. doi: 10.1016/j.epsl.2005.11.026

Gázquez, F., Morellón, M., Bauska, T., Herwartz, D., Surma, J., Moreno, A., et al. (2018). Triple oxygen and hydrogen isotopes of gypsum hydration water for quantitative paleo-humidity reconstruction. *Earth Planet. Sci. Lett.* 481, 177–188. doi: 10.1016/j.epsl.2017.10.020

Gébelin, A., Mulch, A., Teyssier, C., Jessup, M. J., Law, R. D., and Brunel, M. (2013). The Miocene elevation of Mount Everest. *Geology* 41, 799–802. doi: 10.1130/g34331.1

Ghosh, P., Adkins, J., Affek, H., Balta, B., Guo, W., Schauble, E. A., et al. (2006b). 13C–18O bonds in carbonate minerals: a new kind of paleothermometer. *Geochim. Cosmochim. Acta* 70, 1439–1456. doi: 10.1016/j.gca.2005.11.014

Ghosh, P., Garzione, C. N., and Eiler, J. M. (2006a). Rapid uplift of the altiplano revealed through 13C-18O bonds in paleosol carbonates. *Science* 311, 511–515. doi: 10.1126/science.1119365

Gonfiantini, R. (1986). Environmental isotopes in lake studies. *Handb. Environ. Isotop. Geochem.* 2, 113–168. doi: 10.1016/b978-0-444-42225-5.50008-5

Hayles, J., Gao, C., Cao, X., Liu, Y., and Bao, H. (2018). Theoretical calibration of the triple oxygen isotope thermometer. *Geochim. Cosmochim. Acta* 235, 237–245. doi: 10.1016/j.gca.2018.05.032

Hayles, J. A., Cao, X., and Bao, H. (2017). The statistical mechanical basis of the triple isotope fractionation relationship. *Geochem. Perspect. Lett.* 3, 1–11. doi: 10.7185/geochemlet.1701

Henry, C. D. (2008). Ash-flow tuffs and paleovalleys in northeastern Nevada: implications for Eocene paleogeography and extension in the Sevier hinterland, northern Great Basin. *Geosphere* 4, 1–35. doi: 10.1130/ges00122.1

Herwartz, D. (2021). Triple oxygen isotope variations in Earth's crust. *Rev. Mineral Geochem.* 86, 291–322. doi: 10.2138/rmg.2021.86.09

Herwartz, D., Surma, J., Voigt, C., Assonov, S., and Staubwasser, M. (2017). Triple oxygen isotope systematics of structurally bonded water in gypsum. *Geochim. Cosmochim. Acta* 209, 254–266. doi: 10.1016/j.gca.2017.04.026

Horton, T. W., Defliese, W. F., Tripati, A. K., and Oze, C. (2016). Evaporation induced 18O and 13C enrichment in lake systems: A global perspective on hydrologic balance effects. *Quat. Sci. Rev.* 131, 365–379. doi: 10.1016/j.quascirev.2015.06.030

Horton, T. W., and Oze, C. (2012). Are two elements better than one? Dual isotope-ratio detrending of evaporative effects on lake carbonate paleoelevation proxies. *Geochem. Geophys. Geosyst.* 13:Q0AK05.

Horton, T. W., Sjostrom, D. J., Abruzzese, M. J., Poage, M. A., Waldbauer, J. R., Hren, M., et al. (2004). Spatial and temporal variation of Cenozoic surface elevation in the Great Basin and Sierra Nevada. *Am. J. Sci.* 304, 862–888. doi: 10.2475/ajs.304.10.862

Hren, M. T., Pagani, M., Erwin, D. M., and Brandon, M. (2010). Biomarker reconstruction of the early Eocene paleotopography and paleoclimate of the northern Sierra Nevada. *Geology* 38, 7–10. doi: 10.1130/g30215.1

Hren, M. T., Tice, M. M., and Chamberlain, C. P. (2009). Oxygen and hydrogen isotope evidence for a temperate climate 3.42 billion years ago. *Nature* 462, 205–208. doi: 10.1038/nature08518

Hudson, A. M., Quade, J., Ali, G., Boyle, D., Bassett, S., Huntington, K. W., et al. (2017). Stable C, O and clumped isotope systematics and 14C geochronology of carbonates from the Quaternary Chewaucan closed-basin lake system, Great Basin, USA: Implications for paleoenvironmental reconstructions using carbonates. *Geochim. Cosmochim. Acta* 212, 274–302. doi: 10.1016/j.gca.2017.06.024

Hulston, J. R., and Thode, H. G. (1965). Variations in the S33, S34, and S36 contents of meteorites and their relation to chemical and nuclear effects. *J. Geophys. Res.* 70, 3475–3484. doi: 10.1029/jz070i014p03475

Huntington, K. W., Eiler, J. M., Affek, H. P., Guo, W., Bonifacie, M., Yeung, L. Y., et al. (2009). Methods and limitations of "clumped" CO2 isotope (Δ47) analysis by gas-source isotope ratio mass spectrometry. *J. Mass Spectrom.* 44, 1318–1329. doi: 10.1002/jms.1614

Huntington, K. W., and Lechler, A. R. (2015). Carbonate clumped isotope thermometry in continental tectonics. *Tectonophysics* 64, 1–20. doi: 10.1016/j.tecto.2015.02.019

Huntington, K. W., Wernicke, B. P., and Eiler, J. M. (2010). Influence of climate change and uplift on Colorado Plateau paleotemperatures from carbonate clumped isotope thermometry. *Tectonics* 29:1129.

Hyland, E. G., Huntington, K. W., Sheldon, N. D., and Reichgel, T. (2018). Temperature and seasonality in the North American continental interior during the Early Eocene Climatic Optimum. *Clim. Past* 14, 1391–1404. doi: 10.5194/cp-14-1391-2018

Ibarra, D. E., and Chamberlain, C. P. (2015). Quantifying closed-basin lake temperature and hydrology by inversion of oxygen isotope and trace element paleoclimate records. *Am. J. Sci.* 315, 781–808. doi: 10.2475/09.2015.01

Ibarra, D. E., Egger, A. E., Weaver, K. L., Harris, C. R., and Maher, K. (2014). Rise and fall of late Pleistocene pluvial lakes in response to reduced evaporation and precipitation: evidence from Lake Surprise, California. *Bull. Geol. Soc. Am.* 126, 1387–1415. doi: 10.1130/b31014.1

Ingalls, M., Frantz, C. M., Snell, K. E., and Trower, E. J. (2020b). Carbonate facies specific stable isotope data record climate, hydrology, and microbial communities in Great Salt Lake, UT. *Geobiology* 18, 566–593. doi: 10.1111/gbi.12386

Ingalls, M., Rowley, D. B., Currie, B. S., and Colman, A. S. (2020a). Reconsidering the uplift history and peneplanation of the northern Lhasa terrane, Tibet. *Am. J. Sci.* 320, 479–532. doi: 10.2475/06.2020.01

Kim, S. T., and O'Neil, J. R. (1997). Equilibrium and nonequilibrium oxygen isotope effects in synthetic carbonates. *Geochim. Cosmochim. Acta* 61, 3461–3475. doi: 10.1016/s0016-7037(97)00169-5

Kim, S. T., O'Neil, J. R., Hillaire-Marcel, C., and Mucci, A. (2007). Oxygen isotope fractionation between synthetic aragonite and water: influence of temperature and Mg2+ concentration. *Geochim. Cosmochim. Acta* 71, 4704–4715. doi: 10.1016/j.gca.2007.04.019

Knauth, L. P. (1973). *Oxygen and Hydrogen Isotope Ratios in Cherts and Related Rocks*. 378. Ph.D. Thesis, California Institute of Technology, Pasadena, CA.

Knauth, L. P., and Epstein, S. (1976). Hydrogen and oxygen isotope ratios in nodular and bedded cherts. *Geochim. Cosmochim. Acta* 40, 1095–1108. doi: 10.1016/0016-7037(76)90051-x

Kukla, T., Ibarra, D. E., Rugenstein, J. K. C., Gooley, J. T., Mullins, C. E., Kramer, S., et al. (2021). High-resolution stable isotope paleotopography of the John Day Region, Oregon, United States. *Front. Earth Sci.* 9:635181.

Kukla, T., Winnick, M. J., Maher, K., Ibarra, D. E., and Chamberlain, C. P. (2019). The sensitivity of terrestrial δ18O gradients to hydroclimate evolution. *J. Geophys. Res. Atmos.* 124, 563–582. doi: 10.1029/2018jd029571

Lechler, A. R., Niemi, N. A., Hren, M. T., and Lohmann, K. C. (2013). Paleoelevation estimates for the northern and central proto–Basin and Range from carbonate clumped isotope thermometry. *Tectonics* 32, 295–316. doi: 10.1002/tect.20016

Levin, N. E., Raub, T. D., Dauphas, N., and Eiler, J. M. (2014). Triple oxygen isotope variations in sedimentary rocks. *Geochim. Cosmochim. Acta* 139, 173–189. doi: 10.1016/j.gca.2014.04.034

Li, H. C., and Ku, T. L. (1997). δ13C–δ18C covariance as a paleohydrological indicator for closed-basin lakes. *Palaeogeogr. Palaeoclimatol. Palaeoecol.* 133, 69–80. doi: 10.1016/s0031-0182(96)00153-8

Li, S., Levin, N. E., and Chesson, L. A. (2015). Continental scale variation in 17O-excess of meteoric waters in the United States. *Geochim. Cosmochim. Acta* 164, 110–126. doi: 10.1016/j.gca.2015.04.047

Liljestrand, F. L., Laakso, T. A., Macdonald, F. A., Schrag, D. P., and Johnston, D. T. (2020). Isotopically anomalous organic carbon in the aftermath of the Marinoan snowball Earth. *Geobiology* 18, 476–485. doi: 10.1111/gbi.12383

Lowe, D. R., Ibarra, D. E., Drabon, N., and Chamberlain, C. P. (2020). Constraints on surface temperature 3.4 billion years ago based on triple oxygen isotopes of cherts from the Barberton Greenstone Belt, South Africa, and the problem of sample selection. *Am. J. Sci.* 320, 790–814. doi: 10.2475/11.2020.02

Lund Snee, J.-E., Miller, E. L., Grove, M., Hourigan, J. K., and Konstantinou, A. (2016). Cenozoic paleogeographic evolution of the Elko Basin and surrounding region, northeast Nevada. *Geosphere* 12, 464–500. doi: 10.1130/ges01198.1

Luz, B., and Barkan, E. (2010). Variations of 17O/16O and 18O/16O in meteoric waters. *Geochim. Cosmochim. Acta* 74, 6276–6286. doi: 10.1016/j.gca.2010.08.016

Matsuhisa, Y., Goldsmith, J. R., and Clayton, R. N. (1978). Mechanisms of hydrothermal crystallization of quartz at 250 C and 15 kbar. *Geochim. Cosmochim. Acta* 42, 173–182. doi: 10.1016/0016-7037(78)90130-8

McKinney, C. R., McCrea, J. M., Epstein, S., Allen, H. A., and Urey, H. C. (1950). Improvements in mass spectrometers for the measurement of small differences in isotope abundance ratios. *Rev. Sci. Instrum.* 21, 724–730. doi: 10.1063/1.1745698

Meijer, H. A. J., and Li, W. J. (2006). The use of electrolysis for accurate δ17O and δ18O isotope measurements in water. *Isotop. Environ. Health Stud.* 34, 349–369.

Methner, K., Campani, M., Fiebig, J., Löffler, N., Kempf, O., and Mulch, A. (2020). Middle Miocene long-term continental temperature change in and out of pace with marine climate records. *Sci. Rep.* 10, 1–10.

Methner, K., Fiebig, J., Wacker, U., Umhoefer, P., Chamberlain, C. P., and Mulch, A. (2016). Eocene-Oligocene proto-Cascades topography revealed by clumped (Δ47) and oxygen isotope (δ18O) geochemistry (Chumstick Basin, WA, USA). *Tectonics* 35, 546–564. doi: 10.1002/2015tc003984

Micheelsen, H. (1966). The structure of dark flint from Stevns Denmark. *Medd. Fra Dansk Geol.* 16, 285–368.

Miller, M. F. (2002). Isotopic fractionation and the quantification of 17O anomalies in the oxygen three-isotope system: an appraisal and geochemical significance. *Geochim. Cosmochim. Acta* 66, 1881–1889. doi: 10.1016/s0016-7037(02)00832-3

Miller, M. F., and Pack, A. (2021). Why measure 17O? Historical perspective, triple-isotope systematics and selected applications. *Rev. Mineral Geochem.* 86, 1–34. doi: 10.2138/rmg.2021.86.01

Mix, H. T., and Chamberlain, C. P. (2014). Stable isotope records of hydrologic change and paleotemperature from smectite in Cenozoic western North America. *Geochim. Cosmochim. Acta* 141, 532–546. doi: 10.1016/j.gca.2014.07.008

Mix, H. T., Ibarra, D. E., Mulch, A., Graham, S. A., and Chamberlain, C. P. (2016). A hot and high Eocene Sierra Nevada. *Bull. Geol. Soc. Am.* 128, 531–542. doi: 10.1130/b31294.1

Mix, H. T., Mulch, A., Kent-Corson, M. L., and Chamberlain, C. P. (2011). Cenozoic migration of topography in the North American Cordillera. *Geology* 39, 87–90. doi: 10.1130/g31450.1

Mulch, A. (2016). Stable isotope paleoaltimetry and the evolution of landscapes and life. *Earth Planet. Sci. Lett.* 433, 180–191. doi: 10.1016/j.epsl.2015.10.034

Mulch, A., Chamberlain, C. P., Cosca, M. A., Teyssier, C., Methner, K., and Graham, S. A. (2015). Rapid change in western North American high-elevation rainfall patterns during the Mid Eocene Climatic Optimum (MECO). *Am. J. Sci.* 315, 317–336. doi: 10.2475/04.2015.02

Mulch, A., Graham, S. A., and Chamberlain, C. P. (2006). Hydrogen isotopes in Eocene river gravels and paleoelevation of the Sierra Nevada. *Science* 313, 87–89. doi: 10.1126/science.1125986

Mulch, A., Uba, C. E., Strecker, M. R., Schoenberg, R., and Chamberlain, C. P. (2010). Late Miocene climate variability and surface elevation in the central Andes. *Earth Planet. Sci. Lett.* 290, 173–182. doi: 10.1016/j.epsl.2009.12.019

O'Neil, J. R., and Kharaka, Y. K. (1976). Hydrogen and oxygen isotope exchange reactions between clay minerals and water. *Geochim. Cosmochim. Acta* 40, 241–246. doi: 10.1016/0016-7037(76)90181-2

Pack, A., and Herwartz, D. (2014). The triple oxygen isotope composition of the Earth mantle and understanding ΔO17 variations in terrestrial rocks and minerals. *Earth Planet. Sci. Lett.* 390, 138–145.

Passey, B. H., Hu, H., Ji, H., Montanari, S., Li, S., Henkes, G. A., et al. (2014). Triple oxygen isotopes in biogenic and sedimentary carbonates. *Geochim. Cosmochim. Acta* 141, 1–25. doi: 10.1016/j.gca.2014.06.006

Passey, B. H., and Ji, H. (2019). Triple oxygen isotope signatures of evaporation in lake waters and carbonates: A case study from the western United States. *Earth Planet. Sci. Lett.* 518, 1–12. doi: 10.1016/j.epsl.2019.04.026

Passey, B. H., and Levin, N. E. (2021). Triple oxygen isotopes in meteoric waters, carbonates, and biological apatites: implications for continental paleoclimate reconstruction. *Rev. Mineral Geochem.* 86, 429–462. doi: 10.2138/rmg.2021.86.13

Passey, B. H., Levin, N. E., Cerling, T. E., Brown, F. H., and Eiler, J. M. (2010). High-temperature environments of human evolution in East Africa based on bond ordering in paleosol carbonates. *Proc. Natl. Acad. Sci. U.S.A.* 107, 11245–11249. doi: 10.1073/pnas.1001824107

Petersen, S. V., Defliese, W. F., Saenger, C., Daëron, M., Huntington, K. W., John, C. M., et al. (2019). Effects of improved 17O correction on interlaboratory agreement in clumped isotope calibrations, Estimates of mineral-specific offsets, and temperature dependence of acid digestion fractionation. *Geochem. Geophys. Geosyst.* 20, 3495–3519. doi: 10.1029/2018gc008127

Petryshyn, V. A., Lim, D., Laval, B. L., Brady, A., Slater, G., and Tripati, A. K. (2015). Reconstruction of limnology and microbialite formation conditions from carbonate clumped isotope thermometry. *Geobiology* 13, 53–67. doi: 10.1111/gbi.12121

Pingel, H., Strecker, M. R., Mulch, A., Alonso, R. N., Cottle, J., and Rohrmann, A. (2020). Late Cenozoic topographic evolution of the Eastern Cordillera and Puna Plateau margin in the southern Central Andes (NW Argentina). *Earth Planet. Sci. Lett.* 535:116112. doi: 10.1016/j.epsl.2020.116112

Poage, M. A., and Chamberlain, C. P. (2002). Stable isotopic evidence for a Pre-Middle Miocene rain shadow in the western Basin and Range: Implications for the paleotopography of the Sierra Nevada. *Tectonics* 21, 16–11. doi: 10.1029/2001tc001303

Quade, J., Leary, R., Dettinger, M. P., Orme, D., Krupa, A., DeCelles, P. G., et al. (2020). Resetting Southern Tibet: The serious challenge of obtaining primary records of Paleoaltimetry. *Glob. Planet. Change* 191:103194. doi: 10.1016/j.gloplacha.2020.103194

Rowley, D. B., Pierrehumbert, R. T., and Currie, B. S. (2001). A new approach to stable isotope-based paleoaltimetry: implications for paleoaltimetry and paleohypsometry of the High Himalaya since the Late Miocene. *Earth Planet. Sci. Lett.* 188, 253–268. doi: 10.1016/s0012-821x(01)00324-7

Rozanski, K., Araguás-Araguás, L., and Gonfiantini, R. (1993). Isotopic patterns in modern global precipitation. *GMS* 78, 1–36. doi: 10.1029/gm078p0001

San Jose, M., Rugenstein, J. K. C., Cosentino, D., Faccenna, C., Fellin, M. G., Ghinassi, M., et al. (2020). Stable isotope evidence for rapid uplift of the central Apennines since the late Pliocene. *Earth Planet. Sci. Lett.* 544:116376. doi: 10.1016/j.epsl.2020.116376

Santi, L. M., Arnold, A. J., Ibarra, D. E., Whicker, C. A., Mering, J. A., Lomarda, R. B., et al. (2020). Clumped isotope constraints on changes in latest Pleistocene hydroclimate in the northwestern Great Basin: Lake Surprise, California. *Geol. Soc. Am. Bull.* 132, 2669–2683. doi: 10.1130/b35484.1

Schauble, E. A., and Young, E. D. (2021). Mass dependence of equilibrium oxygen isotope fractionation in carbonate, nitrate, oxide, perchlorate, phosphate, silicate, and sulfate minerals. *Rev. Mineral Geochem.* 86, 137–178. doi: 10.2138/rmg.2021.86.04

Schwartz, T. M., Methner, K., Mulch, A., Graham, S. A., and Chamberlain, C. P. (2019). Paleogene topographic and climatic evolution of the Northern Rocky Mountains from integrated sedimentary and isotopic data. *Bulletin* 131, 1203–1223. doi: 10.1130/b32068.1

Sengupta, S., Peters, S. T., Reitner, J., Duda, J. P., and Pack, A. (2020). Triple oxygen isotopes of cherts through time. *Chem. Geol.* 554:119789. doi: 10.1016/j.chemgeo.2020.119789

Sha, L., Mahata, S., Duan, P., Luz, B., Zhang, P., Baker, J., et al. (2020). A novel application of triple oxygen isotope ratios of speleothems. *Geochim. Cosmochim. Acta* 270, 360–378. doi: 10.1016/j.gca.2019.12.003

Sharp, Z. D. (1990). A laser-based microanalytical method for the in situ determination of oxygen isotope ratios of silicates and oxides. *Geochim. Cosmochim. Acta* 54, 1353–1357. doi: 10.1016/0016-7037(90)90160-m

Sharp, Z. D., Gibbons, J. A., Maltsev, O., Atudorei, V., Pack, A., Sengupta, S., et al. (2016). A calibration of the triple oxygen isotope fractionation in the SiO2–H2O system and applications to natural samples. *Geochim. Cosmochim. Acta* 186, 105–119. doi: 10.1016/j.gca.2016.04.047

Sharp, Z. D., and Wostbrock, J. A. G. (2020). Standardization for the triple oxygen isotope system: waters, silicates, carbonates, air, and sulfates. *Rev. Mineral. Geochem.* 86, 179–196. doi: 10.2138/rmg.2021.86.05

Sharp, Z. D., Wostbrock, J. A. G., and Pack, A. (2018). Mass-dependent triple oxygen isotope variations in terrestrial materials. *Geochem. Perspect. Lett* 7, 27–31. doi: 10.7185/geochemlet.1815

Sjostrom, D. J., Hren, M. T., Horton, T. W., Waldbauer, J. R., and Chamberlain, C. P. (2006). Stable isotopic evidence for a pre–late Miocene elevation gradient in the Great Plains–Rocky Mountain region, USA. *Geol. Soc. Am. Spec. Pap*. 398, 309–319.

Smith, J. F. Jr., and Ketner, K. B. (1976). *Stratigraphy of Post-Paleozoic Rocks and Summary of Resources in the Carlin-Pinon Range Area, Nevada. United States Geological Survey Professional Paper 867-B*. Washington, DC: United States Government Printing Office.

Smith, M. E., Cassel, E. J., Jicha, B. R., Singer, B. S., and Canada, A. S. (2017). Hinterland drainage closure and lake formation in response to middle Eocene Farallon slab removal, Nevada. *Earth Planet. Sci. Lett.* 479, 156–169. doi: 10.1016/j.epsl.2017.09.023

Speelman, E. N., Sewall, J. O., Noone, D., Huber, M., von, der Heyt, A., et al. (2010). Modeling the influence of a reduced equator-to-pole sea surface temperature gradient on the distribution of water isotopes in the Early/Middle Eocene. *Earth Planet. Sci. Lett.* 298, 57–65. doi: 10.1016/j.epsl.2010.07.026

Surma, J., Assonov, S., Bolourchi, M. J., and Staubwasser, M. (2015). Triple oxygen isotope signatures in evaporated water bodies from the Sistan Oasis, Iran. *Geophys. Res. Lett.* 42, 8456–8462. doi: 10.1002/2015gl066475

Surma, J., Assonov, S., Herwartz, D., Voigt, C., and Staubwasser, M. (2018). The evolution of 17O-excess in surface water of the arid environment during recharge and evaporation. *Sci. Rep.* 8, 1–10.

Surma, J., Assonov, S., and Staubwasser, M. (2021). Triple oxygen isotope systematics in the hydrologic cycle. *Rev. Mineral Geochem.* 86, 401–428. doi: 10.2138/rmg.2021.86.12

Takeuchi, A., Hren, M. T., Smith, S. V., Chamberlain, C. P., and Larson, P. B. (2010). Pedogenic carbonate carbon isotopic constraints on paleoprecipitation: evolution of desert in the Pacific Northwest, USA, in response to topographic development of the Cascade Range. *Chem. Geol.* 277, 323–335. doi: 10.1016/j.chemgeo.2010.08.015

Takeuchi, A., and Larson, P. B. (2005). Oxygen isotope evidence for the late Cenozoic development of an orographic rain shadow in eastern Washington, USA. *Geology* 33, 313–316. doi: 10.1130/g21335.1

Tong, Y., Ibarra, D. E., Caves, J. K., Mukerji, T., and Graham, S. A. (2017). Constraining basin thermal history and petroleum generation using palaeoclimate data in the Piceance Basin. *Colorado* 29, 542–553. doi: 10.1111/bre.12213

Voarintsoa, N. R. G., Barkan, E., Bergel, S., Vieten, R., and Affek, H. P. (2020). Triple oxygen isotope fractionation between CaCO3 and H2O in inorganically precipitated calcite and aragonite. *Chem. Geol.* 539:119500. doi: 10.1016/j.chemgeo.2020.119500

Wacker, U., Fiebig, J., and Schoene, B. R. (2013). Clumped isotope analysis of carbonates: comparison of two different acid digestion techniques. *Rapid Commun. Mass Spectrom.* 27, 1631–1642. doi: 10.1002/rcm.6609

Wostbrock, J. A., Cano, E. J., and Sharp, Z. D. (2020). An internally consistent triple oxygen isotope calibration of standards for silicates, carbonates and air relative to VSMOW2 and SLAP2. *Chem. Geol.* 533:119432. doi: 10.1016/j.chemgeo.2019.119432

Wostbrock, J. A., and Sharp, Z. D. (2021). Triple oxygen isotopes in silica–water and carbonate–water systems. *Rev. Mineral Geochem.* 86, 367–400. doi: 10.2138/rmg.2021.86.11

Wostbrock, J. A., Sharp, Z. D., Sanchez-Yanez, C., Reich, M., van den Heuvel, D. B., and Benning, L. G. (2018). Calibration and application of silica-water triple oxygen isotope thermometry to geothermal systems in Iceland and Chile. *Geochim. Cosmochim. Acta* 234, 84–97. doi: 10.1016/j.gca.2018.05.007

Yanchilina, A. G., Yam, R., Kolodny, Y., and Shemesh, A. (2020). From diatom opal-A δ18O to chert δ18O in deep sea sediments. *Geochim. Cosmochim. Acta* 268, 368–382. doi: 10.1016/j.gca.2019.10.018

Yeung, L. Y., and Hayles, J. A. (2021). Climbing to the top of mount fuji: uniting theory and observations of oxygen triple isotope systematics. *Rev. Mineral Geochem.* 86, 97–135. doi: 10.2138/rmg.2021.86.03

Yeung, L. Y., Hayles, J. A., Hu, H., Ash, J. L., and Sun, T. (2018). Scale distortion from pressure baselines as a source of inaccuracy in triple-isotope measurements. *Rapid Commun. Mass Spectrom.* 32, 1811–1821. doi: 10.1002/rcm.8247

Young, E. D., Galy, A., and Nagahara, H. (2002). Kinetic and equilibrium mass-dependent isotope fractionation laws in nature and their geochemical and cosmochemical significance. *Geochim. Cosmochim. Acta* 66, 1095–1104. doi: 10.1016/s0016-7037(01)00832-8

Zakharov, D. O., Marin-Carbonne, J., Alleon, J., and Bindeman, I. N. (2021). Triple oxygen isotope trend recorded by Precambrian cherts: a perspective from combined bulk and in situ secondary ion probe measurements. *Rev. Mineral Geochem.* 86, 323–366. doi: 10.2138/rmg.2021.86.10

Conflict of Interest: The authors declare that the research was conducted in the absence of any commercial or financial relationships that could be construed as a potential conflict of interest.

frontiers in Earth Science

PERSPECTIVE
published: 26 March 2021
doi: 10.3389/feart.2021.624961

Molecules to Mountains: A Multi-Proxy Investigation Into Ancient Climate and Topography of the Pacific Northwest, USA

Alexander McLean and John Bershaw*

Department of Geology, Portland State University, Portland, OR, United States

We characterize the topographic evolution of the Pacific Northwest, United States, during the Cenozoic. New paleosol carbonate stable isotope ($\delta^{18}O$) results from central Oregon are presented, along with published proxy data, including fossil teeth, smectites, and carbonate concretions. We interpret a polygenetic history of Cascade Mountain topographic uplift along-strike, characterized by: 1) Steady uplift of the Washington Cascades through the Cenozoic due long-term arc rotation and shortening against a Canadian buttress, and 2) Uplift of the Oregon Cascades to similar-to-modern elevations by the late Oligocene, followed by topographic stagnation as extension developed into the Neogene. Since the Miocene, meteoric water $\delta^{18}O$ values have decreased in Oregon, possibly due to emergence of the Coast Range and westward migration of the coastline. Spatial variability in isotopic change throughout the Pacific Northwest suggests that secular global climate change is not the primary forcing mechanism behind isotopic trends, though Milankovitch cycles may be partly responsible for relatively short-term variation.

Keywords: paleoclimate, cascades, stable isotope, topography, oregon coast range

OPEN ACCESS

Edited by:
Alexis Licht, University of Washington, United States

Reviewed by:
Aude Gebelin, University of Plymouth, United Kingdom
Gregory Retallack, University of Oregon, United States

****Correspondence:***
Alexander McLean
amclean1917@gmail.com

Specialty section:
This article was submitted to Quaternary Science, Geomorphology and Paleoenvironment, a section of the journal Frontiers in Earth Science

Received: *01 November 2020*
Accepted: *18 February 2021*
Published: *26 March 2021*

Citation:
McLean A and Bershaw J (2021) Molecules to Mountains: A Multi-Proxy Investigation Into Ancient Climate and Topography of the Pacific Northwest, USA. Front. Earth Sci. 9:624961. doi: 10.3389/feart.2021.624961

INTRODUCTION

Stable isotope ratios of water illuminate temporal changes in a region's climate and topography (e.g. Savin, 1982; Garzione et al., 2000; Rowley and Garzione, 2007). Oxygen ($\delta^{18}O$) isotope ratios in pedogenic carbonates have been utilized to constrain paleoclimate (Cerling and Quade, 1993; Quade et al., 2007). While studies have looked at Cascade Mountain uplift using single proxies for analysis (e.g. Kohn et al., 2002; Kohn and Law, 2006; Bershaw et al., 2019), few comprehensive studies have taken a multi-proxy approach.

Considering multi-proxy stable isotope data can reduce uncertainty by constraining forcing mechanisms of isotopic change (e.g. Gébelin et al., 2012; Currie et al., 2016). We present new soil carbonate $\delta^{18}O$ data and synthesize existing paleowater proxy data to provide a more comprehensive interpretation of spatial (Pacific Northwest) and temporal (Cenozoic) patterns. Further, by comparing temporal patterns of stable oxygen isotopes in the Pacific Northwest to the record of global Cenozoic $\delta^{18}O$ change and Milankovitch-scale variation (e.g. Zachos et al., 2001), the influence of global climate relative to local topography changes is investigated.

BACKGROUND

The Pacific Northwest is in the mid-latitudes of the northern hemisphere. Orographic precipitation is significant in mountains across the region, including the Cascade Volcanic Arc (Cascades), the Olympic Mountains in Washington, and the Oregon Coast Range. The Cascade Mountains' rainshadow is associated with significant differences in precipitation amount on either side of the range. Average precipitation along at roughly −122°longitude (windward) ranges from 150–210 cm/year, while average precipitation at −121°longitude (lee) ranges from 22–25 cm/year (**Figure 1A**). Westerly air-flow patterns in the region are interpreted to have remained relatively constant during the Cenozoic based on depositional patterns of wind-blown ash (Robinson et al., 1990).

In Oregon and Washington, the Cascades extend north-south from British Columbia, Canada, to CA, United States. The Cascades are a magmatic arc that formed from the subduction of the Juan de Fuca Plate under the North American Plate (Priest, 1990). The onset of Cascade volcanism is interpreted to have begun ~45 Ma (Wells and McCaffrey, 2013). By ~35 Ma, the entire magmatic arc had been established from northern California to Mt. Rainier (Priest, 1990). The Clarno Formation of central Oregon (Bestland et al., 1999), Siletz River, and Crescent Formations of Washington contain significant amounts of subaerial volcanic rock that erupted as early as 51 Ma (Wells et al., 2014), suggesting some terrestrial settings by that time. The first plutons of the Cascade arc appeared at ~26 Ma (du Bray and John, 2011), with a significant volume of ignimbrites erupting starting at 39 Ma (Robinson et al., 1984). Volcanic activity slowed greatly between 17–10 Ma (Priest, 1990). In the mid-Miocene, the Columbia River Flood Basalt Group (CRBG) inundated much of Oregon and southern Washington (Beeson et al., 1989; Sherrod and Smith, 2000). They are absent in the Cascades themselves, suggesting the Cascades served as a topographic barrier. In the Late Miocene, further volcanic activity is evidenced by ash deposition and volcaniclastics of the Deschutes Formation and widespread Rattlesnake Tuff (Smith et al., 1987; Streck and Grunder 1995).

We present new $\delta^{18}O$ from paleosol carbonates from the lee side of the Cascades in Central Oregon (**Figure 1B**). Additionally, we synthesize published stable isotope data from Washington and Oregon, including fossil teeth (Kohn and Fremd, 2007), paleosol carbonates (Retallack et al., 2004; Takeuchi et al., 2010; Lechler et al., 2018), smectites (Takeuchi and Larson, 2005), and carbonate concretions (Methner et al., 2016) (**Figure 1**, **Supplementary Table S1**).

The late Cenozoic topographic history of the Cascades is disputed. Of the publications compiled for this study, Takeuchi and Larson (2005), Takeuchi et al., (2010) and Methner et al. (2016) propose most uplift occurred in the Neogene. Kohn and Fremd (2007) present data that may reflect near modern elevations in the Cascades by the late Oligocene, with an additional ~800 m of uplift in the last ~6 Ma. This interpretation is consistent with an interpretation of volcanic glass data (Bershaw et al., 2019). Retallack (2004a) shows that late Oligocene paleosols track Milankovitch cycles, but also suggests that Cascade uplift and rainshadow development play roles in longer-term trends (Retallack, 2004b). Lastly, dating of igneous rocks and thermochronologic data suggest that the uplift history of the Cascades varies across space and time (Robinson et al., 1984; Verplanck and Duncan, 1987; Conrey et al., 2002; Pesek et al., 2020).

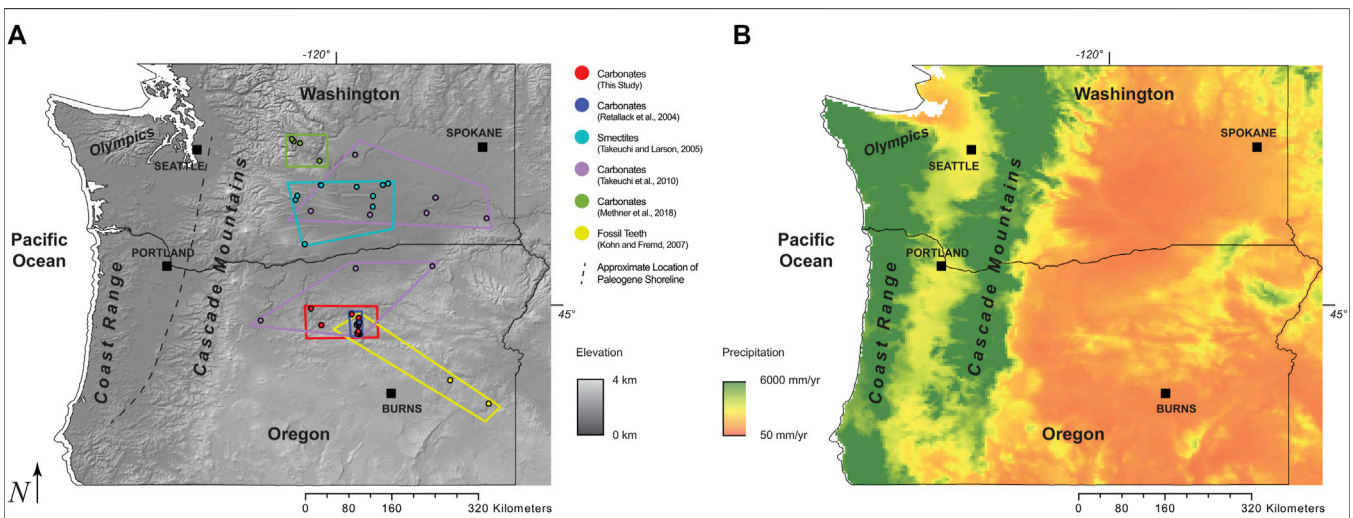

FIGURE 1 | (A) Location map showing the extent of new data (red) and published datasets throughout the Pacific Northwest. Elevation is shown as greyscale in km. Dashed line shows the inferred Paleogene shoreline prior to the emergence of the Oregon Coast Range based on paleogeographic maps by Orr and Orr (1999) and references therein. Digital Elevation Model (DEM) is based on the United States. Geological Survey Global 30 Arc-Second GTOPO30 (https://doi.org/10.5066/F7DF6PQS). **(B)** Map showing annual precipitation amount, averaged from 1981–2010 across the Pacific Northwest. Data Source: PRISM Climate Group (http://prism.oregonstate.edu).

METHODS

Paleosol carbonates throughout the John Day Formation of known age (~30–16 Ma) were sampled from locations described in Retallack et al., (1999) (**Figure 1B**, **Supplementary Figure S3**). ~100 g of sample was collected after removing the upper 30 cm of outcrop to reduce the influence of evaporation. Diagenetically altered samples, identified in the field by spar, calcite veins, and oxidation, were avoided (e.g. Bershaw et al., 2012).

Samples were crushed to powder and reacted with 30% H_2O_2 to remove organics. Analyses were carried out at the Iowa State University Stable Isotope Lab (SIL) on a ThermoFinnigan Delta Plus XL mass spectrometer in continuous-flow mode via Thermo GasBench II with a CombiPal autosampler. The long-term precision of the mass spectrometer for $\delta^{18}O$ is 0.06‰. Isotopic results are reported in standard delta notation ($\delta^{18}O$) relative to Vienna Standard Mean Ocean Water (VSMOW) (**Supplementary Table S1**).

To compare different proxy material, we estimate the stable isotopic composition of meteoric water using empirically derived fractionation factors (O'Neil et al., 1969; Yeh and Savin, 1977). To reduce interpretive bias, we apply a consistent standard for estimating the temperature of carbonate formation using ancient flora (Wolfe, 1994, **Supplementary Table S1**) or Δ47 temperatures when available. Our estimates are consistent with published water values where available. Fossil tooth data was averaged over the length of teeth and converted to water using an empirical relationship between environmental water and tooth chemistry (Kohn and Fremd, 2007). Differences between proxy data may exist that are related to unique conditions of mineral formation, such as the season or temperature of precipitation (Quade et al., 2007; Breecker et al., 2009).

We collected and analyzed 20 carbonate samples in central Oregon which we report here (**Supplementary Table S1**). Sample ages were determined by comparing stratigraphic position with published ages based on radiometric dating of tuff beds (Retallack et al., 1999; Retallack, 2004a). Exceptions are COS197 and COS197b, which are dated based on their position atop the Dayville Basalt (16.1 Ma) and below the Mascall Tuff Bed (15.2 Ma) (Prothero et al., 2006; Bestland et al., 2008; Drewicz and Kohn, 2018).

RESULTS

The average $\delta^{18}O$ value of our data is −11.2‰ with a range from −14.6 to −7.0‰. This is 1.6‰ more positive than the average of modern meteoric water in the lee (east) of the Oregon Cascade Mountains (−12.8‰), but within the range (−16.2 to −8.8‰) (**Supplementary Table S2**).

We combine our results with published data throughout the region, including 172 paleosol carbonates from Washington and Oregon (Takeuchi et al., 2010), 367 paleosol carbonates from Oregon (Retallack et al., 2004), 22 smectites from Washington (Takeuchi and Larson, 2005), 243 fossil teeth from Oregon (Kohn and Fremd, 2007), 31 modern carbonates from Washington (Lechler et al., 2018), and 119 carbonate concretions from Washington (Methner et al., 2016) (**Figures 1B2** and **Supplementary Table S1**). Published modern stream water $\delta^{18}O$ values from Washington and Oregon are reported for comparison (**Supplementary Table S2**), though they integrate less time than mineral proxy material so are inherently more variable. Ages of Eocene carbonates in WA, United States represent maximum ages, as there is uncertainty on the timing of potential diagenesis (Methner et al., 2016).

Together, these data do not show significant relationships between isotopic composition and latitude, longitude, elevation, or age (R^2 of 0.15, 0.00, 0.22, and 0.13, respectively). We separate datasets by state, as this provides a convenient latitudinal break between the northern Cascades of Washington and central Cascades of Oregon. In Washington, the average paleowater $\delta^{18}O$ for all samples is −14.3 ± 2.8‰ (1σ SD) and range from −18.0 to −6.8‰. There is a weak, negative correlation between age and $\delta^{18}O$ in samples from Washington, with an R^2 of 0.40. The average $\delta^{18}O$ in Oregon is −11.9 ± 2.1‰ (1σ SD), ~2.4‰ more positive than Washington, with a range of −15.8 to −8.4‰. Oregon carbonates demonstrate negligible correlation between age and $\delta^{18}O$ (R^2 of 0.03). Sample $\delta^{18}O$ values from individual studies are averaged within 2.5 million-year bins to emphasize trends in climate and topography across geologic time (**Figure 2**).

DISCUSSION

Carbonates as a Proxy for Ancient Meteoric Water

Before interpreting geologic and climatic trends, we assess whether proxies accurately reflect meteoric water at the time of deposition. Several paleosol carbonate samples from central Oregon likely experienced some form of alteration which may change primary carbonate $\delta^{18}O$ values, due to different formation water and/or temperatures of mineral precipitation. One Oligocene sample from our dataset (JDRL02, Figure A-6 of **Supplementary Figure S3**) has an anomalously low $\delta^{18}O$ value (−18.2‰) (open red circle in **Figure 2A**). This sample is purple in hue and only weakly calcareous, so it is likely that it underwent oxidation weathering sometime after deposition, potentially obfuscating the isotopic signal with oxide minerals (Hoefs, 2009). In addition, pedogenic carbonate $\delta^{18}O$ values from Retallack et al. (2004) across the late Oligocene (blue curve in **Figure 2A**) plot more negative (~5‰) than roughly contemporaneous fossil teeth and paleosols. This difference may be explained by higher temperatures of carbonate precipitation. The Turtle Cove Member, which makes up samples 24 Ma and older (Retallack et al., 2004), contains significant amounts of celadonite, which is an alteration product forming between 27–100°C (Weaver, 1989; Lander and Hay, 1993). Hay (1963) provides a narrower range of water temperatures for this interaction (27–55°C) and an age estimate of when this occurred (24 ± 2 Ma). If the temperature of carbonate precipitation was >50°C, as observed in Paleogene carbonates from Washington (Methner et al., 2016), this would cause a decrease in $\delta^{18}O$ of over 5‰ (Kim and O'Neil,

1997), explaining anomalously low $\delta^{18}O$ values (blue curve in **Figure 2**) relative to contemporaneous proxy data.

Regional Synthesis: Oregon

Previous studies have proposed various interpretations of Cenozoic mountain uplift and climate change in Oregon based on proxy data, including late Neogene uplift of the Cascade Mountains (Takeuchi and Larson, 2005; Takeuchi et al., 2010), contrasted by interpretations of high topography by late Oligocene time (Kohn and Fremd, 2007; Bershaw et al., 2020), in addition to the assertion that global climate change exerts a first-order control on isotopic records in Oregon (Retallack et al., 2004). In our regional synthesis, we focus on tectonic (million-year scale) forcing of isotopic data and do not consider carbonates from Retallack et al. (2004) (blue curve in **Figure 2A**), or our sample JDRL02 (open red circle in **Figure 2A**), whose temperature of formation may be higher than we assumed.

Our new time-averaged carbonate data is within the range of other water proxy data in Oregon. The isotopic variability in contemporaneous paleowater proxy material is similar to that observed in modern soils and teeth (grey vertical bar in **Figure 2A**) and smaller than modern meteoric water (black vertical bar in **Figure 2A**). Our paleosol carbonate data and fossil tooth data of Kohn and Fremd (2007) (red and yellow curve in **Figure 2A**) are within the wide range of modern meteoric water (dark vertical bar in **Figure 2A**) in the Oregon Cascade rainshadow, supporting the interpretation that some topography, possibly similar to modern (~1.5 km), existed by the late Oligocene. Additionally, modern coastal water $\delta^{18}O$ values (average −6.8‰, Bershaw et al., 2020) are 5.3‰ more positive than the average $\delta^{18}O$ of Paleogene, non-diagenetic carbonate in Oregon, which average −12.1‰ (n = 5). Our interpretation of near modern topography in the Oregon Cascades by Oligocene time is consistent with evidence of significant volcanism at that time (Verplanck and Duncan, 1987; Priest, 1990; Taylor, 1990) and volcanic glass δD data across the range (Bershaw et al., 2019).

Our new paleosol carbonate $\delta^{18}O$ values decrease by ~2.5‰ from 29 to 16 Ma. However, taken as a whole, our data is within the range of fossil teeth and previously published paleosol carbonate $\delta^{18}O$ results whose average stays relatively constant across the Oligocene and early Miocene, suggesting Cascade Mountain topography was relatively stable during this time. Variation in values (particularly high among teeth) may reflect Milankovitch cycles and/or spatial variability among sample locations within the study area (**Figure 1**). This could reflect local topography and associated microclimates (Retallack, 2004b; Kukla et al., 2021 this volume), as observed in modern meteoric water across the same spatial extent (Bershaw et al., 2020).

Fossil tooth (Kohn and Fremd, 2007) and paleosol carbonate (Takeuchi et al., 2010) $\delta^{18}O$ values from the late Miocene and Pliocene are 2–3‰ more positive than modern carbonates and teeth (**Figure 2A**) in central Oregon. This is likely not caused by global cooling at this time, as northern hemisphere ice sheet expansion resulted in a ~1.5‰ increase in oceanic $\delta^{18}O$, whereas our data reflect a decrease in $\delta^{18}O$ (Zachos et al., 2001). Instead, we suggest this negative shift in isotopic composition since the late Miocene may reflect the westward migration (>100 km) of the Oregon coast, driven by the Neogene emergence of a subaerial Oregon Coast Range (**Figure 1B**). A drop in $\delta^{18}O$ values would be expected as the distance to the Pacific Ocean increased and a subaerial Coast Range created a modest moisture barrier, further depleting ^{18}O in vapor. Emergence of the Coast Range at this time is independently constrained by an analysis of the Portland Basin, which shows a significant decrease in accommodation space

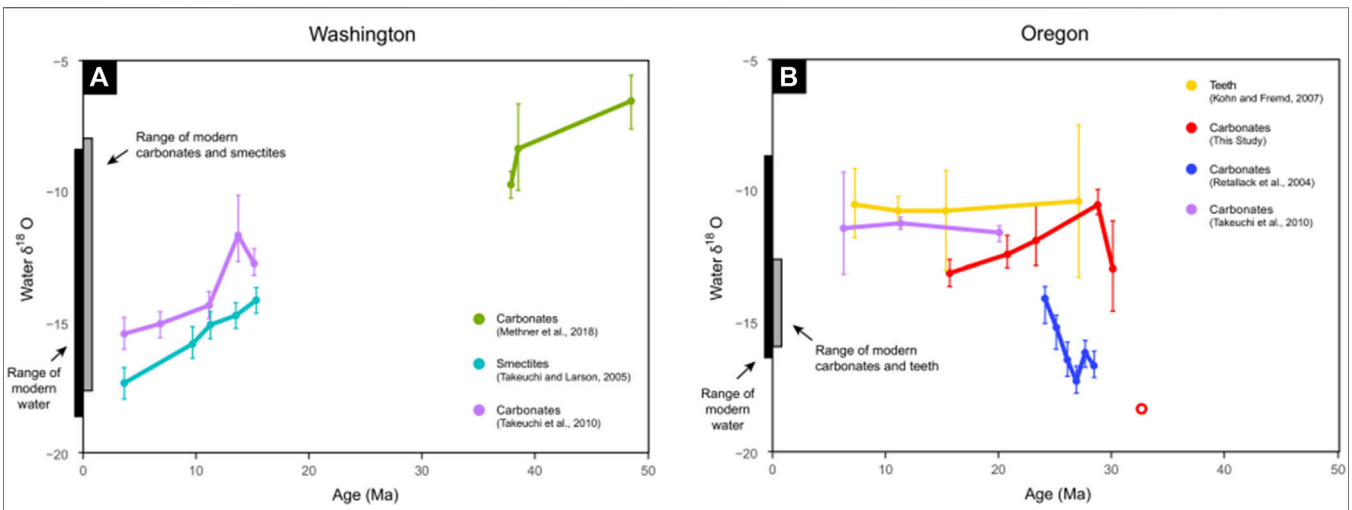

FIGURE 2 | Plots showing temporal variations in meteoric water based on $\delta^{18}O$ values of carbonates, smectites, and fossil teeth for central Washington at ~47 latitude **(A)** and central Oregon at ~45 latitude **(B)**, both in the lee (east side) of the Cascade Mountains. Sample $\delta^{18}O$ values are averaged within 2.5 million-year windows (shown as points) to emphasize trends across geologic time. Uncertainty bars represent the range of $\delta^{18}O$ values found within each time-window. Samples are grouped (color-coded) by publication and sample type. The range of modern meteoric water $\delta^{18}O$ east of the Cascade Mountains is shown (black bar) for both Washington and Oregon based on published stream data (**Table S2**). Ranges in published modern carbonates east of the Cascade Mountains (Takeuchi et al., 2010; Lechler et al., 2018 and this study), smectites (Takeuchi and Larson, 2005), and mammal teeth (Kohn and Fremd, 2007) $\delta^{18}O$ data (**Supplementary Table S1**) are also shown for each state (gray bar). The open red circle (Oregon) represents sample JDRL_02, interpreted to be diagenetic carbonate.

sometime after the eruption of the CRBG in the mid-Miocene and coeval migration of basin depocenters eastward (Scanlon et al., 2019 in press). Modern coastal meteoric water $\delta^{18}O$ values are ~2.4‰ higher than those in the western foothills of the Cascade Mountains (Bershaw et al., 2020), where the coastline was prior to Coast Range uplift. This suggests that uplift of the Coast Range could account for the discrepancy between late Miocene and modern water proxy data.

Regional Synthesis: Washington

Estimated meteoric water $\delta^{18}O$ values from Eocene carbonates in Washington (Methner et al., 2016) are relatively positive (average −8.8‰) compared to both modern water (average −14.6‰) and modern carbonates and smectites nearby (average −14.0‰) (**Figure 2B** and **Supplementary Table S1**). Instead, they are similar to the isotopic composition of modern stream water at low elevations on the west side of the Olympics (−7.1‰) and Cascades in WA, United States (−9.1‰) (Bershaw et al., 2020), suggesting the northern Cascades Mountains were not a significant topographic barrier to westerly derived moisture at that time.

Eocene paleowater $\delta^{18}O$ values are also significantly more positive than Miocene and Pliocene smectite and paleosols (**Figure 2B**), resulting in a progressive trend towards more negative $\delta^{18}O$ values across the Cenozoic. This is not likely the result of global cooling, as temperature change is moderated by an increase in oceanic $\delta^{18}O$ of ~1.8‰ from the late Eocene to Miocene (Zachos et al., 2001). We hypothesize that the northern Cascades in Washington have undergone progressive topographic uplift since the Paleogene. At what point uplift resulted in a rainshadow in central WA, United States is less clear, though paleofloral data from Idaho and paleosol carbonate $\delta^{13}C$ data from Washington suggest arid conditions similar to modern were not established until the late Miocene or Pliocene (Takeuchi et al., 2010; Mustoe and Leopold, 2013). Progressive uplift through much of the Cenozoic is consistent with evidence that the northern Cascades were an active volcanic arc in the Paleogene (Tabor et al., 1984) and thermochronology that shows slow uplift of the Washington Cascades (<0.25 km/m.y.) from the Eocene to the late Miocene (Reiners et al., 2002; Pesek et al., 2020), with ongoing uplift today (Wells and McCaffrey, 2013).

Polygenetic History of Topography Across the Pacific Northwest

Our synthesis of water proxy datasets shows a polygenetic uplift history for the Cascade Mountains along strike. Oregon and Washington carbonates show distinct temporal trends, with differences as large as ~5‰ across the late Miocene, where Oregon paleowaters are more enriched than contemporaneous water in Washington (**Figure 2**). These spatial discrepancies support our assertion that global climate change is not the primary forcing mechanism behind isotopic change in the Pacific Northwest on tectonic (million year) scales. Instead, isotopic proxy records suggest that the Northern Cascades in Washington were not a significant barrier to westerly airflow in the Eocene, but experienced progressive topographic uplift from the Paleogene to now, while the Cascades in Oregon formed a topographic barrier by the late Oligocene, but remained relatively unchanged into the Neogene. This interpretation is consistent with the tectonic framework of the region since mid-Miocene time, where east-west extension (subsidence) has developed in the Oregon Cascades (Conrey et al., 1997; Guffanti and Weaver, 1988) while uplift of the northern Cascades is due to subduction-related rigid block rotation (**Figure 4** from Wells et al., 1998), delamination (Reiners et al., 2002), and/or erosional denudation (Enkelmann et al., 2015). Our interpretation of polygenetic uplift across the Oregon and Washington Cascades in consistent with volcanic glass δD values (Bershaw et al., 2019) and thermochronometry, which shows significant geographic variation in exhumation timing (Pesek et al., 2020), as opposed to contemporaneous, wholesale uplift of the entire Cascade Mountain chain.

Additionally, we hypothesize that the subaerial emergence of the Coast Range in Oregon and westward migration of the coastline (Scanlon et al., 2019 in press) caused a modest depletion in proxy material $\delta^{18}O$ values that is not apparent in Washington proxy data, where the coastline remains at the base of the northern Cascades and the Puget Lowland remains connected to the ocean today. The migration of the coastline west and drying of the Willamette Valley (forearc) in the late Miocene coincides with aridification of central Washington and Idaho (Takeuchi et al., 2010; Mustoe and Leopold, 2013). We speculate that this shift in paleoclimate may reflect an increase in continentality (distance from oceanic water source) as opposed to wholesale Cascade Mountain uplift at that time.

CONCLUSION

We present new pedogenic carbonate $\delta^{18}O$ data from central Oregon and synthesize this with published water proxy data from across the Pacific Northwest. We interpret a polygenetic history of Cascade Mountain topographic uplift along-strike, characterized by: 1) Progressive uplift of the Washington Cascades through the Cenozoic due long-term arc rotation and shortening against a Canadian buttress, and 2) Uplift of the Oregon Cascades to similar-to-modern elevations by the late Oligocene, followed by topographic stagnation as extension developed into Neogene time. Since the Miocene, meteoric water $\delta^{18}O$ values have decreased in Oregon, possibly due to emergence of the Coast Range and westward migration of the coastline. Isotopic trends could also be influenced by changes in seasonality, the isotopic composition of the Pacific Ocean, and Blue or Klamath Mountain topography. Lastly, variability in $\delta^{18}O$ values of proxy materials at any given time is likely forced by Milankovitch cycles, local topography (and associated microclimates), and volatility inherent in arid environments, where evaporation of surface water can be significant.

DATA AVAILABILITY STATEMENT

The original contributions presented in the study are included in the article/**Supplementary Material**, further inquiries can be directed to the corresponding authors.

AUTHOR CONTRIBUTIONS

There are two authors who contributed to this manuscript. AM (corresponding author) contributed to collecting and analyzing samples, writing the manuscript, interpreting the results and compiling figures and tables. JB contributed to collecting samples, writing the manuscript, interpreting results, and compiling figures. Both authors agree to be accountable for the content of the work.

ACKNOWLEDGMENTS

Samples were collected at John Day Fossil Beds National Monument under Permit JODA-2019-SCI-0009. The authors would like to thank Dr. Nicholas Famoso, The National Park Service, and Patrick Gamman for facilitating sample collection and providing insight. Publication of this article in an open access journal was funded by the Portland State University Library's Open Access Fund.

SUPPLEMENTARY MATERIAL

The Supplementary Material for this article can be found online at: https://www.frontiersin.org/articles/10.3389/feart.2021.624961/full#supplementary-material.

REFERENCES

Beeson, M. H., Tolan, T. L., and Anderson, J. L. (1989). "The Columbia River Basalt Group in western Oregon; geologic structures and other factors that controlled flow emplacement patterns," in *Volancism and tectonism in the Columbia River flood-basalt province: Geological Society of America Special Paper*. Editors S. P. Reidel and P. R. Hooper (Boulder, Colorado: Geological Society of America), 239, 223–246.

Bershaw, J., Garzione, C. N., Schoenbohm, L., Gehrels, G., and Tao, L. (2012). Cenozoic evolution of the Pamir plateau based on stratigraphy, zircon provenance, and stable isotopes of foreland basin sediments at Oytag (Wuyitake) in the Tarim Basin (west China). *J. Asian Earth Sci.* 44, 136–148. doi:10.1016/j.jseaes.2011.04.020

Bershaw, J., Cassel, E. J., Carlson, T. B., Streig, A. R., and Streck, M. J. (2019). Volcanic glass as a proxy for Cenozoic elevation and climate in the Cascade Mountains, Oregon, USA. *J. Volcanol. Geotherm. Res.* 381, 157–167. doi:10.1016/j.jvolgeores.2019.05.021

Bershaw, J., Hansen, D. D., and Schauer, A. J. (2020). Deuterium excess and 17O-excess variability in meteoric water across the Pacific Northwest, USA. *Tellus B: Chem. Phys. Meteorol.* 72 (1), 1–17. doi:10.1080/16000889.2020.1773722

Bestland, E. A., Forbes, M. S., Krull, E. S., Retallack, G. J., and Fremd, T. (2008). Stratigraphy, paleopedology, and geochemistry of the middle Miocene Mascall Formation (type area, central Oregon, USA). *PaleoBios.* 28 (2), 41–61.

Bestland, E. A., Hammond, P. E., Blackwell, D. L. S., Kays, M. A., Retallack, G. J., and Stimac, J. (1999). Geologic framework of the clarno unit, John day fossil beds national monument, central Oregon. *Oreg. Geol.* 61 (1), 3–19.

Breecker, D. O., Sharp, Z. D., and McFadden, L. D. (2009). Seasonal bias in the formation and stable isotopic composition of pedogenic carbonate in modern soils from central New Mexico, USA. *Geol. Soc. Am. Bull.* 121, 630–640.

Cerling, T. E., and Quade, J. (1993). Climate change in continental isotopic records. *Geophys. Monogr.* 78, 217–231.

Conrey, R. M., Sherrod, D. R., Hooper, P. R., and Swanson, D. A. (1997). Diverse primitive magmas in the Cascade arc, northern Oregon and southern Washington. *Can. Mineral.* 35 (2), 367–396.

Conrey, R. M., Taylor, E. M., Donnelly-Nolan, J. M., and Sherrod, D. R. (2002). "North-central Oregon Cascades: exploring petrologic and tectonic intimacy in a propagating intra-arc rift," in Field guide geologic process in cascadia; 98th annual meeting of the cordilleran section of the geological society of America. Editor G. W. Moore (Oregon: Oregon Department of Geology and Mineral Industries), 36, 47–90.

Currie, B. S., Polissar, P. J., Rowley, D. B., Ingalls, M., Li, S., Olack, G., et al. (2016). Multiproxy paleoaltimetry of the late Oligocene-Pliocene Oiyug basin, southern Tibet. *Am. J. Sci.* 316 (5), 401–436. doi:10.2475/05.2016.01

Drewicz, A. E., and Kohn, M. J. (2018). Stable isotopes in large herbivore tooth enamel capture a mid-Miocene precipitation spike in the interior Pacific Northwest. *Palaeogeogr. Palaeoclimatol. Palaeoecol.* 495, 1–12. doi:10.1016/j.palaeo.2017.11.022

du Bray, E., and John, D. A. (2011). Petrologic, tectonic, and metallogenic evolution of the Ancestral Cascades magmatic arc, Washington, Oregon, and northern California. *Geosphere* 7 (5), 1102–1133. doi:10.1130/ges00669.1

Enkelmann, E., Ehlers, T. A., Merli, G., and Methner, K. (2015). Thermal and exhumation history of the Eocene chumstick basin, Washington state, USA. *Tectonics* 34 (5), 951–969. doi:10.1002/2014tc003767

Garzione, C. N., Quade, J., DeCelles, P. G., and English, N. B. (2000). Predicting paleoelevation of Tibet and the Himalaya from δ18O vs. altitude gradients in meteoric water across the Nepal Himalaya. *Earth Planet. Sci. Lett.* 183 (1–2), 215–229. doi:10.1016/s0012-821x(00)00252-1

Gébelin, A., Mulch, A., Teyssier, C., Page Chamberlain, C., and Heizler, M. (2012). Coupled basin-detachment systems as paleoaltimetry archives of the western North American Cordillera. *Earth Planet. Sci. Lett.* 335–336, 36–47. doi:10.1016/j.epsl.2012.04.029

Guffanti, M., and Weaver, C. S. (1988). Distribution of late Cenozoic volcanic vents in the Cascade Range: volcanic arc segmentation and regional tectonic considerations. *J. Geophys. Res.* 93 (B6), 6513–6529. doi:10.1029/jb093ib06p06513

Hay, R. L. (1963). *Stratigraphy and zeolitic diagenesis of the john day formation of Oregon*. California: University of California Press

Hayes, J. M. (2001). Fractionation of carbon and hydrogen isotopes in biosynthetic processes. *Rev. Mineral. Geochem.* 43 (1), 225–277. doi:10.2138/gsrmg.43.1.225

Hoefs, J. (2009). *Stable isotope geochemistry*. Berlin: Springer, 285

Kim, S. T., and O'Neil, J. R. (1997). Equilibrium and nonequilibrium oxygen isotope effects in synthetic carbonates. *Geochim. Cosmochim. Acta* 61 (16), 3461–3475. doi:10.1016/s0016-7037(97)00169-5

Kohn, M. J., and Fremd, T. J. (2007). Tectonic controls on isotope compositions and species diversification, John Day Basin, central Oregon. *PaleoBios.* 27 (2), 48–61.

Kohn, M. J., and Law, J. M. (2006). Stable isotope chemistry of fossil bone as a new paleoclimate indicator. *Geochim. Cosmochim. Acta.* 70 (4), 931–946. doi:10.1016/j.gca.2005.10.023

Kohn, M. J., Miselis, J. L., and Fremd, T. J. (2002). Oxygen isotope evidence for progressive uplift of the Cascade Range, Oregon. *Earth Planet. Sci. Lett.* 204 (1–2), 151–165. doi:10.1016/s0012-821x(02)00961-5

Kukla, T., Ibarra, D. E., Caves, J. K., Gooley, J. T., Mullins, C. E., Kramer, S., et al. (2021). High-resolution stable isotope paleotopography of the John day region, Oregon, USA. *Front. Earth Sci.* 9, 30. doi:10.3389/feart.2021.635181

Lander, R. H., and Hay, R. L. (1993). Hydrogeologic control on zeolitic diagenesis of the White River sequence. *Geol. Soc. Am. Bull.* 105 (3), 361–376. doi:10.1130/0016-7606(1993)105<0361:hcozdo>2.3.co;2

Lechler, A. R., Huntington, K. W., Breecker, D. O., Sweeney, M. R., and Schauer, A. J. (2018). Loess-paleosol carbonate clumped isotope record of late Pleistocene-Holocene climate change in the Palouse region, Washington State, USA. *Quat. Res.* 90 (2), 331–347. doi:10.1017/qua.2018.47

Mack, G. H., Cole, D. R., and Treviño, L. (2000). The distribution and discrimination of shallow, authigenic carbonate in the Pliocene-Pleistocene Palomas Basin, southern Rio Grande rift. *Geol. Soc. Am. Bull.* 112 (5), 643–656. doi:10.1130/0016-7606(2000)112<643:tdados>2.0.co;2

Methner, K., Fiebig, J., Wacker, P., Umhoefer, J., Chamberlain, C. P., and Mulch, L. A. (2016). Eocene-Oligocene proto-Cascades topography revealed by clumped (Δ47) and oxygen isotope (δ18O) geochemistry (Chumstick Basin, WA, USA). *Tectonics* 35, 546–564.

Mulch, A., and Chamberlain, C. P. (2007). Stable isotope paleoaltimetry in orogenic belts the silicate record in surface and crustal geological archives. *Rev. Mineral. Geochem.* 66 (1), 89–118. doi:10.2138/rmg.2007.66.4

Mustoe, G. E., and Leopold, E. B. (2014). Paleobotanical evidence for the post-Miocene uplift of the Cascade Range. *Can. J. Earth Sci.* 51, 809–824.

O'Neil, J. R., Clayton, R. N., and Mayeda, T. K. (1969). Oxygen isotope fractionation in divalent metal carbonates. *J. Chem. Phys.* 51 (12), 5547–5558. doi:10.1063/1.1671982

Orr, E. L., and Orr, W. N. (1999). *Geology of Oregon*. 5th Edition. Dubuque, Iowa: Kendall Hunt Publishing Company

Pesek, M. E., Perez, N. D., Meigs, A., Rowden, C. C., and Giles, S. M. (2020). Exhumation timing in the Oregon Cascade Range decoupled from deformation, magmatic, and climate patterns. *Tectonics* 39 (9), e2020TC006078. doi:10.1029/2020tc006078

Priest, G. R. (1990). Volcanic and tectonic evolution of the Cascade volcanic arc, central Oregon. *J. Geophys. Res.* 95 (B12), 19583–19599. doi:10.1029/jb095ib12p19583

Prothero, D. R., Draus, E., and Foss, S. E. (2006). Magnetic stratigraphy of the lower portion of the middle Miocene Mascall Formation, central Oregon. *PaleoBios* 26 (1), 37–42.

Quade, J., Garzione, C., and Eiler, J. (2007). Paleoelevation reconstruction using pedogenic carbonates. *Rev. Mineral. Geochem.* 66 (1), 53–87. doi:10.2138/rmg.2007.66.3

Reidel, S. P., Camp, V. E., Tolan, T. L., and Martin, B. S. (2013). The Columbia River flood basalt province: stratigraphy, areal extent, volume, and physical volcanology. *Geol. Soc. Am. Spec. Pap.* 497, 1–43. doi:10.1130/2013.2497(1)

Reiners, P. W., Ehlers, T. A., Garver, J. I., Mitchell, S. G., Montgomery, D. R., Vance, J. A., et al. (2002). Late Miocene exhumation and uplift of the Washington cascade range. *Geology* 30 (9), 767–770. doi:10.1130/0091-7613(2002)030<0767:lmeauo>2.0.co;2

Retallack, G. J. (2004a). Late Oligocene bunch grassland and early Miocene sod grassland paleosols from central Oregon, USA. *Palaeogeogr. Palaeoclimatol. Palaeoecol.* 207 (3–4), 203–237. doi:10.1016/j.palaeo.2003.09.027

Retallack, G. J. (2004b). Late Miocene climate and life on land in Oregon within a context of Neogene global change. *Palaeogeogr. Palaeoclimatol. Palaeoecol.* 214 (1–2), 97–123. doi:10.1016/s0031-0182(04)00394-3

Retallack, G. J., Bestland, E. A., and Fremd, T. J. (1999). *Eocene and Oligocene paleosols of central Oregon*. Boulder, Colorado: Geological Society of America, 344

Retallack, G. J., Tanaka, S., and Tate, T. (2002). Late Miocene advent of tall grassland paleosols in Oregon. *Palaeogeogr. Palaeoclimatol. Palaeoecol.* 183 (3–4), 329–354. doi:10.1016/s0031-0182(02)00250-x

Retallack, G. J., Wynn, J. G., and Fremd, T. J. (2004). Glacial-interglacial-scale paleoclimatic change without large ice sheets in the Oligocene of central Oregon. *Geology* 32 (4), 297–300. doi:10.1130/g20247.1

Robinson, P. T., Brem, G. F., and McKee, E. H. (1984). John Day Formation of Oregon: a distal record of early Cascade volcanism. *Geology* 12 (4), 229–232. doi:10.1130/0091-7613(1984)12<229:jdfooa>2.0.co;2

Robinson, P. T., Walker, G. W., and McKee, E. H. (1990). "Eocene (?), Oligocene, and lower Miocene rocks of the blue mountains region," in *Geology of the blue mountains region of Oregon, Idaho, and Washington: cenozoic geology of the blue mountains region*. Editor G. W. Walker (Reston, Virginia: US Geological Survey), 29–62.

Rowley, D. B., and Garzione, C. N. (2007). Stable isotope-based paleoaltimetry. *Annu. Rev. Earth Planet. Sci.* 35, 463–508. doi:10.1146/annurev.earth.35.031306.140155

Sanyal, P., Bhattacharya, S. K., and Prasad, M. (2005). Chemical diagenesis of Siwalik sandstone: isotopic and mineralogical proxies from Surai Khola section, Nepal. *Sediment. Geol.* 180 (1–2), 57–74. doi:10.1016/j.sedgeo.2005.06.005

Savin, S. M. (1982). "Stable isotopes in climatic reconstructions," in *Climate and Earth history*. Washington, DC: Natl. Acad. Press, 164–171.

Scanlon, D. P., Bershaw, J., Wells, R. E., and Streig, A. R. (2019). The spatial and temporal evolution of the Portland and tualatin forearc basins, Oregon, USA. MS Thesis. Oregon: Portland State University.

Sherrod, D. R., and Smith, J. G. (2000). *Geologic map of upper Eocene to Holocene volcanic and related rocks of the Cascade Range, Oregon*. Washington, DC: US Geological Survey, 17

Smith, G. A., Snee, L. W., and Taylor, E. M. (1987). Stratigraphic, sedimentologic, and petrologic record of late Miocene subsidence of the central Oregon High Cascades. *Geology* 15 (5), 389–392. doi:10.1130/0091-7613(1987)15<389:ssapro>2.0.co;2

Snavely, P. D., MacLeod, N. S., and Wagner, H. C. (1973). Miocene tholeiitic basalts of coastal Oregon and Washington and their relations to coeval basalts of the Columbia Plateau. *Geol. Soc. Am. Bull.* 84 (2), 387–424. doi:10.1130/0016-7606(1973)84<387:mtboco>2.0.co;2

Streck, M. J., and Grunder, A. L. (1995). Crystallization and welding variations in a widespread ignimbrite sheet; the Rattlesnake Tuff, eastern Oregon, USA. *Bull. Volcanol.* 57 (3), 151–169. doi:10.1007/s004450050086

Tabor, R. W., Frizzell, V. A., Vance, J. A., and Naeser, C. W. (1984). Ages and stratigraphy of lower and middle Tertiary sedimentary and volcanic rocks of the central Cascades, Washington: application to the tectonic history of the Straight Creek fault. *Geol. Soc. Am. Bull.* 95 (1), 26–44. doi:10.1130/0016-7606(1984)95<26:aasola>2.0.co;2

Takeuchi, A., Hren, M. T., Smith, S. V., Chamberlain, C. P., and Larson, P. B. (2010). Pedogenic carbonate carbon isotopic constraints on paleoprecipitation: evolution of desert in the Pacific Northwest, USA, in response to topographic development of the Cascade Range. *Chem. Geol.* 277 (3–4), 323–335. doi:10.1016/j.chemgeo.2010.08.015

Takeuchi, A., and Larson, P. B. (2005). Oxygen isotope evidence for the late Cenozoic development of an orographic rain shadow in eastern Washington, USA. *Geology* 33 (4), 313–316. doi:10.1130/g21335.1

Taylor, E. M. (1990). Volcanic history and tectonic development of the Central High Cascade Range, Oregon. *J. Geophys. Res.* 95 (B12), 19611–19622. doi:10.1029/jb095ib12p19611

Verplanck, E. P., and Duncan, R. A. (1987). Temporal variations in plate convergence and eruption rates in the Western Cascades, Oregon. *Tectonics* 6 (2), 197–209. doi:10.1029/tc006i002p00197

Weaver, C. E. (1989). *Clays, muds, and shales*. Amsterdam, NL: Elsevier

Wells, R., Bukry, D., Friedman, R., Pyle, D., Duncan, R., Haeussler, P., et al. (2014). Geologic history of Siletzia, a large igneous province in the Oregon and Washington Coast Range: correlation to the geomagnetic polarity time scale and implications for a long-lived yellowstone hotspot. *Geosphere* 10 (4), 692–719. doi:10.1130/ges01018.1

Wells, R. E., and McCaffrey, R. (2013). Steady rotation of the Cascade arc. *Geology* 41 (9), 1027–1030. doi:10.1130/g34514.1

Wells, R. E., Weaver, C. S., and Blakely, R. J. (1998). Fore-arc migration in Cascadia and its neotectonic significance. *Geology* 26 (8), 759–762. doi:10.1130/0091-7613(1998)026<0759:famica>2.3.co;2

Wolfe, J. A. (1994). Tertiary climatic changes at middle latitudes of western North America. *Palaeogeogr. Palaeoclimatol. Palaeoecol.* 108 (3–4), 195–205. doi:10.1016/0031-0182(94)90233-x

Yeh, H.-W., and Savin, S. M. (1977). Mechanism of burial metamorphism of argillaceous sediments: 3. O-isotope evidence. *Geol. Soc. Am. Bull.* 88 (9), 1321–1330. doi:10.1130/0016-7606(1977)88<1321:mobmoa>2.0.co;2

Zachos, J., Pagani, M., Sloan, L., Thomas, E., and Billups, K. (2001). Trends, rhythms, and aberrations in global climate 65 Ma to present. *Science* 292 (5517), 686–693. doi:10.1126/science.1059412

Conflict of Interest: The authors declare that the research was conducted in the absence of any commercial or financial relationships that could be construed as a potential conflict of interest.

frontiers in Earth Science

MINI REVIEW
published: 09 April 2021
doi: 10.3389/feart.2021.633687

Triple Oxygen Isotope Paleoaltimetry of Crystalline Rocks

C. Page Chamberlain[1], Daniel E. Ibarra[1,2,3], Tyler Kukla[1], Katharina A. Methner[1] and Yuan Gao[4]*

[1] Department of Geological Sciences, Stanford University, Stanford, CA, United States, [2] Department of Earth and Planetary Science, University of California, Berkeley, Berkeley, CA, United States, [3] Institute at Brown for Environment and Society and the Department of Earth, Environmental and Planetary Science, Brown University, Providence, RI, United States, [4] Earth Sciences and Resources, China University of Geosciences (Beijing), Beijing, China

Triple oxygen isotopes of hydrothermally altered minerals from crystalline rocks can be used to determine past elevations of mountain ranges. This method uses all three isotopes of oxygen (^{16}O, ^{17}O, and ^{18}O) to create arrays that can be extrapolated back to the meteoric water line. One advantage of this technique is that it relies only on oxygen isotopes in contrast to previous studies that use oxygen and hydrogen isotopes to determine the isotopic composition of meteoric waters. Our analysis suggests that hydrogen isotopes may exchange with ambient fluids. Triple oxygen isotopes provide an independent check on the reliability of hydrogen isotope studies.

Keywords: paleoaltimetry, triple oxygen isotopes, meteoric fluids, granites, Rocky Mountains

OPEN ACCESS

Edited by:
Steven L. Forman, Baylor University, United States

Reviewed by:
Ilya Bindeman, University of Oregon, United States
Christian Teyssier, University of Minnesota Twin Cities, United States

****Correspondence:***
C. Page Chamberlain
chamb@stanford.edu

Specialty section:
This article was submitted to Quaternary Science, Geomorphology and Paleoenvironment, a section of the journal Frontiers in Earth Science

Received: *25 November 2020*
Accepted: *05 March 2021*
Published: *09 April 2021*

Citation:
Chamberlain CP, Ibarra DE, Kukla T, Methner KA and Gao Y (2021) Triple Oxygen Isotope Paleoaltimetry of Crystalline Rocks. Front. Earth Sci. 9:633687. doi: 10.3389/feart.2021.633687

INTRODUCTION

With the advent of stable isotope paleoaltimetry over 20 years ago (Chamberlain et al., 1999; Garzione et al., 2000; Rowley et al., 2001), we now have excellent constraints on the topographic history of many of the world's mountain belts. This work builds on the well-known relationship between $\delta^{18}O$ and δD of meteoric water and elevation (Dansgaard, 1964), which is governed by Rayleigh distillation as airmasses and resultant precipitation pass over a mountain range. Indeed, it was recognized very early on that the isotope composition of authigenic minerals could be used to determine past elevations (Taylor, 1974; Winograd et al., 1985; Lawrence and Rashkes Meaux, 1993), before the sub-field of paleoaltimetry was established. So where are we today?

At the root of stable isotope paleoaltimetry studies are the theoretical and experimental advances that allow for a deeper understanding of isotopic records and increased number of proxies for the isotopic composition of paleo-precipitation. On the theoretical side we now have excellent Rayleigh distillation models (Rowley et al., 2001), one-dimensional isotopic vapor transport models that allow for vapor recycling (Winnick et al., 2014) as well as orographic precipitation (Kukla et al., 2019), and isotopic enabled Global Climate Models (GCMs) (Ehlers and Poulsen, 2009). Although there are many complications with these types of models, including vapor recycling (Kukla et al., 2019), changing isotopic lapse rates with temperature (Poulsen and Jeffery, 2011), and mixing of different moisture sources (Caves Rugenstein and Chamberlain, 2018), to name a few, the modern isotopic lapse rates across Earth are remarkably constant except at high latitudes (Poage and Chamberlain, 2001). Thus, many studies employ multiple approaches to reconstruct past elevation of orogens—often with similar results (c.f. Mix et al., 2011 and Feng et al., 2013). On the experimental side researchers have developed oxygen isotopic proxies for carbonate in paleosols (Quade et al., 2007) and paleolake sediments (Davis et al., 2009), fossil teeth (Kohn et al., 2002),

clay minerals (Chamberlain et al., 1999), and chert (Ibarra et al., 2021). For hydrogen isotopes we have the additional proxies such as hydrated volcanic glasses (Mulch et al., 2008; Cassel et al., 2009; Hudak and Bindeman, 2018), clay minerals (Capuano, 1992; Delgado and Reyes, 1996; Mulch et al., 2006), plant leaf waxes (Hren et al., 2010) and metamorphic micas (Mulch et al., 2004).

These authigenic mineral proxies allow determination of meteoric water isotopic values if the temperature of formation and the appropriate fractionation factor are known. It is, however, also possible to determine meteoric water values using two isotopic systems and arrays of mineral isotopic compositions and extrapolating these arrays to the meteoric water line. This approach typically uses hydrogen and oxygen isotopes of hydrothermally altered minerals (see Criss and Taylor, 1983) or hydrogen and oxygen isotopes of chert from evaporative lakes (Abruzzese et al., 2005) to determine the original meteoric waters that altered or formed these minerals. The one difficulty with this approach is that it requires that both the hydrogen and oxygen isotopes behave similarly during mineral formation, mineral alteration, cooling, etc., which for hydrogen may not be the case (Graham, 1981; Graham et al., 1987). Thus, there is considerable power in leveraging isotopic systems that only use one element—such as provided by the analysis of the three isotopes of oxygen (^{16}O, ^{17}O, ^{18}O).

Thus, this mini-review discusses the new proxy afforded by the use of all three isotopes of oxygen – or triple oxygen isotope paleoaltimetry. This new proxy is particularly useful for determining the paleoelevations of the crystalline cores of mountain ranges, but also can be used to back out original meteoric waters from lake sediments (Ibarra et al., 2021). Here we review the application of triple oxygen isotopes in hydrothermally altered crystalline rocks.

TERMINOLOGY AND EQUATIONS

Triple oxygen isotope studies use all three stable oxygen isotopes of oxygen (^{16}O, ^{17}O and ^{18}O). The method exploits the very small deviations from mass dependent fractionations that govern most processes on Earth (Sharp et al., 2018). These deviations are caused by kinetic effects, such as occur during evaporation from water body etc. (Barkan and Luz, 2005) and temperature dependent equilibrium process during isotope exchange reactions reactions (e.g., Sharp et al., 2016). The equation describing these deviations is given by:

$$\triangle'^{17}O = \delta'^{17}O - \lambda_{RL} \times \delta'^{18}O + \gamma \quad (1)$$

In this equation $\triangle'^{17}O$ is called "Cap 17" or "^{17}O-excess" and is the deviation from the reference slope λ_{RL} of the mass dependent line for Earth materials which is 0.528 (Miller, 2002; Pack and Herwartz, 2014; Sharp et al., 2018) and γ is the y-intercept of this line (taken as zero). $\delta'^{17}O$ and $\delta'^{18}O$ are the linearized forms (Miller, 2002) of standard δ-notation and is calculated by:

$$\delta'^{x}O = 1000ln\left(\frac{\delta^{x}O}{1000} + 1\right) \quad (2)$$

For a more detailed description of these equations see Sharp et al. (2018).

PALEOALTIMETRY WITH TRIPLE OXYGEN ISOTOPES

Method and Example

The use of triple oxygen isotopes for paleoaltimetry was inspired by Herwartz et al. (2015) (see also Zakharov et al., 2017), who used triple oxygen isotopes of hydrothermally altered rocks of Proterozoic age to determine the oxygen isotope composition of meteoric waters during Snowball Earth. The approach uses arrays of δ^{17}O and δ^{18}O of hydrothermally altered minerals created by varying water/rock ratios to extrapolate to the triple oxygen meteoric water line (e.g., Passey and Ji, 2019). The logical extension was to apply this approach to paleoaltimetry (Chamberlain et al., 2020).

The method is similar to that used for hydrogen and oxygen isotopes of hydrothermal systems used to determine the isotopic composition of ancient meteoric waters (Taylor, 1978). Yet, the use of triple oxygen uses only one element's isotopic system. The approach involves: 1) Targeting meteoric water hydrothermal systems that have varying degrees or water/rock interaction. This would include such samples as low ^{18}O granites (Taylor, 1978), detachment faults of metamorphic core complexes (Mulch et al., 2004), and fault zones, or even hydrothermal veins (Sharp et al., 2005). 2) Obtaining pure mineral separates of minerals that readily exchange with fluids such as altered feldspars. 3) Collecting Δ'^{17}O and δ^{18}O with the precision necessary to build tight arrays in Δ'^{17}O- δ^{18}O space. 4) Extrapolation of a fitted line through this array, using water/rock equations for both δ^{17}O and δ^{18}O (Taylor, 1978), to the meteoric water line with the added and small water/rock equilibrium fractionation factor. An excellent example of this approach is given in Zakharov et al. (2019) who used triple oxygen isotopes to study fluid–rock interaction in the well-known hydrothermal systems in Iceland. Through careful analysis of minerals and fluids they were able to demonstrate how triple oxygen can be used assess the complicated processes that occur in hydrothermal systems—thereby setting the stage too apply this approach to ancient hydrothermal systems. We recently used (Chamberlain et al., 2020) this approach to determine the Eocene meteoric waters of the classic hydrothermal systems of the Idaho Batholith (Criss and Taylor, 1983).

The Cretaceous Idaho Batholith and later Eocene plutonic and volcanic rocks lies in the core of the northern Rocky Mountains with intermontane basins on both flanks (**Figure 1**). This area has been the subject of numerous paleoaltimetry studies of both the flanking basins and crystalline core. While most of the paleoaltimetry estimates come from clay and carbonate in paleosols and lake sediments (e.g., Kukla et al., 2021) the elevation estimates for the crystalline core rely almost exclusively on hydrogen isotopes of metamorphic (McFadden et al., 2015) and igneous micas (Criss and Taylor, 1983). The Eocene plutons created large Eocene (between 45 and 37 Ma) meteoric hydrothermal systems that exchanged with the

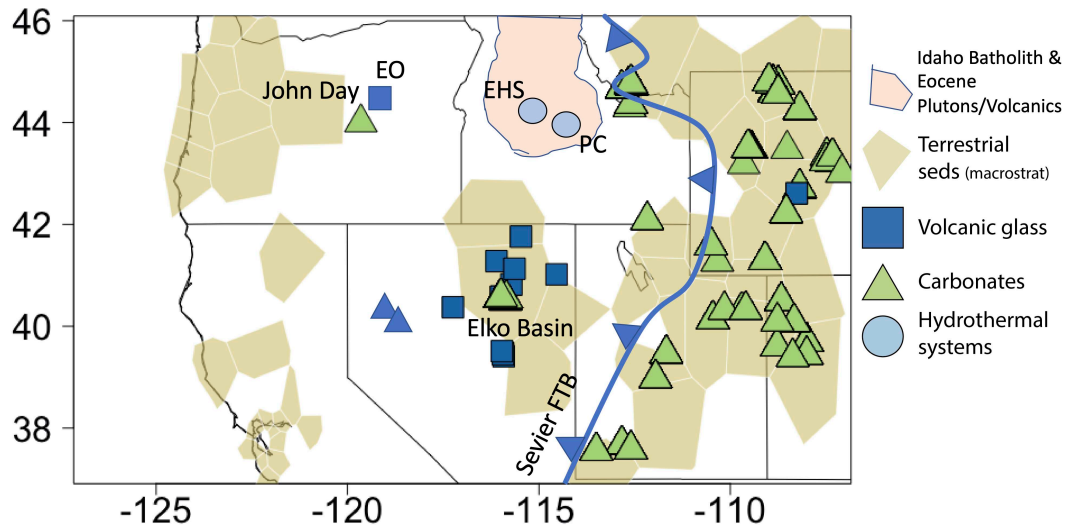

FIGURE 1 | Map of the Idaho batholith and Eocene plutons and volcanics and surrounding Eocene basins. Shown are the sites sampled for paleoaltimetry analysis for the Eocene. The triple oxygen isotope study of the Eocene hydrothermal system (Chamberlain et al., 2020) is given as the dot (EHS), the Pioneer core complex (PC; from McFadden et al., 2015), and the Early Oligocene volcanic glass in Blue Mountains (EO; from Bershaw et al., 2019). Shown is the eastern margin of the Sevier fold and thrust belt (Sevier FTB).

granites resulting in low ^{18}O minerals and rocks. As such, this represents an ideal target for triple oxygen isotope studies (Chamberlain et al., 2020), with the added benefit that these results are directly comparable to nearby hydrogen isotope paleoaltimetry studies.

There are two key results of our dataset from the Eocene plutons (**Figure 2**). First, the $\Delta'^{17}O$ and $\delta'^{18}O$ of hydrothermally altered feldspars form arrays that allow for extrapolation to the meteoric water line. Second, in contrast, the more resistant quartz samples are minimally altered from their original igneous values and, thus, provide no leverage on determining the composition of meteoric waters. These two results are similar to those found by Taylor (1974, 1978) that feldspar is more likely to exchange with later fluids than the more resistant quartz. Yet, with the addition of ^{17}O we have the leverage to determine the isotopic composition of the fluid using oxygen isotope values alone.

Based on this analysis the $\delta^{18}O$ of the Eocene meteoric waters is relatively low ($-12 \pm 1‰$) indicating high Eocene elevations (Chamberlain et al., 2020). But, how does this result compare to the results using hydrogen isotope analyses?

Hydrogen Exchange Problems

One key advantage of the triple oxygen isotope method for paleoaltimetry is that this approach only relies on one isotopic system (O) and is independent of hydrogen that may exchange later with the environment. To test this idea, we (Chamberlain et al., 2020) analyzed the hydrogen isotopes of coexisting biotite in these samples and arrive at a $\delta^{18}O = -15.3 \pm 1.12‰$, which is 3‰ lower than the results from triple oxygen isotope analysis of the same rocks and similar to the value derived by Criss and Taylor (1983). This difference strongly suggests that the biotites we have measured have undergone later hydrogen exchange. The concept of hydrogen exchange after mineral formation was the subject of numerous studies over 40 years ago and was demonstrated to occur in many hydrous minerals including micas (O'Neil and Kharaka, 1976; Graham, 1981; Graham et al., 1987). Moreover, Graham (1981) showed that hydrogen continued to exchange with ambient fluids while cooling to temperatures between 300 and 100°C. Further, O'Neil and Kharaka (1976) suggested that hydrogen exchange is independent of oxygen exchange and may be occurring by proton diffusion rather than by OH^- groups or H_2O molecules. Our work on triple oxygen confirms this conclusion.

This result indicates that paleoaltimetry estimates based on hydrogen isotopes may be inaccurate. For example, using the Eocene lapse rate of Rowley et al. (2001) (approximately 2.8‰/km but changes with elevation becoming shallower at high elevations) the calculated elevation from the triple oxygen isotope data is 3.11 km +0.31/−3.8 (1σ). In contrast, the dD versus $\delta^{18}O$ of biotite gives higher elevations of 4.46 km +0.60/−3.6 (1σ). The lower elevations given by triple oxygen isotope analysis are also inconsistent with other elevation estimates based on hydrogen isotope measurements made on nearby metamorphic core complexes. McFadden et al. (2015) used hydrogen isotopes of micas from the detachment zone of the 38 to 37 Ma core complex to the west of the area studied by Chamberlain et al. (2020) and determined a $\delta^{18}O$ of −16‰ for the meteoric water, which gives a higher elevation of 4.74 km +0.64/−0.49. In addition, hydrogen isotope measurements of volcanic glasses just west of the study area give earliest Oligocene (32.7 Ma) meteoric water equivalent $\delta^{18}O$ values of −17‰ (Bershaw et al., 2019). These authors argue that the low $\delta^{18}O$ waters reflect a high elevation proto-Cascades in Oregon. Since the Cascade mountains intercept airmasses upstream of the study area of

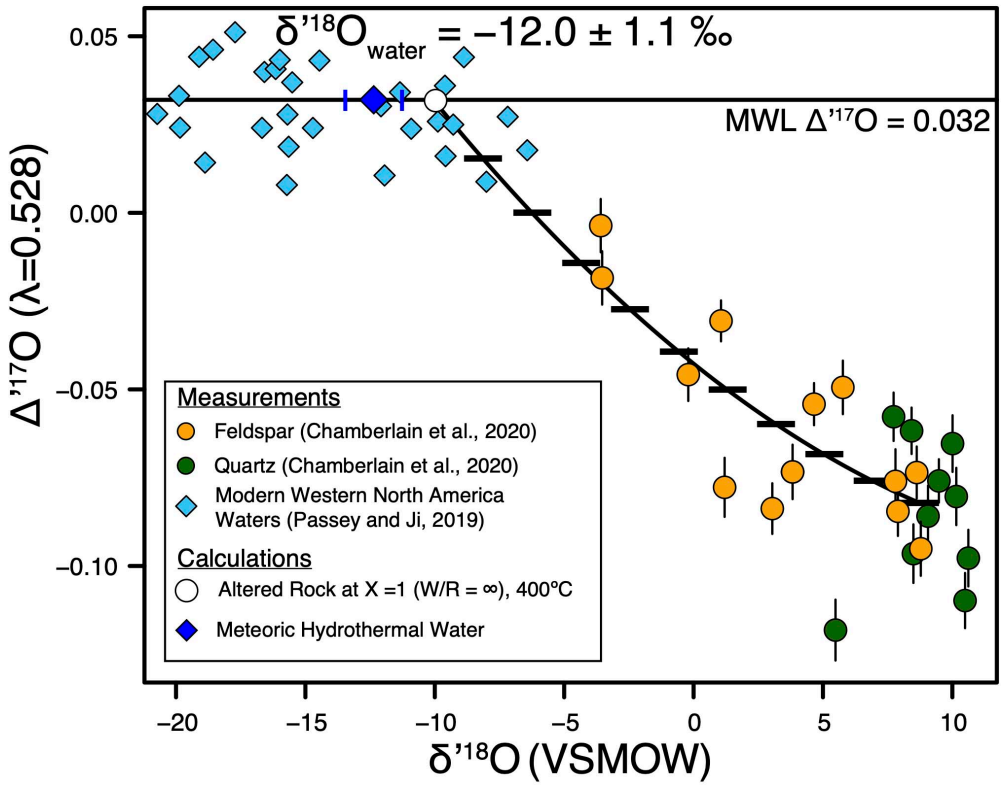

FIGURE 2 | The $\delta'^{18}O$–$\Delta'^{17}O$ alteration relationship (black line) of feldspar (modified from Chamberlain et al., 2020). The meteoric water line is from Passey and Ji (2019).

Chamberlain et al. (2020), it is difficult to reconcile these lower values of meteoric waters. There are three options. Either there was a major uplift event of the Cascades between the latest Eocene (37 Ma – this study) or the earliest Oligocene or the area where these glasses was sampled was higher (the Blue Mountains) than the Idaho Batholith, or these glasses have undergone later hydrogen exchange. However, no uplift event is observed in basins immediately east of the Cascades during this time period (Kukla et al., 2021) nor is there any other evidence that the Blue Mountains were that high. Indeed, the bulk of the uplift of the Cascades occurred in the Miocene as demonstrated by stable isotopic studies (Kohn et al., 2002; Takeuchi and Larson, 2005; Takeuchi et al., 2010).

Thus, we conclude that hydrogen isotope exchange most likely occurred in the Oligocene glasses analyzed by Bershaw et al. (2019). That hydrogen exchange does occur is clearly demonstrated in the experiments of Nolan and Bindeman (2013). They showed that rapid exchange of hydrogen occurs even at relatively low temperature while the oxygen of the glasses remains unchanged. There are experiments that suggest that treatment with hydrofluoric acid could remove the exchanged hydrogen (Cassel and Breecker, 2017), but this requires that their remains some pristine hydrogen in the volcanic glass. Additional evidence for hydrogen exchange in volcanic glass is also indicated in other studies. For example, triple oxygen isotope studies of Eocene chert in Nevada also give lower $\delta^{18}O$ values than those determined by hydrogen isotope results of volcanic glasses (Ibarra et al., 2021). We suggest that the combined study of triple oxygen and hydrogen isotopes of multiple proxies could resolve this issue.

IMPLICATIONS AND FUTURE DIRECTIONS

There are a number of advantages to using triple oxygen isotopes for paleoaltimetry studies. First, the use of triple oxygen isotope paleoaltimetry allows the estimation of elevations of the crystalline cores of mountain belts. By targeting hydrothermal meteoric water hydrothermal systems, it is possible to determine elevations using oxygen isotopes alone. It is well known that meteoric waters penetrate deeply into the crust during orogenesis even in the absence of igneous activity (Templeton et al., 1998). Thus, this approach could be applied to hydrothermal quartz veins, fault zones, as well as low ^{18}O granites.

Second, as discussed above, triple oxygen isotopes can be used to test the reliability of hydrogen isotope results. This is particularly important because hydrogen isotope analyses are easier to collect and are more readily available than triple oxygen isotope analyses and each triple oxygen isotope analysis requires long count times (1.5–2 h) necessary to obtain the counting statistics for the needed level of precision.

Third, although not the subject of this paper, triple oxygen isotopes on carbonates and chert (Ibarra et al., 2021) from paleolakes and clays and carbonates from paleosols can be used to test for evaporative effects and diagenesis. Evaporation of lake and soil water will increase the $\delta^{18}O$ of the remaining water, thus obscuring paleoelevation estimates (e.g. Davis et al., 2009). These evaporative effects can be used in conjunction with well calibrated triple oxygen isotope systems such as silica- water (Sharp et al., 2016) and carbonate-water (Wostbrock et al., 2020) to retrieve the original meteoric water compositions. Moreover, it should also be possible to use triple oxygen to test for diagenesis as is frequently done using clumped isotopes (e.g., Methner et al., 2016).

AUTHOR CONTRIBUTIONS

All authors contributed to the thinking and writing of this manuscript.

FUNDING

This research was funded by NSF EAR-1322084 and Heising–Simons' grants to CC. DI was supported by the UC Berkeley Miller Institute for Basic Research and UC President's Postdoctoral Fellowships. KM was supported by the Alexander von Humboldt Postdoctoral Fellowship.

REFERENCES

Abruzzese, M. J., Waldbauer, J. R., and Chamberlain, C. P. (2005). Oxygen and hydrogen isotope ratios in freshwater chert as indicators of ancient climate and hydrologic regime. *Geochim. Cosmochim. Acta* 69, 1377–1390. doi: 10.1016/j.gca.2004.08.036

Barkan, E., and Luz, B. (2005). High precision measurements of $^{17}O/^{16}O$ and $^{18}O/^{16}O$ ratios in H_2O. *Rapid Commun. Mass Spectrom.* 19, 3737–3742.

Bershaw, J., Cassel, E. J., Carlson, T. B., Streig, A. R., and Streck, M. J. (2019). Volcanic glass as a proxy for Cenozoic elevation and climate in the Cascade Mountains, Oregon, USA. *J. Volcanol. Geothermal Res.* 381, 157–167. doi: 10.1016/j.jvolgeores.2019.05.021

Capuano, R. N. (1992). The temperature dependence of hydrogen isotope fractionation between clay minerals and water: evidence from a geopressured system. *Geochimica Cosmochimica Acta* 56, 2547–2554. doi: 10.1016/0016-7037(92)90208-z

Cassel, E. J., and Breecker, D. O. (2017). Long-term stability of hydrogen isotope ratios of hydrated volcanic glass. *Geochimi. Cosmochim. Acta* 200, 67–86. doi: 10.1016/j.gca.2016.12.001

Cassel, E. J., Graham, S. A., and Chamberlain, C. P. (2009). Cenozoic tectonic and topographic evolution of the northern Sierra Nevada, California, through stable isotope paleoaltimetry in volcanic glass. *Geology* 37, 547–550. doi: 10.1130/g25572a.1

Caves Rugenstein, J. K., and Chamberlain, C. P. (2018). The evolution of hydroclimate in Asia over the Cenozoic: a stable-isotope perspective. *Earth Sci. Rev.* 185, 1129–1156. doi: 10.1016/j.earscirev.2018.09.003

Chamberlain, C. P., Ibarra, D. E., Lloyd, M. K., Kukla, T., Sharp, Z. D., Gao, Y., et al. (2020). Triple oxygen isotopes of meteoric hydrothermal system–implications for paleoaltimetry. *Geochem. Perspect. Lett.* 15, 6–9. doi: 10.7185/geochemlet.2026

Chamberlain, C. P., Poage, M., Craw, D., and Reynolds, R. (1999). Topographic development of the Southern Alps recorded by the isotopic composition of authigenic clay minerals, South Island, New Zealand. *Chem. Geol.* 155, 279–294. doi: 10.1016/S0009-2541(98)00165-X

Criss, R. R., and Taylor, H. P. Jr. (1983). An $^{18}O/^{16}O$ and D/H study of Tertiary hydrothermal system in the southern half of the Idaho batholith. *Geol. Soc. Am. Bull.* 94, 640–663. doi: 10.1130/0016-7606(1983)94<640:aoadso>2.0.co;2

Dansgaard, W. (1964). Stable isotopes in precipitation. *Tellus* 16, 436–468. doi: 10.3402/tellusa.v16i4.8993

Davis, S. J., Mix, H. T., Wiegand, B. A., Carroll, A. R., and Chamberlain, C. P. (2009). Synorogenic evolution of large-scale drainage patterns. Isotope paleohydrology of sequential Laramide Basins. *Am. J. Sci.* 309, 549–602. doi: 10.2475/07.2009.02

Delgado, A., and Reyes, E. (1996). Oxygen and hydrogen isotope compositions in clay minerals: a potential single mineral thermometer. *Geochim. Cosmochim. Acta* 60, 4285–4289. doi: 10.1016/s0016-7037(96)00260-8

Ehlers, T. A., and Poulsen, C. J. (2009). Influence of Andean uplift on climate paleoaltimetry estimates. *Earth Planet. Sci. Lett.* 281, 238–248. doi: 10.1016/j.epsl.2009.02.026

Feng, R., Poulsen, C. J., Werner, M., Chamberlain, C. P., Mix, H. T., and Mulch, A. (2013). Evolution of Early Cenozoic topography, climate and stable isotopes of precipitation in the North America Cordillera. *Am. J. Sci.* 313, 613–648. doi: 10.2475/07.2013.01

Garzione, C. N., Quade, J., DeCelles, P. G., and English, N. B. (2000). Predicting paleoelevation of Tibet and the Himalaya from $\delta^{18}O$ vs. altitude gradients in meteoric water across the Nepal Himalaya. *Earth Planet. Sci. Lett.* 183, 215–229. doi: 10.1016/s0012-821x(00)00252-1

Graham, C. M. (1981). Experimental hydrogen isotope studies II: diffusion of hydrogen in hydrous minerals, and stable isotope exchange in metamorphic rocks. *Contribut. Mineral. Petrol.* 76, 216–228. doi: 10.1007/bf00371961

Graham, C. M., Viglino, J. A., and Harmon, R. S. (1987). Experimental study of hydrogen-isotope exchange between aluminous chlorite and water and of hydrogen diffusion in chlorite. *Am. Mineral.* 72, 566–579.

Herwartz, D., Pack, A., Krylov, D., Xiao, Y., Muehlenbachs, K., Sengupta, S., et al. (2015). Revealing the climate of snowball Earth from $\Delta^{17}O$ systematics of hydrothermal rocks. *Proc. Nat. Acad. Sci.U.S.A.* 112, 5337–5341. doi: 10.1073/pnas.1422887112

Hren, M. T., Pagani, M., Erwin, D. M., and Brandon, M. (2010). Biomarker reconstruction of the early Eocene paleotopography and paleoclimate of the northern Sierra Nevada. *Geology* 38, 7–10. doi: 10.1130/g30215.1

Hudak, M. R., and Bindeman, I. N. (2018). Conditions of pinnacle formation and glass hydration in cooling ignimbrite sheets from H and O isotope systematics at Crater Lake and the Valley of Ten Thousand Smokes. *Earth Planet. Sci. Lett.* 500, 56–66. doi: 10.1016/j.epsl.2018.07.032

Ibarra, D. E., Kukla, T., Methner, K. A., Mulch, A., and Chamberlain, C. P. (2021). Reconstructing past elevations from triple oxygen isotopes of, lacustrine chert: application to the Eocene Nevadaplano, Elko Basin, Nevada, USA. *Front. Earth Sci.* 9:169. doi: 10.3389/feart.2021.628868

Kohn, M. J., Miselis, J. L., and Fremd, T. J. (2002). Oxygen isotope evidence for progressive uplift of the Cascade Range. *Oregon. Earth Planet. Sci. Lett.* 204, 151–165. doi: 10.1016/s0012-821x(02)00961-5

Kukla, T., Ibarra, D. E., Caves Rugenstein, J. K., Golley, J., Mullins, C. E., Morange, D. Y., et al. (2021). High-resolution stable isotope paleotopography of the John day region, oregon, United States. *Front. Earth Sci.* 9:635181.

Kukla, T., Winnick, M. J., Maher, K., Ibarra, D. E., and Chamberlain, C. P. (2019). The sensitivity of terrestrial $\delta^{18}O$ gradients to hydroclimate. *J. Geophys. Res. Atmos.* 124, 563–582. doi: 10.1029/2018jd029571

Lawrence, J. R., and Rashkes Meaux, J. (1993). "The stable isotopic composition of ancient kaolinites of North America," in *Climate Change in Continental Isotopic Records. Geophysical Monograph Series*, Vol. 78, eds P. K. Swart, K. C. Lohmann, J. McKenzie, and S. Savin 249–261. doi: 10.1029/gm078p0249

McFadden, R. R., Mulch, A., Teyssier, C., and Heizker, M. (2015). Extension and meteoric fluid flow in the Wildhorse detachment, Pioneer metamorphic core complex, Idaho. *Lithosphere* 7, 355–366. doi: 10.1130/l429.1

Methner, K., Feibig, J., Umhoefer, P., Chamberlain, C. P., and Mulch, A. (2016). Eo-Oligocene proto-Cascades topography revealed by clumped (Δ_{47}) and

oxygen isotope ($\delta^{18}O$) geochemistry (Chumstick Basin, WA, USA). *Tectonics* 35, 546–564. doi: 10.1002/2015TCC003984

Miller, M. F. (2002). Isotopic fractionation and the quantification of ^{17}O anomalies in the oxygen three-isotope system:An appraisal and geochemical significance. *Geochimica Cosmochimica Acta* 66, 1881–1889. doi: 10.1016/s0016-7037(02)00832-3

Mix, H. T., Mulch, A., Kent-Corson, M. L., and Chamberlain, C. P. (2011). Cenozoic migration of topography in the North American Cordillera. *Geology* 39, 87–90. doi: 10.1130/g31450.1

Mulch, A., Graham, S. A., and Chamberlain, C. P. (2006). Hydrogen isotopes in Eocene river gravels and paleoelevation of the Sierra Nevada. *Science* 313, 87–89. doi: 10.1126/science.1125986

Mulch, A., Sarna-Wojcicki, A. M., Perkins, M. E., and Chamberlain, C. P. (2008). A Miocene to Pleistocene climate and elevation record of the Sierra Nevada. *Proc. Nat. Acad. Sci.* 105, 6819–6824. doi: 10.1073/pnas.0708811105

Mulch, A., Teyssier, C., Cosca, M. A., Vanderhaeghe, O., and Vennemann, T. (2004). Reconstructing paleoelevation in eroded orogens. *Geology* 32, 525–528. doi: 10.1130/g20394.1

Nolan, G. S., and Bindeman, I. N. (2013). Experimental investigations of rates and mechanisms of isotope exchange (H,O) between volcanic ash and isotopically-labeled water. *Geochim. Cosmochim. Acta* 111, 5–27. doi: 10.1016/j.gca.2013.01.020

O'Neil, J. R., and Kharaka, Y. K. (1976). Hydrogen and oxygen isotope exchange reactions between clay minerals and water. *Geochim. Cosmochim. Acta* 40, 241–246. doi: 10.1016/0016-7037(76)90181-2

Pack, A., and Herwartz, D. (2014). The triple oxygen isotope composition of the Earth mantle and understanding $\Delta 17O$ variations in terrestrial rocks and minerals. *Earth Planet. Sci. Lett.* 390, 138–145.

Passey, B. H., and Ji, H. (2019). Triple oxygen isotope signatures of evaporation in lake waters and carbonates: a case study from the western United States. *Earth Planet. Sci. Lett.* 518, 1–12. doi: 10.1016/j.epsl.2019.04.026

Poage, M. A., and Chamberlain, C. P. (2001). Empirical relationships between elevation and the stable isotope composition of precipitation and surface waters: considerations for studies of paleoelevation change. *Am. J. Sci.* 301, 1–15. doi: 10.2475/ajs.301.1.1

Poulsen, C. J., and Jeffery, M. L. (2011). Climate change imprinting on stable isotopic compositions of high-elevation meteoric water cloaks past surface elevations of major orogens. *Geology* 39, 595–598. doi: 10.1130/G32052.1

Quade, J., Garzione, C., and Eiler, J. (2007). "Paleoelevation reconstruction using pedogenic carbonates," in *Paleoaltimetry: Geochemical and Thermodynamic Approaches: Reviews in Mineralogy and Geochemistry*, Vol. 66, ed. M. J. Kohn 53–87. doi: 10.1515/9781501508608-005

Rowley, D. B., Pierrehumbert, R. T., and Currie, B. S. (2001). A new approach to stable isotope-based paleoaltimetry: implications for paleoaltimetry and paleohypsometry of the high Himalaya since the Late Miocene. *Earth Planet. Sci. Lett.* 188, 253–268. doi: 10.1016/s0012-821x(01)00324-7

Sharp, Z. D., Gibbons, J. A., Maltsev, O., Atudorei, V., Pack, A., Sengupta, S., et al. (2016). A calibration of the triple oxygen isotope fractionation in the SiO_2–H_2O system and applications to natural samples. *Geochim. Cosmochim. Acta* 186, 105–119. doi: 10.1016/j.gca.2016.04.047

Sharp, Z. D., Masson, H., and Lucchini, R. (2005). Stable isotope geochemistry and formation mechanisms of quartz veins: extreme paleoaltitudes of the central Alps in the Neogene. *Am. J. Sci.* 305, 187–219. doi: 10.2475/ajs.305.3.187

Sharp, Z. D., Wostbrock, J. A. G., and Pack, A. (2018). Mass-dependent triple oxygen isotope variations in terrestrial materials. *Geochem. Perspect. Lett.* 7, 27–31. doi: 10.7185/geochemlet.1815

Takeuchi, A., Hren, M. T., Smith, S. V., Chamberlain, C. P., and Larsen, P. B. (2010). Pedogenic carbonate carbon isotopic constraints on paleoprecipitation: evolution of desert in the Pacific Northwest, USA, in response to topographic development of the Cascade Range. *Chem. Geol.* 277, 323–335. doi: 10.1016/j.chemgeo.2010.08.015

Takeuchi, A., and Larson, P. B. (2005). Oxygen isotope evidence for the late Cenozoic development of an orographic rain shadow in eastern Washington. *USA: Geology* 33, 313–316. doi: 10.1130/G21335.1

Taylor, H. P. Jr. (1974). The application of oxygen and hydrogen isotope studies to problems of hydrothermal alteration and ore deposition. *Econ. Geol.* 69, 843–883. doi: 10.2113/gsecongeo.69.6.843

Taylor, H. P. Jr. (1978). Oxygen and hydrogen isotope systematics of plutonic granitic rocks. *Earth Planet. Sci. Lett.* 38, 177–210. doi: 10.1016/0012-821x(78)90131-0

Templeton, A. S., Chamberlain, C. P., Koons, P., and Craw, D. (1998). Tectonically driven mixing between midcrustal fluids and surface-derived waters during recent uplift of the Southern Alps, New Zealand. *Earth Planet. Sci. Lett.* 154, 73–92. doi: 10.1016/s0012-821x(97)00143-x

Winnick, M. J., Chamberlain, C. P., Caves, J., and Welker, J. M. (2014). Quantifying the Isotopic "Continental Effect". *Earth Planet. Sci. Lett.* 406, 123–133. doi: 10.1016/j.epsl.2014.09.005

Winograd, I. J., Szabo, B. J., Coplen, T. B., Riggs, A. C., and Kolesar, P. T. (1985). Two-million record of deuterium depletion in Great Basin ground waters. *Science* 227, 519–522. doi: 10.1126/science.227.4686.519

Wostbrock, J. A. G., Brand, U., Coplen, T. B., Swart, P. K., Carlson, S. J., Brearley, A. J., et al. (2020). Calibration of carbonate-water triple oxygen isotope fractionation: Seeing through diagenesis in ancient carbonates. *Geochim. Cosmochim. Acta* 288, 369–388. doi: 10.1016/j.gca.2020.07.045

Zakharov, D. O., Bindeman, I. N., Slabunov, A. I., Ovtcharova, M., Coble, M. A., Serebryakov, N. S., et al. (2017). Dating the Paleoproterozoic snowball Earth glaciations using contemporaneous subglacial hydrothermal systems. *Geology* 45, 667–670. doi: 10.1130/g38759.1

Zakharov, D. O., Bindeman, I. N., Tanaka, R., Frioleifsson, G. O., Reed, M. H., and Hampton, R. L. (2019). Triple oxygen isotope systematics as a tracer of fluids in the crust: a study from modern geothermal systems of Iceland. *Chem. Geol.* 530:119312. doi: 10.1016/j.chemgeo.2019.119312

Conflict of Interest: The authors declare that the research was conducted in the absence of any commercial or financial relationships that could be construed as a potential conflict of interest.

frontiers in Earth Science

BRIEF RESEARCH REPORT
published: 28 May 2021
doi: 10.3389/feart.2021.664590

Impact of the Southern Ecuadorian Andes on Oxygen and Hydrogen Isotopes in Precipitation

Aude Gébelin[1], Cesar Witt[2], Maksymilian Radkiewicz[1]* and Andreas Mulch[3,4]*

[1]School of Geography, Earth and Environmental Sciences, University of Plymouth, Plymouth, United Kingdom, [2]Univ, Lille, CNRS, Univ, Littoral Côte d'Opale, UMR 8187, LOG, Laboratoire d'Océanologie et de Géosciences, Lille, France, [3]Senckenberg Biodiversity and Climate Research Centre (SBiK-F), Frankfurt, Germany, [4]Institute of Geosciences, Goethe University Frankfurt, Frankfurt, Germany

Determining how the elevation of the Northern Andes has evolved over time is of paramount importance for understanding the response of the Northern Andes to deformational and geodynamic processes and its role as an orographic barrier for atmospheric vapor transport over geologic time. However, a fundamental requirement when using stable isotope data for paleoaltimetry reconstructions is knowledge about the present-day changes of $\delta^{18}O$ and δD with elevation (isotopic lapse rate). This study defines the present-day river isotopic lapse rate near the Equator (~3°S) based on analysis of $\delta^{18}O$ and δD of surface waters collected from streams across the Western Cordillera and the Inter-Andean depression in Southern Ecuador. The results for the two domains show a decrease of $\delta^{18}O$ with elevation which fits a linear regression with a slope of –0.18‰/100 m (R^2 = 0.73, n = 83). However, we establish a present-day lapse rate of –0.15‰/100 m for $\delta^{18}O$ (R^2 = 0.88, n = 19) and -1.4‰/100 m for δD (R^2 = 0.93, n = 19) from water samples collected along the west facing slopes of the Western Ecuadorian Cordillera which is mainly subject to moisture transport from the Pacific. We argue that this empirical relationship, consistent with those obtained in different tropical areas of the world, can inform stable isotope paleoaltimetry reconstructions in tropical latitudes.

Keywords: stable isotope paleoaltimetry, isotopic lapse rate, tropical precipitation, hydrogen isotopes, oxygen isotopes, Northern Andes, Western Southern Ecuadorian Cordillera, Inter-Andean depression

OPEN ACCESS

Edited by:
Alexis Licht,
University of Washington,
United States

Reviewed by:
Lin Li,
Rochester Institute of Technology,
United States
Lily Jackson,
University of Texas at Austin,
United States
Landon Burgener,
North Carolina State University,
United States

****Correspondence:***
Aude Gébelin
aude.gebelin@gmail.com.uk
Maksymilian Radkiewicz
maxradkiewicz@gmail.com

Specialty section:
This article was submitted to Quaternary Science, Geomorphology and Paleoenvironment, a section of the journal Frontiers in Earth Science

Received: *05 February 2021*
Accepted: *05 May 2021*
Published: *28 May 2021*

Citation:
Gébelin A, Witt C, Radkiewicz M and Mulch A (2021) Impact of the Southern Ecuadorian Andes on Oxygen and Hydrogen Isotopes in Precipitation. Front. Earth Sci. 9:664590. doi: 10.3389/feart.2021.664590

INTRODUCTION

The long-term climatic evolution and atmospheric circulation patterns of the Earth are influenced on the first order by the topography of large mountain chains (e.g., Molnar and England, 1990; Boos and Kuang, 2010; Barnes et al., 2012).

The Andes are a non-collisional subduction orogen and represent one of the main topographic features on Earth. However, uncertainties remain about how long this belt has been acting as a barrier to atmospheric circulation and moisture transport (e.g., Garzione et al., 2006; Garzione et al., 2008; Rech et al., 2006; Barnes and Ehlers, 2009; Ehlers and Poulson, 2009; Mulch 2016; Garzione et al., 2017; Sundell et al., 2019). Most studies aiming at understanding the links among geodynamic processes, Andean topography, and climate have focused on the Southern and Central Andes; the role and overall long-term landscape evolution of the Northern Andes remains enigmatic. This negligence is partly due to the scarce paleoaltimetry data obtained in the Northern Andes, and especially in the Ecuadorian Andes, a region of intense debate about the timing and rate of topographic development (e.g., Steinmann et al., 1999; Gregory-Wodzicky, 2000; Hungerbuhler et al., 2002; Witt et al., 2017; Jackson et al., 2019).

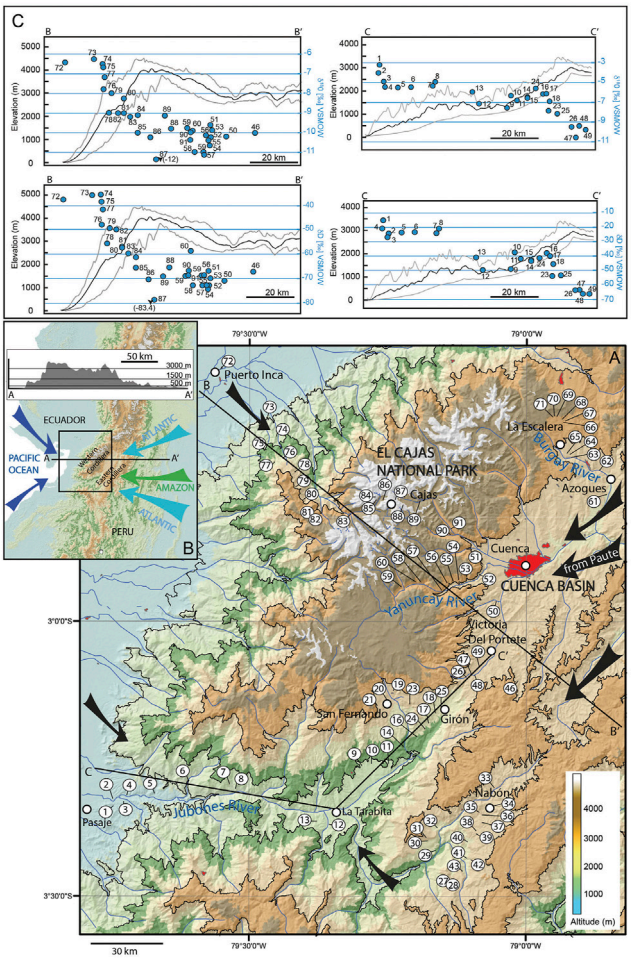

FIGURE 1 | (A) Digital elevation model (90 m resolution) of Southern Ecuador showing water sample locations. Black arrows indicate direction and movements of air masses during our water samples collection. **(B)** Schematic diagram showing major air mass trajectories affecting Ecuador as well as an E-W trending elevation profile across the Southern Ecuadorian Andes. **(C)** Modern $\delta^{18}O_{water}$ and δD_{water} values (blue dots) from our sampling sites along two main transects across the Western Southern Ecuadorian Cordillera (see location in A). Minimum and maximum topographic profiles (gray lines) were obtained at a swath distance of 5 km at each side of the main central section.

Most paleoaltimetry studies use the stable oxygen ($\delta^{18}O$) and hydrogen (δD) isotopic composition of meteoric water that scales with elevation in a predictable fashion to retrieve the elevation signal from near-surface paleoenvironmental archives (e.g., Garzione et al., 2000; Mulch et al., 2006; Sundell et al., 2019) or crustal-scale deformation zones (e.g., Mulch et al., 2004; Gébelin et al., 2012; Gébelin et al., 2013). This relationship results from distillation of heavy isotopes (^{18}O or D) through condensation and precipitation as air masses rising across a mountain range cool adiabatically during ascent. As a result, oxygen ($\delta^{18}O$) and hydrogen (δD) isotope ratios of rainfall scale systematically with elevation on the windward side of a mountain range. Compilations of isotope data sets from regions in the low to mid-latitudes provide an average of ~2.8 ‰ in $\delta^{18}O$ or ~20 ‰ in δD per km (Poage and Chamberlain, 2001; Quade et al., 2011).

Here, we present the first comprehensive study of this empirical relationship near the Equator across the Western Andean Cordillera and the Inter-Andean depression in southern Ecuador by analysing surface waters from tributaries along five transects (**Figure 1**, **Supplementary Table S1**). In agreement with previous studies identifying the altitude effect on the isotopic composition of tropical precipitation (e.g., Garcia et al., 1998; Gonfiantini et al., 2001; Saylor et al., 2009), our results indicate that $\delta^{18}O$ and δD values of tributary waters decrease systematically as a function of increasing elevation on the windward side of the Western Cordillera, yet with a lower lapse rate than commonly observed at mid-latitudes (e.g., Poage and Chamberlain, 2001). Projecting such isotope—elevation relationship to past environments is inherently difficult, yet an important parameter in paleoaltimetry reconstructions. Present-day lapse rates established in different climate zones, latitudes or hydrological settings allows us to explore how different environmental settings in the past may have affected isotope lapse rates.

CLIMATE OF THE ECUADORIAN ANDES

Topography exerts an important control on atmospheric moisture flux over the Northern Andes (Garcia et al., 1998; Windhorst et al., 2013). Due to the presence of two north-south trending Eastern and Western Cordilleras separated by an Inter-Andean valley, their equatorial location, at the junction between the Pacific Ocean and the Amazon Basin, the Ecuadorian Andes are characterized by a complex climate (**Figure 1B**). Currently, Ecuador is influenced by two main precipitation sources: 1) Air masses originating from the Pacific (Garcia et al., 1998), and 2) Atlantic air masses carried across the Amazon Basin (Windhorst et al., 2013). Also, precipitation regime and atmospheric circulation patterns in Ecuador are governed by three main factors: 1) Altitude of the Andes acting as a weather divide between Pacific air masses from the west and Atlantic air masses from the east (Garreaud et al., 2009), 2) Passage of the Intertropical Convergence Zone (ITCZ) (e.g., Rozanski and Araguas-Araguas, 1995), and 3) El Niño-Southern Oscillation (ENSO) (e.g., Rossel and Cardier, 2009). The Western Cordillera and coastal areas are affected by western trade winds advecting moisture from the Pacific Ocean (Emsk, 2007). This Pacific domain is marked by a unimodal precipitation regime with increased rainfall from December to April that accounts for more than 90% of annual precipitation and coincides with the southernmost extent of the ITCZ (Rozanski and Araguas-Araguas, 1995; Garcia et al., 1998; Campozano et al., 2016).

The South Ecuadorian Coast is affected by ENSO cyclicity that brings warm surface waters carried by trade winds from the West Pacific and causes heavy rainfall during the El Niño years (Philander, 1983; Rossel and Cardier, 2009). Convective storms from the Pacific cause a significant decrease in $\delta^{18}O$ and δD values of precipitation in the coastal areas of Ecuador (Garcia et al., 1998). The impact of ENSO on precipitation

depends on the local topography; it is highest at low to moderate elevations on west facing slopes of the Cordillera (< 1500 m) and negligible at high elevations (Rossel et al., 1998; Rollenbeck and Bendix, 2011; Ochoa et al., 2016). Rainfall intensity also depends on the latitude and is higher in the north (> 700 and 3,500 mm in the coast and foothills, respectively) than in the south (< 80 and 800 mm in the coast and foothills, respectively) (Garcia et al., 1998). This latitudinal effect is reflected in the isotopic composition of precipitation of Pacific coastal stations, which display lower mean $\delta^{18}O_{water}$ values in the north (~−5‰) than in the south (~−2‰) (Garcia et al., 1998).

The Eastern Cordillera is controlled by moisture-bearing winds from the Atlantic and the Amazon Basin and not by the Pacific westerlies (Emck, 2007; Windhorst et al., 2013). Atlantic air masses are carried by strong south-easterly winds, that once they have reached the eastern slopes of the Eastern Cordillera, are adiabatically lifted forming the Andean Occurring System (AOS, Campozano et al., 2016) that is progressively transported to the Inter-Andean depression (Celleri et al., 2007; Windhorst et al., 2013; Mora et al., 2014; Ochoa et al., 2016).

The climate of the Inter-Andean valley is influenced by moisture sources in the Western Pacific and continental and tropical Atlantic air masses (Vuille et al., 2000). Strong south-easterly trade winds carry moisture from the Amazon and enter the Inter-Andean valley leading to a mixing of moisture with Pacific trade winds (Campozano et al., 2016). Air masses in the Inter-Andean depression can also originate in the Atlantic, and may get enriched in ^{18}O or D due to high evapotranspiration during passage over the Amazon Basin (e.g., Salati et al., 1979). The Cuenca Basin (**Figure 1A**) is part of this domain and has an outlet towards the east, into the Amazon Basin (Ochoa et al., 2016). In contrast to the Pacific domain that shows a unimodal distribution of precipitation, the Inter-Andean depression is characterized by two contrasting rainfall regimes, a unimodal (UMR) and a bimodal (BMR) regime that respectively cover ~15 and ~85% of the Cuenca basin area (Celleri et al., 2007). Based on different distributions of mean annual rainfall, two UMR with a single rainfall peak in June and July (UM1: 2,900–3,400 mm a^{-1} and UM2: 1,100–1,600 mm a^{-1}) are defined in the eastern part of the basin, and two BMR with rainfall peaks in April and October (BM1: 660–100 mm a^{-1} and BM2: 1,000–1,800 mm a^{-1}) occur on the high eastern and western flanks of the basin (see Figure 5 in Celleri et al., 2007). The UMR is closely related to the AOS reaching the basin *via* the Paute Canyon (**Figure 1A**), and the difference in precipitation amount is interpreted to reflect an abrupt change in elevation where moisture originating from the Amazon Basin produces high orographic rainfall volumes (UM1), followed by reduced orographic precipitation (UM2) (Celleri et al., 2007). The BMR is identified at the junction between the Inter-Andean depression, the Amazon and Pacific basin and is controlled by the seasonal north-south migration of the ITCZ that causes peak rainfall and low $\delta^{18}O$ (and low δD) precipitation values in March-April and then October-November (Rozanski and Araguas-Araguas, 1995; Garcia et al., 1998; Celleri et al., 2007; Ochoa et al., 2016).

METHODS

To establish a river-based δD- and $\delta^{18}O$-elevation relationship at the Equator, we sampled a total of 89 surface waters from perennial streams during the dry season (mid September) from an array of elevations across the Southern part of the Ecuadorian Western Cordillera and the adjacent Inter-Andean depression (**Figure 1** and **Supplementary Table S1**). River-based isotope-elevation relationships may be skewed to select elevation intervals due to uneven precipitation intensity within a given hypsometry (e.g., Bookhagen and Burbank, 2006) or biased by groundwater recharge from unknown catchment sizes. However, they have proven extremely informative as a) they reflect the competing effects of climatic and topographic controls on regional isotopic lapse rates (e.g., Rohrmann et al., 2014), and b) contribute largely to averaging precipitation events or seasonality of precipitation (e.g., Garzione et al., 2000; Schemmel et al., 2013). We hence feel confident that, with respect to paleaoaltimetry applications where time scales of isotopic proxy development play an important role, such river-based lapse rates are robust since nature has already provided a lot of the spatial averaging.

We established two main transects (Puerto Inca and Pasaje) on the windward side from the Ecuadorian Pacific coast (near sea level) to the top of the mountain range (~4,000 m). We analyzed δD and $\delta^{18}O$ values from tributaries along three transects in the Inter-Andean valley. Two of them have been conducted in the Cuenca Basin along the Yanuncay and Burgay Rivers and one further south in the Nabón Basin to 1) test whether the δD and $\delta^{18}O$ values of stream waters reflect the presence of an orographic rain shadow on the leeward side of the Western Cordillera, 2) analyze surface waters sourced at high elevations, and 3) evaluate the influence of the mixing between Pacific and Atlantic air masses as well as from the Amazon rainforest on δD and $\delta^{18}O$ values in precipitation. The deuterium excess values defined as $d = \delta D - 8x\delta^{18}O$ (Craig and Gordon, 1965) have been used to estimate the amount of evaporation in meteoric water that may have affected this depression area (e.g., Windhorst et al., 2013).

At each sampling site 30 ml of water was collected in polyethylene bottles with little to no air in the closed bottles. Samples were stored in the dark at room temperature until returned to the laboratory for analysis. Measurements of stable hydrogen (δD) and oxygen ($\delta^{18}O$) isotope ratios were carried out on 1 ml aliquots using an LGR LWIA-24d (CRD Laser Spectroscopy) liquid isotope water analyzer in the joint Goethe University-Senckenberg BiK-F Stable Isotope Facility, Frankfurt. δD and $\delta^{18}O$ values were corrected against internal lab standards that are calibrated against VSMOW. The analytical precision is 1.0 and 0.3‰ (both 2σ) for δD and $\delta^{18}O$, respectively. Absolute stable isotope values range from −15 to −83‰ for δD and −3.2 to −12.0‰ for $\delta^{18}O$ (**Figure 2** and **Supplementary Table S1**).

Sampling perennial streams provides an amount-weighted long-term average of precipitation for each catchment, but can lead to an underestimation of the elevation at which the majority of the precipitation falls, especially in high-relief or large catchments areas (Currie, et al., 2005; Rowley and Garzione,

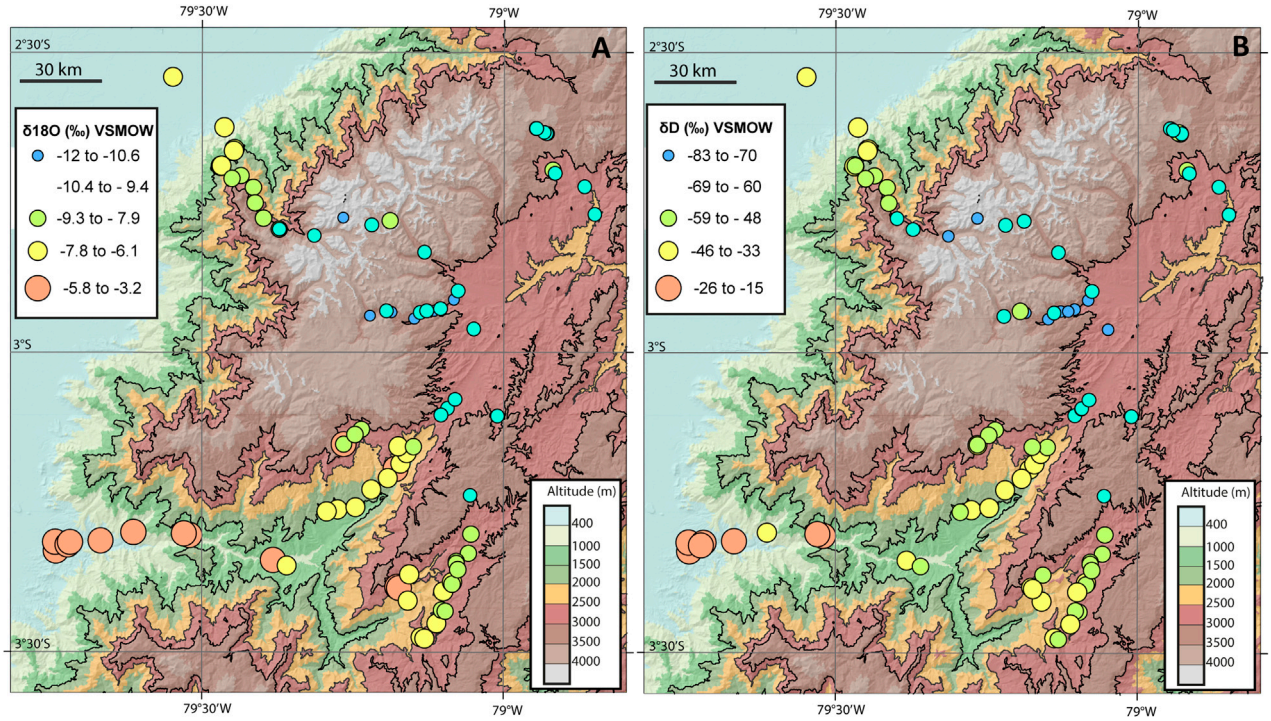

FIGURE 2 | Spatial distribution of $\delta^{18}O$ **(A)** and δD **(B)** values from our water samples collected over southern Ecuador.

2007; Quade et al., 2011; Schemmel et al., 2013). We calculated mean catchment elevations for each sample using an elevation-weighted flow accumulation model in ESRI® ArcGISTM 10.0 based on version 11 of the National Aeronautics and Space Administration (NASA) ASTER Global Digital Elevation Model at a spatial resolution of 1 arc-second (~30 m). $\delta^{18}O$ and δD lapse rates use results from all water samples except 1) WS21 (lake de Busa; Pasaje transect), WS30 and WS31 (lake and related stream; Nabón Basin) that reflect evaporative lake conditions, 2) WS61 and WS62 (near Azogues; Cuenca Basin) affected by urban pollution and, 3) WS72 (Canar River; Puerto Inca transect) for which an accurate mean catchment elevation calculation is difficult due to large catchment size and insignificant relief.

RESULTS

Two main observations characterize our δD and $\delta^{18}O$ data. 1) Air masses from the Pacific Ocean that directly rise across the Western Cordillera (Puerto Inca transect) experience Rayleigh distillation on the windward side; δD and $\delta^{18}O$ values define a linear relationship between $\delta^{18}O$ and altitude of -0.15‰/100 m (**Figure 3A**) (δD = −1.4‰/100 m; **Figure 3B**). 2) The δD and $\delta^{18}O$ values of precipitation in the Inter-Andean valley cannot be directly correlated with elevation; they display additional variability that can be explained by a combination of factors such as mixing of air masses from the Pacific, the Atlantic and the Amazon Basin, evaporation, and seasonality.

Spatial Distribution of δD and $\delta^{18}O$ Values

We observe a generally good correlation between δD and $\delta^{18}O$ values of surface water and elevation at the map scale of southern Ecuador. On the windward flanks of the Western Cordillera, between Puerto Inca and El Cajas National Park, low elevation areas (0 < mean catchment elevations <2000 m) display relatively high δD and $\delta^{18}O$ values ranging from −42 to −36‰ and −7.2 to −6.3‰, respectively, and contrast mountainous areas (2000 m < mean catchment elevations <4200 m) with δD = −83 to −48‰ and $\delta^{18}O$ = −12.0 to −7.8‰ for $\delta^{18}O$ (**Figures 1,2** and **Supplementary Table S1**). We additionally collected water samples further south between ~50 m and ~2,800 m elevation along the Pasaje transect (**Figure 1A**). All samples show strong correlation with elevation with $\delta^{18}O$ values varying from −3.2 to −10.6‰ between the lowest (~300 m) and highest (~3000 m) mean catchment elevation while equivalent δD values range between −15 and −71‰ (**Figures 1C,2** and **Supplementary Table S1**). The difference in δD and $\delta^{18}O$ values between lowland and mountainous areas on the windward flanks of the Western Cordillera is also observed in deuterium excess values with higher d-excess values (d = 15.0 ± 3.5) below 2,000 m mean catchment elevations when compared to the highlands (d = 11.0 ± 3.4) (**Supplementary Figure 1S**).

We further collected water samples between the Western and Eastern Cordilleras, in the Cuenca Basin and the Nabón area (**Figure 1A**) including tributaries of the Yanuncay River with sampling elevations varying from 3,239 and 2,689 m (**Supplementary Table S1**). $\delta^{18}O$ values display large variability between −11.2 and −9.6‰ and δD values are low

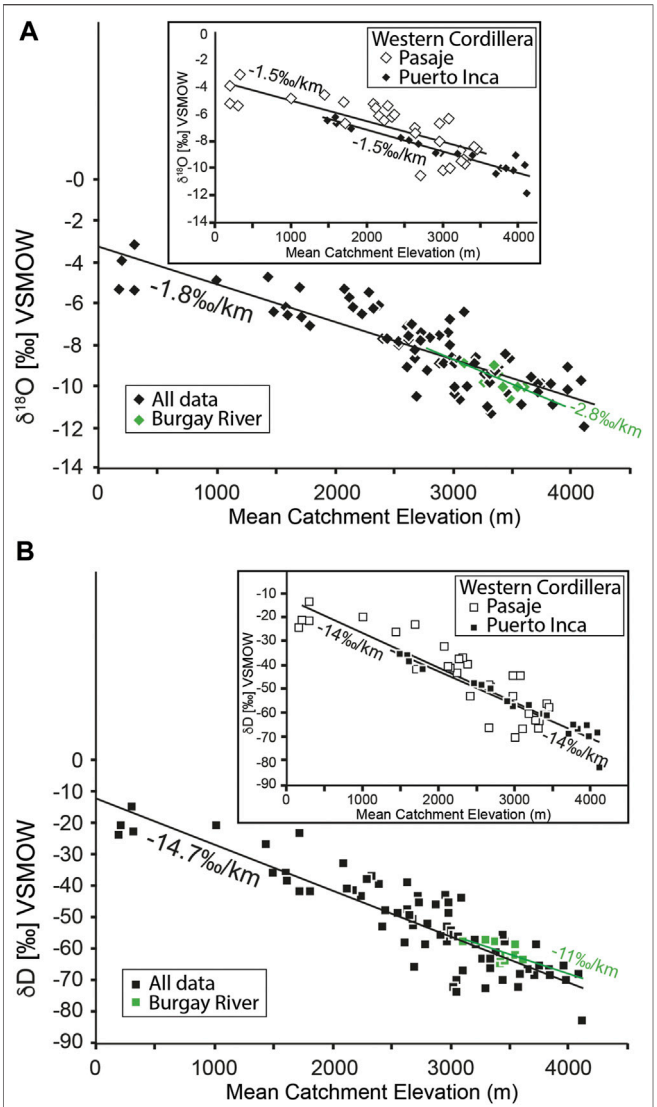

FIGURE 3 | (A) $\delta^{18}O$ of river water vs. mean catchment elevation for all data (n = 83, black diamonds) defining a slope of −1.8‰/ km (or −0.18‰/ 100 m, R^2 = 0.73). Highlighted using green diamonds are samples collected in the Cuenca basin along the Burgay River that define an isotope-elevation lapse rate of −2.8‰/ km (or −0.28‰/100 m). Inset: Plot of the $\delta^{18}O$ of river water vs. mean catchment elevation (m) for the Puerto Inca (small black diamonds) and Pasaje (small white diamonds) transects (windward side of the Western Ecuadorian Cordillera). Note that both transects provide a same lapse rate of −1.5‰/ km (or −0.15‰/100 m). **(B)**δD of river water vs. mean catchment elevation for all data (n = 83, black squares) providing a slope of −14.7‰/ km (or −1.47‰/100 m, R^2 = 0.79). Highlighted using green squares are samples collected in the Cuenca basin along the Burgay River that define an elevation lapse rate of −11‰/ km (or −1.1‰/100 m). Inset highlights data from the Puerto Inca and Pasaje transects plotted against mean catchment elevation. The decrease in δD values on the windward side of the Western Cordillera allows to define an isotopic lapse rate for both transects of −14.7‰/ km (or −1.47‰/100 m).

ranging from −75 to −59‰ (**Figure 2** and **Supplementary Table S1**).

We further focused on the north-north east part of the Cuenca region where we sampled tributaries of the Burgay River between

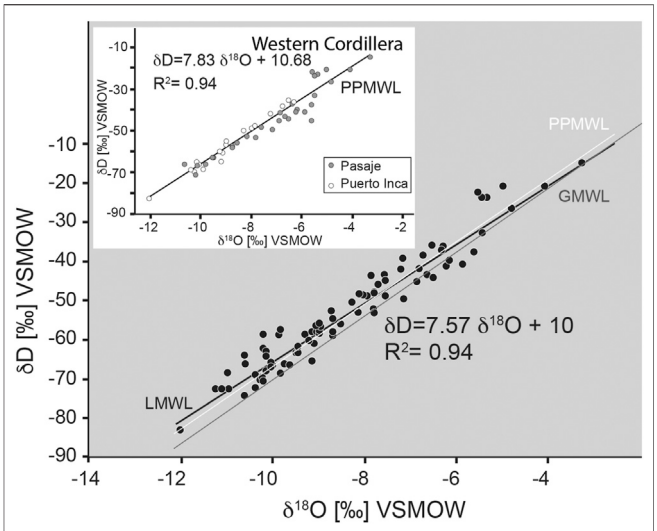

FIGURE 4 | δD vs. $\delta^{18}O$ values of water samples allowing to define LMWL (Local Meteoric Water Line) and PPMWL (Puerto Inca—Pasaje Meteoric Water Line). LMWL has been defined from all our sampling sites (black circles, n = 83). GMWL: Global Meteoric Water Line defined by Rozanski et al. (1993). Inset highlights PPMWL defined from values obtained from the Puerto Inca (white circles) and Pasaje (grey samples) that cross the Western Ecuadorian Cordillera. (See text for explanations).

Azogues and La Escalera (**Figure 1A**). $\delta^{18}O$ and δD values vary from −10.6 to −9.0‰ and −65 to −58‰, respectively (**Figure 2** and **Supplementary Table S1**).

Finally, we collected water samples from the Nabón area (**Figure 1A**), located within close proximity of the Amazon rainforest. Sampling occurred between 2,340 and 2,754 m of elevation. $\delta^{18}O$ and δD values vary between −9.28 and −7.52‰ and −59 to −44‰ respectively and are generally higher than those obtained from the two other areas investigated in the Inter-Andean valley (**Figure 2** and **Supplementary Table S1**). Although mean catchment elevations are systematically above 2,000 m elevation, d-excess values are generally higher than those in high areas of the windward side of the Western Cordillera with d = 14.0 ± 3.7 for Yanuncay, d = 17.1 ± 3.2 for Burgay, and d = 12.8 ± 7.4 for Nabón (**Supplementary Table S1** and **Supplementary Figure 1S**).

Meteoric Water Lines

The δD and $\delta^{18}O$ values of all our surface water samples collected in southern Ecuador define a Local Meteoric Water line (LMWL) with $\delta D = 7.57\ \delta^{18}O + 10$ (R^2 = 0.94) (**Figure 4**). When plotting only results from the windward side of the Western Cordillera (Puerto Inca and Pasaje transects) we obtain a meteoric water line with $\delta D = 7.83\ \delta^{18}O + 10.68$ (PPMWL, R^2 = 0.94) (**Figure 4**). The close resemblance of the LMWL and PPMWL with the GMWL ($\delta D = 8.17\ \delta^{18}O + 10.35$; Rozanski et al. (1993) highlights the robustness of our results.

Establishment of Isotopic Lapse Rates

We evaluated the magnitude of δD and $\delta^{18}O$ gradients across the Western Cordillera based on the results obtained on the windward side of the range. Some studies have constrained the

absolute elevation of precipitation by directly sampling rainfall via open rainfall sampling (Windhorst et al., 2013) or shallow groundwater springs (Maldonado et al., 1995) or by using International Atomic Energy Agency (IAEA) weather stations (Rozanski and Araguas-Araguas, 1995; Garcia et al., 1998). Here, we use a flow accumulation model in ArcGIS (see above). $\delta^{18}O$ values of samples collected along the Puerto Inca transect and plotted against mean catchment elevation yield a slope of −0.15‰/100 m (**Figure 3A**; R^2 = 0.88, n = 19). The δD vs. elevation relationship displays a linear regression with a slope of −1.4‰/100 m for δD (**Figure 3B**; R^2 = 0.93, n = 19). This result is also supported by the linear regression calculated from the Pasaje transect that gives a slope of −0.15‰/100 m (R^2 = 0.65, n = 30) for $\delta^{18}O$ and −1.4‰/100 m for δD (R^2 = 0.78, n = 30) (**Figures 3A,B**).

In the Inter-Andean valley, the correlation between $\delta^{18}O$ values and elevation is absent, especially along the Yanuncay River and Nabón area (**Figure 1A**). An isotope-elevation relationship of −0.28‰/100 m for $\delta^{18}O$ (R^2 = 0.52, **Figure 3A**) and −1.1‰/100 m for δD (R^2 = 0.33, **Figure 3B**) can be defined from samples collected to the north of Cuenca (Burgay River) but display low correlation coefficients.

When plotting $\delta^{18}O$ values from all samples against mean catchment elevation, a linear regression vs. elevation can be defined and provides a slope of −0.18‰/100 m (**Figure 3A**; R^2 = 0.73, n = 83). Similarly, all δD values vs. elevation yield a slope of −1.47‰/100 m (**Figure 3B**; R^2 = 0.79, n = 83).

DISCUSSION

Impact of Pacific Air Masses on Stable Isotopes in Precipitation

The spatial patterns of δD and $\delta^{18}O$ values of stream waters collected in southern Ecuador across the Western Cordillera and the Inter-Andean depression reflect the topography of this region. First, samples collected from the windward flanks of the Western Cordillera between Puerto Inca and El Cajas National Park (**Figure 1A**) show a net decrease in both δD and $\delta^{18}O$ values (50‰ in δD and 6‰ in $\delta^{18}O$ from near sea level to ∼ 4,000 m) across the mountain range (**Figure 1C**). This decrease in both $\delta^{18}O$ and δD values allows to define an isotopic lapse rate of -0.15‰/100 m for $\delta^{18}O$ (R^2 = 0.88; **Figure 3A**) and -1.4‰/100 m for δD (R^2 = 0.93; **Figure 3B**). We interpret this lapse rate to reflect the altitude effect for δD and $\delta^{18}O$ originating from Pacific air masses and orographic rainout on the western facing slopes of the Ecuadorian Andes.

Although calculated from samples sourced at lower elevation, the lapse rate from the Pasaje transect provides a $\delta^{18}O$ and δD vs. altitude relationship of -0.15‰/100 m ($\delta^{18}O$; R^2 = 0.65; **Figure 3A**) and -1.4‰/100 m (δD; R^2 = 0.78; **Figure 3B**) and confirms the altitude effect on the isotope composition of tropical rains observed at higher elevation. These lapse rates are lower than those compiled or modeled for mid-latitude settings (-0.28 ‰/100 m in $\delta^{18}O$ or -2.0 ‰/100 m in δD) (e.g., Poage and Chamberlain, 2001; Quade et al., 2011). However, they are in good agreement with isotope-elevation relationships defined from the isotopic composition of tropical rains in Cameroon (−0.156‰/100 m in $\delta^{18}O$; Gonfiantini et al., 2001), in the Colombian Eastern Cordillera (-0.18‰/100 m in $\delta^{18}O$ and −1.46‰/100 m in δD; Saylor et al., 2009) and in Ecuador (−0.17‰/100 m in $\delta^{18}O$; Garcia et al., 1998) using water samples from springs and IAEA weather stations along two transects across the Western and Eastern Cordillera near 1 and 3°S latitude (**Supplementary Table S1** and **Supplementary Figure 2S**). In the latter study, $\delta^{18}O_{water}$ and δD_{water} values are influenced by the amount of precipitation which varies over the year and causes D and ^{18}O-depleted precipitation during the wet season. In addition to this amount effect, Garcia and coauthors highlight a latitudinal effect in their dataset which is also well illustrated in our data, as $\delta^{18}O_{water}$ values are ∼ −3‰ more negative to the north along the Puerto Inca transect (**Figures 1C,2**). The latitudinal difference for our low elevation sites that share the same Pacific moisture source can be explained by a lower precipitation amounts in the south (from Pasaje to La Tarabita) when compared to the north (Puerto Inca).

Comparison Between Results Obtained Along the Puerto Inca and Pasaje Transects

Samples collected along the Puerto Inca and Pasaje transects define a similar elevation lapse rate of −0.15‰/100 m for $\delta^{18}O$. However, we note a better correlation for Puerto Inca than for Pasaje that can be explained by two main factors shared by Puerto Inca samples: 1) the location on the windward side of the Western Cordillera and, 2) an unique moisture source (the Pacific Ocean). Although the main moisture source for samples collected along the Pasaje transect is provided by the Pacific trade winds, we cannot preclude the possibility of mixing with Atlantic air masses that experienced evapo-transpiration over the Amazon (Salati et al., 1979). This is consistent with the observation of moist air masses along the Pasaje transect through side valleys (e.g., to the south-east of La Tarabita, black arrow on **Figure 1A**). In addition, evaporation associated with the dry climate that characterizes part of this transect could explain some of the variability in the results with enrichment of ^{18}O and D (e.g., Schemmel et al., 2013) observable in some samples (e.g., WS13 and WS24, **Supplementary Table S1**).

The Inter-Andean Valley

In contrast to samples from the windward side of the Western Cordillera, $\delta^{18}O$ and δD values from the Cuenca region, in the Inter-Andean valley and further south in the Nabón Basin, do not show a clear correlation with elevation.

Data acquired along the Puerto Inca transect on the leeward side of the Western Cordillera display relatively low $\delta^{18}O$ and δD values that can be explained by Rayleigh distillation of the heavy isotopes on the windward side (**Figure 1C**). However, together with data acquired from tributaries along the Yanuncay River (from sample 51 to 60 on **Figure 1C** and **Supplementary Table S1**), the $\delta^{18}O$ and δD values on the leeward side cannot be correlated with elevation and show increased variability. However, leeward $\delta^{18}O$ and δD vs. elevation gradients are

inherently more complex once an orographic rain shadow develops (e.g., Quade et al., 2011). In addition to local evaporation that may shift near surface ground water $\delta^{18}O$ and δD values to higher values (consistent with d = 14.0 ± 3.7), ^{18}O or D-depleted precipitation from the windward side, moisture mixing, and continental water vapor recycling represent multiple and confounding factors that render the interpretation of leeward rainfall $\delta^{18}O$ and δD signals difficult (e.g., Blisniuk and Stern, 2005; Schemmel et al., 2013). Also, stable isotopic variability in our dataset could reflect the passage of the ITCZ, which significantly affects this area as highlighted by the BMR (Celleri et al., 2007). However, the ENSO system seems to have a negligible effect on the basin's seasonal distribution of rainfall due to the high elevation of the Cuenca area (1840–4680 m; Celleri et al., 2007).

Second, the $\delta^{18}O$ and δD values acquired north of Cuenca, between Azogues and La Escalera (**Figure 1A**) show a weak correlation with altitude that allows to define a $\delta^{18}O$ vs. elevation relationship of −0.28‰/100 m with R^2 = 0.52 (−1.1‰/100 m with R^2 = 0.33 for δD) (see green line and samples on **Figure 3**). While the correlation coefficient is moderate, the isotope-elevation relationship is close to −0.22‰/100 m for $\delta^{18}O$ and −1.12‰/100 m for δD defined by Windhorst et al. (2013) who investigated the isotopic composition of precipitation in South Ecuadorian montane cloud forests from 1,800 to 2,800 m elevation using open rainfall sampling (on the east-facing slopes of the Andes in the San Francisco Valley). Windhorst et coauthors have highlighted an enrichment of heavy isotopes during southeasterly trade winds that carry re-evaporated and recycled precipitation from the Amazon Basin.

Results obtained from samples collected in the Nabón Basin display higher $\delta^{18}O$ (>2‰), and δD (>13‰) values than those measured from samples in the Cuenca Basin. No elevation lapse rate can be defined from these values that vary from −9.3 to −7.5‰ for $\delta^{18}O$, and −59 and −44‰ for δD. This lack of correlation with elevation could be partly explained by the small range of mean catchment elevations, which does not exceed ~600 m. In addition, and as highlighted in previous work conducted in South America (e.g., Nieto-Moreno et al., 2016), the variation of these tropical rainfall values could reflect a mixed signal resulting from different air mass trajectories.

CONCLUSION

We analysed the oxygen and hydrogen isotope ratios of surface waters from tributaries across the Ecuadorian Northern Andes to establish a $\delta^{18}O$ and δD vs. elevation gradients near the Equator (~3°S); essential for stable isotope paleoaltimetry reconstructions.

The west facing slopes of the Western Cordillera are subject to moisture incoming from the Pacific which gets orographically lifted and produces a lapse rate of −0.15‰/100 m for $\delta^{18}O$ (R^2 = 0.88, n = 19) and −1.4‰/100 m for δD (R^2 = 0.93, n = 19) that takes into account precipitation from near sea level up to 4,000 m elevation (Puerto Inca transect). This isotope-elevation relationship is supported by results acquired further south along the Pasaje transect that provides a similar result [−0.15‰/100 m with R^2 = 0.65 (n = 30) for $\delta^{18}O$ and −1.4‰/100 m for δD with R^2 = 0.78 (n = 30)], although covering a lower range of mean catchment elevation.

Evaluating the magnitude of $\delta^{18}O$ and δD gradients across the Inter-Andean depression is more difficult as this domain receives air masses from the Pacific, Atlantic, and Amazon Basin. In addition, part of this region experiences the seasonal passage of the ITCZ that impacts the temperature and humidity of air masses. Therefore, the $\delta^{18}O$ and δD values obtained from our water samples here reflect a mixed signal resulting from a combination of factors including air mass mixing, evaporation, humidity.

In agreement with previous studies conducted in Ecuador (e.g., Maldonado et al., 1995; Garcia et al., 1998; Jackson et al., 2019; **Supplementary Table 1S** and **Supplementary Figure 2S**) and other tropical regions (e.g., Gonfiantini et al., 2001; Saylor et al., 2009), our work demonstrates that an empirical relationship between elevation and the stable isotope composition of precipitation and surface waters can be established at (or near) the Equator. Therefore, the $\delta^{18}O$ and δD elevation relationships of −0.15‰/100 m for $\delta^{18}O$ and −1.4‰/100 m for δD may serve as a guide for stable isotope paleoaltimetry reconstructions at tropical latitudes.

DATA AVAILABILITY STATEMENT

The original contributions presented in the study are included in the article/**Supplementary Material**, further inquiries can be directed to the corresponding author.

AUTHOR CONTRIBUTIONS

AG wrote the manuscript, made the figures, and conducted the study (collection of water samples in the field, results analysis and interpretation). CW participated in writing the manuscript, made some figures and collected samples in the field. MR collected samples in the field, participated in the results analysis and interpretation. AM participated in writing and interpreting the data.

ACKNOWLEDGMENTS

We thank Ulrich Treffert (Senckenberg BiK-F) for continuous laboratory support. Comments and suggestions by L. J. Jackson, two anonymous reviewers and the editor, A. Licht, are gratefully acknowledged.

SUPPLEMENTARY MATERIAL

The Supplementary Material for this article can be found online at: https://www.frontiersin.org/articles/10.3389/feart.2021.664590/full#supplementary-material

REFERENCES

Barnes, J. B., and Ehlers, T. A. (2009). End Member Models for Andean Plateau Uplift. *Earth-Science Rev.* 97, 105–132. doi:10.1016/j.earscirev.2009.08.003

Barnes, J. B., Ehlers, T. A., Insel, N., McQuarrie, N., and Poulsen, C. J. (2012). Linking Orography, Climate, and Exhumation across the central Andes. *Geology* 40 (12), 1135–1138. doi:10.1130/G33229

Blisniuk, P. M., and Stern, L. A. (2005). Stable Isotope Paleoaltimetry: a Critical Review. *Am. J. Sci.* 305 (10), 1033–1074. doi:10.2475/ajs.305.10.1033

Bookhagen, B., and Burbank, D. W. (2006). Topography, Relief, and TRMM-Derived Rainfall Variations along the Himalaya. *Geophys. Res. Lett.* 33 (8), L08405. doi:10.1029/2006GL026037

Boos, W. R., and Kuang, Z. (2010). Dominant Control of the South Asian Monsoon by Orographic Insulation versus Plateau Heating. *Nature* 463, 218–222. doi:10.1038/Nature08707

Campozano, L., Célleri, R., Trachte, K., Bendix, J., and Samaniego, E. (2016). Rainfall and Cloud Dynamics in the Andes: A Southern Ecuador Case Study. *Adv. Meteorology* 2016, 15. doi:10.1155/2016/3192765

Celleri, R., Willems, P., Buytaert, W., and Feyen, J. (2007). Space-time Rainfall Variability in the Paute basin, Ecuadorian Andes. *Hydrol. Process.* 21, 3316–3327. doi:10.1002/hyp.6575

Craig, H., and Gordon, L. I. (1965). "Deuterium and Oxygen-18 Variations in the Ocean and the marine Atmosphere," in *Stable Isotopes in Oceanographic Studies and Paleotemperatures*. Editor E. Tongiorgi Pisa: Consiglio Nazionale delle Riche, Laboratorio de Geologia Nucleare), 1–122.

Currie, B. S., Rowley, D. B., and Tabor, N. J. (2005). Middle Miocene Paleoaltimetry of Southern Tibet: Implications for the Role of Mantle Thickening and Delamination in the Himalayan Orogen. *Geol.* 33 (3), 181–184. doi:10.1130/G21170.1

Ehlers, T. A., and Poulsen, C. J. (2009). Influence of Andean Uplift on Climate and Paleoaltimetry Estimates. *Earth Planet. Sci. Lett.* 281 (3-4), 238–248. doi:10.1016/j.epsl.2009.02.026

Emck, P. (2007). "A Climatology of South Ecuador – with Special Focus on the Major Andean ridge as Atlantic-Pacific Climate divide,", 1–159. Friedrich-Alexander-University of Erlangen-Nurnberg. PhD.

Garcia, M., Villalba, F., Araguas-Araguas, L., and Rozanski, K. (1998). "The Role of Atmospheric Circulation Patterns in Controlling the Regional Distribution of Stable Isotope Contents in Precipitation: Preliminary Results from Two Transects in the Ecuadorian Andes," in *Isotope Techniques in the Study of Environmental Change* (Vienna: International Atomic Energy Agency), 127–140.

Garreaud, R. D., Vuille, M., Compagnucci, R., and Marengo, J. (2009). Present-day South American Climate. *Palaeogeogr. Palaeoclimatol. Palaeoecol.* 281, 180–195. doi:10.1016/j.palaeo.2007.10.032

Garzione, C. N., Hoke, G. D., Libarkin, J. C., Withers, S., MacFadden, B., Eiler, J., et al. (2008). Rise of the Andes. *Science* 320, 1304–1307. doi:10.1126/science.1148615

Garzione, C. N., McQuarrie, N., Perez, N. D., Ehlers, T. A., Beck, S. L., Kar, N., et al. (2017). Tectonic Evolution of the Central Andean Plateau and Implications for the Growth of Plateaus. *Annu. Rev. Earth Planet. Sci.* 45, 529–559. doi:10.1146/annurev-earth-063016-020612

Garzione, C. N., Molnar, P., Libarkin, J. C., and MacFadden, B. J. (2006). Rapid Late Miocene Rise of the Bolivian Altiplano: Evidence for Removal of Mantle Lithosphere. *Earth Planet. Sci. Lett.* 241 (3–4), 543–556. doi:10.1016/j.epsl.2005.11.026

Garzione, C. N., Quade, J., DeCelles, P. G., and English, N. B. (2000). Predicting Paleoelevation of Tibet and the Himalaya from δ18O vs. Altitude Gradients in Meteoric Water across the Nepal Himalaya. *Earth Planet. Sci. Lett.* 183, 215–229. doi:10.1016/S0012-821X(00)00252-1

Gébelin, A., Mulch, A., Teyssier, C., Jessup, M. J., Law, R. D., and Brunel, M. (2013). The Miocene Elevation of Mount Everest. *Geology* 41, 799–802. doi:10.1130/G34331.1

Gébelin, A., Mulch, A., Teyssier, C., Page Chamberlain, C., and Heizler, M. (2012). Coupled basin-detachment Systems as Paleoaltimetry Archives of the Western North American Cordillera. *Earth Planet. Sci. Lett.* 335-336, 36–47. doi:10.1016/j.epsl.2012.04.029

Gonfiantini, R., Roche, M.-A., Olivry, J.-C., Fontes, J.-C., and Zuppi, G. M. (2001). The Altitude Effect on the Isotopic Composition of Tropical rains. *Chem. Geology.* 181, 147–167. doi:10.1016/s0009-2541(01)00279-0

Gregory-Wodzicki, K. M. (2000). Uplift History of the Central and Northern Andes: A Review. *Geol. Soc. America Bull.* 112 (7), 1091–1105. doi:10.1130/0016-7606(2000)112<1091:UHOTCA>2.0.CO;2

Hungerbühler, D., Steinmann, M., Winkler, W., Seward, D., Egüez, A., Peterson, D. E., et al. (2002). Neogene Stratigraphy and Andean Geodynamics of Southern Ecuador. *Earth-Science Rev.* 57, 75–124. doi:10.1016/S0012-8252(01)00071-X

Jackson, L. J., Horton, B. K., Beate, B. O., Bright, J., and Breecker, D. O. (2019). Testing Stable Isotope Paleoaltimetry with Quaternary Volcanic Glasses from the Ecuadorian Andes. *Geology* 47, 411–414. doi:10.1130/G45861.1

Maldonado, A. S., Cepeda, T. H., and Araguás Araguás, L. (1995). "Hydrogeological and Isotopic Study of Groundwater in the Chacras-Huaquillas Area (Ecuador)," International Atomic Energy Agency Technical Document IAEA-TECDOC-835, 195–209.

Molnar, P., and England, P. (1990). Late Cenozoic Uplift of Mountain Ranges and Global Climate Change: Chicken or Egg? *Nature* 346 (6279), 29–34. doi:10.1038/346029a0

Mora, D. E., Campozano, L., Cisneros, F., Wyseure, G., and Willems, P. (2014). Climate Changes of Hydrometeorological and Hydrological Extremes in the Paute basin, Ecuadorean Andes. *Hydrol. Earth Syst. Sci.* 18 (2), 631–648. doi:10.5194/hess-18-631-2014

Mulch, A., Graham, S. A., and Chamberlain, C. P. (2006). Hydrogen Isotopes in Eocene River Gravels and Paleoelevation of the Sierra Nevada. *Science* 313, 87–89. doi:10.1126/science.1125986

Mulch, A. (2016). Stable Isotope Paleoaltimetry and the Evolution of Landscapes and Life. *Earth Planet. Sci. Lett.* 433, 180–191. doi:10.1016/j.epsl.2015.10.034

Mulch, A., Teyssier, C., Cosca, M. A., Vanderhaeghe, O., and Vennemann, T. W. (2004). Reconstructing Paleoelevation in Eroded Orogens. *Geol.* 32, 525–528. doi:10.1130/g20394.1

Nieto-Moreno, V., Rohrmann, A., van der Meer, M. T. J., Sinninghe Damsté, J. S., Sachse, D., Tofelde, S., et al. (2016). Elevation-dependent Changes in N -alkane δ D and Soil GDGTs across the South Central Andes. *Earth Planet. Sci. Lett.* 453, 234–242. doi:10.1016/j.epsl.2016.07.049

Ochoa, A., Campozano, L., Sánchez, E., Gualán, R., and Samaniego, E. (2016). Evaluation of Downscaled Estimates of Monthly Temperature and Precipitation for a Southern Ecuador Case Study. *Int. J. Climatol.* 36 (3), 1244–1255. doi:10.1002/joc.4418

Philander, S. G. H. (1983). El Niño Southern Oscillation Phenomena. *Nature* 302, 295–301. doi:10.1038/302295a0

Poage, M. A., and Chamberlain, C. P. (2001). Empirical Relationships between Elevation and the Stable Isotope Composition of Precipitation and Surface Waters: Considerations for Studies of Paleoelevation Change. *Am. J. Sci.* 301, 1–15. doi:10.2475/ajs.301.1.1

Quade, J., Breecker, D. O., Daeron, M., and Eiler, J. (2011). The Paleoaltimetry of Tibet: an Isotopic Perspective. *Am. J. Sci.* 311 (2), 77–115. doi:10.2475/02.2011.01

Rech, J. A., Currie, B. S., Michalski, G., and Cowan, A. M. (2006). Neogene Climate Change and Uplift in the Atacama Desert, Chile. *Geol.* 34 (9), 761–764. doi:10.1130/G22444.1

Rohrmann, A., Strecker, M. R., Bookhagen, B., Mulch, A., Sachse, D., Pingel, H., et al. (2014). Can Stable Isotopes Ride Out the Storm? the Role of Convection for Water Isotopes in Models, Records, and Paleoaltimetry Studies in the central Andes. *Earth Planet. Sci. Lett.* 407, 187–195. doi:10.1016/j.epsl.2014.09.021

Rollenbeck, R., and Bendix, J. (2011). Rainfall Distribution in the Andes of Southern Ecuador Derived from Blending Weather Radar Data and Meteorological Field Observations. *Atmos. Res.* 99 (2), 277–289. doi:10.1016/j.atmosres.2010.10.018

Rossel, F., and Cadier, E. (2009). El Niño and Prediction of Anomalous Monthly Rainfalls in Ecuador. *Hydrol. Process.* 23, 3253–3260. doi:10.1002/hyp.7401

Rossel, F., Mejía, R., and Ontaneda, G. (1998). Régionalisation de l'influence du El Nino sur les précipitations de l'Equateur. *Bull. Inst. Fr. Études Andines* 27 (3), 643–654.

Rowley, D. B., and Garzione, C. N. (2007). Stable Isotope-Based Paleoaltimetry. *Annu. Rev. Earth Planet. Sci.* 35, 463–508. doi:10.1146/annurev.earth.35.031306.140155

Rozanski, K., and Araguas Araguas, L. (1995). Spatial and Temporal Variability of Stable Isotope Composition of Precipitation over the South American Continent. *Bull. de l'Institut Francais d'études Andines* 24 (3), 379–390.

Rozanski, K., Araguaś-Araguaś, L., and Gonfiantini, R. Isotopic Patterns in Modern Global Precipitation in *Climate Change in Continental Isotopic Records: Geophysical Monograph Series*. Editors P. K. Swart, K. C. Lohmann, J. McKenzie, and S. Savin 78, 1–36. doi:10.1029/GM078p0001

Salati, E., Dall'Olio, A., Matsui, E., and Gat, J. R. (1979). Recycling of Water in the Amazon Basin: An Isotopic Study. *Water Resour. Res.* 15 (5), 1250–1258. doi:10.1029/WR015i005p01250

Saylor, J. E., Mora, A., Horton, B. K., and Nie, J. (2009). Controls on the Isotopic Composition of Surface Water and Precipitation in the Northern Andes, Colombian Eastern Cordillera. *Geochimica et Cosmochimica Acta* 73, 6999–7018.doi:10.1016/j.gca.2009.08.030

Schemmel, F., Mikes, T., Rojay, B., and Mulch, A. (2013). The Impact of Topography on Isotopes in Precipitation across the Central Anatolian Plateau (Turkey). *Am. J. Sci.* 313 (2), 61–80. doi:10.2475/02.2013.01

Steinmann, M., Hungerbühler, D., Seward, D., and Winkler, W. (1999). Neogene Tectonic Evolution and Exhumation of the Southern Ecuadorian Andes: a Combined Stratigraphy and Fission-Track Approach. *Tectonophysics* 307, 255–276. doi:10.1016/s0040-1951(99)00100-6

Sundell, K. E., Saylor, J. E., Lapen, T. J., and Horton, B. K. (2019). Implications of Variable Late Cenozoic Surface Uplift across the Peruvian central Andes. *Scientific Rep.* 9, 4877. doi:10.1038/s41598-019-41257-3

Vuille, M., Bradley, R. S., and Keimig, F. (2000). Climate Variability in the Andes of Ecuador and its Relation to Tropical Pacific and Atlantic Sea Surface Temperature Anomalies. *J. Clim.* 13 (14), 2520–2535. doi:10.1175/1520-0442(2000)013<2520:CVITAO>2.0.CO;2

Windhorst, D., Waltz, T., Timbe, E., Frede, H.-G., and Breuer, L. (2013). Impact of Elevation and Weather Patterns on the Isotopic Composition of Precipitation in a Tropical Montane Rainforest. *Hydrol. Earth Syst. Sci.* 17 (1), 409–419. doi:10.5194/hess-17-409-2013

Witt, C., Rivadeneira, M., Poujol, M., Barba, D., Beida, D., Beseme, G., et al. (2017). Tracking Ancient Magmatism and Cenozoic Topographic Growth within the Northern Andes Forearc: Constraints from Detrital U-Pb Zircon Ages. *Geol. Soc. America Bull.* 129 (3-4), 415–428. doi:10.1130/B31530.1

Conflict of Interest: The authors declare that the research was conducted in the absence of any commercial or financial relationships that could be construed as a potential conflict of interest.

frontiers in Earth Science

MINI REVIEW
published: 10 June 2021
doi: 10.3389/feart.2021.648605

Rise of the Colorado Plateau: A Synthesis of Paleoelevation Constraints From the Region and a Path Forward Using Temperature-Based Elevation Proxies

Emma O. Heitmann[1], Ethan G. Hyland[2], Philip Schoettle-Greene[1], Cassandra A. P. Brigham[1] and Katharine W. Huntington[1]**

[1]*Department of Earth and Space Sciences, University of Washington, Seattle, WA, United States,* [2]*Department of Marine, Earth, & Atmospheric Sciences, North Carolina State University, Raleigh, NC, United States*

OPEN ACCESS

Edited by:
Heiko Pingel,
University of Potsdam, Germany

Reviewed by:
Cari Johnson,
The University of Utah, United States
Richard Ott,
German Research Center for Geosciences, Germany
Laura Crossey,
University of New Mexico, United States

***Correspondence:**
Emma O. Heitmann
eoh322@uw.edu
Katharine W. Huntington
kate1@uw.edu

Specialty section:
This article was submitted to Sedimentology, Stratigraphy and Diagenesis, a section of the journal Frontiers in Earth Science

Received: *01 January 2021*
Accepted: *14 May 2021*
Published: *10 June 2021*

Citation:
Heitmann EO, Hyland EG, Schoettle-Greene P, Brigham CAP and Huntington KW (2021) Rise of the Colorado Plateau: A Synthesis of Paleoelevation Constraints From the Region and a Path Forward Using Temperature-Based Elevation Proxies. Front. Earth Sci. 9:648605. doi: 10.3389/feart.2021.648605

The Colorado Plateau's complex landscape has motivated over a century of debate, key to which is understanding the timing and processes of surface uplift of the greater Colorado Plateau region, and its interactions with erosion, drainage reorganization, and landscape evolution. Here, we evaluate what is known about the surface uplift history from prior paleoelevation estimates from the region by synthesizing and evaluating estimates 1) in context inferred from geologic, geomorphic, and thermochronologic constraints, and 2) in light of recent isotopic and paleobotanical proxy method advancements. Altogether, existing data and estimates suggest that half-modern surface elevations were attained by the end of the Laramide orogeny (~40 Ma), and near-modern surface elevations by the mid-Miocene (~16 Ma). However, our analysis of paleoelevation proxy methods highlights the need to improve proxy estimates from carbonate and floral archives including the ~6–16 Ma Bidahochi and ~34 Ma Florissant Formations and explore understudied (with respect to paleoelevation) Laramide basin deposits to fill knowledge gaps. We argue that there are opportunities to leverage recent advancements in temperature-based paleoaltimetry to refine the surface uplift history; for instance, via systematic comparison of clumped isotope and paleobotanical thermometry methods applied to lacustrine carbonates that span the region in both space and time, and by use of paleoclimate model mediated lapse rates in paleoelevation reconstruction.

Keywords: Colorado Plateau, paleoaltimetry, clumped isotopes, paleobotany, temperature proxies, Southern Rocky Mountains

INTRODUCTION

Scientists have long debated the uplift of the Colorado Plateau region (CP), including the modern Colorado River (CR) drainage from the Rocky Mountains to where it exits the modern plateau southwest of Grand Canyon (GC; **Figure 1**). This region was a tectonically stable sedimentary basin near sea-level until the Laramide orogeny initiated in the Late Cretaceous (Hunt, 1956; Nations et al., 1991) and now resides ~2–3 km above sea level. Proposed mechanisms for plateau rise make testable predictions of uplift patterns due to processes including: lower-crustal flow (McQuarrie and Chase, 2000) or shear-removal of

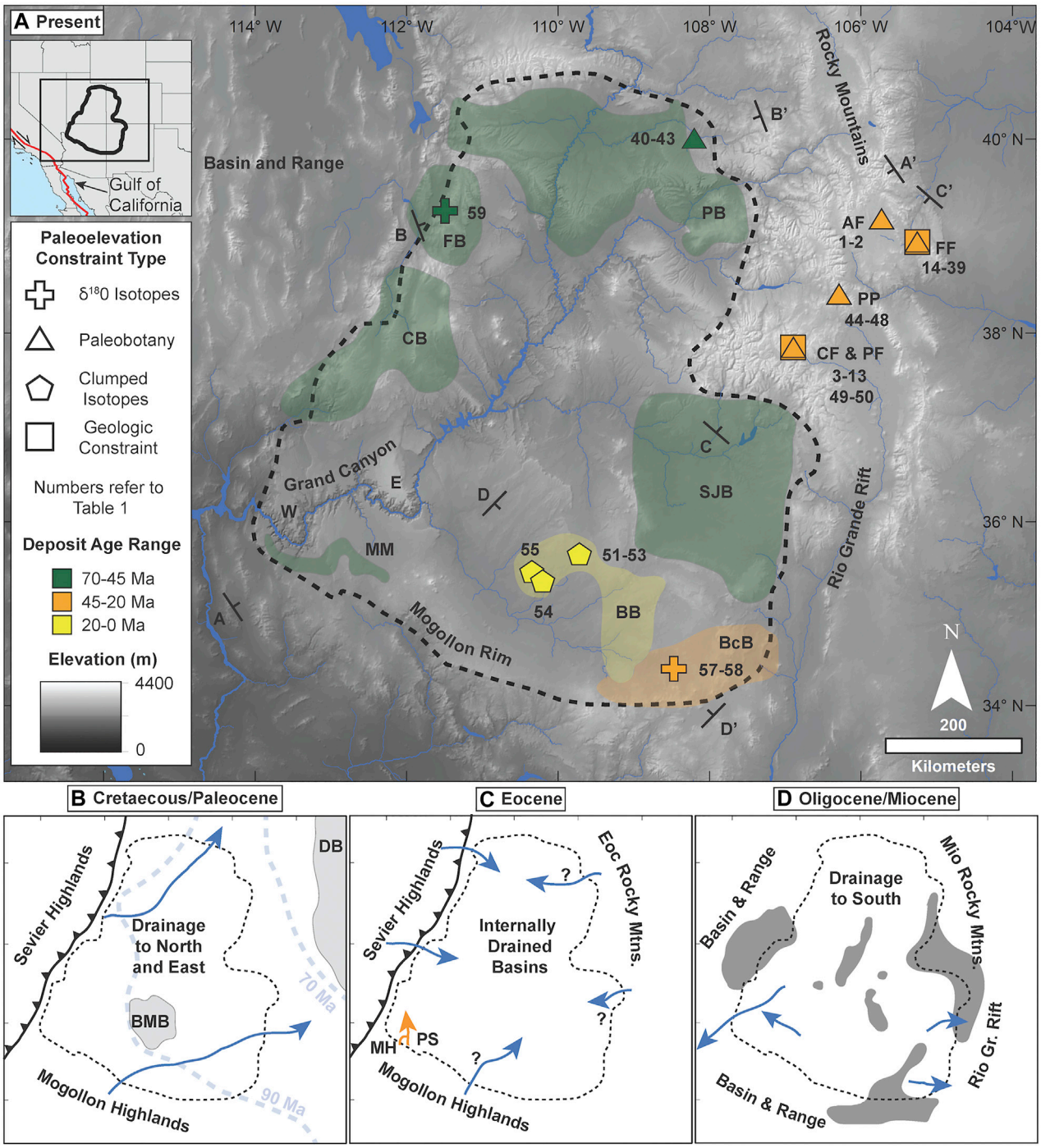

FIGURE 1 | (A) Modern elevation of the Colorado Plateau region with relevant geographic features and depositional basins, locations of paleoaltimetry estimates, and transects corresponding to **Figure 2**. Symbols represent the paleoaltimetry method applied at each location, and superscripts refer to paleo-elevation estimate ID in **Supplementary Table S1**. SJB = San Juan Basin; BcB = Baca Basin; BB = Bidahochi Basin; MM = Music Mountain Formation; CB = Claron Basin; FB = Flagstaff Basin; UB = Uinta Basin; PB = Piceance Basin; CF = Creede Formation; AF = Antero Formation; FF = Florissant Formation; PP = Pitch-Pinnacle Formation; PF = Platoro Formation. **(B–D)** Relevant paleogeographic reconstructions to provide context for interpreting uplift of the Colorado Plateau region (see *Overview* section for discussion). **(B)** In the Late Cretaceous-Paleocene, evidence of the Laramide orogeny and uplift of the CP is marked by the disappearance of marine deposits (gray shading with inferred paleo-shoreline contours based on deposit ages; BMB = Black Mesa Basin; DB = Denver Basin - Fox Hills Group). The Sevier thrust front schematically shows the edge of the Sevier highlands and marks the western boundary of the CP. **(C)** By the Eocene, North-flowing paleocanyons had incised the southwestern plateau (orange arrows; MH = Milkweed-Hindu, PS = Peach Springs). Uplift to the north and east caused internal drainage and drainage reorganization (blue arrows). **(D)** In the Oligocene-Miocene, there was widespread volcanism (gray shading) on the edges of the CP. Continental extension and normal faulting to the West and South (Basin and Range, Rio Grande Rift) caused a drop in base-level and aided drainage reversal to the southwest (blue arrows). Paleogeographic reconstructions were adapted from these compilations: Hunt, 1956; Potochnik et al., 2001; Davis et al., 2009; Cather et al., 2012; Young and Crow, 2014; Hill et al., 2016; Karlstrom et al., 2020.

lithospheric mantle by the Farallon slab during the Laramide (Hernández-Uribe and Palin, 2019); lithospheric foundering (Bird, 1979) or hydration (Porter et al., 2017) in the mid-Cenozoic; and mantle upwelling (e.g., Moucha et al., 2009) or isostatic response to denudation (e.g., Lazear et al., 2013) in the late Cenozoic. Accurate paleoelevation constraints can evaluate hypothesized uplift mechanisms and provide context for CR evolution.

Here, we build on previous syntheses (e.g., Cather et al., 2012) to examine proposed CP paleoelevation estimates and highlight opportunities to refine the elevation history in light of recent proxy method advances. Decades of paleoelevation reconstructions combined with constraints from geology, geomorphology, and thermochronology support the interpretation that the CP was elevated through multi-stage, spatially differential uplift since the Laramide. Paleobotanical and geochemical proxy methods and the use of climate models to infer paleoelevation from proxy data have advanced significantly in the past 10–15 years and can be leveraged to refine and expand temperature-based paleoelevation reconstructions across the CP region.

CONSTRAINTS ON COLORADO PLATEAU PALEOTOPOGRAPHY

Numerous geologic, thermochronologic, and geomorphic investigations constrain CP paleotopography, providing context for evaluating paleoaltimetry estimates (for details, see reviews by Hunt, 1956; Young and Spamer, 2001; Beard et al., 2011; Cather et al., 2012; Karlstrom et al., 2014; Ranney, 2014; Karlstrom et al., 2017; Crow et al., 2019; Karlstrom et al., 2019; Leopold and Zaborac-Reed, 2019; Hill and Polyak, 2020; Karlstrom et al., 2020).

Overview

CP pre-Cenozoic stratigraphy is characterized by relatively flat-lying sedimentary sequences, which suggests that the region was a comparatively stable sedimentary basin near or below sea-level for most of the Paleozoic-Mesozoic (Hunt, 1956). Coincident with onset of the Laramide (≥90 Ma; Carrapa et al., 2019), CP uplift likely swept from southwest to northeast (**Figure 1B**) suggested by the diachronous disappearance of Cretaceous Interior Seaway deposits (Nations et al., 1991; Raynolds and Johnson, 2003); barbed NE-flowing tributaries along sections of GC; and substantial (~2 km) Paleozoic-Mesozoic to late Cretaceous-Paleogene denudation on the southwestern plateau indicated by erosional unconformities (e.g., Young, 2001; Hill et al., 2016). Imbricated gravels deposited in incised paleo-canyons (e.g., Milkweed-Hindu, Peach Springs, Salt River) on the southwestern CP margin in the late Cretaceous and Paleocene-Eocene support this view (e.g., Young, 2001; Potochnik et al., 2011), although the magnitude of Paleogene relief is debated (e.g., Karlstrom et al., 2014; Young and Crow, 2014).

The mid-Cenozoic (**Figure 1C**) was a period of internal drainage from the Sevier highlands to the west (e.g., Davis et al., 2009; Ibarra et al., 2021) and uplifts to the northeast (e.g., Cather et al., 2012). Drainage reorganization and tilting are evidenced by widespread fluvial and lacustrine deposits across the CP (Hunt, 1956) and lacustrine carbonate oxygen isotopic records (Davis et al., 2009). Late Cenozoic (**Figure 1D**) continental extension caused subsidence on the western and southern CP margins (McQuarrie and Wernicke, 2005). Drainage reversed to the southwest (e.g., Potochnik et.al., 2001), and a scarcity of late Cenozoic deposits suggests regional erosion (Hunt, 1956).

The modern CR was integrated from its headwaters in the Rocky Mountains through GC coincident with development of the Salton Trough by ~6 Ma, recorded by CR deposits in the Muddy Creek Formation (e.g., Longwell, 1946; Lucchitta, 1972; Karlstrom et al., 2014). The CR reached its current base-level in the Gulf of California at 4.80–4.63 Ma (Crow et al., 2021).

Additional Uplift Constraints

Studies have investigated CP paleoelevation through reconstructions of erosion and river incision, which may occur in response to relief, drainage, and base-level changes that accompany surface uplift. Erosional exhumation may drive cooling of crustal rocks, which can be recorded by mineral thermal histories reconstructed from thermochronology (Reiners and Shuster, 2009), or constrained by other burial and thermal history information (Nuccio and Condon, 1996). For instance, thermochronometer cooling ages and peak burial temperature constraints from the southwestern CP surface suggests >1.5 km of denudation during the Laramide (e.g., Flowers et al., 2008), and ~1.9–2.5 km of denudation prior to the Neogene (Ryb et al., 2021), supporting the interpretation that uplift of the southwestern CP margin initiated during the Laramide and may have continued into the late Cenozoic. Recent (<10 Ma) cooling of the southwestern CP surface rocks may reflect an erosional response to integration of the CR and a drop in base-level (e.g., Lee et al., 2013; Murray et al., 2016).

Cooling histories from canyon-rim and river-level samples track paleo-relief of GC (Flowers et al., 2008; Flowers and Farley, 2012; Flowers and Farley, 2013; Lee et al., 2013; Karlstrom et al., 2014; Winn et al., 2017) and constrain minimum plateau paleoelevation. A synthesis of thermochronologic datasets by Karlstrom et al. (2020) indicates segments of the GC were incised at different times before becoming integrated 6–5 Ma; the Western GC was likely a paleo-canyon with substantial relief incised by a northeast-flowing river by ~65 Ma, whereas the Eastern GC was likely incised by a NW-flowing paleo-river by ~20 Ma. These trends are compatible with multi-stage uplift prior to ~20 Ma. Additional erosion constraints from volcanic deposits (e.g., Aslan et al., 2008; Donahue et al., 2013), cave deposits (Karlstrom et al., 2008; Polyak et al., 2008), and strath terraces show increased incision rates since ~6 Ma, for example in eastern GC (Crow et al., 2014) and the Lower Colorado River (Karlstrom et al., 2017), potentially reflecting small-scale (<400 m) uplift of the southwestern plateau related to Neogene volcanism (Crow et al., 2011; Crow et al., 2019).

River longitudinal profiles may also constrain CP uplift timing (Roberts et al., 2012). However, complications due to varying rock erodibility (Cook et al., 2009; Pederson and Tressler, 2012),

normal faulting and paleocanyon integration (Karlstrom et al., 2014), as well as drainage reorganization and resulting changes to stream power (Schwanghart and Scherler, 2020) limit straightforward correlation between river profiles and uplift. Nevertheless, an inverse correlation between channel steepness and upper mantle p-wave velocity in the Virgin River drainage suggests epeirogenic uplift affects modern CP river profiles (Walk et al., 2019). Projection of relict channels buried by Miocene and younger basalt (Hamblin et al., 1981), and knickpoint-bound upper reaches in CR tributaries (Darling and Whipple, 2015), indicate ~1 km relief growth both prior to and since the Miocene. Such constraints do not distinguish between relief growth in response to CP uplift or subsidence at the plateau margin (Ott et al., 2018).

PREVIOUS PALEOALTIMETRY

Many workers have developed and applied direct paleoelevation proxies to resolve CP paleoelevation, though little agreement on methods or results has been reached (**Figure 2**; **Supplementary Table S1**). For instance, CP paleoelevation estimates based on basalt-vesicle paleobarometry (Sahagian et al., 2002a; Sahagian et al., 2002b; Sahagian et al., 2003), while elegant in theory, are problematic (Bondre, 2003; Libarkin and Chase, 2003), and the approach has not been replicated. Below, we evaluate CP paleoelevation estimates from oxygen-isotopic and paleothermometry-based methodologies.

δ^{18}O-Based Paleoaltimetry

δ^{18}O of precipitation decreases as air masses traverse increasing elevation (e.g., Rowley and Garzione, 2007). δ^{18}O of authigenic carbonates ($\delta^{18}O_c$) precipitated from meteoric waters can be used to infer δ^{18}O of precipitation and thus elevation, but several factors must be considered (Botsyun and Ehlers, 2021). In southwestern North America, summer and winter precipitation originate from different sources and commonly exhibit different δ^{18}O values (Douglas et al., 1993; Blasch and Bryson, 2007), and summer monsoon precipitation is impacted by the "amount effect" (i.e., heavy precipitation is depleted in ^{18}O

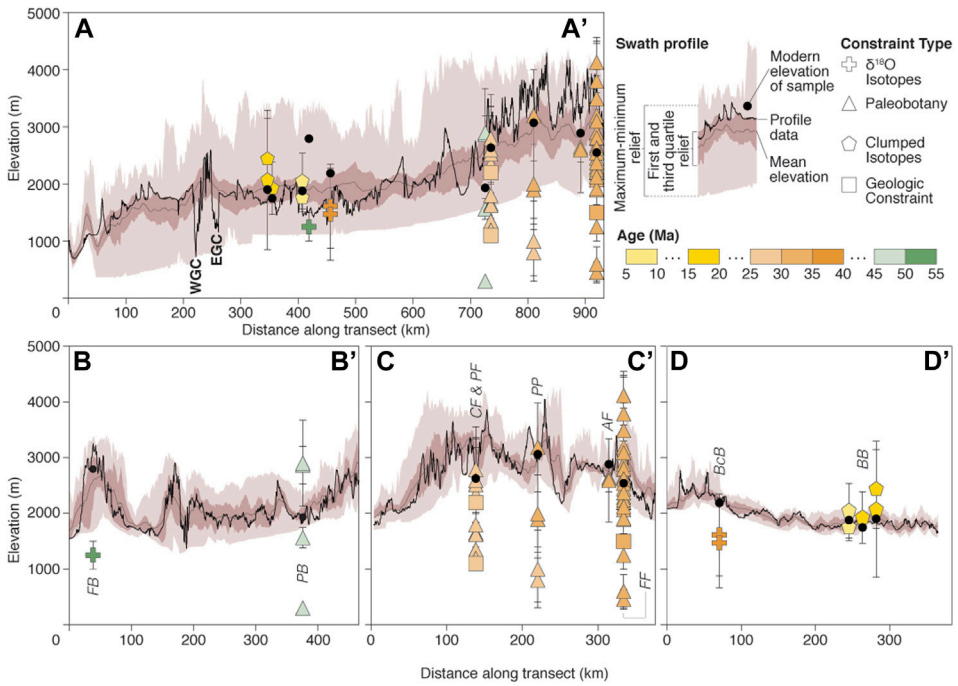

FIGURE 2 | Compilation of paleoelevation estimates for the Colorado Plateau region. Error bars shown where available and represent reported uncertainties or range of possible elevations. Symbols correspond to proxy-type and color corresponds to age (consistent with **Figure 1**). For all panels, elevation profiles (black line) correspond to transects in **Figure 1**. Swath profiles of these transects are shown by mean elevation (gray line), the first and third quartile relief (dark shading), and the full maximum-minimum relief (light shading). **(A)** Compilation of all estimates projected onto elevation transect **(A-A')**; swath profile is cropped to the CP region and is 660 km across at its widest extent (330 km on either side of the transect). **(B-D)** Regional topographic swath profiles are 60 km wide (30 km on either side of the transect). Estimates are labeled by name of their geologic unit consistent with **Figure 1** (BcB = Baca Basin; BB = Bidahochi Basin; FB = Flagstaff Basin; PB = Piceance Basin; CF = Creede Formation; AF = Antero Formation; FF = Florissant Formation; PP = Pitch-Pinnacle Formation; PF = Platoro Formation). **(B)** Estimates from the northern plateau projected onto elevation transect B-B'. **(C)** Estimates from the present-day Rocky Mountains projected onto elevation transect **(C-C')**. **(D)** Estimates from the southern plateau projected onto elevation transect **(D-D')**. All data and references are presented in **Supplementary Table S1**; data from MacGinitie, 1953; Steven and Ratté, 1965; MacGinitie, 1969; Axelrod and Bailey, 1976; Meyer, 1986; Axelrod, 1987; Wolfe and Schorn, 1989; Gregory and Chase, 1992; Meyer, 1992; Wolfe, 1992a; Wolfe, 1992b; Gregory, 1994; Wolfe, 1994; Gregory and McIntosh, 1996; Axelrod, 1998; Wolfe et al., 1998; Gregory-Wodziki, 2001; Leopold and Claypoole 2001; Boyle et al., 2008; Leopold et al., 2008; Huntington et al., 2010; Cather et al., 2012; Baumgartner and Meyer, 2014; Leopold and Zaborac-Reed, 2014; VanDevelde and Bowen, 2014; Zaborac-Reed and Leopold, 2016; Licht et al., 2017; Leopold and Zaborac-Reed, 2019; Allen et al., 2020.

whereas sparse precipitation is enriched in ^{18}O; Dansgaard, 1964). Changing atmospheric conditions can further complicate precipitation $\delta^{18}O$ through time (Licht et al., 2017). Moreover, various factors can blur the $\delta^{18}O$-elevation relationship preserved in $\delta^{18}O_c$, including temperature (e.g., Kim and O'Neil, 1997), evaporation (e.g., Licht et al., 2017), seasonal-bias (e.g., Breecker et al., 2009), and/or drainage reorganization (Davis et al., 2008).

Novel carbonate isotopic approaches have been developed to circumvent some complexities of reconstructing water $\delta^{18}O$ values, for example by providing independent information on temperature (e.g., clumped isotopes; Huntington et al., 2010) and on unevaporated catchment water composition from triple-oxygen isotopes (Passey and Ji, 2019) or ^{13}C-excess (Horton and Oze, 2012). Licht et al. (2017) and VanDeVelde and Bowen (2014) used these methods to estimate ~1.5 km paleoelevation for the Baca Formation (~38 Ma) and 1–1.5 km mean hypsometric paleoelevation for the Flagstaff Formation (~50 Ma), respectively (**Figure 2**). Despite limitations, $\delta^{18}O_c$ values from CP Eocene north-western basins may record increased mean hypsometric elevation (**Figure 1A**), lake closures resulting from local topographic growth diverting flows, and southward progression of drainage integration (Davis et al., 2009).

Paleobotanical Thermometry-Based Paleoaltimetry

The steepest temperature gradients on Earth are vertical, making surface temperature proxies attractive paleoaltimeters. Proxies have been used to estimate depositional mean annual surface temperature (paleo-MAST), which may be combined with coeval near-sea-level temperature reference data and an estimated rate of temperature decrease with elevation ("lapse-rate") to infer paleoelevation.

Paleobotanical methods are perhaps the oldest and most widely used paleotemperature proxies (e.g., Bailey and Sinnott, 1915; Wolfe, 1979; Wolfe, 1994; Greenwood et al., 2004) and have been applied throughout the Cenozoic of North America (e.g., Retallack et al., 2004; Wing et al., 2005; Peppe et al., 2010). Bioclimatic proxies identify climate "envelopes" defined by the physical tolerances of sampled plant assemblages or their nearest living relatives (e.g., Mosbrugger and Utescher, 1997; Boyle et al., 2008; Thompson et al., 2012). Leaf physiognomic proxies are based on empirical correlations between temperature and physical properties of modern leaves, applied quantitatively to ancient floras using several different methods (e.g., Wolfe, 1993; Wilf, 1997; Spicer et al., 2009; Peppe et al., 2011). Paleobotanical proxies have been used widely and resulted in widely varying temperature and elevation reconstructions—as well as debate over when and where they are applicable in the geologic past (e.g., Kowalski and Dilcher, 2003; Royer and Wilf, 2006; Little et al., 2010; Peppe et al., 2010).

Studies of key Eocene-Oligocene sites (**Figure 1**) highlight this variability and permit several CP uplift histories (**Figure 2**; **Supplementary Table S1** and references therein). MAST estimates based on different methodologies applied to the same fossil assemblage span a ~13°C range for the Florissant flora, and other key floral sites at Creede and Pitch-Pinnacle have similarly wide ranges of temperature estimates (Leopold and Zaborac-Reed, 2019). Existing paleoelevation reconstructions based on paleobotanical-proxy temperatures and estimated lapse-rates (either study-specific lapse-rates, or using Wolfe, 1992a; Meyer, 1986; Meyer, 1992; discussed in *Challenges and Recent Advances* section) contain significant uncertainty—in some cases estimates range from <0.5 to >4 km for the same flora (e.g., Florissant; **Figure 2C**). Additional estimates calculated here using the refined Meyer (2007) approach (i.e., sea-level correction, local lapse-rate), based on paleobotanical-proxy temperature estimates that lack published paleoelevation evaluations, show similarly broad possibilities (**Supplementary Table S1**). This highlights the need for an evaluation of paleobotanical methods and their application, as well as the independent verification of temperature estimates and paleoelevation approaches.

Clumped Isotope Thermometry-Based Paleoaltimetry

Carbonate clumped isotope (Δ_{47}) thermometry (Ghosh et al., 2006; Eiler, 2007; Eiler, 2011) is commonly used for reconstructing surface temperature and paleoelevation (Huntington and Lechler, 2015). The Δ_{47} value refers to the ratio of "clumped" carbonate molecules containing heavy isotopes ^{13}C and ^{18}O, relative to the random distribution of isotopes among isotopologues. Heavy isotope clumping is directly temperature-dependent, and the carbonate temperature estimates ($T\Delta_{47}$) are thermodynamically based; thus, the method can be applied in the geologic past without concern for plant evolutionary changes or variable paleobotanical-proxy methods, provided authigenic carbonates are available and well preserved. Clumped isotope data also constrain water $\delta^{18}O$ values, and were used by Licht et al. (2017) to assess diagenesis and complement $\delta^{18}O$-based CP paleoaltimetry. $T\Delta_{47}$ for the Miocene lacustrine Bidahochi Formation (16–6 Ma), combined with $T\Delta_{47}$ of coeval near-sea-level deposits and a modern-lake-carbonate $T\Delta_{47}$ lapse-rate, estimated a paleoelevation of ~1.9 km, suggesting that near-modern surface elevations of the southern CP were attained by 16 Ma (**Figure 2**; Huntington et al., 2010), consistent with thermochronology data (Karlstrom et al., 2017).

DISCUSSION

Existing Estimates and Remaining Questions

Existing paleoelevation estimates are compatible with multi-stage, spatially differential uplift (**Figure 2**). Laramide-age deposits imply ≳1 km rise of the northwestern and southeastern CP by ~50 and ~38 Ma, respectively, consistent with paleo-canyon and paleo-relief studies. Geologic constraints from mid-Cenozoic (~38 Ma) deposits suggest half- to near-modern elevations in the northeastern CP (Steven and Ratté, 1965; Cather et al., 2012), consistent with some paleobotanical-

based estimates. Late-Cenozoic (~16–6 Ma) deposits suggest near-modern elevations in the southwestern CP. Altogether, this suggests half-modern surface elevations by ~38 Ma, and near-modern surface elevations by ~16–6 Ma. The timing supports hypothesized Laramide and mid-Cenozoic uplift mechanisms but does not preclude more recent modest surface uplift or subsidence, or rock uplift that is balanced by erosion (<6 Ma on the southern CP).

Except for some paleobotanical-based estimates in the southern Rocky Mountains, for all regions and time periods paleoaltimetry data suggest that elevations were likely lower than or close to modern; this is consistent with geodynamic models and other constraints (e.g., Cather et al., 2012) and implies multi-stage uplift without a complex late-Cenozoic uplift and subsidence (c.f., Wolfe, 1994). The following remain to be resolved: the 1) amount and spatio-temporal pattern of Laramide-related surface uplift; 2) rate and timing of southern Rocky Mountains uplift, with implications for drainage reversal; 3) magnitude of possible ≲16 Ma CP elevation change; and 4) cause of variation in paleobotanical paleoelevation estimates.

A Path Forward With Temperature-Based Paleoaltimetry

Challenges and Recent Advances

Temperature-based paleoaltimetry methodologies are challenging, but have advanced substantially in the last decade and have potential to help address these remaining questions. Multiple factors independent of elevation influence MAST, including short- (e.g., El-Nino Southern Oscillation) and long-term climate changes (e.g., Cenozoic cooling). Additionally, climate variability on decadal to millennial time scales may be integrated differently depending on the resolution of the proxy, and seasonal bias may impact different proxy types and settings (e.g., Burgener et al., 2016). MAST varies spatially due to local vegetation cover, aspect, precipitation regime, or proximity to water bodies/the ocean (e.g., Kelson et al., 2020), which can change with secular or periodic changes in climate—potentially complicating comparison of known near-sea-level deposits with contemporaneous inland deposits of unknown elevation. Workers have addressed such complications in various ways; e.g., Huntington et al. (2010) analyzed the Bouse Formation as a near-sea-level anchor in two sub-basins, and opted to use estimates from the warmer sub-basin farther from the coast instead of the marine-biased colder sub-basin proximal to the coast. Feng and Poulsen (2016) used paleoclimate simulations of Eocene North America to make improved predictions of contemporaneous sea-level temperatures for Cordilleran floral sites.

There have also been varied approaches to determining lapse-rates, such as applying the average modern global (5.5°C/km), regional (3°C/km; Wolfe, 1992b), or local (e.g., 5.9°C/km; Meyer, 1986) lapse rate for the CP (e.g., Meyer, 2007). Lapse-rate may change with aridity/humidity and latitude (e.g., Neumann, 1955; Li et al., 2015), leading to skepticism about whether modern or global lapse-rates are applicable to ancient reconstructions. Paleoclimate models have advanced significantly since initial rates were proposed and demonstrate that significant error can be generated by applying linear modern lapse-rates to ancient climates and paleogeographies; model-mediated lapse-rates should be a key component of future temperature-based paleoaltimetry studies (e.g., Feng and Poulsen, 2016; Farnsworth et al., 2021; Botsyun and Ehlers, 2021).

Confidence and accuracy in paleobotanical temperature estimates also have improved significantly. Advances include new standardizations in leaf physiognomic methods (e.g., Peppe et al., 2011), regional corrections and character re-evaluations in multivariate methods (e.g., Spicer et al., 2021), larger comparative datasets and refined statistical methods in bioclimatic analyses (e.g., Chevalier, 2019), and improvements in paleofloral identifications and taxonomy (e.g., Manchester, 2014). Additionally, the number of available CP-region collections has increased; local and regional stratigraphy refinements have improved context and relationships between existing floras (e.g., Prothero, 2008), allowing for subsampling and clear division in collection units; and geochronology has refined ages and durations of distinct floras (e.g., Lipman and Bachmann, 2015), allowing for higher-resolution reconstructions and more precise application of corrections/lapse-rates.

Challenges of $T\Delta_{47}$ paleoaltimetry include: the need for up to tens of milligrams of carbonate to achieve precise temperature estimates, and relatively large elevation uncertainties (~0.5 km; Huntington and Lechler, 2015); time integration during carbonate precipitation that can vary depending on climate (e.g., Kelson et al., 2020); and potential for carbonate temperature resetting by post-depositional diagenesis and heating (e.g., Huntington et al., 2011). Despite this, confidence and accuracy in Δ_{47} measurements have improved significantly in the last decade—with capability for higher sample throughput, more robust calibrations, new carbonate standards, and improved instrument precision and data normalization (e.g., Bernasconi et al., 2018; Petersen et al., 2019; Saenger et al., 2021). Evaluation of carbonate diagenesis also has improved (e.g., Lacroix and Niemi, 2019), and recent work indicates that the burial/exhumation history can be reconstructed from reset $T\Delta_{47}$ values with implications for paleotopography (e.g., Ning et al., 2019).

While transfer functions have been proposed to translate carbonate $T\Delta_{47}$ to MAST by assuming the seasonal timing of carbonate formation (Hren and Sheldon, 2012), using modern-carbonate-based lapse-rates may capture similar seasonal bias of ancient samples and reduce assumptions (e.g., Li et al., 2021). Quaternary lacustrine carbonates from southwest North America apparently record summer-biased temperature instead of MAST (Huntington et al., 2010). However, this bias may not hold for the paleo-record, particularly under Cretaceous and early Paleogene greenhouse climates. Novel isotopic approaches (triple-oxygen isotopes, ^{13}C-excess) can help correct for evaporative effects and estimate the unevaporated $\delta^{18}O$ of catchment waters, which may aid in constraining paleo-hydrology and provide context for estimating carbonate temperature seasonality and lapse-rates.

Future Opportunities

These advances can be leveraged to refine temperature-based proxy reconstructions and expand their use in the CP region. The region is well suited to temperature-based paleoaltimetry because its paleo-latitude has changed little for ~80 Ma; the mid-latitude setting allows for a steeper and better-constrained temperature-elevation gradient, thus minimizing elevation uncertainty; and target deposits are widespread in space and time and unlikely to have been deeply buried and diagenetically altered.

Essential to resolving paleobotanical estimates is independent comparison of carbonate $T\Delta_{47}$ and well-studied floral records from the same lacustrine formations (e.g., Florissant, Creede, Antero). Systematic comparison could expand the applicability and comparability of techniques across additional Laramide-age localities (**Figure 1A**) that may contain either carbonates or fossil floras (Claron, Flagstaff, Uinta, Piceance, and San Juan Basins), and potentially provide context for interpreting 14–19°C early calcite cements from the ~64 Ma southwestern CP Music Mountain Formation (Huntington et al., 2011). Additionally, there is opportunity to re-evaluate late-Cenozoic Bidahochi and Bouse Formation paleotemperatures (Huntington et al., 2010) with higher temporal/spatial resolution. In all cases, we recommend using paleoclimate model-mediated lapse-rates and sea-level corrections to minimize uncertainty and align methods for extrapolating temperature to elevation. Our analysis suggests that temperature-based paleoaltimetry methods are key to refining CP paleoelevation, with implications for understanding uplift mechanisms and CR drainage evolution.

AUTHOR CONTRIBUTIONS

EOH and KH (corresponding authors) conceived of the manuscript, with input from EGH. EOH did much of the literature review, first drafts of writing, and compilation of datasets. KH contributed to the writing and literature review on the Colorado Plateau, paleoaltimetry, and clumped isotopes. EGH contributed to the writing and literature review for paleobotanical methods. PSG drafted **Figure 1** and contributed to the writing and literature review of river profile modelling. CB drafted **Figure 2**. All authors provided input on data analysis, interpretation, and writing.

ACKNOWLEDGMENTS

We acknowledge funding from the University of Washington, Quaternary Research Center, and Endowed Professorship for the College of the Environment in Earth Systems. We thank Dave Sharrow, Elena Stiles, the IsoLab Clumped Group, Alex Lechler, Megan Mueller and Susannah Morey for insightful conversations. We thank Alexis Licht and Paolo Ballato for encouraging this submission and Associate Editor Heiko Pingel for editorial support and suggestions. We also thank Laura Crossey, Cari Johnson, and Richard Ott for their insightful comments that greatly improved this manuscript.

SUPPLEMENTARY MATERIAL

The Supplementary Material for this article can be found online at: https://www.frontiersin.org/articles/10.3389/feart.2021.648605/full#supplementary-material

REFERENCES

Allen, S. E., Lowe, A. J., Peppe, D. J., and Meyer, H. W. (2020). Paleoclimate and Paleoecology of the Latest Eocene Florissant flora of central Colorado, U.S.A. *Palaeogeogr. Palaeoclimatol. Palaeoecol.* 551, 109678. doi:10.1016/j.palaeo.2020.109678

Aslan, A., Karlstrom, K., Hood, W. C., Cole, R. D., Oesleby, T. W., Betton, C., et al. (2008). River Incision Histories of the Black Canyon of the Gunnison and Unaweep Canyon: Interplay between Late Cenozoic Tectonism, Climate Change, and Drainage Integration in the Western Rocky Mountains. *GSA Field Guide 10: Roaming the Rocky Mountains and Environs: Geological Field Trips*. Colorado: Geological Society of America, 175–202.doi:10.1130/2008.fld010(09)

Axelrod, D. I. (1987). *The Late Oligocene Creede flora*. Colorado: University of California Press (LosAngeles, CA), 235.

Axelrod, D. I., and Bailey, H. P. (1976). Tertiary Vegetation, Climate, and Altitude of the Rio Grande Depression, New Mexico-Colorado. *Paleobiology* 2, 235–254. doi:10.1017/s0094837300004814

Axelrod, D. I. (1998). The Oligocene Haynes Flora of Eastern Idaho. Colorado: University of California Publications *Geol. Sci.* 143, 1–235.

Bailey, I. W., and Sinnott, E. W. (1915). A Botanical index of Cretaceous and Tertiary Climates. *Science* 41, 831–834. doi:10.1126/science.41.1066.831

Baumgartner, K. A., and Meyer, H. W. (2014). Coexistence Climate Analysis of the Late Eocene Florissant Flora, *Colorado. GSA Abstracts with Programs* 490, 46.

Beard, L. S., Karlstrom, K. E., Young, R. A., and Billingsley, G. H. (2011). in C Revolution 2—Origin and evolution of the Colorado River system, workshop abstracts: U.S. Geological Survey Open-File Report 2011–1210, 300p., 2011 Available at https://pubs.usgs.gov/of/2011/1210/ (Accessed December 16, 2020).

Bernasconi, S. M., Müller, I. A., Bergmann, K. D., Breitenbach, S. F. M., Fernandez, A., Hodell, D. A., et al. (2018). Reducing Uncertainties in Carbonate Clumped Isotope Analysis through Consistent Carbonate-Based Standardization. *Geochem. Geophys. Geosyst.* 19, 2895–2914. doi:10.1029/2017GC007385

Bird, P. (1979). Continental Delamination and the Colorado Plateau. *J. Geophys. Res.* 84, 7561–7571. doi:10.1029/JB084iB13p07561

Blasch, K. W., and Bryson, J. R. (2007). Distinguishing Sources of Ground Water Recharge by Using ?^{2}H and ?^{18}O. *Ground Water* 45, 294–308. doi:10.1111/j.1745-6584.2006.00289.x

Bondre, N. R. (2003). Analysis of Vesicular Basalts and Lava Emplacement Processes for Application as a Paleobarometer/Paleoaltimeter: A Discussion. *J. Geology.* 111, 499–502. doi:10.1086/375279

Botsyun, S., and Ehlers, T. A. (2021). How Can Climate Models Be Used in Paleoelevation Reconstructions?. *Front. Earth Sci.*9, 624542. doi:10.3389/feart.2021.624542

Boyle, B., Meyer, H. W., Enquist, B., and Salas, S. (2008). Higher Taxa as Paleoecological and. Paleoclimatic Indicators: A Search for the Modern Analog of the Florissant Fossil flora. *Geol. S. Am. S.* 435, 33–51. doi:10.1130/2008.2435(03)

Breecker, D. O., Sharp, Z. D., and McFadden, L. D. (2009). Seasonal Bias in the Formation and Stable Isotopic Composition of Pedogenic Carbonate in Modern Soils from central New Mexico, USA. *Geol. Soc. America Bull.* 121, 630–640. doi:10.1130/B26413.1

Burgener, L., Huntington, K. W., Hoke, G. D., Schauer, A., Ringham, M. C., Latorre, C., et al. (2016). Variations in Soil Carbonate Formation and Seasonal Bias over >4 Km of Relief in the Western Andes (30°S) Revealed by Clumped Isotope Thermometry. *Earth Planet. Sci. Lett.* 441, 188–199. doi:10.1016/j.epsl.2016.02.033

Carrapa, B., DeCelles, P. G., and Romero, M. (2019). Early Inception of the Laramide Orogeny in Southwestern Montana and Northern Wyoming: Implications for Models of Flat-Slab Subduction. *J. Geophys. Res. Solid Earth* 124, 2102–2123. doi:10.1029/2018JB016888

Cather, S. M., Chapin, C. E., and Kelley, S. A. (2012). Diachronous Episodes of Cenozoic Erosion in Southwestern North America and Their Relationship to Surface Uplift, Paleoclimate, Paleodrainage, and Paleoaltimetry. *Geosphere* 8, 1177–1206. doi:10.1130/GES00801.1

Chevalier, M. (2019). Enabling Possibilities to Quantify Past Climate from Fossil Assemblages at Aglobal Scale. *Glob. Planet. Change* 175, 27–35. doi:10.3917/dunod.cheva.2019.01

Cook, K. L., Whipple, K. X., Heimsath, A. M., and Hanks, T. C. (2009). Rapid Incision of the Colorado River in Glen Canyon - Insights from Channel Profiles, Local Incision Rates, and Modeling of Lithologic Controls. *Earth Surf. Process. Landforms* 34 (7), 994–1010. doi:10.1002/esp.1790

Crow, R., Karlstrom, K., Asmerom, Y., Schmandt, B., Polyak, V., and DuFrane, S. A. (2011). Shrinking of the Colorado Plateau via Lithospheric Mantle Erosion: Evidence from Nd and Sr Isotopes and Geochronology of Neogene Basalts. *Geology* 39, 27–30. doi:10.1130/G31611.1

Crow, R., Karlstrom, K., Darling, A., Crossey, L., Polyak, V., Granger, D., et al. (2014). Steady Incision of Grand Canyon at the Million Year Timeframe: A Case for Mantle-Driven Differential Uplift. *Earth Planet. Sci. Lett.* 397, 159–173. doi:10.1016/j.epsl.2014.04.020

Crow, R. S., Howard, K. A., Beard, L. S., Pearthree, P. A., House, P. K., Karlstrom, K. E., et al. (2019). Insights into post-Miocene Uplift of the Western Margin of the Colorado Plateau from the Stratigraphic Record of the Lower Colorado River. *Geosphere* 15, 1826–1845. doi:10.1130/GES02020.1

Crow, R. S., Schwing, J., Karlstrom, K. E., Heizler, M., Pearthree, P. A., House, P. K., et al. (2021). Redefining the Age of the Lower Colorado River, Southwestern United States. *Geology* 49, 7. doi:10.1130/G48080.1

Dansgaard, W. (1964). Stable Isotopes in Precipitation. *Tellus* 16, 436–468. doi:10.3402/tellusa.v16i4.8993

Darling, A., and Whipple, K. (2015). Geomorphic Constraints on the Age of the Western Grand Canyon. *Geosphere* 11, 958–976. doi:10.1130/GES01131.1

Davis, S. J., Mulch, A., Carroll, A. R., Horton, T. W., and Chamberlain, C. P. (2006). Paleogene Landscape Evolution of the central North American Cordillera: Developing Topography and Hydrology in the Laramide Foreland. *Geol. Soc. America Bull.* preprint, 1–116. doi:10.1130/B26308.1

Davis, S. J., Wiegand, B. A., Carroll, A. R., and Chamberlain, C. P. (2008). The Effect of Drainage Reorganization on Paleoaltimetry Studies: An Example from the Paleogene Laramide Foreland. *Earth Planet. Sci. Lett.* 275, 258–268. doi:10.1016/j.epsl.2008.08.009

Donahue, M., Karlstrom, K. E., Aslan, A., Darling, A., Granger, D., Wan, E., et al. (2013). Incision History of the Black Canyon of Gunnison, Colorado, over the Past ~1 ma Inferred from Dating of Fluvial Gravel Deposits. *Geosphere* 9, 815–826. doi:10.1130/GES00847.1

Douglas, M. W., Maddox, R. A., Howard, K., and Reyes, S. (1993). The Mexican Monsoon. *J. Clim.* 6, 1665–1677. doi:10.1175/1520-0442(1993)006<1665:TMM>2.0.CO;2

Eiler, J. M. (2007). "Clumped-isotope" Geochemistry-The Study of Naturally-Occurring, Multiply-Substituted Isotopologues. *Earth Planet. Sci. Lett.* 262, 309–327. doi:10.1016/j.epsl.2007.08.020

Eiler, J. M. (2011). Paleoclimate Reconstruction Using Carbonate Clumped Isotope Thermometry. *Quat. Sci. Rev.* 30, 3575–3588. doi:10.1016/j.quascirev.2011.09.001

Farnsworth, A., Valdes, P. J., Spicer, R. A., Ding, L., Witkowski, C., Lauretano, V., et al. (2021). Paleoclimate Model-Derived thermal Lapse Rates: Towards Increasing Precision in Paleoaltimetry Studies. *Earth Planet. Sci. Lett.* 564, 116903. doi:10.1016/j.epsl.2021.116903

Feng, R., and Poulsen, C. J. (2016). Refinement of Eocene Lapse Rates, Fossil-Leaf Altimetry, and North American Cordilleran Surface Elevation Estimates. *Earth Planet. Sci. Lett.* 436, 130–141. doi:10.1016/j.epsl.2015.12.022

Flowers, R. M., and Farley, K. A. (2012). Apatite 4He/3He and (U-Th)/He Evidence for an Ancient Grand Canyon. *Science* 338, 1616–1619. doi:10.1126/science.1229390

Flowers, R. M., and Farley, K. A. (2013). Response to Comments on "Apatite 4He/3He and (U-Th)/He Evidence for an Ancient Grand Canyon". *Science* 340, 143. doi:10.1126/science.1234203

Flowers, R. M., Wernicke, B. P., and Farley, K. A. (2008). Unroofing, Incision, and Uplift History of the Southwestern Colorado Plateau from Apatite (U-Th)/He Thermochronometry. *Geol. Soc. America Bull.* 120, 571–587. doi:10.1130/B26231.1

Ghosh, P., Adkins, J., Affek, H., Balta, B., Guo, W., Schauble, E. A., et al. (2006). 13C-18O Bonds in Carbonate Minerals: A New Kind of Paleothermometer. *Geochimica et Cosmochimica Acta* 70, 1439–1456. doi:10.1016/j.gca.2005.11.014

Greenwood, D. R., Wilf, P., Wing, S. L., and Christophel, D. C. (2004). Paleotemperature Estimation Usingleaf-Margin Analysis: Is Australia Different? *Palaios* 19, 129–142. doi:10.4324/9780203500804

Gregory, K. M., and Chase, C. G. (1992). Tectonic Significance of Paleobotanically Estimated Climate and Altitude of the Late Eocene Erosion Surface, Colorado. *Geology* 20, 581–585. doi:10.1130/0091-7613(1992)020<0581:TSOPEC>2.3.CO;2

Gregory, K. M., and McIntosh, W. C. (1996). Paleoclimate and Paleoelevation of the Oligocene Pitch-Pinnacle flora, Sawatch Range. *Colo. GSA Bull.* 108, 545–561. doi:10.1130/0016-7606(1996)108<0545:PAPOTO>2.3.CO;2

Gregory, K. M. (1994). Paleoclimate and Paleoelevation of the 35 Ma Florissant flora. *Front. Range, Coloradopaleoclimates* 1, 23–57.

Gregory-Wodziki, K. M. (2001). "Paleoclimatic Implications of Tree-Ring Growth Characteristics of 34.1 Ma Sequoioxylon Pearsallii from Florissant, Colorado," in *Fossil Flora and Stratigraphy of the Florissant Formation, Colorado*. Editors E. Evanoff, K. M. Gregory-Wodziski, and K. R. Johnson (Denver, CO: Proceedings of the Denver Museum of Nature and Science Series), 4, 163–186.

Hamblin, W. K., Damon, P. E., and Bull, W. B. (1981). Estimates of Vertical crystal Strain Rates Alongthe Western Margins of the Colorado Plateau. *Geology* 9 (7), 293–298. doi:10.1130/0091-7613(1981)9<293:EOVCSR>2.0.CO;2

Hernández-Uribe, D., and Palin, R. M. (2019). Catastrophic Shear-Removal of Subcontinental Lithospheric Mantle beneath the Colorado Plateau by the Subducted Farallon Slab. *Sci. Rep.* 9, 1–10. doi:10.1038/s41598-019-44628-y

Hill, C. A., and Polyak, V. J. (2020). A Karst Hydrology Model for the Geomorphic Evolution of Grand Canyon, Arizona, USA. *Earth-Science Rev.* 208, 103279. doi:10.1016/j.earscirev.2020.103279

Hill, C. A., Polyak, V. J., Asmerom, Y., and P. Provencio, P. (2016). Constraints on a Late Cretaceous Uplift, Denudation, and Incision of the Grand Canyon Region, Southwestern Colorado Plateau, USA, from U-Pb Dating of Lacustrine limestone. *Tectonics* 35, 896–906. doi:10.1002/2016TC004166

Horton, T. W., and Oze, C. (2012). Are Two Elements Better Than One? Dual Isotope-Ratio Detrending of Evaporative Effects on lake Carbonate Paleoelevation Proxies. *Geochem. Geophys. Geosyst.* 13 (6), Q0AK05. doi:10.1029/2012GC004132

Hren, M. T., and Sheldon, N. D. (2012). Temporal Variations in lake Water Temperature: Paleoenvironmental Implications of lake Carbonate δ18O and Temperature Records. *Earth Planet. Sci. Lett.* 337-338, 77–84. doi:10.1016/j.epsl.2012.05.019

Hunt, C. B. (1956). Cenozoic Geology of the Colorado Plateau. in (USGS Numbered Series No. 279). *Professional Paper* 279, 103. doi:10.3133/pp279

Huntington, K. W., Budd, D. A., Wernicke, B. P., and Eiler, J. M. (2011). Use of Clumped-Isotope Thermometry to Constrain the Crystallization Temperature of Diagenetic Calcite. *J. Sediment. Res.* 81, 656–669. doi:10.2110/jsr.2011.51

Huntington, K. W., and Lechler, A. R. (2015). Carbonate Clumped Isotope Thermometry in continental Tectonics. *Tectonophysics* 647-648, 1–20. doi:10.1016/j.tecto.2015.02.019

Huntington, K. W., Wernicke, B. P., and Eiler, J. M. (2010). Influence of Climate Change and Uplift on Colorado Plateau Paleotemperatures from Carbonate Clumped Isotope Thermometry. *Tectonics* 29 (3), TC3005. doi:10.1029/2009TC002449

Ibarra, D. E., Kukla, T., Methner, K. A., Mulch, A., and Chamberlain, C. P. (2021). Reconstructing Past Elevations From Triple Oxygen Isotopes of Lacustrine Chert: Application to the Eocene Nevadaplano, Elko Basin, Nevada, United States. *Front. Earth Sci.*9, 628868. doi:10.3389/feart.2021.628868

Karlstrom, K. E., Crossey, L. J., Embid, E., Crow, R., Heizler, M., Hereford, R., et al. (2017). Cenozoic Incision History of the Little Colorado River: Its Role in Carving Grand Canyon and Onset of Rapid Incision in the Past Ca. 2 Ma in the Colorado River System. *Geosphere* 13, 49–81. doi:10.1130/GES01304.1

Karlstrom, K. E., Crossey, L. J., Humphreys, E., Shuster, D., and Whipple, K. (2019). AGE AND CARVING OF GRAND CANYON TOWARDS A

RESOLUTION OF 150 yearS OF DEBATE. GSA Annual Meeting in Phoenix. USA-: Arizona, September 22–25, 2019. doi:10.1130/abs/2019am-338944

Karlstrom, K. E., Crow, R., Crossey, L. J., Coblentz, D., and Van Wijk, J. W. (2008). Model for Tectonically Driven Incision of the Younger Than 6 Ma Grand Canyon. *Geol* 36, 835–838. doi:10.1130/G25032A.1

Karlstrom, K. E., Jacobson, C. E., Sundell, K. E., Eyster, A., Blakey, R., Ingersoll, R. V., et al. (2020). Evaluating the Shinumo-Sespe Drainage Connection: Arguments against the "old" (70-17 Ma) Grand Canyon Models for Colorado Plateau Drainage Evolution. *Geosphere* 16, 1425–1456. doi:10.1130/GES02265.1

Karlstrom, K. E., Lee, J. P., Kelley, S. A., Crow, R. S., Crossey, L. J., Young, R. A., et al. (2014). Formation of the Grand Canyon 5 to 6 Million Years Ago through Integration of Older Palaeocanyons. *Nat. Geosci* 7, 239–244. doi:10.1038/ngeo2065

Kelson, J. R., Huntington, K. W., Breecker, D. O., Burgener, L. K., Gallagher, T. M., Hoke, G. D., et al. (2020). A Proxy for All Seasons? A Synthesis of Clumped Isotope Data from Holocene Soil Carbonates. *Quat. Sci. Rev.* 234, 106259. doi:10.1016/j.quascirev.2020.106259

Kim, S.-T., and O'Neil, J. R. (1997). Equilibrium and Nonequilibrium Oxygen Isotope Effects in Synthetic Carbonates. *Geochimica et Cosmochimica Acta* 61, 3461–3475. doi:10.1016/S0016-7037(97)00169-5

Kowalski, E. A., and Dilcher, D. L. (2003). Warmer Paleotemperatures for Terrestrial Ecosystems. *Natl. Acad. Sci. USA*, 100, 167–170. doi:10.1073/pnas.232693599

Lacroix, B., and Niemi, N. A. (2019). Investigating the Effect of Burial Histories on the Clumped Isotope Thermometer: An Example from the Green River and Washakie Basins, Wyoming. *Geochimica et Cosmochimica Acta* 247, 40–58. doi:10.1016/j.gca.2018.12.016

Lazear, G., Karlstrom, K., Aslan, A., and Kelley, S. (2013). Denudation and Flexural Isostatic Response of the Colorado Plateau and Southern Rocky Mountains Region since 10 Ma. *Geosphere* 9, 792–814. doi:10.1130/GES00836.1

Lee, J. P., Stockli, D. F., Kelley, S. A., Pederson, J. L., Karlstrom, K. E., and Ehlers, T. A. (2013). New Thermochronometric Constraints on the Tertiary Landscape Evolution of the central and Eastern Grand Canyon, Arizona. *Geosphere* 9, 216–228. doi:10.1130/GES00842.1

Leopold, E. B., and Claypoole, S. T. (2001). "Florissant Leaf and Pollen Floras of Colorado Compared Climatic Implications," in *Fossil flora and Stratigraphy of the Florissant Formation, Colorado*. Editors E. Evanoff, K. M. Gregory-Wodzicki, and K. Johnson (Denver, CO): Denver Museum of Nature and Science), 17–70.

Leopold, E. B., Manchester, S., and Meyer, H. W. (2008). "Phytogeography of the Late EoceneFlorissant flora Reconsidered,". *Paleontology of the Upper Eocene Florissant Formation*. Editors H. W. Meyer and D. M. Smith (Colorado: Geological Society of America Special Paper), 435, 53–70. doi:10.1130/2008.2435(04)

Leopold, E. B., and Zaborac-Reed, S. (2019). Pollen Evidence of Floristic Turnover Forced by Cool Aridity during the Oligocene in Colorado. *Geosphere* 15, 254–294. doi:10.1130/GES01689.1

Leopold, E., and Zaborac-Reed, S. (2014). "Biogeographic History of Abies bracteata (D. Don) A. Poit. in the Western United States,". *Paleobotany and Biogeography*. Editors W. D. Stevens, O. M. Montiel, and P. H. Raven (St. Louis, MO: Missouri Botanical Garden Press), 252–286.

Li, H., Liu, X., Arnold, A., Elliott, B., Flores, R., Kelley, A. M., et al. (2021). Mass 47 Clumped Isotope Signatures in Modern Lacustrine Authigenic Carbonates in Western China and Other Regions and Implications for Paleotemperature and Paleoelevation Reconstructions. *Earth Planet. Sci. Lett.* 562, 116840. doi:10.1016/j.epsl.2021.116840

Li, Y., Zeng, Z., Zhao, L., and Piao, S. (2015). Spatial Patterns of Climatological Temperature Lapse Rate in mainland China: A Multi-Time Scale Investigation. *J. Geophys. Res. Atmos.* 120, 2661–2675. doi:10.1002/2014JD022978

Libarkin, J. C., and Chase, C. G. (2003). Timing of Colorado Plateau Uplift: Initial Constraints from Vesicular basalt-derived Paleoelevations: Comment and ReplyCOMMENT. *Geology* 31, 191. doi:10.1130/0091-7613(2003)031<0191:TOCPUI>2.0.CO;2

Licht, A., Quade, J., Kowler, A., de los Santos, M., Hudson, A., Schauer, A., et al. (2017). Impact of the North American Monsoon on Isotope Paleoaltimeters: Implications for the Paleoaltimetry of the American Southwest. *Am. J. Sci.* 317, 1–33. doi:10.2475/01.2017.01

Lipman, P. W., and Bachmann, O. (2015). Ignimbrites to Batholiths: Integrating Perspectives from Geological, Geophysical, and Geochronological Data. *Geosphere*, 11, 705–743. doi:10.1130/GES01091.1

Little, S. A., Kembel, S. W., and Wilf, P. (2010). Paleotemperature Proxies from Leaf Fossils Reinterpreted in Light of Evolutionary History. *PLoS One* 5, E15161. doi:10.1017/cbo9780511709371

Longwell, C. R. (1946). How Old Is the Colorado River? *Am. J. Sci.* 244, 817–835. doi:10.2475/ajs.244.12.817

Lucchitta, I. (1972). Early History of the Colorado River in the Basin and Range Province. *GSA Bull.* 83, 1933–1948. doi:10.1130/0016-7606(1972)83[1933:EHOTCR]2.0.CO;2

MacGinitie, H. D. (1953). Fossil Plants of the Florissant Beds, Colorado. *Carnegie Wash. Pub.* 599, 1–188.

MacGinitie, H. D. (1969). *The Eocene green River flora of Northwestern Colorado and Northeastern*. Utah. University of California Press. doi:10.1037/e463452008-093

Manchester, S. R. (2014). Revisions to Roland Brown's North American Paleocene flora. *Acta Musei. Nationalis. Pragae, Series B-Historia. Naturalis* 70, 153–210. doi:10.14446/AMNP.2014.153

McQuarrie, N., and Chase, C. G. (2000). Raising the Colorado Plateau. *Geology* 28, 91–94. doi:10.1130/0091-7613(2000)028<0091:RTCP>2.0.CO;2

McQuarrie, N., and Wernicke, B. P. (2005). An Animated Tectonic Reconstruction of Southwestern North America since 36 Ma. *Geosphere* 1, 147–172. doi:10.1130/GES00016.1

Meyer, H. W. (2007). A Review of Paleotemperature Lapse Rate Methods for Estimating Paleoelevation from Fossil Floras. *Rev. Mineralogy Geochem.* 66, 155–171. doi:10.2138/rmg.2007.66.6

Meyer, H. W. (1986). *An Evaluation of the Methods for Estimating Paleoaltitudes Using Tertiary Floras from the Rio Grande Rift Vicinity*. in *New Mexico and Colorado*(Oligocene Mountain Climates) (Ph.D) (University of California, Berkeley, United States – California.)

Meyer, H. W. (1992). Lapse Rates and Other Variables Applied to Estimating Paleoaltitudes from Fossil, *Floras. Palaeogeogr. Palaeocl.* 99, 71–99. doi:10.3386/w4197

Mosbrugger, V., and Utescher, T. (1997). The Coexistence Approach – A Method for Quantitative Reconstructions of Tertiary Terrestrial Paleoclimate Data Using Plant Fossils. *Palaeogeogr. Palaeocl.*, 134, 203–214. doi:10.1016/S0031-0182(96)00154-X

Moucha, R., Forte, A. M., Rowley, D. B., Mitrovica, J. X., Simmons, N. A., and Grand, S. P. (2009). Deep Mantle Forces and the Uplift of the Colorado Plateau. *Geophys. Res. Lett.* 36 (19), L19310. doi:10.1029/2009GL039778

Murray, K. E., Reiners, P. W., and Thomson, S. N. (2016). Rapid Pliocene-Pleistocene Erosion of the central Colorado Plateau Documented by Apatite Thermochronology from the Henry Mountains. *Geology* 44, 483–486. doi:10.1130/G37733.1

Nations, D., Nations, J. D., and Eaton, J. G. (1991). *Stratigraphy, Depositional Environments, and Sedimentary Tectonics of the Western MarginCretaceous Western Interior Seaway*. Colorado: Geological Society of America.

Neumann, J. (1955). Latitudinal Variation of Tropospheric Temperature Lapse Rate. *Arch. Met. Geoph. Biokl. A.* 8, 351–353. doi:10.1007/BF02247093

Ning, Z., Zhang, L., Huntington, K. W., Wang, C., Dai, J., Han, Z., et al. (2019). The Burial and Exhumation History of the Liuqu Conglomerate in the Yarlung Zangbo Suture Zone, Southern Tibet: Insights from Clumped Isotope Thermometry. *J. Asian Earth Sci.* 174, 205–217. doi:10.1016/j.jseaes.2018.12.009

Nuccio, V. F., and Condon, S. M. (1996). Burial and thermal History of the Paradox Basin, Utah and Colorado, and Petroleum Potential of the Middle Pennsylvanian Paradox Formation. *U.S. Geological Survey Bulletin 2000-O.* 57–76.

Ott, R. F., Whipple, K. X., and van Soest, M. (2018). Incision History of the Verde Valley Region and Implications for Uplift of the Colorado Plateau (central Arizona). *Geosphere* 14, 1690–1709. doi:10.1130/GES01640.1

Passey, B. H., and Ji, H. (2019). Triple Oxygen Isotope Signatures of Evaporation in lake Waters and Carbonates: A Case Study from the Western United States. *Earth Planet. Sci. Lett.* 518, 1–12. doi:10.1016/j.epsl.2019.04.026

Pederson, J. L., and Tressler, C. (2012). Colorado River Long-Profile Metrics, Knickzones and Their Meaning. *Earth Planet. Sci. Lett.* 345-348, 171–179. doi:10.1016/j.epsl.2012.06.047

Peppe, D. J., Royer, D. L., Cariglino, B., Oliver, S. Y., Newman, S., Leight, E., et al. (2011). Sensitivity of leaf size and shape to climate: Global patterns and paleoclimatic applications. *New Phytol.* 190, 724–739. doi:10.1037/t44508-000

Peppe, D. J., Royer, D. L., Wilf, P., and Kowalski, E. A. (2010). Quantification of Large Uncertainties in Fossil Leaf Paleoaltimetry. *Tectonics* 29 (3), TC3015. doi:10.1029/2009TC002549

Petersen, S. V., Defliese, W. F., Saenger, C., Daëron, M., Huntington, K. W., John, C. M., et al. (2019). Effects of Improved 17 O Correction on Interlaboratory Agreement in Clumped Isotope Calibrations, Estimates of Mineral-Specific Offsets, and Temperature Dependence of Acid Digestion Fractionation. *Geochem. Geophys. Geosyst.* 20, 3495–3519. doi:10.1029/2018GC008127

Polyak, V., Hill, C., and Asmerom, Y. (2008). Age and Evolution of the Grand Canyon Revealed by U-Pb Dating of Water Table-type Speleothems. *Science* 319, 1377–1380. doi:10.1126/science.1151248

Porter, R., Hoisch, T., and Holt, W. E. (2017). The Role of Lower-Crustal Hydration in the Tectonic Evolution of the Colorado Plateau. *Tectonophysics* 712-713, 221–231. doi:10.1016/j.tecto.2017.05.025

Potochnik, A. R., Beard, L. S., Karlstrom, K. E., Young, R. A., and Billingsley, G. H. (2011). Ancestral Colorado River Exit from the Plateau Province—Salt River Hypothesis. *CRevolution2: US Geological Survey Open-File Report* 1210, 222–231.

Potochnik, A. R., Young, R. A., and Spamer, E. E. (2001). *Paleogeomorphic Evolution of the Salt River region*: *Implications for Cretaceous-Laramide Inheritance for Ancestral Colorado River Drainage. Colorado River Origin and Evolution*: Grand Canyon, Arizona. Grand Canyon Association, 17–24.

Prothero, D. R. (2008). Magnetic Stratigraphy of the Eocene-Oligocene Floral Transition in westernPaleontology of the Upper Eocene Florissant Formation North America. *Paleontology of the Upper Eocene Florissant Formation, Colorado* 435, 71. doi:10.1130/2008.2435(05)

Ranney, W. (2014). A Pre-21st century History of Ideas on the Origin of the Grand Canyon. *Geosphere* 10, 233–242. doi:10.1130/GES00960.1

Raynolds, R. G., and Johnson, K. R. (2003). Synopsis of the Stratigraphy and Paleontology of the Uppermost Cretaceous and Lower Tertiary Strata in the Denver Basin, Colorado. *Rocky Mountain Geology.* 38, 171–181. doi:10.2113/gsrocky.38.1.171

Reiners, P. W., and Shuster, D. L. (2009). Thermochronology and Landscape Evolution. *Phys. Today* 62, 31–36. doi:10.1063/1.3226750

Orr, G. J., Prothero, W. N., Duncan, D. R., Kester, R. A., Ambers, P. R., and au, C. P. (2004). Eocene-Oligocene Extinction and Paleoclimatic Change Near Eugene, Oregon. *Geol. Soc. America Bull.* 116, 817–839. doi:10.1130/b25281.1

Roberts, G. G., White, N. J., Martin-Brandis, G. L., and Crosby, A. G. (2012). An Uplift History of the Colorado Plateau and its Surroundings from Inverse Modeling of Longitudinal River Profiles. *Tectonics* 31 (4), TC4022. doi:10.1029/2012TC003107

Rowley, D. B., and Garzione, C. N. (2007). Stable Isotope-Based Paleoaltimetry. *Annu. Rev. Earth Planet. Sci.* 35, 463–508. doi:10.1146/annurev.earth.35.031306.140155

Royer, D. L., and Wilf, P. (2006). Why Do Toothed Leaves Correlate with Cold Climates? Gas Exchange Atleaf Margins Provides New Insights into a Classic Paleotemperature Proxy. *Int. J. Plant Sci.* 167, 11–18.

Ryb, U., Lloyd, M. K., and Eiler, J. M., (2021). Carbonate Clumped Isotope Constraints on Burial, Uplift and exhumation histories of the Colorado Plateau. *Earth Planet. Sci. Lett.*, 566, 116964. doi:10.1016/j.epsl.2021.116964

Saenger, C. P., Schauer, A. J., Heitmann, E. O., Huntington, K. W., and Steig, E. J. (2021). How 17O excessIn Clumped Isotope Reference-Frame Materials and ETH Standards Affects Reconstructed Temperature. *Chem. Geology.*, 563, 120059. doi:10.1007/s11002-021-09561-z

Sahagian, D. L., Proussevitch, A. A., and Carlson, W. D., (2002a). Analysis of Vesicular Basalts and Lava Emplacement Processes for Application as a Paleobarometer/Paleoaltimeter. *J. Geology.* 110, 671–685. doi:10.1086/342627

Sahagian, D., Proussevitch, A., and Carlson, W., (2002b). Timing of Colorado Plateau Uplift: Initial Constraints from Vesicular basalt-derived Paleoelevations. *Geology* 30, 807–810. doi:10.1130/0091-7613(2002)030<0807:TOCPUI>2.0.CO;2

Sahagian, D., Proussevitch, A., and Carlson, W. (2003). Analysis of Vesicular Basalts and Lava Emplacement Processes for Application as a Paleobarometer/Paleoaltimeter: A Reply. *J. Geology.* 111, 502–504. doi:10.1086/375278

Schwanghart, W., and Scherler, D. (2020). Divide Mobility Controls Knickpoint Migration on the RoanPlateau (Colorado, USA). *Geology* 48 (7), 698–702. doi:10.1130/G47054.1

Spicer, R. A., Su, T., Valdes, P. J., Farnsworth, A., Wu, F. X., Shi, G., et al. (2021). The Topographic Evolution of the Tibetan Region as Revealed by Palaeontology. *Palaeobiodiversity and Palaeoenvironments* 101 (1), 213–243. doi:10.1007/s12549-020-00452-1

Spicer, R. A., Valdes, P. J., Spicer, T. E. V., Craggs, H. J., Srivastava, G., Mehrotra, R. C., et al. (2009). New Developments in CLAMP: Calibration Using Global Gridded Meteorological Data: Palaeogeogr. *Palaeocl* 283, 91–98. doi:10.1016/j.palaeo.2009.09.009

Steven, T. A., and Ratte, J. C. (1965). Geology and Structural Control of Ore Deposition in the Creede District, San Juan Mountains, Colorado. *Professional Paper. U.S. G.P.O.* 487, 95. doi:10.3133/pp487

Thompson, R., Anderson, K., Pelltier, R., Strickland, L., Bartlein, P., and Shafer, S. (2012). Quantitative estimationOf Climatic Parameters from Vegetation Data in North America by the Mutual Climatic Range Technique. *Quat. Sci. Rev.*, 51, 18–39. doi:10.3133/pp1650f

VanDeVelde, J. H., and Bowen, G. J. (2014). Isotope Hydrology of Early Paleogene Lake Flagstaff, central Utah: Implications for Cordilleran Evolution. *Am. J. Sci.* 314, 1436–1461. doi:10.2475/10.2014.02

Walk, C. J., Karlstrom, K. E., Crow, R. S., and Heizler, M. T. (2019). Birth and Evolution of the Virgin River Fluvial System: ~1 km of post–5 ma Uplift of the Western Colorado Plateau. *Geosphere*, 15(3), 759–782.

Wilf, P. (1997). When Are Leaves Good Thermometers? A New Case for Leaf Margin Analysis. *Palaeobiology*, 23, 373–390.

Wing, S. L., Harrington, G. J., Smith, F. A., Bloch, J. I., Boyer, D. M., and Freeman, K. H. (2005). Transient floral Change and Rapid Global Warming at the Paleocene-Eocene Boundary. *Science* 310, 993–996. doi:10.1126/science.1116913

Winn, C., Karlstrom, K. E., Shuster, D. L., Kelley, S., and Fox, M. (2017). 6 Ma Age of Carving Westernmost Grand Canyon: Reconciling Geologic Data with Combined AFT, (U-Th)/He, and 4He/3He Thermochronologic Data. *Earth Planet. Sci. Lett.* 474, 257–271. doi:10.1016/j.epsl.2017.06.051

Wolfe, J. A. (1993). A Method of Obtaining Climatic Parameters from Leaf Assemblages. *USGS Bull* 2040, 1–73. doi:10.1117/12.1438371–73

Wolfe, J. A., (1992a). An Analysis of Present-Day Terrestrial Lapse Rates in the Western Conterminous United States and Their Significance to Paleoaltitudinal Estimates: U.S. *Geol. Surv. Bull.* 1964, 35. doi:10.3133/b1964

Wolfe, J. A., (1992b). "Climatic, Floristic, and Vegetational Changes Near the Eocene/Oligocene Boundary in North America,". *Late Eocene-Oligocene Climatic and Biotic Evolution*. Editors D. R. Prothero and W. A. Berggren (Princeton, NJ: Princeton University Press), 421–436.

Wolfe, J. A., Forest, C. E., and Molnar, P. (1998). Paleobotanical Evidence of Eocene and Oligocene Paleoaltitudes in Midlatitude Western North America. *GSA Bull.* 110, 664–678. doi:10.1130/0016-7606(1998)110<0664:PEOEAO>2.3.CO;2

Wolfe, J. A. (1979). Temperature Parameters of Humid to Mesic Forests of Eastern Asia and Relation to Forests of Other Regions in the Northern Hemisphere and Australasia. *USGS Bull.* 1964, 1–35. doi:10.3133/pp1106

Wolfe, J. A., and Schorn, H. E. (1989). Paleoecologic, Paleoclimatic, and Evolutionary Significance of the Oligocene Creede flora, Colorado. *Paleobiology* 15, 180–198. doi:10.1017/s0094837300009350

Wolfe, J. A. (1994). Tertiary Climatic Changes at Middle Latitudes of Western North America. *Palaeogeogr. Palaeoclimatol. Palaeoecol.* 108, 195–205. doi:10.1016/0031-0182(94)90233-X

Young, R. A., and Crow, R. (2014). Paleogene Grand Canyon Incompatible with Tertiary Paleogeography and Stratigraphy. *Geosphere* 10, 664–679. doi:10.1130/GES00973.1

Young, R. A. (2001). "The Laramide-Paleogene History of the Western Grand Canyon Region: Setting the Stage,". *Colorado River Origin and Evolution*. Editors R. A. Young and E. E. Spamer (Grand Canyon, Arizona: Grand Canyon Association), 7–16.

Young, R. A., and Spamer, E. E. (2001). *Colorado River Origin and Evolution*. Grand Canyon, Arizona: Grand Canyon Association Monograph 12, 280.

Zaborac-Reed, S. J., and Leopold, E. B. (2016). Determining the Paleoclimate and Elevation of the Late Eocene Florissant flora: Support from the Coexistence Approach. *Can. J. Earth Sci.* 53, 565–573. doi:10.1139/cjes-2015-0165

Conflict of Interest: The authors declare that the research was conducted in the absence of any commercial or financial relationships that could be construed as a potential conflict of interest.

frontiers in Earth Science

ORIGINAL RESEARCH
published: 17 September 2021
doi: 10.3389/feart.2021.665324

Organic Molecular Paleohypsometry: A New Approach to Quantifying Paleotopography and Paleorelief

Michael T. Hren[1,2]* *and William Ouimet*[1,3]

[1]Department of Geosciences, University of Connecticut, Storrs, CT, United States, [2]Department of Chemistry, University of Connecticut, Storrs, CT, United States, [3]Department of Geography, University of Connecticut, Storrs, CT, United States

Stable isotope paleoaltimetry is one of the most commonly used approaches for quantifying the paleoelevation history of an orogen yet this methodology is often limited to arid to semi-arid climates, mountain systems with a clear orographic rainshadow and terrestrial basins. We present a new approach to reconstructing past topography and relief that uses the catchment-integrated signature of organic molecular biomarkers to quantify the hypsometry of fluvially-exported biomass. Because terrestrially-produced biomolecules are synthesized over the full range of global climate conditions and can be preserved in both terrestrial and marine sediments, the geochemistry of fluvially-transported sedimentary biomarkers can provide a means of interrogating the evolution of topography for a range of environments and depositional settings, including those not well suited for a traditional isotope paleoaltimetry approach. We show an example from Taiwan, a rapidly eroding tropical mountain system that is characterized by high rates of biomass production and short organic residence time and discuss key factors that can influence molecular isotope signal production, transport and integration. Data show that in high relief catchments of Taiwan, river sediments can record integration of biomass produced throughout the catchment. Sedimentary biomarker δ^2H_{nC29} in low elevation river deposition sites is generally offset from the δ^2H_{nC29} value observed in local soils and consistent with an isotope composition of organics produced at the catchment mean elevation. We test the effect of distinct molecular production and erosion functions on the expected δ^2H_{nC29} in river sediments and show that elevation-dependent differences in the production and erosion of biomarkers/sediment may yield only modest differences in the catchment-integrated isotopic signal. Relating fluvial biomarker isotope records to quantitative estimates of organic source elevations in other global orogens will likely pose numerous challenges, with a number of variables that influence molecular production and integration in a river system. We provide a discussion of important parameters that influence molecular biomarker isotope signatures in a mountain system and a framework for employing a molecular paleohypsometry approach to quantifying the evolution of other orogenic systems.

Keywords: paleoelevation, paleotopography, stable isotopes, biomarker, catchment integration

OPEN ACCESS

Edited by:
Paolo Ballato,
Roma Tre University, Italy

Reviewed by:
Yan Bai,
Center for Excellence in Tibetan Plateau Earth Science (CAS), China
Joel Saylor,
University of British Columbia, Canada

***Correspondence:**
Michael T. Hren
michael.hren@uconn.edu

Specialty section:
This article was submitted to Quaternary Science, Geomorphology and Paleoenvironment, a section of the journal Frontiers in Earth Science

Received: *07 February 2021*
Accepted: *30 August 2021*
Published: *17 September 2021*

Citation:
Hren MT and Ouimet W (2021) Organic Molecular Paleohypsometry: A New Approach to Quantifying Paleotopography and Paleorelief. Front. Earth Sci. 9:665324. doi: 10.3389/feart.2021.665324

INTRODUCTION

The development of large orogens can produce fundamental shifts in global physical and chemical fluxes, atmospheric dynamics, biologic change, and even long-term changes in the redox state of the mantle (Kutzbach et al., 1989; Ruddiman and Kutzbach, 1989; Ramstein et al., 1997; Ruddiman, 2013). Records of the paleoelevation history of an orogen or the evolution of orogenic relief are critical for quantifying the feedbacks among climate, erosion and tectonics, yet challenging to produce. As a result, developing reliable records of paleotopography remains one of the grand challenges in the Earth sciences (National Academies of Sciences, Engineering, and Medicine et al., 2020).

Over the past 20 years, numerous approaches have been developed to quantify changes in the topography of an orogen (Axelrod, 1997; Forest et al., 1999; Garzione et al., 2000; Poage and Chamberlain, 2001; Poage and Chamberlain, 2002; Sahagian et al., 2002; Ghosh et al., 2006; Rowley, 2006/8; Clark, 2007; Rowley and Garzione, 2007; Sahagian and Proussevitch, 2007; Hren et al., 2010). Yet, there continues to be a fundamental information gap with regard to approaches for quantifying topographic change for numerous types of orogens. In particular, current methodologies are commonly limited to application in systems that are characterized by simple orographic rainshadows and a semi-arid to arid climate, terrestrial foreland basin systems, and temperate to cool terrestrial settings with mild to moderate chemical weathering rates. There remain few paleotopography reconstruction approaches that are successful for wet, tropical mountain belts with complex climatology and moisture sourcing, or systems with predominantly marine deposition.

Here we discuss a new approach to quantifying the paleohypsometry of an orogen using the stable isotope composition of organic molecular biomarkers that are produced within a catchment and exported via river networks. This approach is similar to the time-tested methods of cosmogenic isotope determination of catchment erosion rate (Bierman, 1994; Bierman and Steig, 1996; Granger et al., 1996; Heimsath et al., 2001). Specifically, in an evolving orogen, organic biomass may be produced throughout a catchment. As an orogen and associated catchments evolve, distinct elevation and precipitation isotope and temperature patterns emerge for all points in the catchment. Biomolecules produced by plants or microorganisms at each point in the landscape can record the signature of precipitation isotopes or temperature at the point of production. These molecules are incorporated into soils, bound to clay particles and mobilized throughout a catchment. The geochemical signature of fluvial sediments sampled along the length of a river profile should therefore reflect changes in the source areas of contributing sediment. If the molecular production function and catchment-wide biomass integration can be characterized, the geochemical record preserved in exported and buried sediments can be used to derive a catchment-specific signature of topography and relief through time.

This method focuses on geochemical signatures preserved in material exported from an orogen through river networks. While there are a host of process-specific relationships to resolve for different climate and erosion regimes, the potential power of this approach is that it greatly expands the possible range of sediments that quantitatively capture orogenic events and provides a template for producing measures of catchment hypsometry through time.

Stable Isotope Paleoaltimetry

There are a number of approaches that have been developed to constrain paleotopography (e.g., Kohn, 2018 and references therein). These generally rely on environmental variables that are related to elevation such as temperature (Quade et al., 2013; Quade et al., 2007), pressure (Sahagian and Maus, 1994; Sahagian et al., 2002; Sahagian and Proussevitch, 2007), plant physiology (Wolfe et al., 1997; Forest et al., 1999), or water isotopes (Garzione et al., 2000; Poage and Chamberlain, 2001; Poage and Chamberlain, 2002; Rowley and Garzione, 2007; Hren et al., 2009). Over the past several decades, stable isotope paleoaltimetry has become one of the most commonly utilized paleoelevation techniques (e.g., Huntington et al., 2015; Wheeler et al., 2016; Fan et al., 2017; Tang et al., 2017; Bershaw et al., 2019; Li et al., 2019; Zhuang et al., 2019). This is due in part, to the abundance of materials that preserve the isotopic signature of ambient water such as carbonates and clays (Chamberlain and Poage, 2000; Sjostrom et al., 2006; Mulch and Chamberlain, 2007; Mulch et al., 2007), volcanic glasses (Cassel et al., 2009; Bershaw et al., 2019; Colwyn et al., 2019; Colwyn and Hren, 2019), fossils (Kohn et al., 2002), and leaf waxes (Polissar et al., 2009; Hren et al., 2010; Anderson et al., 2015; Zhuang et al., 2019). Application of stable isotope-based approaches has provided fundamental insight into how Cordilleran orogens evolve (Fan et al., 2017; Feng et al., 2013; Kent-Corson et al., 2006; Andreas Mulch and Chamberlain, 2007), long-timescale changes in the elevation of orogenic plateaus (Dettman et al., 2003; Ghosh et al., 2006; Molnar et al., 2006; Rowley and Currie, 2006; Hoke et al., 2014; Currie et al., 2016), even the role of tectonic change on biological diversification (Phillips et al., 2013).

Stable isotope paleoaltimetry is founded on the principle that as a moist airmass encounters a topographic barrier, it can undergo lifting, cooling and rainout (Rowley et al., 2001; Rowley and Garzione, 2007; Rowley, 2007). Oxygen and hydrogen fractionation of the rainwater results from the strong temperature-dependence of isotopic partitioning between vapor and liquid or solid phases. Condensation across an orogen progressively removes the "heavy" isotope species producing a characteristic Rayleigh distillation pattern in precipitation that is often described as the isotopic "altitude effect" (Dansgaard, 1964; Gonfiantini et al., 2001) (**Figure 1**).

While frequently applied as a geochemical technique, there are several key requirements for isotope paleoaltimetry to reliably record changes to topography: 1) changes in surface topography must impart a predictable change in the isotopic composition of ambient water and/or local temperature (i.e., signal generation); 2) proxy materials that form in equilibrium with ambient waters (i.e., clays, glasses, carbonates, or organic matter) must record these changes (signal recording); and 3) proxy records of this change must be preserved in sedimentary environments in

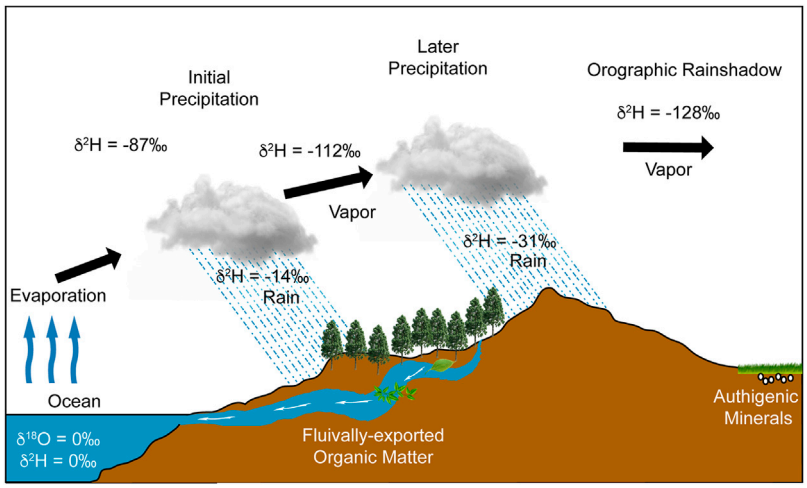

FIGURE 1 | Schematic of the "rainout" effect on precipitation (modified from Hoefs, 1997). Biomaker and organic matter export on the windward side and authigenic mineral formation and preservation within the a basin in the rainshadow.

proximity to the area of evolving topography (signal preservation).

In large accretionary collision zones, sediment is commonly preserved in foreland basin systems - elongate regions of sediment accommodation that form in response to geodynamic processes related to subduction (e.g., DeCelles and Giles, 1996). As orogens evolve, sediment deposition sites can vary from deep marine to fluvial and lacustrine deposition in a range of accommodation spaces. Thus, the sedimentary record of orogenesis spans a range of sediment composition and depositional settings. However, records of paleotopography frequently derive from only the terrestrial sediments associated with orogenesis. The most commonly utilized methodology for paleotopography reconstruction, stable isotope paleoaltimetry, is generally not applicable to marine sediments.

In many terrestrial continental environments such as the western North American interior, the Andes or Tibetan Plateau, prevailing wind directions and the orientation of the orogens produce large "orographic rainshadows" and a clear isotopic shift in precipitation that can be preserved in materials deposited within basin sediments close to the orogen. Conventional stable isotope paleoaltimetry generally assumes an airmass travels over an orogen, imparting a clear "elevation" signature on precipitation isotopes (**Figure 1**). Indeed, most paleoelevation studies utilize materials preserved in basin sediments within an orographic rainshadow. For example, virtually all records of the paleotopography of the Tibetan Plateau are generated from sediments deposited in basins now on the Plateau itself (Rowley et al., 2001; Molnar et al., 2006; Rowley and Currie, 2006; Rowley, 2006/8; Polissar et al., 2009; Xu et al., 2010; Quade et al., 2011; Staisch et al., 2014; Huntington et al., 2015; Currie et al., 2016; Tang et al., 2017; Li et al., 2019), with few studies from the Himalayan front (e.g., Hoke et al., 2014; Grujic et al., 2018).

While most paleotopography approaches require an orographic and isotopic rainshadow, in reality, variables such as atmospheric stability and wind-speed influence the path an airmass travels (e.g., Roe, 2005; Galewsky, 2009; Lechler and Galewsky, 2013). As orogens reach critical elevations, airmasses can travel laterally along a barrier rather than over, producing heterogeneous patterns of isotopes of precipitation in the leeward side of a range (Roe, 2005; Galewsky, 2009; Lechler and Galewsky, 2013; Wheeler et al., 2016). Similarly, changes to thermal heating of the landscape can alter moisture transport and isotope fractionation patterns (Poulsen et al., 2010; Insel et al., 2012; Insel et al., 2013; Botsyun et al., 2019). This can produce highly spatially heterogeneous geochemical signatures of topography. As a result, uplift of an orogen may not always produce clear isotopic signatures of elevation within an orographic rainshadow (e.g., Hren et al., 2009; Insel et al., 2010; Insel et al., 2012; Feng et al., 2013; Insel et al., 2013; Botsyun et al., 2016; Botsyun et al., 2019; Shen and Poulsen, 2019). A prime example of this process is observed in the Himalaya and Tibetan Plateau. Here, water isotope records show a large precipitation isotope gradient on the front of the Himalayan orogen, yet large-scale enrichment of water isotope values with progressive distance into the continental interior (Garzione et al., 2000; Hren et al., 2009; Jay; Quade et al., 2011; Bershaw et al., 2012; Yang et al., 2012; Yang et al., 2012). The isotopic shift that results from progressive mixing of multiple moisture sources combined with increased evaporation in the high elevation, arid landscape of the Tibetan plateau, can dwarf the isotopic signature that is related to elevation and observed on the range front or in close proximity to the orogen.

In contrast to the complex isotopic patterns observed in the leeward side of large orogens, particularly with increasing distance from an orographic barrier, along the range front of virtually all orogens on the globe, isotopes of precipitation generally show a clear and consistent relationship between elevation and water $\delta^{18}O$ or $\delta^{2}H$ and temperature. This geochemical signature can exhibit greater noise at lower elevations (less than 1 km) where local climatic and

atmospheric conditions can dominate (e.g., blocking and temperature inversions). However, over larger topographic ranges (several km) this pattern of temperature and precipitation isotope change in relation to elevation is fairly consistent. This pattern is true in the windward face of the Sierra Nevada (Ingraham and Taylor, 1991), Cascades (Hren, Unpublished), Himalaya (e.g., Garzione et al., 2000; Hren et al., 2009; Li and Garzione, 2017), northern and southern Andes on both east and west sides (Gonfiantini et al., 2001; Stern and Blisniuk, 2002; Smith and Evans, 2007; Saylor et al., 2009; Hoke et al., 2013; Valdivielso et al., 2020), the Alps (Giustini et al., 2016), Southern Alps (Poage and Chamberlain, 2001), topical mountain systems such as the Sierra Oriental of Mexico (Quezadas et al., 2015) and Taiwan (This study), tropical regions within Africa and South America (Gonfiantini et al., 2001), even isolated peaks such as Mauna Loa, Hawaii (Scholl et al., 1996; Scholl et al., 2007) and Mount Kilimanjaro (Zech et al., 2015). In fact, the pattern of precipitation isotopes and temperature as a function of elevation is far simpler to predict for the windward side of an orogen, where the majority of water vapor is removed from an airmass during orographic lifting and cooling, than for the leeward side, where atmospheric oscillations, high degrees of evaporation and mixing of multiple moisture sources can produce complex and spatially heterogeneous water isotope patterns. This observation highlights the need for new paleotopography approaches that take advantage of climatic and isotopic patterns observed on the windward side of an orogen, as well as materials that are preserved in marine deposition sites.

Organic Molecular Biomarkers and Paleoelevation

Terrestrial plants produce a variety of compounds within and on their leaves to minimize water loss and provide protection from predation (Holloway, 1969; Barthlott and Neinhuis, 1997). These molecules are produced in abundance and can be preserved over long timescales with minimal or no isotopic alteration (Schimmelmann et al., 1999; Schimmelmann et al., 2006; Yang and Huang, 2003/3). Plants utilize ambient water during biosynthesis and incorporate the isotopic signature of that water into biomolecules. The chemistry of these molecular compounds records water isotopes modified by factors such as evapotranspiration and carbon assimilation rates (e.g., Ehleringer et al., 1990; Chikaraishi and Naraoka, 2003/6; Chikaraishi et al., 2004; Sachse et al., 2004; Sachse et al., 2004; Sachse et al., 2006; Hou et al., 2008; Sachse et al., 2012). Compound-specific D/H fractionation in plant molecules is primarily dependent on water isotope composition, the biosynthetic pathway (Hayes, 1993) and stomatal water loss in response to water and CO_2 limitation, but integrated soil biomarkers commonly show consistent D/H fractionation in warm/temperate and moist environments (e.g., Sachse et al., 2012; Tipple and Pagani, 2013; Wang et al., 2017). In temperate and tropical environments, soil *n*-alkane δ^2H is correlated with precipitation δ^2H due to ecosystem level homogeneities of the vegetation (e.g. Jia et al., 2008; Tipple and Pagani, 2013; Tipple and Pagani 2013; Bai et al., 2015; Zhuang et al., 2015; Liu et al., 2016; Vogts et al., 2016; Bai et al., 2017; Wang et al., 2017; Liu and An 2019). For example, a study of precipitation isotopes and plant wax δ^2H along an elevation gradient of nearly 4 km on the SE margin of the Tibetan plateau shows a strong correlation between ambient water isotopes and *n*-alkane δ^2H over a range of elevations (Wang et al., 2017). In addition, the magnitude of change in *n*-alkane δ^2H observed on the SE Tibetan Plateau margin mirrors that observed in other regional studies from the SE Asian region (Jia et al., 2008; Bai et al., 2015). Some studies suggest that the relationship between plant wax δ^2H and ambient water may vary as a function of climate and/or elevation in some circumstances, however this remains a subject of debate with recent studies showing no climatic effect on apparent fractionation (Struck et al., 2020), and is similar to questions surrounding uncertainties in water of formation for authigenic minerals and glasses that are commonly used for paleoelevation reconstruction. Plant waxes, including long-carbon chain normal alkanes, can thus provide a geochemical record of ambient water δ^2H with similar or less uncertainty than other commonly used paleoprecipitation isotope proxies such as soil carbonates, clays, or volcanic glass. In addition, the molecules that are produced by plants and some terrestrial microorganisms, can be uniquely identifiable from molecules produced by marine organisms, meaning they can be identified and isolated from marine sediments.

Organic molecular biomarkers are produced by plants and microorganisms over nearly the entire range of global climatic conditions (with the exception of extreme cold environments) and can be preserved in nearly all sedimentary sinks associated with orogenesis. As a result, organic molecular biomarkers are increasingly utilized for paleoclimate/paleohydrology and paleotopography reconstruction (e.g., Polissar et al., 2009; Hren et al., 2010; Aichner et al., 2015; Hepp et al., 2015; Tuthorn et al., 2015; Rohrmann et al., 2016; Schafer et al., 2018; Bliedtner et al., 2020). These molecules can record two specific parameters that are commonly linked to elevation, present and past: 1) the stable isotopic composition of environmental water, and 2) the temperature at which molecules are synthesized. These two variables are related to processes associated with changes to ambient conditions and elevation such as Rayleigh distillation of water vapor during orographic lifting or adiabatic cooling of ambient air as a function of elevation. What is unique about organic molecular biomarkers in comparison to other records of environmental conditions, water isotopes and topography, is that these biomarkers can be produced and preserved on the windward and leeward sides of an orogen and are actually produced in greater abundance in warm and wet environments. As an archive of terrestrial environments, these materials provide a potential record of geochemical conditions on land, independent of whether or not they are preserved in a terrestrial or marine setting.

Organic Molecular Hypsometry: Catchment Integration of Water and Sediment

The $\delta^{18}O$ and δ^2H of stream waters record the precipitation and precipitation isotope-weighted hypsometry of the upstream catchment (e.g., Hren et al., 2009; Rowley et al., 2001; Rowley

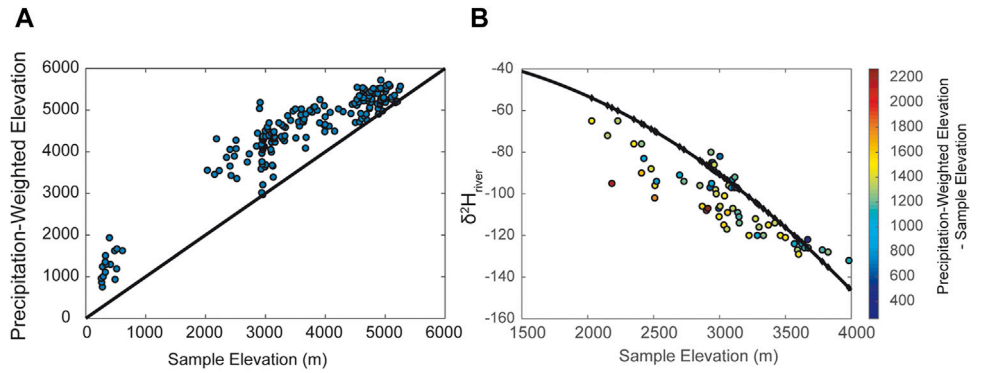

FIGURE 2 | (A) Comparision of sample elevation vs. precipitation weighted elevation for catchments from southern Tibet along the Brahmaputra and tributaries. **(B)** Sample elevation vs. hydeogen isotopes of stream waters from Southern Tibet relative to predicted water isotope δ^2H using a simple model of Rayleigh distillation after Rowley and Peirrehumbert 2001 (Data and predicted δ^2H taken from Hren et al., 2009). Shading of individuals points reflects the difference between the elevation at the location of the river water sample, and the upstream precipitation–weighted elevation for the point. Large deviations between measure δ^2H and pressure δ^2H generally result from significant differences between precipitation–weighted elevation and local sample elevation. Large offsets equal greater water contributions from higher elevations.

and Garzione, 2007). For example, along the Himalayan front, the $\delta^{18}O$ or δ^2H of river water from low sample elevations reflects isotopically depleted values that are consistent with precipitation-weighted elevation (Hren et al., 2009). Thus, the isotopic signature of water at any point on a river will generally reflect the isotopic composition of the precipitation-weighted elevation of the upstream area (**Figure 2**). Conceptually, this principle is quite simple and river water isotope signatures should reflect the distribution of water isotopes throughout the catchment weighted by the contributions from different portions of the basin. Indeed, more than 25 years ago, Norris and others (1996) argued that isotopic records of the Eocene Green River lakes provided clear indication of a high elevation paleo-Uinta Mountain range (Norris et al., 1996).

Annual precipitation δ^2H typically varies by ~15–30‰ per km of elevation in tropical to temperate settings (e.g., Poage and Chamberlain, 2001). The relationship between precipitation isotopes and elevation is most consistent in close proximity to an orogen and tends to increase in noise when the scale of the study area exceeds the scale of the processes that generate the geochemical signal. In large catchments, the isotopic composition of precipitation can vary by more than 100‰ in δ^2H from headwaters to river mouth (**Figure 2**), and the isotopic composition of water at any point along the river (which integrates the entire upstream area) can be quite distinct from the composition of precipitation falling on that point of the landscape. As one moves up a river profile, local elevation increases and catchment size decreases, and the offset between the local elevation of a point on a river and the mean elevation of the upstream area decreases to zero (**Figure 2**). As these come closer together, precipitation-weighted δ^2H becomes identical to ambient precipitation δ^2H.

Like water, fluvially-transported organic biomarkers can record the hypsometry of a catchment through their isotopic composition (where $\delta^2H_{biomarker}$ varies in relation to elevation-dependent variations in source water δ^2H) or in molecules that reflect the temperature of formation at a specific location in the catchment. To first order, plant waxes record the hydrogen isotope composition of water used during growth and show a similar $\Delta\delta^2H_{n\text{-alkane}}$ with elevation as precipitation (e.g., Jia et al., 2008; Bai et al., 2015; Zhuang et al., 2015; Nieto-Moreno et al., 2016; Wang et al., 2017). There are a number of factors that can influence the apparent fractionation between plant waxes and ambient water, including plant-specific differences in evapotranspiration and biosynthesis (e.g., Sachse et al., 2012), and some data suggests potential changes in apparent fractionation with elevation (Bai et al., 2017). However, other data suggests no clear correlation between climate and apparent fractionation (Struck et al., 2020) and numerous studies of biomarkers in soils show a generally consistent fractionation between water and wax (Jia et al., 2008; Tipple and Pagani 2013; Bai et al., 2015; Zhuang et al., 2015; Liu et al., 2016; Vogts et al., 2016; Bai et al., 2017; Wang et al., 2017; Liu and An 2019). Here we present new organic molecular biomarker and water isotope data from soils and rivers of Taiwan to test whether organic biomarker isotopes can reflect catchment integrated signatures of catchment hypsometry.

Taiwan: A Model System for Studying Catchment Integration and Biomarker Records

The island of Taiwan marks the active boundary of the Eurasian and Philippine Sea plates (Teng, 1990) and hosts some of the highest rates of convergence, exhumation (Yu and Chow, 1997; Dadson et al., 2003; Lee et al., 2015), erosion (Hovius et al., 2000; Dadson et al., 2003; Schaller et al., 2005; Siame et al., 2011/4; Derrieux et al., 2014), and precipitation on the globe. The nearly 400 km long orogenic belt is a product of the oblique collision of the north-trending Luzon Arc and the northeast-trending passive margin of southeast China and is commonly used as a model for an active accretionary wedge (Ho, 1986; Y.-H.; Lee et al., 2006;

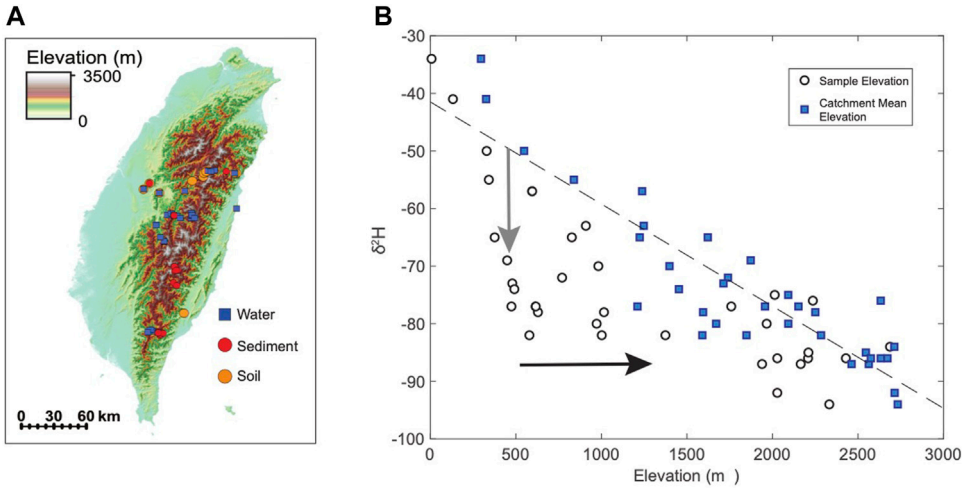

FIGURE 3 | (A) Sample location of water, soil, and sediment samples used in this study. **(B)** δ^2H of river waters (plotted as sample elevation and as catchments mean elevation). Gray arrow represents the deviation between the δ^2H of waters at a sample elevation and the expected δ^2H of local precipitation. Black arrow shows the deviation between the elevation of a sample vs. the elevation of the contributing watershed.

Teng, 1990). Taiwan is also provided as an example of an orogenic system that is in a topographic steady state (Suppe et al., 1981; Willett and Brandon, 2002; Stolar et al., 2007), where the flux of material to the base and front are balanced by the removal of material through physical and chemical erosion (Suppe et al., 1981; Deffontaines et al., 1994; Willett and Brandon, 2002). As a potential steady state orogen, Taiwan serves as an example for understanding the links and feedbacks among tectonics, climate, and erosion (Roe et al., 2006). However, to date, there is no known methodology to constrain the elevation history of orogens such as Taiwan due to the lack of an orographic rainshadow, extremely rapid erosion with minimal onshore terrestrial sediment storage, and the lack of datable carbonates, clays or glasses that could preserve a record of isotopic change due to uplift. As such, it is an ideal location to test a new approach to constraining paleotopographic change.

Taiwan does not have an orographic rainshadow (with high precipitation and moisture sourced from both the east and west), however it is characterized by large temperature and precipitation isotope gradients with elevation. We sampled thirty-three stream waters (**Table 1**) and twelve modern soils (**Table 2**) across Taiwan from 0 to 3,500 m to examine the modern relationship between $\delta^2H_{n\text{-alkane}}$, elevation, and precipitation δ^2H (**Figure 3**). In addition, we collected sixteen river sediments (**Table 3**) at sites adjacent to soil collection localities to assess catchment integration signatures within the organic molecular biomarker pool. Soils were collected from locations in close proximity to the river channel, but well above any modern floodplain to avoid contributions from the modern river, and therefore are assumed to reflect only "local" biomarker production for this study. Fluvial sediments were collected from within the channel in an attempt to capture an integrated sediment signature. For each water and river sediment sample, we used ArcGIS to quantify the histogram of the contributing catchment and key parameters such as max/min/mean catchment elevation. Thus, water and sediment samples are characterized by both a "local" and "catchment mean" elevation that reflects the elevation the samples were collected at and the mean elevation of all areas potentially contributing to the sample collection point. Soil samples are considered "local" and may only be represented as a single sample elevation for the purposes of this work.

For biomarker extraction and analysis, samples were freeze-dried and approximately 150 g of sediment extracted via Soxhlet apparatus using a 400 ml mixture of dichloromethane:methanol (2:1, v:v). Organics were separated by polarity using silica gel column chromatography with hexane, methylene chloride and methanol. The nonpolar hexane fraction (S1) containing *n*-alkanes were further purified by urea adduction and silver nitrate ($AgNO_3$) chromatography to separate branched and cyclic alkanes. The distribution of normal alkanes was quantified using a Thermo-Scientific Trace GC Ultra equipped with a flame ionization detector (FID-GC-FID), using a BP-5 column (30 m × 0.25 mm i.d., 0.25 μm film thickness) with helium as the carrier gas at a constant flow rate of 1.5 ml/min. *n*-alkane δ^2H was analyzed for peaks of sufficient abundance using a GC-Isolink coupled to a Thermo- Scientific MAT 253 isotope ratio mass spectrometer (IRMS) using a BP-5 column (30 m × 0.25 mm i.d., 0.25 μm film thickness). The temperature program was set at 50°C for 1 min, ramped to 180°C at 12°C/min, then ramped to 320°C at 4°C/min and held isothermally for 4 min. During the interval of measurement, standards were analyzed every 4-5 four samples across a range of concentrations to correct for size and scale effects. Repeat analyses throughout the run and for a range of standard concentrations yield an external precision of <5‰ for δ^2H. All values are expressed in standard delta notation relative to VSMOW. The δ^2H of waters was analyzed by the Stable Isotope Laboratory at Louisiana State University and reported relative to VSMOW. Precision is <2‰ for δ^2H.

Water samples span the drainage divide and annual precipitation exceeds several m/yr over the study area. All areas

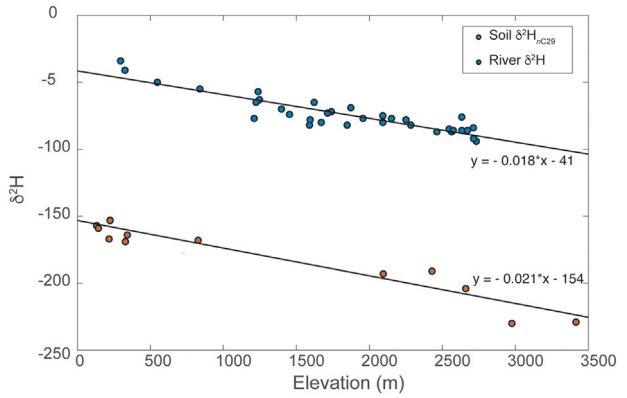

FIGURE 4 | Comparison of river water (mean upstream elevation) vs. δ^2H and soil site elevation vs. *n*-alkane δ^2H_{nC29}.

are also subject to extreme convection events, different seasonal monsoonal precipitation and typhoons. Given the high relief present in the Taiwan orogen, there is significant contribution from high elevation upstream areas to any given point in the river network. Given the extreme climate variability in Taiwan, one might predict that relationships between isotopes of precipitation and elevation would be highly variable between E and W sides and any elevation-dependent signatures could be muted by the large convective rainfall events. River waters represent a time-integrated groundwater signal. When river waters are plotted as a function of area-weighted elevation (the mean elevation of all portions of the catchment that contribute water to a specific sampling point on the river), the data reveal a classic elevation-dependent Rayleigh distillation pattern. Our data show that waters from the north to the south and collected over multiple years produce a well-defined isotope-elevation relationship (~18‰ per 1,000 m) (**Figures 3A,B**) when plotted as a function of catchment mean elevation. We suggest that river waters provide the best estimate of the time-integrated water isotopes incorporated into plants in Taiwan during biosynthesis. This is likely due to the fact that large rainfall events in Taiwan are associated with significant overland flow from the steep slopes of the high relief catchments. Thus, soil water and amount-weighted precipitation δ^2H may not be the same. Thus, we focus on river water isotope data which provide a clear expectation for an elevation-dependent isotopic signal within molecular biomarkers produced across the Taiwan landscape.

Soil-derived long-carbon chain *n*-alkanes show a similar pattern to water δ^2H, in support of our emphasis on river water data, and are suggestive of a consistent relationship between $\delta^2H_{n\text{-alkane}}$ and elevation (**Figure 4**). This pattern is not surprising, given the high degree of primary productivity at nearly all elevations across Taiwan and C3-dominated forests across nearly all elevations of the subtropical study area. The modern biomarker isotope lapse is on the order of ~21‰ for δ^2H_{nC29}, with a slightly lower lapse rate for nC_{31} and higher for nC_{27}. Thus, the isotopic lapse observed in plant biomarkers closely tracks that of river waters. This likely results from the subtropical climate, long-growing season, high precipitation, and angiosperm-dominated forests at all elevations. Thus, we can confidently argue that to first order, plant wax δ^2H records variations in the geochemical signature of precipitation that is a function of elevation and observed in countless other orogenic systems.

The isotope and molecular geochemistry of biomolecules produced throughout a catchment reflect the conditions at the location and time of biosynthesis. The pattern of precipitation isotopes that is observed within a catchment is thus reflected in the isotopic composition of organic biomarkers that are produced throughout that catchment. One might reasonably expect that organics produced at points throughout a catchment would reflect the pattern of water isotopes on the landscape in the form of an organic molecular isoscape. To illustrate this, we show the digital elevation map of the Mugua basin of eastern Taiwan (**Figure 5A**), with the expected biomarker δ^2H_{nC29} overlain as a colormap (**Figure 5B**). The "expected" biomarker δ^2H_{nC29} shown in **Figure 5B** is based on modern measured Taiwan soils from varied elevations (this study) using a simple linear isotope-elevation lapse for illustration purposes. At sea level, we assume a local soil δ^2H_{nC29} of ~-150‰ (equal to our most isotopically enriched, low elevation soil value), and a decrease of ~20‰ per kilometer of elevation, which lies between the measured lapse rate for river waters (18‰) and soils (~21‰).

As plants shed leaves and surface molecules are ablated throughout the catchment, molecular biomarkers can be integrated into soils and bound to clay minerals. Erosion of soils and downslope movement of biomass can then produce a mixed organic molecular isotope signature in river sediments that reflects the degree of integration of biomolecules sourced throughout the catchment (**Figure 5A**). Indeed, work in the Himalaya (e.g., Galy et al., 2011) and recent work in the Gaoping River system of Southeast Taiwan (Chang et al., 2021) shows evidence for downslope transport of organics and indicate that proximity to high relief, steep topography exerts considerable control over the degree of sediment and organic molecular integration in fluvial sediments. One of the great challenges of interpreting fluvial biomarker records is how sediments and organics integrate as they move from source to sink.

Taiwan catchments are generally steep and high relief, often spanning more than 3 km of elevation. Water samples collected at any point in a river reflect all the processes that occur upstream of the sample point. The high topography and steep Taiwan orogen means that the mean elevations of large Taiwan catchments are generally significantly higher (>1 km) than the elevation of the river mouth. Modern Taiwan river water data (this study) shows a significant offset between the isotopic composition of water sampled at a point in a river and the expected composition of precipitation isotopes that might fall at the elevation of the river water sample site (**Figure 3**). The offset between the expected δ^2H composition of precipitation for a given elevation and measured river water δ^2H at that elevation can be up to 30‰. This difference is greatest at low elevations, where the offset between the site elevation and the hypsometric mean elevation of the upstream area is largest.

Modern water δ^2H and soil-derived *n*-alkane δ^2H data can be used to predict the magnitude of isotopic offset that would result from catchment integration of sediments and molecular biomarkers. Data show that in a Taiwan catchment with

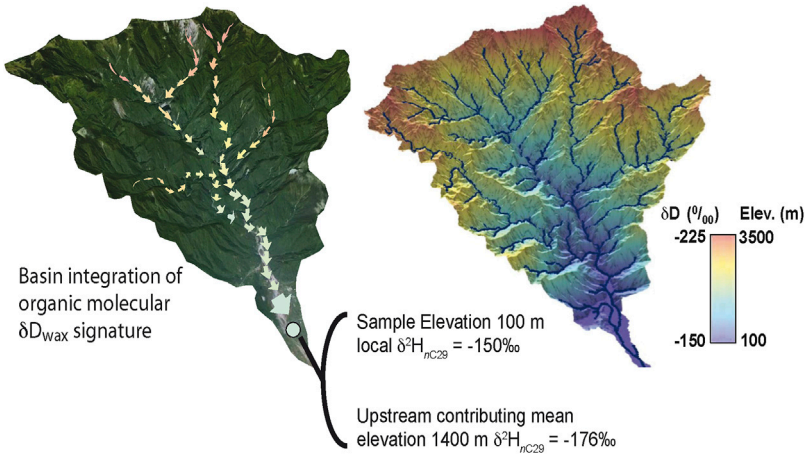

FIGURE 5 | (A) Schematic of basin integration of sediment and contributing molecular components. **(B)** Modeled δ^2H_{nC29} of plant–derived normal alkanes throughout the Mugua basin of eastern Taiwan. Plant wax δ^2H_{nC29} values reflect modern soil δ^2H_{nC29} data from samples acreoss Taiwan.

3.5 km of relief such as the Mugua basin (**Figure 5**), soil *n*-alkane δ^2H should vary from ~150‰ at low elevation to as negative as −225‰ at elevations in excess of 3 km (**Figures 4**, **5**). Erosion and basin integration of this material will bias the isotopic signature of sediments deposited in floodplains and low elevation sites. If the expected change in *n*-alkane δ^2H in plants and soils as a function of elevation is known (signal generation) and one can estimate the contribution of biomolecules from each point in the landscape (a molecular production and erosion function), it is possible to calculate the expected $\delta^2H_{n\text{-alkane}}$ of an integrated sedimentary flux. For example, based on modern Taiwan soil *n*-alkane δ^2H data from varied elevations, the δ^2H of *n*-alkanes deposited at the river mouth within a hypothetical catchment with relief of >3 km and a mean elevation of ~1.25 km, should be ~25‰ more negative than the ambient vegetation growing at that elevation (**Figures 5A,B**), if all areas of the catchment contribute equally to the biomarker flux and the catchment is characterized by a constant apparent fractionation between ambient water and biomarker δ^2H and no loss (oxidation) of *n*-alkanes during transit. In practice, the question is whether or not the organic molecular signal preserved in fluvial sediments is biased to specific elevations or portions of a catchment, much as lithology, relief and landslide frequency might bias cosmogenic isotope signatures of catchment average erosion rates in non-equilibrium landscapes (e.g., Willenbring et al., 2013).

To test this conceptual model of catchment integration of biomarkers, we measured the offset between modern soil-derived *n*-alkane δ^2H_{nC29} and those preserved in fluvial sediments at similar elevations along the river profile. The expectation is that for a given point along a river profile, local soils should show δ^2H_{nC29} values consistent with local elevation whereas samples collected from within the river system should reflect integration of materials sourced from both local and upstream areas. Our data show that the hydrogen isotope signature of *n*-alkanes preserved in modern river sediments are strongly controlled by the hypsometry of the source catchment (**Figure 6**). Specifically, we plot the δ^2H_{nC29} in soils adjacent to river systems as a function of their sample elevation. This is compared to the δ^2H_{nC29} in sediments within the river channel, which should reflect some degree of sediment/organic contributions from upstream contributing areas (**Figure 6A**). The hydrogen isotope signature of fluvially-transported *n*-alkanes sampled at low elevation deposition sites (i.e., floodplains) are commonly depleted by tens of per mil relative to low elevation soils (**Figure 6A**). At higher elevations within the catchment (areas of sediment generation rather than sediment sink), there is no observable offset between soil δ^2H_{nC29} (local signal) and sediment δ^2H_{nC29}. What this means is that not surprisingly, low elevation fluvial sediments preserve a geochemical signature of upstream contributions of organic matter and that this signature can be quite significant. The isotopic shift associated with this downslope transport of organic matter is shown by the grey arrow (**Figure 6A**) which indicates more negative fluvial sedimentary δ^2H_{nC29} relative to local soils at the same sample elevation. For example, river sediments collected at a local elevation of ~500 m may yield a δ^2H_{nC29} value of −180‰, which is 20‰ more negative than one might expect for local soils at that elevation. We can examine what the magnitude of the observed offset between soil and fluvial sediment δ^2H_{nC29} means by considering a scenario where all portions of the landscape contribute equally to the biomarker flux exported in river sediments. If the biomarker δ^2H data from river sediments are plotted as a function of contributing upstream hypsometry (area-weighted elevation), soil and river alkane δ^2H_{nC29} data reconcile and fall along the same profile. This qualitative agreement strongly suggests that exported sediments reflect the hypsometry of organic matter within the catchment and means that if all areas of the upstream catchment equally contribute to this river sediment, we might expect that the mean elevation the sedimentary organic matter is sourced from is actually 1–1.5 km higher than the elevation of the sample point along the river. Thus, the geochemical signal of river sediments records information about catchment integration and source elevation. For Taiwan, the δ^2H_{nC29} of fluvially-

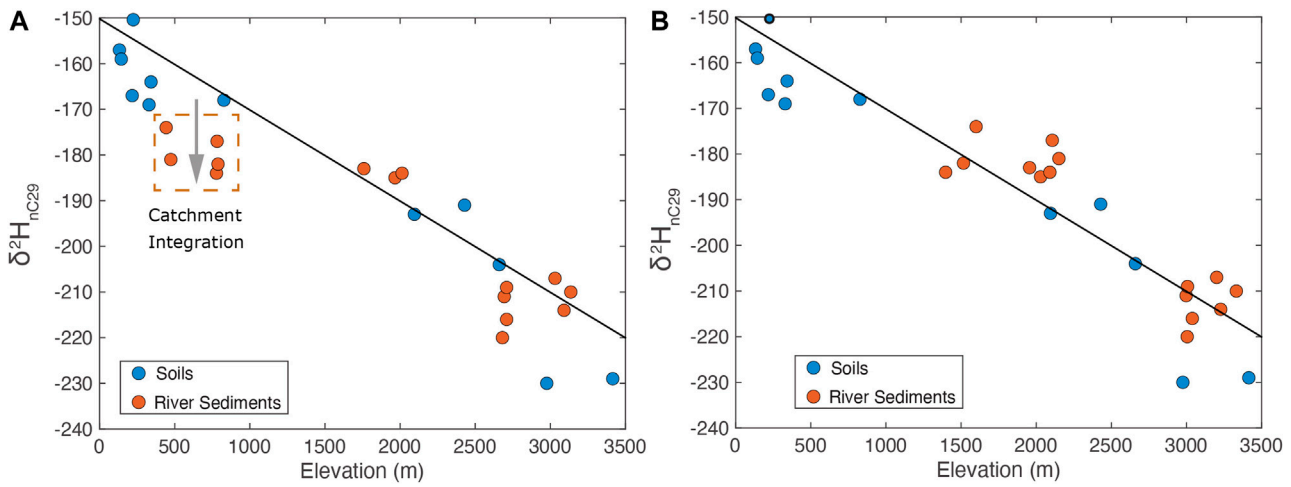

FIGURE 6 | (A) Soil δ^2H_{nC29} (blue circles) and ricer sediment δ^2H_{nC29} (orange circles) vs. sample elevation. Biomarkers produced throughout the Taiwan orogen generally mirror the pattern of δ^2H_{nC29} variation observed in ambient waters. The δ^2H_{nC29} of low elevation, fluvially–deposited alkanes are negative relative to the δ^2H_{nC29} from low elevation soils. The gray arrows shows the direction that downslope transport/catchment integration of biomarkers will shift the δ^2H_{nC29} fluvially–transported alkanes. The solid line represents soil δ^2H_{nC29} data as a function of elevation with a sea level value of –150‰ and a lapse rate of –20‰ per km. **(B)** Soil δ^2H_{nC29} vs. sample collection elevation (blue cicles) and river sediments δ^2H_{nC29} vs. the mean elevation for all areas of the catchment upstream of the river sediment sample location. Plotting river sediments δ^2H_{nC29} as a function of mean elevation of the area upstream of the sample collection elevation reconciles soil (local) and river sediment (integrated) data, demonstrating significant contributions biomarkers produced throughout the catchment to the site of sediment deposition.

transported organics is consistent with the integrated isotopic signature of organic matter produced throughout the catchment (i.e., δ^2H_{nC29} of organics produced at the catchment mean elevation).

In general, there is a solid basis for the expectation that fluvially-transported biomarkers might represent a catchment mean isotopic signature in Taiwan. First, river water isotopes show a clear isotope-elevation relationship when considered in the context of catchment integrated signals (area-weighted contributions). To first order, catchment integration of water should behave similarly to integration of other components of the system (sediment, organic matter). Second, Taiwan's subtropical/tropical climate results in a high degree of biomass production over nearly the entire elevation range of the orogen. All portions of Taiwan catchments contribute to biomarker production, though we recognize that climatic and biologic factors may impose variations in biomarker production rates with elevation. Third, the Taiwan landscape is characterized by extremely high rates of exhumation and erosion (associated with the frequent earthquakes, numerous annual typhoons, and high precipitation rates) and rapid turnover of the soil carbon pool. Hilton et al. (2008) suggests that up to 77% of non-fossil carbon may be exported via large events on the decadal timescale and ^{14}C ages of fluvial biomarkers in Taiwan rivers yield ages on the order of hundreds of years old (Eglington et al., 2021). Rapid export of organics is readily replaced by new vegetation due to the high temperature and abundant precipitation over nearly all elevations within the tropical setting. Thus, there is relatively short carbon residence time in soils and sediments within the Taiwan orogen. Fourth, *n*-alkane δ^2H are not significantly affected by degradation effects that may occur during transport or storage (Zech et al., 2011; Brittingham et al., 2017).

One consideration when measuring biomarker integration signatures is the potential contribution of legacy carbon that can bias the contributions of fluvially-exported leaf waxes. In Taiwan, much of the exposed and rapidly eroding sediments present in the orogen have undergone metamorphism at temperatures in excess of several hundred degrees. This heating results in a breakdown of long-carbon chain normal alkanes that tends to degrade many of the compounds analyzed for organic molecular reconstructions. As a result, legacy carbon is not a significant complication in a setting such as this. Indeed, modern bedrock samples from the slate belt of Taiwan show minimal to no long-carbon chain *n*-alkanes that would potentially bias the modern isotopic signature of organic molecules. This is not the case in all locations of the western foreland, where Plio-Pleistocene sediments are being uplifted and eroded and contain measurable long-chain normal alkanes. However, ancient sediments there are generally characterized by low abundances of target biomarkers, so while they are likely to be a potential contaminant of concern, legacy contributions are minor compared to active input from primary production in the warm and wet tropical climate.

Applying Organic Molecular Paleohypsometry

In recent years, multiple studies have observed downstream transport of organic biomarkers sourced from higher elevations. This includes both plant-derived biomolecules such as *n*-alkanes and fatty acids, as well as soil-derived compounds commonly utilized to reconstruct past temperature. (e.g., Galy et al., 2011; Ponton et al., 2014; Feakins et al., 2016; Hoffmann et al., 2016; Feakins et al., 2018; Usman et al., 2018; Zhuang et al.,

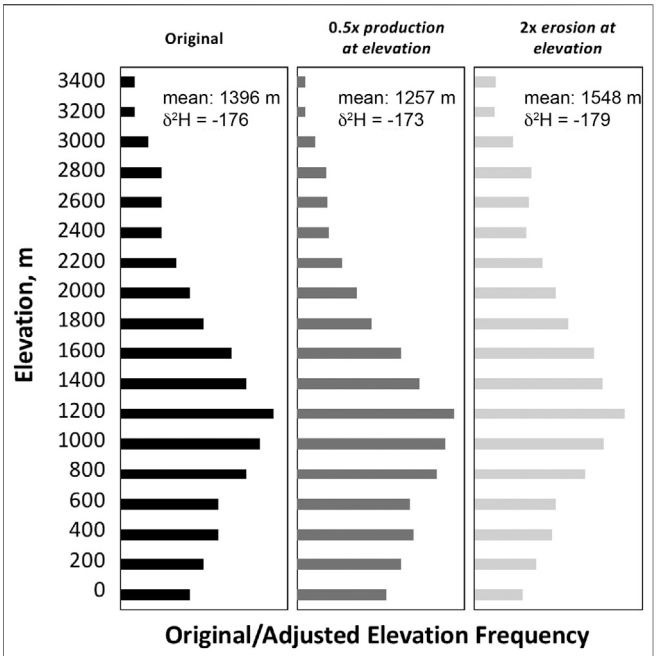

FIGURE 7 | Modeled biomarker–weighted area/elevation distribution for three scenarios of biomass production and erosion as a fuction of elevation. These include **(A)** constant production and erosion as a function of elevation, **(B)** a halving of biomass production from 0 to 3000 m, and **(C)** a doubling of erosion as a function from 0 to 3000 m. Each scenario assumes a constant isotopic lapse rate.

2019; Kirkels et al., 2020). Studies from a range of landscapes show downslope transport of biomarkers can bias geochemical signatures preserved in low elevation sites yet interpreting these data may be complicated. For example, storm and mass wasting events are shown to produce greater mobilization of materials from the steep proportions of a catchment (Wang et al., 2020). While organic molecular paleohypsometry has the potential to provide a means of quantifying changes in the elevation distribution of biomass within an orogen, reliable application of such an approach to ancient sediments requires constraints on several variables. In particular, how does catchment geometry and climate influence the degree of contribution of biomass from across a catchment? Is the contribution of biomolecules uniform or weighted to specific elevation ranges within a catchment? In the Taiwan example shown above, we used the assumption that all areas of the landscape contributed equally to the biomolecule flux. Is this a reasonable assumption? How do changes to climate that are associated with the evolution of an orogen influence the contribution of biomarkers from different portions of a catchment?

Application of an organic molecular paleohypsometry approach requires a number of assumptions to relate measured *n*-alkane δ^2H to catchment/molecular hypsometry. To examine how sensitive resultant paleohypsometry interpretations are to assumptions for molecular production and integration, we modeled three scenarios of biomarker production, erosion and integration for a hypothetical catchment (**Figure 7**; Supplemental file). We use a synthetic catchment histogram (area-elevation distribution) and chose three elevation-dependent functions for production and sediment erosion, and display these in elevation frequency plots (**Figure 7**), where the bar length is proportional to the area-elevation contribution within the hypothetical catchment. The goal of this sensitivity test is to ask the question, how do elevation-dependent differences in the production or erosion of molecular biomarkers affect the integrated signature of materials mobilized through a catchment and deposited in the river mouth. These tests include an assumption of 1) constant biomarker production and sediment erosion at all elevations within a catchment; 2) A decrease in biomarker production by 50% from sea level to 3,000 m and constant sediment erosion for all elevations in the catchment; and 3) constant biomarker production at all elevations in the tropical catchment but a doubling of erosion rates/contribution as a function of elevation from 0 to 3,000 m. These scenarios represent some of the endmember conditions that shape the isotopic signature of catchment integration but are based on observed patterns of organic biomass production or sediment erosion observed in the real world. We include two additional scenarios (shown in **Supplementary Scenario**) where 4) organic production decreases exponentially as a function of elevation by 75% from 0 to 2000 m and almost 90% by 3,000 m and 5) erosion increases exponentially as a function of elevation with more than 8 times the erosion rate at 3,000 m as at sea level, and biomass production decreases by 50% from 0 to 3,000 m.

Differences in production or erosion as a function of elevation will produce a difference in the area-weighted elevation of source materials (biomarkers). For example, if biomarkers are produced and eroded evenly throughout a catchment, mass balance dictates that the mean source elevation of biomarkers exported to the river mouth is equal to the catchment mean elevation. For a constant isotope-elevation lapse rate, the δ^2H of exported biomarkers is therefore equal to the δ^2H of biomarkers produced at the mean elevation. Factors that bias the production or erosion of biomarkers to higher or lower elevations in a catchment would then shift the mean biomarker source elevation higher or lower. To test how different assumptions for biomarker production and sediment erosion as a function of elevation might affect the δ^2H_{nC29} of river sediments and biomarkers transported through the river system and deposited at a river mouth (reflecting the integrated signature of production and erosion throughout a catchment), we use modern Taiwan soil δ^2H_{nC29} data and assume that soils formed at sea level are characterized by a δ^2H_{nC29} of −150‰, and those formed at elevation are modified by a biomarker δ^2H_{nC29} lapse of 20‰ per km elevation in the catchment, similar to the pattern observed in surface waters.

For the different endmember conditions of production/erosion we modeled, there is a distinct pattern of biomarker contribution from different elevations to the overall riverine flux. These produce distinct histograms (**Supplementary Scenarios S1–3** shown in **Figure 7**) with the bar length representing the overall biomarker contribution to the fluvial load from each elevation bin. Each of these scenarios uses the same elevation histogram (the same catchment) but produces distinct mean-

biomass contribution elevations (the abundance-weighted elevation of all organic matter contributing to the fluvial signal at the river mouth) and biomarker δ^2H_{nC29} associated with that mean-biomass value. The calculated δ^2H_{nC29} of each scenario can be thought of as the isotopic composition that one would expect to measure in sediments collected at the river mouth for the hypothetical catchment with the associated production/erosion functions. What this shows is that differences in production/erosion of biomarkers over the range of elevations in a catchment can bias the exported geochemical signal to higher or lower portions of a catchment. Yet, for each of the three different production/erosion functions, the calculated δ^2H_{nC29} values for the sediments deposited at the river mouth are relatively consistent, ranging from −173 to −179 (**Figure 7**). In the context of isotope-elevation lapse rates, this translates to ~300 m elevation difference. What this sensitivity test means is that for these three scenarios of varied molecular production and erosion as a function of elevation, we might expect that fluvial sedimentary biomarkers deposited at the river mouth are 23–29‰ more negative in δ^2H than soils formed in the ambient environment at the sediment deposition site, with mean organic matter contribution elevations of 1,257–1,548 m for the three scenarios. These values closely align with the true area-weighted mean elevation of the catchment of 1,396 m. Thus, regardless of our assumptions of the production/erosion function, the measured δ^2H_{nC29} value of organics sampled at the river mouth closely approximate the δ^2H_{nC29} value of organics one would predict to form at and represent the catchment mean elevation. This quantitative examination is generally consistent with the qualitative agreement shown in **Figure 6B**.

Sensitivity test results suggest that in the context of evolving topography through time, a range of changes to primary production or erosion over time could occur without dramatically influencing the overall relationship between catchment hypsometry and exported isotope signature. If true, then sedimentary records of biomarker δ^2H_{nC29} could reliably record changes in catchment hypsometry through time, even though there remain considerable uncertainties in molecular production and erosion. We caution however, that other changes such as factors that could produce a bimodal distribution of biomarker export as a function of elevation, or climatic effects that result in significant decrease in organic production with elevation, could in fact exert significant changes to the magnitude of offset between the elevation of sediment deposition site, and the elevation predicted based on fluvial biomarker δ^2H_{nC29}. For example, if organic biomarker production decreased by 50% from sea level to 1 km and by 75% at 2 km elevation (**Supplementary Scenarios S4**), the mean source elevation of fluvial sediments sampled at sea level would be 1,004 m, ~400 m below the true catchment mean elevation. Sediments sampled here would be expected to have a δ^2H_{nC29} of ~ −168‰. Such a scenario is not realistic for a setting such as Taiwan as data from tropical settings indicates a decrease in primary productivity on the order of 50% between 0 and 3,000 m elevation (e.g., Mahli et al., 2017). Likewise, if erosion increased exponentially with elevation and organic production decreased by 50% from 0 to 3,000 m (**Supplementary Scenarios S5**), the mean source elevation of organics would be 1720 m and sediments sampled at the river mouth would be expected to have a δ^2H_{nC29} of ~ −182‰. This scenario produces a source elevation ~300 m higher than the catchment mean. These examples illustrate how differences in production or erosion could bias to the elevation distribution and isotopic composition of contributing organics. Importantly however, all scenarios produce values within several hundred meters of the catchment mean elevation.

New data from Taiwan demonstrates the potential utility of fluvially-exported molecular biomarker isotopes to quantify the hypsometry of a catchment and we provide qualitative and quantitative arguments to suggest these data are consistent with a catchment mean elevation signature in a rapidly eroding tropical landscape. However, as a tool for long-term topographic reconstruction, organic molecular paleohypsometry faces similar constraints to the application of cosmogenic isotopes to quantify catchment average erosion rates (after Dosseto and Schaller, 2016). Specifically, what is the molecular production function? Is there temporal variability in the storage in the weathering profile? How does hillslope transport change over time? What are the timescales of river transport and temporary storage in river alluvium? Further refinement of this approach requires greater examination of the above and other factors. Here we provide a summary of several key steps in utilizing a molecular paleohypsometry approach to constrain changes to topography through time or the development of catchment relief.

(1) Molecular production function: The first consideration for application of a molecular paleohypsometry approach is the determination of a molecular production function. For each pixel of a catchment, how many molecules of the biomarker of interest are produced? Is this function uniform, is it biased as a function of elevation? How does climate influence this function? We show one potential example of a molecular production function in **Figures 5A,B** that is based on the modern soil δ^2H_{nC29} and assumes even production throughout the catchment. In reality, primary productivity of terrestrial biomass is generally a function of temperature and water availability (Amthor and Baldocchi, 2001). Studies from tropical forests of Peru show a nearly halving of gross and net primary productivity from sea level to 3,000 m elevation (Malhi et al., 2017). The decrease in primary productivity with elevation could lead to a biomarker production function that is nonlinear with elevation. Strong primary productivity differences could result in substantially greater molecular inputs at lower elevations relative to higher elevation sites. This scenario is obvious for locations with a treeline–above this elevation, molecular inputs would effectively be zero. Likewise, because primary productivity is known to scale with temperature and precipitation, the production function for specific biomolecules may vary as a function of current or paleo climatic conditions.

(2) Decay function: What is the rate of molecular degradation and is there a relationship to transit time? Malhi et al. (2017) show a halving of primary production over a 3 km gradient but also a general increase in carbon residence time with elevation, with longer residence time in higher elevation,

TABLE 1 | River water samples and basin parameters.

Name	Sample Date	δ^2H(water)	Longitude (dec. deg.)	Latitude (dec. deg.)	DEM Elevation	Drainage Area (km^2)	Basin Elevation			
							Elevation Mean (m)	Elevation Minimum (m)	Elevation Maximum (m)	Basin Relief (m)
OT13-01	2013	–65	120.951	23.789	376	16.7	1622	376	2862	2486
OT13-02	2013	–57	120.987	23.801	595	2.2	1238	595	1903	1308
OT13-03	2013	–77	121.014	23.785	474	689.7	2152	467	3822	3355
OT13-04	2013	–69	121.012	23.787	449	794.3	1873	449	3561	3112
OT13-05	2013	–78	120.925	23.549	1015	50.3	2250	1015	3926	2911
OT13-06	2013	–82	120.926	23.551	1002	33.3	2284	1002	3847	2845
OT13-07	2013	–72	120.891	23.587	770	91.0	1740	770	2858	2088
OT13-08	2013	–73	120.850	23.697	479	366.2	1713	479	3926	3447
OT13-09	2013	–63	121.041	23.782	909	0.4	1247	909	1519	610
OT13-10	2013	–82	121.073	23.761	1374	0.9	1848	1374	2264	890
OT13-11	2013	–87	121.174	23.764	2165	0.9	2462	2165	2785	620
OT13-12	2013	–76	121.179	23.785	2236	3.3	2633	2236	2782	546
OT13-13	2013	–86	121.185	23.796	2208	5.3	2633	2208	2928	720
OT13-14	2013	–87	121.177	23.807	1939	38.2	2563	1937	3258	1321
OT13-15	2013	–85	121.182	23.790	2210	0.5	2546	2258	2678	420
OT13-19	2013	–84	121.204	23.765	2687	0.1	2712	2676	2757	81
OT14-02	2014	–82	120.806	22.753	579	115.7	1590	579	2429	1850
OT14-03	2014	–78	120.817	22.759	629	39.5	1594	629	2219	1590
OT14-04	2014	–80	120.836	22.747	972	20.4	1670	972	2219	1247
OT14-05	2014	–70	120.837	22.746	982	2.3	1398	982	1730	748
OT14-07a	2014	–80	120.883	22.731	1966	0.7	2092	1966	2179	213
OT14-08	2014	–75	120.886	22.737	2013	1.7	2092	2012	2202	190
OT14-09	2014	–77	120.900	22.714	1759	2.1	1956	1752	2159	407
OT14-19	2014	–77	120.815	22.756	616	1.3	1211	616	1695	1079
OT14-20	2014	–74	120.789	22.737	491	8.7	1453	491	2703	2212
OT-15-1	2015	–41	120.727	24.016	132	3.0	326	143	744	601
OT-15-2	2015	–50	120.874	23.984	329	3.2	548	320	777	457
OT-15-3	2015	–65	121.111	24.006	827	3.4	1224	858	1568	710
OT-15-7	2015	–86	121.326	24.186	2429	0.3	2672	2448	2810	362
OT-15-9	2015	–94	121.353	24.184	2332	0.4	2732	2326	3001	675

(Continued on following page)

TABLE 1 | (*Continued*) River water samples and basin parameters.

Name	Sample Date	δ^2H(water)	Longitude (dec. deg.)	Latitude (dec. deg.)	DEM Elevation	Drainage Area (km^2)	Basin Elevation			
							Elevation Mean (m)	Elevation Minimum (m)	Elevation Maximum (m)	Basin Relief (m)
OT-15-10A	2015	–86	121.385	24.193	2028	1.5	2575	2016	3052	1036
OT-15-10B	2015	–92	121.385	24.193	2028	5.3	2714	2025	3336	1311
OT-15-11	2015	–55	121.571	24.169	342	0.4	839	359	1315	956
OT-15-12	2015	–34	121.594	23.853	7	6.9	296	19	585	566

TABLE 2 | Modern soil samples and *n*-alkane hydrogen isotopes.

Sample	Latitude	Longitude	Sample Elevation	n	δ^2H_{nC27}	δ^2H_{nC29}	δ^2H_{nC31}	$\delta^2H_{nC27-31}$	ACL
OT-15-1	24.016	120.727	132	2	–145	–157	–167	–157	28.5
19TW-LW19 A	24.171	121.590	144	2	–158	–159	–162	–176	-
OT-15-13	22.913	121.119	217	2	–167	–167	–162	–165	30.0
MT-TW-07b	120.781	24.069	224	1	–145	–150	–154	–151	-
OT-15-2	23.984	120.874	329	2	–167	–169	–162	–164	29.4
OT-15-11	24.169	121.571	342	4	–169	–164	–161	–162	30.5
OT-15-3	24.006	121.111	827	2	–171	–168	–157	–159	30.4
OT-15-4	24.096	121.178	2095	4	–187	–193	–186	–189	30.0
OT-15-7	24.186	121.326	2429	4	–186	–191	–184	–187	28.8
OT-15-8	24.181	121.308	2660	3	–206	–204	–196	–200	29.9
OT-15-6	24.164	121.288	2976	5	–249	–230	–223	–231	29.8
OT-15-5	24.135	121.281	3415	4	–242	–229	–226	–231	29.2

TABLE 3 | Modern Taiwan river sediment *n*-alkane δ^2H, sample elevation, and basin mean elevation.

Sample	Latitdue	Longitude	Sample Elevation	Catchment Mean Elevation	δ^2H_{nC27}	δ^2H_{nC29}	δ^2H_{nC31}	$\delta^2H_{nC27-31}$
OT-13-3	23.785	121.014	474	2151	—	–181	–175	–178
WT-11-12	121.049	23.158	778	1397	–167	–184	–174	–179
WT-11-10	121.018	23.185	782	2107	–168	–177	–175	–175
WH02	120.928	22.729	788	1516	—	–182	–170	–174
OT-14-09	120.9	22.714	1759	1956	–183	–183	–183	–183
WT-14-07A	120.883	22.731	1966	2029	–193	–185	–187	–187
OT-14-08	120.886	22.737	2013	2091	–166	–184	–176	–178
WT-11-4	121.024	23.327	2681	3005	–228	–220	–217	–220
WT-11-02	121.026	23.328	2693	2998	–217	–211	–207	–210
WT-11-03	121.025	23.327	2709	3039	–210	–216	–205	–207
WT-11-01	121.025	23.328	2709	3007	–210	–209	–207	–209
WT-11-07	121.03	23.286	3091	3228	–218	–214	–209	–213
WT-11-6	121.042	23.293	3136	3332	–217	–210	–209	–211
WT-11-05	121.054	23.293	3031	3201	–215	–207	–213	–214
19TW-LW16-Sedi	121.495	24.182	443	1600	–198	–174	–165	–179
MT-TW-07c	24.069	120.781	224	390	—	–166	–164	–165.6

cooler conditions. If changes in primary production as a function of elevation are offset by changes in degradation, it could yield a uniform effective production function across elevation ranges in an orogen.

(3) Erosion function: Organic biomarkers make their way into river sediments through a combination of ablation from leaves, transport in surface or groundwater and soil erosion. Soil erosion rates commonly scale with slope

(Braun et al., 2001; Heimsath et al., 2001) and mass wasting is often a function of relief. Thus, variations in slope throughout a catchment could impart an elevation-dependent bias on organic export. However, sediment generation and transport is not the same as organic molecular generation and transport and contributions will be controlled by a combination of biomass production and soil storage.

(4) Detrital Contribution: Ancient sediments, and in particular, clay-bearing sediments, can contain a significant reservoir of molecular compounds identical to modern plant or microbially-produced biomarkers. Detrital inputs of molecular components are generally of minimal significance in igneous terrain, however of greater concern during stages of orogenesis where there may be significant thin skin deformation and erosion of foreland sediments.

(5) Local and integrated sampling sites: For quantification of paleorelief, reconstructions must incorporate records of low elevation local (*in situ*) water isotopes as well as catchment-integrated signals or models that can approximate both. An example may be a system that is dominated by local inputs for the bulk of time, punctuated by sporadic mass wasting or erosive events. A second example could be a scenario characterized by beds of paleobotanical remains in low elevation floodplain sites (intact fossil leaf materials) in combination with sediment-bound leaf waxes. This is due to the fact that leaf transport studies show that intact leaves preserved in sedimentary sequences generally indicate short transport distances on the order of 100s of meters or less prior to deposition. Longer transport distances are commonly associated with greater degradation and breakage of intact leaves. In contrast, fine-grained sediments that contain leaf waxes bound to mineral (clay) surfaces, may be readily transported long distances. Thus comparison of waxes from intact leaf mats relative to fine grained sediments, may provide one measure of catchment relief.

(6) Elevation-dependent isotope and/or temperature relationships and constant or known fractionations between ambient water and molecular biomarkers. In order to reliably apply an organic molecular paleohypsometry approach, there must be a consistent elevation-dependent geochemical signature and a means of quantifying or constraining the relationship between that signature and organic biomarkers (for plant wax δ^2H_{nC29} this is the apparent fractionation). This relates to the factors that control signal generation.

In total, determination of catchment paleohypsometry requires attention to the key factors identified above. In addition, in order to determine a catchment-wide organic molecular hypsometry, one must assume that: 1) The production of molecular biomarkers is at steady-state at the catchment scale; and 2) Each eroding area of the catchment contributes plant- or microbial-derived biomarkers to the river sediment in proportion to the above defined production, erosion and degradation functions. In practice, it is likely that different climatic/tectonic/erosive regimes will be characterized by distinct relationships between the geochemical signature of organic matter integration and catchment hypsometry. Thus, the relationships observed in Taiwan may not readily translate to every global orogen. In addition, we note that there is a distinct difference between hypsometry and topography and comment that organic molecular hypsometry provides insight into the elevation distribution of source organics in a catchment—it does not specifically record the maximum elevation of an orogen. However, the approach presented above provides a framework for interrogation of fluvially-exported sediments as a record of the topographic evolution of an orogen and the catchments that drain a landscape.

CONCLUSION

We discuss a new approach to investigating the topographic evolution of an orogen using the isotopic signature of plant waxes preserved in fluvial deposits. Modern plant biomarker and water isotope data from Taiwan show that the $\delta^2H_{n\text{-alkane}}$ of fluvially-transported leaf waxes reflects the hypsometry of organic matter produced throughout a catchment. The isotopic composition of exported waxes is generally consistent with the $\delta^2H_{n\text{-alkane}}$ value observed at the catchment mean elevation. As a result, the $\delta^2H_{n\text{-alkane}}$ of detrital organics in fluvially-transported sediments can theoretically provide a record of catchment hypsometry through time. Models for different catchment molecular production and erosion functions show that differences in these factors can shape the relationship between the isotopic signature of fluvially-exported leaf waxes and catchment morphology, yet in our test case the effect of these varied functions is on the order of only several per mil and several hundred meters for highly distinct boundary conditions. Application of this methodology in other orogens will require further investigation of the controls on biomarker integration. Despite this, data presented here demonstrates the potential utility of organic molecular paleohypsometry as a new tool for interrogating the evolution of global orogens.

DATA AVAILABILITY STATEMENT

The original contributions presented in the study are included in the article/**Supplementary Material**, further inquiries can be directed to the corresponding author.

AUTHOR CONTRIBUTIONS

MH conceived the idea, collected and analyzed samples, and wrote the article. WO contributed to field sampling, data analysis and writing the article.

FUNDING

National Science Foundation CAREER 1752815 to MH.

SUPPLEMENTARY MATERIAL

The Supplementary Material for this article can be found online at: https://www.frontiersin.org/articles/10.3389/feart.2021.665324/full#supplementary-material

REFERENCES

Aichner, B., Feakins, S. J., Lee, J. E., Herzschuh, U., and Liu, X. (2015). High-resolution Leaf Wax Carbon and Hydrogen Isotopic Record of the Late Holocene Paleoclimate in Arid Central Asia. *Clim. Past* 11 (4), 619–633. doi:10.5194/cp-11-619-2015

Amthor, J. S., and Baldocchi, D. D. (2001). "Terrestrial Higher Plant Respiration and Net Primary Production," in *Terrestrial Global Productivity*. Editors J. Roy, B. Saugier, and H. A. Mooney (Academic Press), 33–59. doi:10.1016/b978-012505290-0/50004-1

Anderson, V. J., Saylor, J. E., Shanahan, T. M., and Horton, B. K. (2015). Paleoelevation Records from Lipid Biomarkers: Application to the Tropical Andes. *Geol. Soc. America Bull.* 127, 1604–1616. doi:10.1130/b31105.1

Axelrod, D. I. (1997). Paleoelevation Estimated from Tertiary Floras. *Int. Geology. Rev.* 39 (12), 1124–1133. doi:10.1080/00206819709465319

Bai, Y., Chen, C., Fang, X., Liu, X., and Guo, H. (2017). Altitudinal Effect of Soil N-Alkane δD Values on the Eastern Tibetan Plateau and Their Increasing Isotopic Fractionation with Altitude. *Sci. China Earth Sci.* 60 (9), 1664–1673. doi:10.1007/s11430-016-9055-4

Bai, Y., Fang, X., Jia, G., Sun, J., Wen, R., and Ye, Y. (2015). Different Altitude Effect of Leaf Wax N -alkane δD Values in Surface Soils along Two Vapor Transport Pathways, southeastern Tibetan Plateau. *Geochimica et Cosmochimica Acta* 170, 94–107. doi:10.1016/j.gca.2015.08.016

Barthlott, W., and Neinhuis, C. (1997). Purity of the Sacred lotus, or Escape from Contamination in Biological Surfaces. *Planta* 202 (1), 1–8. doi:10.1007/s004250050096

Bershaw, J., Cassel, E. J., Carlson, T. B., Streig, A. R., and Streck, M. J. (2019). Volcanic Glass as a Proxy for Cenozoic Elevation and Climate in the Cascade Mountains, Oregon, USA. *J. Volcanology Geothermal Res.* 381, 157–167. doi:10.1016/j.jvolgeores.2019.05.021

Bershaw, J., Penny, S. M., and Garzione, C. N. (2012). Stable Isotopes of Modern Water across the Himalaya and Eastern Tibetan Plateau: Implications for Estimates of Paleoelevation and Paleoclimate. *J. Geophys. Res.* 117 (D2), a–n. doi:10.1029/2011JD016132

Bierman, P. R. (1994). Using *In Situ* Produced Cosmogenic Isotopes to Estimate Rates of Landscape Evolution: A Review from the Geomorphic Perspective. *J. Geophys. Res.* 99 (B7), 13885–13896. doi:10.1029/94jb00459

Bierman, P., and Steig, E. J. (1996). Estimating Rates of Denudation Using Cosmogenic Isotope Abundances in Sediment. *Earth Surf. Process. Landforms* 21 (2), 125–139. doi:10.1002/(sici)1096-9837(199602)21:2<125:aid-esp511>3.0.co;2-8

Bliedtner, M., Zech, R., Zech, J., Schäfer, I., and Suchodoletz, H. (2020). A First Holocene Leaf Wax Isotope-based Paleoclimate Record from the Semi-humid to Semi-arid South-eastern Caucasian Lowlands. *J. Quat. Sci.* 35 (5), 625–633. doi:10.1002/jqs.3210

Botsyun, S., Sepulchre, P., Donnadieu, Y., Risi, C., Licht, A., and Caves Rugenstein, J. K. (2019). Revised Paleoaltimetry Data show low Tibetan Plateau Elevation during the Eocene. *Science* 363 (6430), eaaq1436. doi:10.1126/science.aaq1436

Botsyun, S., Sepulchre, P., Risi, C., and Donnadieu, Y. (2016). Impacts of Tibetan Plateau Uplift on Atmospheric Dynamics and Associated Precipitation δ18O. *Clim. Past* 12 (6), 1401–1420. doi:10.5194/cp-12-1401-2016

Braun, J., Heimsath, A. M., Chappell, J., and John, C. (2001). Sediment Transport Mechanisms on Soil-Mantled Hillslopes. *Geol.* 29 (8), 683. doi:10.1130/0091-7613(2001)029<0683:stmosm>2.0.co;2

Brittingham, A., Hren, M. T., and Hartman, G. (2017). Microbial Alteration of the Hydrogen and Carbon Isotopic Composition of N-Alkanes in Sediments. *Org. Geochem.* 107, 1–8. doi:10.1016/j.orggeochem.2017.01.010

Cassel, E. J., Graham, S. A., and Chamberlain, C. P. (2009). Cenozoic Tectonic and Topographic Evolution of the Northern Sierra Nevada, California, through Stable Isotope Paleoaltimetry in Volcanic Glass. *Geology* 37 (6), 547–550. doi:10.1130/g25572a.1

Chang, Q., Hren, M., Lin, A. T., Tabor, C., Yu, S.-W., Eley, Y., et al. (2021). Terrestrial Biomarker Isotope Records of Late Quaternary Climate and Source-To-Sink Sediment Transport Processes in Southwestern Taiwan. *Am. J. Sci.* 321, 393–423. doi:10.2475/04.2021.01

Chikaraishi, Y., and Naraoka, H. (2003). Compound-specific δD-δ13C Analyses of N-Alkanes Extracted from Terrestrial and Aquatic Plants. *Phytochemistry* 63 (3), 361–371. doi:10.1016/s0031-9422(02)00749-5

Chikaraishi, Y., Naraoka, H., and Poulson, S. R. (2004). Hydrogen and Carbon Isotopic Fractionations of Lipid Biosynthesis Among Terrestrial (C3, C4 and CAM) and Aquatic Plants. *Phytochemistry* 65 (10), 1369–1381. doi:10.1016/j.phytochem.2004.03.036

Clark, M. K. (2007). The Significance of Paleotopography. *Rev. Mineralogy Geochem.* 66 (1), 1–21. doi:10.2138/rmg.2007.66.1

Colwyn, D. A., Brandon, M. T., Hren, M. T., Hourigan, J., Pacini, A., Cosgrove, M. G., et al. (2019). Growth and Steady State of the Patagonian Andes. *Am. J. Sci.* 319 (6), 431–472. doi:10.2475/06.2019.01

Colwyn, D. A., and Hren, M. T. (2019). An Abrupt Decrease in Southern Hemisphere Terrestrial Temperature during the Eocene-Oligocene Transition. *Earth Planet. Sci. Lett.* 512, 227–235. doi:10.1016/j.epsl.2019.01.052

Currie, B. S., Polissar, P. J., Rowley, D. B., Ingalls, M., Li, S., Olack, G., et al. (2016). Multiproxy Paleoaltimetry of the Late Oligocene-Pliocene Oiyug Basin, Southern Tibet. *Am. J. Sci.* 316 (5), 401–436. doi:10.2475/05.2016.01

Dadson, S. J., Hovius, N., Chen, H., Dade, W. B., Hsieh, M.-L., Willett, S. D., et al. (2003). Links between Erosion, Runoff Variability and Seismicity in the Taiwan Orogen. *Nature* 426 (6967), 648–651. doi:10.1038/nature02150

Dansgaard, W. (1964). Stable Isotopes in Precipitation. *Tell'Us* 16 (4), 436–468. doi:10.1111/j.2153-3490.1964.tb00181.x

DeCelles, P. G., and Giles, K. A. (1996). Foreland basin Systems. *Basin Res.* 8 (2), 105–123. doi:10.1046/j.1365-2117.1996.01491.x

Deffontaines, B., Lee, J.-C., Angelier, J., Carvalho, J., and Rudant, J.-P. (1994). New Geomorphic Data on the Active Taiwan Orogen: a Multisource Approach. *J. Geophys. Res.* 99 (B10), 20243–20266. doi:10.1029/94jb00733

Derrieux, F., Siame, L. L., Bourlès, D. L., Chen, R.-F., Braucher, R., Léanni, L., et al. (2014). How Fast Is the Denudation of the Taiwan Mountain belt? Perspectives from *In Situ* Cosmogenic 10Be. *J. Asian Earth Sci.* 88, 230–245. doi:10.1016/j.jseaes.2014.03.012

Dettman, D. L., Fang, X., Garzione, C. N., and Li, J. (2003). Uplift-driven Climate Change at 12 Ma: a Long δ18O Record from the NE Margin of the Tibetan Plateau. *Earth Planet. Sci. Lett.* 214 (1–2), 267–277. doi:10.1016/s0012-821x(03)00383-2

Dosseto, A., and Schaller, M. (2016). The Erosion Response to Quaternary Climate Change Quantified Using Uranium Isotopes and *In Situ* - Produced Cosmogenic Nuclides. *Earth-Science Rev.* 155, 60–81. doi:10.1016/j.earscirev.2016.01.015

Ehleringer, J. R., White, J. W., Johnson, D. A., and Brick, M. (1990). Carbon Isotope Discrimination, Photosynthetic Gas Exchange and Transpiration Efficiency in Beans and Range Grasses. *Acta Oecologica* 11 (4), 611–625.

Fan, M., Constenius, K. N., and Dettman, D. L. (2017). Prolonged High Relief in the Northern Cordilleran Orogenic Front during Middle and Late Eocene Extension Based on Stable Isotope Paleoaltimetry. *Earth Planet. Sci. Lett.* 457, 376–384. doi:10.1016/j.epsl.2016.10.038

Feakins, S. J., Bentley, L. P., Salinas, N., Shenkin, A., Blonder, B., Goldsmith, G. R., et al. (2016). Plant Leaf Wax Biomarkers Capture Gradients in Hydrogen Isotopes of Precipitation from the Andes and Amazon. *Geochimica et Cosmochimica Acta* 182, 155–172. doi:10.1016/j.gca.2016.03.018

Feakins, S. J., Wu, M. S., Ponton, C., Galy, V., and West, A. J. (2018). Dual Isotope Evidence for Sedimentary Integration of Plant Wax Biomarkers across an Andes-Amazon Elevation Transect. *Geochimica et Cosmochimica Acta* 242, 64–81. doi:10.1016/j.gca.2018.09.007

Feng, R., Poulsen, C. J., Werner, M., Chamberlain, C. P., Mix, H. T., and Mulch, A. (2013). Early Cenozoic Evolution of Topography, Climate, and Stable Isotopes in Precipitation in the North American Cordillera. *Am. J. Sci.* 313 (7), 613–648. doi:10.2475/07.2013.01

Forest, C. E., Wolfe, J. A., Molnar, P., and Emanuel, K. A. (1999). Paleoaltimetry Incorporating Atmospheric Physics and Botanical Estimates of Paleoclimate. *Geol. Soc. America Bull.* 111 (4), 497–511. doi:10.1130/0016-7606(1999)111<0497:piapab>2.3.co;2

Galewsky, J. (2009). Rain Shadow Development during the Growth of Mountain Ranges: An Atmospheric Dynamics Perspective. *J. Geophys. Res.* 114 (F1), F01018. doi:10.1029/2008jf001085

Galy, V., Eglinton, T., France-Lanord, C., and Sylva, S. (2011). The Provenance of Vegetation and Environmental Signatures Encoded in Vascular Plant Biomarkers Carried by the Ganges–Brahmaputra Rivers. *Earth Planet. Sci. Lett.* 304 (1), 1–12. doi:10.1016/j.epsl.2011.02.003

Garzione, C. N., Quade, J., DeCelles, P. G., and English, N. B. (2000). Predicting Paleoelevation of Tibet and the Himalaya from δ18O vs. Altitude Gradients in

Meteoric Water across the Nepal Himalaya. *Earth Planet. Sci. Lett.* 183, 215–229. doi:10.1016/s0012-821x(00)00252-1

Ghosh, P., Garzione, C. N., and Eiler, J. M. (2006). Rapid Uplift of the Altiplano Revealed through 13C-18O Bonds in Paleosol Carbonates. *Science* 311 (5760), 511–515. doi:10.1126/science.1119365

Giustini, F., Brilli, M., and Patera, A. (2016). Mapping Oxygen Stable Isotopes of Precipitation in Italy. *J. Hydrol. Reg. Stud.* 8, 162–181. doi:10.1016/j.ejrh.2016.04.001

Gonfiantini, R., Roberto, G., Michel-Alain, R., Jean-Claude, O., Jean-Charles, F., and Zuppi, G. M. (2001). The Altitude Effect on the Isotopic Composition of Tropical rains. *Chem. Geology* 181 (1-4), 147–167. doi:10.1016/s0009-2541(01)00279-0

Granger, D. E., Kirchner, J. W., and Finkel, R. (1996). Spatially Averaged Long-Term Erosion Rates Measured from In Situ-Produced Cosmogenic Nuclides in Alluvial Sediment. *J. Geology* 104 (3), 249–257. doi:10.1086/629823

Grujic, D., Govin, G., Barrier, L., Bookhagen, B., Coutand, I., Cowan, B., et al. (2018). Formation of a Rain Shadow: O and H Stable Isotope Records in Authigenic Clays from the Siwalik Group in Eastern Bhutan. *Geochem. Geophys. Geosyst.* 19, 3430–3447. doi:10.1029/2017GC007254

Hayes, J. M. (1993). Factors Controlling 13C Contents of Sedimentary Organic Compounds: Principles and Evidence. *Mar. Geology* 113 (1-2), 111–125. doi:10.1016/0025-3227(93)90153-m

Heimsath, A. M., Dietrich, W. E., Nishiizumi, K., and Finkel, R. C. (2001). Stochastic Processes of Soil Production and Transport: Erosion Rates, Topographic Variation and Cosmogenic Nuclides in the Oregon Coast Range. *Earth Surf. Process. Landforms* 26 (5), 531–552. doi:10.1002/esp.209

Hepp, J., Tuthorn, M., Zech, R., Mügler, I., Schlütz, F., Zech, W., et al. (2015). Reconstructing lake Evaporation History and the Isotopic Composition of Precipitation by a Coupled δ18O-δ2H Biomarker Approach. *J. Hydrol.* 529, 622–631. doi:10.1016/j.jhydrol.2014.10.012

Ho, C. S. (1986). A Synthesis of the Geologic Evolution of Taiwan. *Tectonophysics* 125 (1), 1–16. doi:10.1016/0040-1951(86)90004-1

Hoffmann, B., Feakins, S. J., Bookhagen, B., Olen, S. M., Adhikari, D. P., Mainali, J., et al. (2016). Climatic and Geomorphic Drivers of Plant Organic Matter Transport in the Arun River, E Nepal. *Earth Planet. Sci. Lett.* 452 (Suppl. C), 104–114. doi:10.1016/j.epsl.2016.07.008

Hoke, G. D., Aranibar, J. N., Viale, M., Araneo, D. C., and Llano, C. (2013). Seasonal Moisture Sources and the Isotopic Composition of Precipitation, Rivers, and Carbonates across the Andes at 32.5-35.5°S. *Geochem. Geophys. Geosyst.* 14 (4), 962–978. doi:10.1002/ggge.20045

Hoke, G. D., Liu-Zeng, J., Hren, M. T., Wissink, G. K., and Garzione, C. N. (2014). Stable Isotopes Reveal High Southeast Tibetan Plateau Margin since the Paleogene. *Earth Planet. Sci. Lett.* 394, 270–278. doi:10.1016/j.epsl.2014.03.007

Holloway, P. J. (1969). The Effects of Superficial Wax on Leaf Wettability. *Ann. Appl. Biol.* 63 (1), 145–153. doi:10.1111/j.1744-7348.1969.tb05475.x

Hou, J., D'Andrea, W. J., and Huang, Y. (2008). Can Sedimentary Leaf Waxes Record D/H Ratios of continental Precipitation? Field, Model, and Experimental Assessments. *Geochimica et Cosmochimica Acta* 72 (14), 3503–3517. doi:10.1016/j.gca.2008.04.030

Hovius, N., Stark, C. P., Hao-Tsu, C., and Jiun-Chuan, L. (2000). Supply and Removal of Sediment in a Landslide-Dominated Mountain Belt: Central Range, Taiwan. *J. Geology* 108 (1), 73–89. doi:10.1086/314387

Hren, M. T., Bookhagen, B., Blisniuk, P. M., Booth, A. L., and Chamberlain, C. P. (2009). δ18O and δD of Streamwaters across the Himalaya and Tibetan Plateau: Implications for Moisture Sources and Paleoelevation Reconstructions. *Earth Planet. Sci. Lett.* 288 (1), 20–32. doi:10.1016/j.epsl.2009.08.041

Hren, M. T., Pagani, M., Erwin, D. M., and Brandon, M. (2010). Biomarker Reconstruction of the Early Eocene Paleotopography and Paleoclimate of the Northern Sierra Nevada. *Geology* 38 (1), 7–10. doi:10.1130/g30215.1

Huntington, K. W., Saylor, J., Quade, J., and Hudson, A. M. (2015). High Late Miocene-Pliocene Elevation of the Zhada Basin, Southwestern Tibetan Plateau, from Carbonate Clumped Isotope Thermometry. *Geol. Soc. America Bull.* 127, 181–199. doi:10.1130/b31000.1

Ingraham, N. L., and Taylor, B. E. (1991). Light Stable Isotope Systematics of Large-Scale Hydrologic Regimes in California and Nevada. *Water Res. Res.* 27 (1), 77–90.

Insel, N., Poulsen, C. J., and Ehlers, T. A. (2010). Influence of the Andes Mountains on South American Moisture Transport, Convection, and Precipitation. *Clim. Dyn.* 35 (7), 1477–1492. doi:10.1007/s00382-009-0637-1

Insel, N., Poulsen, C. J., Ehlers, T. A., and Sturm, C. (2012). Response of Meteoric δ18O to Surface Uplift - Implications for Cenozoic Andean Plateau Growth. *Earth Planet. Sci. Lett.* 317-318, 262–272. doi:10.1016/j.epsl.2011.11.039

Insel, N., Poulsen, C. J., Sturm, C., and Ehlers, T. A. (2013). Climate Controls on Andean Precipitation δ18O Interannual Variability. *J. Geophys. Res. Atmos.* 118 (17), 9721–9742. doi:10.1002/jgrd.50619

Jia, G., Wei, K., Chen, F., and Peng, P. a. (2008). Soil N-Alkane δD vs. Altitude Gradients along Mount Gongga, China. *Geochimica et Cosmochimica Acta* 72 (21), 5165–5174. doi:10.1016/j.gca.2008.08.004

Kent-Corson, M. L., Sherman, L. S., Mulch, A., and Chamberlain, C. P. (2006). Cenozoic Topographic and Climatic Response to Changing Tectonic Boundary Conditions in Western North America. *Earth Planet. Sci. Lett.* 252 (3–4), 453–466. doi:10.1016/j.epsl.2006.09.049

Kirkels, F. M. S. A., Ponton, C., Galy, V., West, A. J., Feakins, S. J., Peterse, F., et al. (2020). From Andes to Amazon: Assessing Branched Tetraether Lipids as Tracers for Soil Organic Carbon in the Madre de Dios River System. *J. Geophys. Res. Biogeosci.* 125 (Issue 1). doi:10.1029/2019jg005270

Kohn, M. J., Miselis, J. L., and Fre, T. J. (2002). Oxygen Isotope Evidence for Progressive Uplift of the Cascade Range, Oregon. *Earth Planet. Sci. Lett.* 204 (1-2), 151–165. doi:10.1016/s0012-821x(02)00961-5

Kohn, M. J. (2018). Paleoaltimetry: Geochemical and Thermodynamic Approaches, in *Mineralogy & Geochemistry* (Walter de Gruyter GmbH & Co KG), Vol. 66.

Kutzbach, J. E., Guetter, P. J., Ruddiman, W. F., and Prell, W. L. (1989). Sensitivity of Climate to Late Cenozoic Uplift in Southern Asia and the American West: Numerical Experiments. *J. Geophys. Res.* 94 (D15), 18393. doi:10.1029/jd094id15p18393

Lechler, A. R., and Galewsky, J. (2013). Refining Paleoaltimetry Reconstructions of the Sierra Nevada, California, Using Air Parcel Trajectories. *Geology* 41 (2), 259–262. doi:10.1130/g33553.1

Lee, T.-Y., Huang, J.-C., Lee, J.-Y., Jien, S.-H., Zehetner, F., and Kao, S.-J. (2015). Magnified Sediment Export of Small Mountainous Rivers in Taiwan: Chain Reactions from Increased Rainfall Intensity under Global Warming. *PLoS One* 10 (9), e0138283. doi:10.1371/journal.pone.0138283

Lee, Y.-H., Chen, C.-C., Liu, T.-K., Ho, H.-C., Lu, H.-Y., and Lo, W. (2006). Mountain Building Mechanisms in the Southern Central Range of the Taiwan Orogenic Belt—From Accretionary Wedge Deformation to Arc--continental Collision. *Earth Planet. Sci. Lett.* 252 (3-4), 413–422. doi:10.1016/j.epsl.2006.09.047

Li, L., Fan, M., Davila, N., Jesmok, G., Mitsunaga, B., Tripati, A., et al. (2019). Carbonate Stable and Clumped Isotopic Evidence for Late Eocene Moderate to High Elevation of the East-central Tibetan Plateau and its Geodynamic Implications. *GSA Bull.* 131, 831–844. doi:10.1130/b32060.1

Li, L., and Garzione, C. N. (2017). Spatial Distribution and Controlling Factors of Stable Isotopes in Meteoric Waters on the Tibetan Plateau: Implications for Paleoelevation Reconstruction. *Earth Planet. Sci. Lett.* 460, 302–314. doi:10.1016/j.epsl.2016.11.046

Liu, J., and An, Z. (2019). Variations in Hydrogen Isotopic Fractionation in Higher Plants and Sediments across Different Latitudes: Implications for Paleohydrological Reconstruction. *Sci. Total Environ.* 650, 470–478. doi:10.1016/j.scitotenv.2018.09.047

Liu, J., Liu, W., An, Z., and Yang, H. (2016). Different Hydrogen Isotope Fractionations during Lipid Formation in Higher Plants: Implications for Paleohydrology Reconstruction at a Global Scale. *Sci. Rep.* 6, 19711. doi:10.1038/srep19711

Malhi, Y., Girardin, C. A. J., Goldsmith, G. R., Doughty, C. E., Salinas, N., Metcalfe, D. B., et al. (2017). The Variation of Productivity and its Allocation along a Tropical Elevation Gradient: a Whole Carbon Budget Perspective. *New Phytol.* 214 (3), 1019–1032. doi:10.1111/nph.14189

Molnar, P., Houseman, G. A., and England, P. C. (2006). Palaeo-altimetry of Tibet. *Nature* 444 (7117), E4. doi:10.1038/nature05368

Mulch, A., and Chamberlain, C. P. (2007). Stable Isotope Paleoaltimetry in Orogenic Belts the Silicate Record in Surface and Crustal Geological Archives. *Rev. Mineralogy Geochem.* 66 (1), 89–118. doi:10.2138/rmg.2007.66.4

Mulch, A., Teyssier, C., Cosca, M. A., and Chamberlain, C. P. (2007). Stable Isotope Paleoaltimetry of Eocene Core Complexes in the North American Cordillera. *Tectonics* 26 (4), TC4001. doi:10.1029/2006tc001995

National Academies of Sciences, Engineering, and Medicine (2020). Division on Earth and Life Studies, Board on Earth Sciences and Resources, & Committee

on Catalyzing Opportunities for Research in the Earth Sciences (CORES): A Decadal Survey for NSFâ¬"s Division of Earth Sciences. *A Vision for NSF Earth Sciences 2020-2030: Earth in Time*. Washington, DC: National Academies Press.

Nieto-Moreno, V., Rohrmann, A., van der Meer, M. T. J., Sinninghe Damsté, J. S., Sachse, D., Tofelde, S., et al. (2016). Elevation-dependent Changes in N -alkane δ D and Soil GDGTs across the South Central Andes. *Earth Planet. Sci. Lett.* 453, 234–242. doi:10.1016/j.epsl.2016.07.049

Norris, R. D., Jones, L. S., Corfield, R. M., and Cartlidge, J. E. (1996). Skiing in the Eocene Uinta Mountains? Isotopic Evidence in the Green River Formation for Snow Melt and Large Mountains. *Geol.* 24 (5), 403. doi:10.1130/0091-7613(1996)024<0403:siteum>2.3.co;2

Page Chamberlain, C., and Poage, M. A. (2000). Reconstructing the Paleotopography of Mountain Belts from the Isotopic Composition of Authigenic Minerals. *Geology* 28 (2), 115–118. doi:10.1130/0091-7613(2000)028<0115:rtpomb>2.3.co;2

Phillips, M. J., Page, T. J., de Bruyn, M., Huey, J. A., Humphreys, W. F., Hughes, J. M., et al. (2013). The Linking of Plate Tectonics and Evolutionary Divergence. *Curr. Biol.* 23 (14), R603–R605. doi:10.1016/j.cub.2013.06.001

Poage, M. A., and Chamberlain, C. P. (2001). Empirical Relationships between Elevation and the Stable Isotope Composition of Precipitation and Surface Waters: Considerations for Studies of Paleoelevation Change. *Am. J. Sci.* 301 (1), 1–15. doi:10.2475/ajs.301.1.1

Poage, M. A., and Chamberlain, C. P. (2002). Stable Isotopic Evidence for a Pre-middle Miocene Rain Shadow in the Western Basin and Range: Implications for the Paleotopography of the Sierra Nevada. *Tectonics* 21 (4), 16–10. doi:10.1029/2001tc001303

Polissar, P. J., Freeman, K. H., Rowley, D. B., McInerney, F. A., and Currie, B. S. (2009). Paleoaltimetry of the Tibetan Plateau from D/H Ratios of Lipid Biomarkers. *Earth Planet. Sci. Lett.* 287 (1–2), 64–76. doi:10.1016/j.epsl.2009.07.037

Ponton, C., West, A. J., Feakins, S. J., and Galy, V. (2014). Leaf Wax Biomarkers in Transit Record River Catchment Composition. *Geophys. Res. Lett.* 41 (18), 6420–6427. doi:10.1002/2014gl061328

Poulsen, C. J., Ehlers, T. A., and Insel, N. (2010). Onset of Convective Rainfall during Gradual Late Miocene Rise of the central Andes. *Science* 328 (5977), 490–493. doi:10.1126/science.1185078

Quade, J., Breecker, D. O., Daëron, M., and Eiler, J. (2011). The Paleoaltimetry of Tibet: An Isotopic Perspective. *Am. J. Sci.* 311 (2), 77–115. doi:10.2475/02.2011.01

Quade, J., Eiler, J., Daëron, M., and Achyuthan, H. (2013). The Clumped Isotope Geothermometer in Soil and Paleosol Carbonate. *Geochimica et Cosmochimica Acta* 105, 92–107. doi:10.1016/j.gca.2012.11.031

Quade, J., Garzione, C., and Eiler, J. (2007). Paleoelevation Reconstruction Using Pedogenic Carbonates. *Rev. Mineralogy Geochem.* 66 (1), 53–87. doi:10.2138/rmg.2007.66.3

Quezadas, J. P., Silva, A. C., Inguaggiato, S., Ortegadel, M. d. R. S. R. S., Pérez, J. C., and Heilweil, V. M. (2015). Meteoric Isotopic Gradient on the Windward Side of theSierra Madre Oriental Area, Veracruz - Mexico. *Geofísica Internacional* 54 (3), 267–276. doi:10.1016/j.gi.2015.04.021

Ramstein, G., Fluteau, F., Besse, J., and Joussaume, S. (1997). Effect of Orogeny, Plate Motion and Land-Sea Distribution on Eurasian Climate Change over the Past 30 Million Years. *Nature* 386 (6627), 788–795. doi:10.1038/386788a0

Roe, G. H. (2005). OROGRAPHIC PRECIPITATION. *Annu. Rev. Earth Planet. Sci.* 33 (1), 645–671. doi:10.1146/annurev.earth.33.092203.122541

Roe, G. H., Stolar, D. B., and Willett, S. D. (2006). Response of a Steady-State Critical Wedge Orogen to Changes in Climate and Tectonic Forcing. *SPECIAL PAPERS-GEOLOGICAL SOCIETY AMERICA* 398, 227. doi:10.1130/2005.2398(13)

Rohrmann, A., Sachse, D., Mulch, A., Pingel, H., Tofelde, S., Alonso, R. N., et al. (2016). Miocene Orographic Uplift Forces Rapid Hydrological Change in the Southern central Andes. *Sci. Rep.* 6, 35678. doi:10.1038/srep35678

Rowley, D. B., and Currie, B. S. (2006). Palaeo-altimetry of the Late Eocene to Miocene Lunpola basin, central Tibet. *Nature* 439 (7077), 677–681. doi:10.1038/nature04506

Rowley, D. B., and Garzione, C. N. (2007). Stable Isotope-Based Paleoaltimetry. *Annu. Rev. Earth Planet. Sci.* 35 (1), 463–508. doi:10.1146/annurev.earth.35.031306.140155

Rowley, D. B. (2006). Oxygen Isotope Based Paleoaltimetry: Modern Data-Model Comparison and Paleo-Elevation History of Tibet. *Geochimica et Cosmochimica Acta* 70 (18), A541. doi:10.1016/j.gca.2006.06.999

Rowley, D. B., Pierrehumbert, R. T., and Currie, B. S. (2001). A New Approach to Stable Isotope-Based Paleoaltimetry: Implications for Paleoaltimetry and Paleohypsometry of the High Himalaya since the Late Miocene. *Earth Planet. Sci. Lett.* 188 (1-2), 253–268. doi:10.1016/s0012-821x(01)00324-7

Ruddiman, W. F., and Kutzbach, J. E. (1989). Forcing of Late Cenozoic Northern Hemisphere Climate by Plateau Uplift in Southern Asia and the American West. *J. Geophys. Res.* 94 (D15), 18409. doi:10.1029/jd094id15p18409

Ruddiman, W. F. (2013). *Tectonic Uplift and Climate Change*. Springer Science & Business Media.

Sachse, D., Billault, I., Bowen, G. J., Chikaraishi, Y., Dawson, T. E., Feakins, S. J., et al. (2012). Molecular Paleohydrology: Interpreting the Hydrogen-Isotopic Composition of Lipid Biomarkers from Photosynthesizing Organisms. *Annu. Rev. Earth Planet. Sci.* 40, 221–249. doi:10.1146/annurev-earth-042711-105535

Sachse, D., Radke, J., and Gleixner, G. (2004). Hydrogen Isotope Ratios of Recent Lacustrine Sedimentary N-Alkanes Record Modern Climate Variability. *Geochimica et Cosmochimica Acta* 68 (23), 4877–4889. doi:10.1016/j.gca.2004.06.004

Sachse, D., Radke, J., and Gleixner, G. (2006). δD Values of Individual N-Alkanes from Terrestrial Plants along a Climatic Gradient - Implications for the Sedimentary Biomarker Record. *Org. Geochem.* 37 (4), 469–483. doi:10.1016/j.orggeochem.2005.12.003

Sahagian, D. L., and Maus, J. E. (1994). Basalt Vesicularity as a Measure of Atmospheric Pressure and Palaeoelevation. *Nature* 372 (6505), 449–451. doi:10.1038/372449a0

Sahagian, D. L., Proussevitch, A. A., and Carlson, W. D. (2002). Analysis of Vesicular Basalts and Lava Emplacement Processes for Application as a Paleobarometer/Paleoaltimeter. *J. Geology* 110 (6), 671–685. doi:10.1086/342627

Sahagian, D., and Proussevitch, A. (2007). Paleoelevation Measurement on the Basis of Vesicular Basalts. *Rev. Mineralogy Geochem.* 66 (1), 195–213. doi:10.2138/rmg.2007.66.8

Saylor, J. E., Mora, A., Horton, B. K., and Nie, J. (2009). Controls on the Isotopic Composition of Surface Water and Precipitation in the Northern Andes, Colombian Eastern Cordillera. *Geochimica et Cosmochimica Acta* 73 (23), 6999–7018. doi:10.1016/j.gca.2009.08.030

Schäfer, I. K., Bliedtner, M., Wolf, D., Kolb, T., Zech, J., Faust, D., et al. (2018). A δ13C and δ2H Leaf Wax Record from the Late Quaternary Loess-Paleosol Sequence El Paraíso, Central Spain. *Palaeogeogr. Palaeoclimatol. Palaeoecol.* 507, 52–59. doi:10.1016/j.palaeo.2018.06.039

Schaller, M., Hovius, N., Willett, S. D., Ivy-Ochs, S., Synal, H.-A., and Chen, M.-C. (2005). Fluvial Bedrock Incision in the Active Mountain belt of Taiwan Fromin Situ-Produced Cosmogenic Nuclides. *Earth Surf. Process. Landforms* 30 (8), 955–971. doi:10.1002/esp.1256

Schimmelmann, A., Lewan, M. D., Wintsch, R. P., and Wintsch, R. P. (1999). D/H Isotope Ratios of Kerogen, Bitumen, Oil, and Water in Hydrous Pyrolysis of Source Rocks Containing Kerogen Types I, II, IIS, and III. *Geochimica et Cosmochimica Acta* 63 (22), 3751–3766. doi:10.1016/s0016-7037(99)00221-5

Schimmelmann, A., Sessions, A. L., and Mastalerz, M. (2006). HYDROGEN ISOTOPIC (D/H) COMPOSITION OF ORGANIC MATTER DURING DIAGENESIS AND THERMAL MATURATION. *Annu. Rev. Earth Planet. Sci.* 34 (1), 501–533. doi:10.1146/annurev.earth.34.031405.125011

Scholl, M. A., Giambelluca, T. W., Gingerich, S. B., Nullet, M. A., and Loope, L. L. (2007). Cloud Water in Windward and Leeward Mountain Forests: The Stable Isotope Signature of Orographic Cloud Water: ISOTOPE SIGNATURE of CLOUD WATER. *Water Resour. Res.* 43 (12), 5105. doi:10.1029/2007wr006011

Scholl, M. A., Ingebritsen, S. E., Janik, C. J., and Kauahikaua, J. P. (1996). Use of Precipitation and Groundwater Isotopes to Interpret Regional Hydrology on a Tropical Volcanic Island: Kilauea Volcano Area, Hawaii. *Water Resour. Res.* 32 (12), 3525–3537. doi:10.1029/95wr02837

Shen, H., and Poulsen, C. J. (2019). Precipitation δ18O on the Himalaya-Tibet Orogeny and its Relationship to Surface Elevation. *Clim. Past* 15, 169–187. doi:10.5194/cp-15-169-2019

Siame, L. L., Angelier, J., Chen, R.-F., Godard, V., Derrieux, F., Bourlès, D. L., et al. (2011). Erosion Rates in an Active Orogen (NE-Taiwan): A Confrontation of

Cosmogenic Measurements with River Suspended Loads. *Quat. Geochronol.* 6 (2), 246–260. doi:10.1016/j.quageo.2010.11.003

Sjostrom, D. J., Hren, M. T., Horton, T. W., Waldbauer, J. R., and Chamberlain, C. P. (2006). Stable Isotopic Evidence for a Pre--late Miocene Elevation Gradient in the Great Plains--Rocky Mountain Region, USA. *Geol. Soc. America Spec. Pap.* 398, 309–319. doi:10.1130/2006.2398(19)

Smith, R. B., and Evans, J. P. (2007). Orographic Precipitation and Water Vapor Fractionation over the Southern Andes. *J. Hydrometeorology* 8 (1), 3–19. doi:10.1175/jhm555.1

Staisch, L. M., Niemi, N. A., Hong, C., Clark, M. K., Rowley, D. B., and Currie, B. (2014). A Cretaceous-Eocene Depositional Age for the Fenghuoshan Group, Hoh Xil Basin: Implications for the Tectonic Evolution of the Northern Tibet Plateau. *Tectonics* 33 (3), 2013TC003367. doi:10.1002/2013tc003367

Stern, L. A., and Blisniuk, P. M. (2002). Stable Isotope Composition of Precipitation across the Southern Patagonian Andes. *J. Geophys. Res. Atmospheres* 107 (D23), 4667. doi:10.1029/2002jd002509

Stolar, D. B., Willett, S. D., and Montgomery, D. R. (2007). Characterization of Topographic Steady State in Taiwan. *Earth Planet. Sci. Lett.* 261 (3), 421–431. doi:10.1016/j.epsl.2007.07.045

Struck, J., Bliedtner, M., Strobel, P., Bittner, L., Bazarradnaa, E., Andreeva, D., et al. (2020). Leaf Waxes and Hemicelluloses in Topsoils Reflect the δ2H and δ18O Isotopic Composition of Precipitation in Mongolia. *Front. Earth Sci.* 8, 343. doi:10.3389/feart.2020.00343

Suppe, J., Liou, J. G., and Ernst, W. G. (1981). Paleogeographic Origins of the Miocene East Taiwan Ophiolite. *Am. J. Sci.* 281 (3), 228–246. doi:10.2475/ajs.281.3.228

Tang, M., Liu-Zeng, J., Hoke, G. D., Xu, Q., Wang, W., Li, Z., et al. (2017). Paleoelevation Reconstruction of the Paleocene-Eocene Gonjo basin, SE-central Tibet. *Tectonophysics* 712-713, 170–181. doi:10.1016/j.tecto.2017.05.018

Teng, L. S. (1990). Geotectonic Evolution of Late Cenozoic Arc-Continent Collision in Taiwan. *Tectonophysics* 183 (1), 57–76. doi:10.1016/0040-1951(90)90188-e

Tipple, B. J., and Pagani, M. (2013). Environmental Control on Eastern Broadleaf forest Species' Leaf Wax Distributions and D/H Ratios. *Geochimica et Cosmochimica Acta* 111, 64–77. doi:10.1016/j.gca.2012.10.042

Tuthorn, M., Zech, R., Ruppenthal, M., Oelmann, Y., Kahmen, A., del Valle, H. F., et al. (2015). Coupling δ2H and δ18O Biomarker Results Yields Information on Relative Humidity and Isotopic Composition of Precipitation - a Climate Transect Validation Study. *Biogeosciences* 12 (12), 3913–3924. doi:10.5194/bg-12-3913-2015

Usman, M. O., Kirkels, F. M. S. A., Zwart, H. M., Basu, S., Ponton, C., Blattmann, T. M., et al. (2018). Reconciling Drainage and Receiving basin Signatures of the Godavari River System. *Biogeosciences* 15 (11), 3357–3375. doi:10.5194/bg-15-3357-2018

Valdivielso, S., Vázquez-Suñé, E., and Custodio, E. (2020). Origin and Variability of Oxygen and Hydrogen Isotopic Composition of Precipitation in the Central Andes: A Review. *J. Hydrol.* 587, 124899. doi:10.1016/j.jhydrol.2020.124899

Vogts, A., Badewien, T., Rullkötter, J., and Schefuß, E. (2016). Near-constant Apparent Hydrogen Isotope Fractionation between Leaf Wax N-Alkanes and Precipitation in Tropical Regions: Evidence from a marine Sediment Transect off SW Africa. *Org. Geochem.* 96, 18–27. doi:10.1016/j.orggeochem.2016.03.003

Wang, C., Hren, M. T., Hoke, G. D., Liu-Zeng, J., and Garzione, C. N. (2017). Soil N-Alkane δD and Glycerol Dialkyl Glycerol Tetraether (GDGT) Distributions along an Altitudinal Transect from Southwest China: Evaluating Organic Molecular Proxies for Paleoclimate and Paleoelevation. *Org. Geochem.* 107, 21–32. doi:10.1016/j.orggeochem.2017.01.006

Wang, J., Howarth, J. D., McClymont, E. L., Densmore, A. L., Fitzsimons, S. J., Croissant, T., et al. (2020). Long-term Patterns of Hillslope Erosion by Earthquake-Induced Landslides Shape Mountain Landscapes. *Sci. Adv.* 6 (23), eaaz6446. doi:10.1126/sciadv.aaz6446

Wheeler, L. B., Galewsky, J., Herold, N., and Huber, M. (2016). Late Cenozoic Surface Uplift of the Southern Sierra Nevada (California, USA): A Paleoclimate Perspective on lee-side Stable Isotope Paleoaltimetry. *Geology* 44 (6), 451–454. doi:10.1130/g37718.1

Willenbring, J. K., Gasparini, N. M., Crosby, B. T., and Brocard, G. (2013). What Does a Mean Mean? the Temporal Evolution of Detrital Cosmogenic Denudation Rates in a Transient Landscape. *Geology* 41 (12), 1215–1218. doi:10.1130/g34746.1

Willett, S. D., and Brandon, M. T. (2002). On Steady States in Mountain Belts. *Geol.* 30 (2), 175–178. doi:10.1130/0091-7613(2002)030<0175:ossimb>2.0.co;2

Wolfe, J. A., Schorn, H. E., Forest, C. E., and Molnar, P. (1997). Paleobotanical Evidence for High Altitudes in Nevada during the Miocene. *Science*, 276, 1672–1675. doi:10.1126/science.276.5319.1672

Xu, Q., Ding, L., Zhang, L., Yang, D., Cai, F., Lai, Q., et al. (2010). Stable Isotopes of Modern Herbivore Tooth Enamel in the Tibetan Plateau: Implications for Paleoelevation Reconstructions. *Chin. Sci. Bull.* 55 (1), 45–54. doi:10.1007/s11434-009-0543-2

Yang, H., and Huang, Y. (2003). Preservation of Lipid Hydrogen Isotope Ratios in Miocene Lacustrine Sediments and Plant Fossils at Clarkia, Northern Idaho, USA. *Org. Geochem.* 34 (3), 413–423. doi:10.1016/s0146-6380(02)00212-7

Yang, X., Xu, B., Yang, W., and Qu, D. (2012). The Indian Monsoonal Influence on Altitude Effect of δ 18O in Surface Water on Southeast Tibetan Plateau. *Sci. China Earth Sci.* 55, 438–445. doi:10.1007/s11430-011-4342-7

Yu, H.-S., and Chow, J. (1997). Cenozoic Basins in Northern Taiwan and Tectonic Implications for the Development of the Eastern Asian continental Margin. *Palaeogeogr. Palaeoclimatol. Palaeoecol.* 131, 133–144. doi:10.1016/s0031-0182(96)00124-1

Zech, M., Pedentchouk, N., Buggle, B., Leiber, K., Kalbitz, K., Marković, S. B., et al. (2011). Effect of Leaf Litter Degradation and Seasonality on D/H Isotope Ratios of N-Alkane Biomarkers. *Geochimica et Cosmochimica Acta* 75 (17), 4917–4928. doi:10.1016/j.gca.2011.06.006

Zech, M., Zech, R., Rozanski, K., Gleixner, G., and Zech, W. (2015). Don-alkane Biomarkers in Soils/sediments Reflect theδ2H Isotopic Composition of Precipitation? A Case Study from Mt. Kilimanjaro and Implications for Paleoaltimetry and Paleoclimate Research. *Isotopes Environ. Health Stud.* 51 (4), 508–524. doi:10.1080/10256016.2015.1058790

Zhuang, G., Pagani, M., Chamberlin, C., Strong, D., and Vandergoes, M. (2015). Altitudinal Shift in Stable Hydrogen Isotopes and Microbial Tetraether Distribution in Soils from the Southern Alps, NZ: Implications for Paleoclimatology and Paleoaltimetry. *Org. Geochem.* 79, 56–64. doi:10.1016/j.orggeochem.2014.12.007

Zhuang, G., Zhang, Y. G., Hourigan, J., Ritts, B., Hren, M., Hou, M., et al. (2019). Microbial and Geochronologic Constraints on the Neogene Paleotopography of Northern Tibetan Plateau. *Geophys. Res. Lett.* 46 (3), 1312–1319. doi:10.1029/2018gl081505

Conflict of Interest: The authors declare that the research was conducted in the absence of any commercial or financial relationships that could be construed as a potential conflict of interest.

Publisher's Note: All claims expressed in this article are solely those of the authors and do not necessarily represent those of their affiliated organizations, or those of the publisher, the editors and the reviewers. Any product that may be evaluated in this article, or claim that may be made by its manufacturer, is not guaranteed or endorsed by the publisher.

Advantages of publishing in Frontiers

OPEN ACCESS
Articles are free to read for greatest visibility and readership

FAST PUBLICATION
Around 90 days from submission to decision

HIGH QUALITY PEER-REVIEW
Rigorous, collaborative, and constructive peer-review

TRANSPARENT PEER-REVIEW
Editors and reviewers acknowledged by name on published articles

Frontiers
Avenue du Tribunal-Fédéral 34
1005 Lausanne | Switzerland

Visit us: www.frontiersin.org
Contact us: frontiersin.org/about/contact

REPRODUCIBILITY OF RESEARCH
Support open data and methods to enhance research reproducibility

DIGITAL PUBLISHING
Articles designed for optimal readership across devices

FOLLOW US
@frontiersin

IMPACT METRICS
Advanced article metrics track visibility across digital media

EXTENSIVE PROMOTION
Marketing and promotion of impactful research

LOOP RESEARCH NETWORK
Our network increases your article's readership